Experiments and modelling of plasma-based N_2 fixation and CO_2 conversion:

a new chapter towards sustainable energy transition

Ivan Tsonev

Supervisor **Prof. Dr. Annemie Bogaerts**

Thesis submitted for the degree of Doctor of Science
Faculty of Science | Antwerp, 2025

University of Antwerp

Faculteit Wetenschappen
Departement Chemie

Experiments and modelling of plasma-based N_2 fixation and CO_2 conversion: a new chapter towards sustainable energy transition

Proefschrift voorgelegd tot het behalen van de graad
Doctor in de wetenschappen
Aan de Universiteit Antwerpen
Te verdedigen door

Ivan Tsonev
Promotor: prof. dr. Annemie Bogaerts
Antwerpen, 2025

Juryvoorzitter
Prof. dr. Patrice Perreault, Universiteit Antwerpen, België

Promotor
Prof. dr. Annemie Bogaerts, Universiteit Antwerpen, België
Leden
Prof. dr. Dirk Van Dyck, Universiteit Antwerpen, België
Prof. dr. Siegfried Denys, Universiteit Antwerpen, België
Prof. dr. Richard van de Sanden, TU Eindhoven, Nederland
Dr. Anton Nikiforov, Universiteit Gent, België
Prof. dr. Stanimir Kolev, Sofia University "St. Kliment Ohridski", Bulgaria

The PhD researcher and supervisor declare that the PhD research was conducted according to the principles of scientific integrity, as mentioned in the general PhD regulations and charter for PhD researchers of UAntwerp and the integrity charter for PhD researchers and supervisors affiliated with the University of Antwerp.

Universiteit Antwerpen
Faculteit Wetenschappen
Groenenborgerlaan 171, 2610, Antwerpen, België

Onderzoekgroep PLASMANT
Plasma Lab for Applications in Sustainability and Medicine – ANTwerp

Summary

Plasma-based gas conversion is gaining traction as a potential technology capable of aiding the green transition. The aim of this thesis is to develop a better understanding of the underlying processes governing plasma-based N_2 fixation into NO, and plasma-based CO_2 conversion. Indeed, despite its potential, plasma-based gas conversion exhibits somewhat limited energy efficiency. Hence, it is imperative to look for ways to push beyond thermodynamic equilibrium and understand the potential limitations of the technology.

Chapter 1 explores the impact of CO_2 emissions on global warming and the potential of plasma-based gas conversion technologies to decarbonize the chemical industry. We show that plasma-based gas conversion is a promising solution, enabling processes like CO_2 splitting and N_2 fixation. We further show various plasma types and discharge methods, for their efficiency, and we discuss the current state-of-the-art on plasma-based N_2 oxide production, which is the main topic of this work.

Chapter 2 presents a novel computational fluid dynamics (CFD) plasma model, developed for N_2 plasma, to explore how the cathode emission mechanism influences the plasma discharge in a direct current arc, and to determine which design is more suitable for gas conversion applications. Indeed, direct current discharges are among the most investigated plasma types in literature for gas conversion applications. They can exist in two modes: arc and glow, depending on the emission mechanisms on the cathode surface. Experimental investigations on how the different mode influences the plasma columns are scarce and difficult to execute: they require a complicated design in order to cool the cathode sufficiently, to make it transition into a glow discharge with currents higher than 100 mA. We investigated how the glow and arc regimes influence the plasma column, by developing a novel CFD plasma model, which resolves the plasma sheaths near the cathode by incorporating secondary electron emission and thermionic field emission (characteristic for the glow and arc, respectively). The model shows that arc discharges will be more efficient than glow discharges for gas conversion applications.

Chapter 3 experimentally explores the performance of N_2 fixation in a direct current arc reactor, and more specifically the effect of elevated pressures in a rotating gliding arc discharge. We show that elevating the pressure slightly (from 0 to 3 barg) reduces the energy cost and increases the production rate for NO and NO_2 formation. Indeed, pressure – an often overlooked parameter in plasma-based gas conversion applications - proves to be one of the utmost important variables in pushing the limits of the process.

Chapter 4 focuses on CO_2 splitting, and presents a novel six-temperature computational model for pulsed CO_2 plasma, which is aimed to be compatible with CFD models, as

developed in Chapter 2. Indeed, CFD simulations of plasma discharges, focusing on vibrational-translational non-equilibrium, are either scarce, or employ approximations that make these simulations unsuitable for reactor design and predictive modelling. This is because such processes are traditionally modelled by utilizing a large number of reactions in order to computationally resolve the vibrationally excited states. In this chapter, we present a new, six-temperature plasma model that overcomes these limitations by modelling each of the vibrational modes with energy balance equations instead of a group of individual particles, significantly reducing the computational load. We validate the model against a low-pressure pulsed glow discharge in CO_2, and we find good agreement between the experimental measurements and the model predictions. In addition, we revealed the importance of cluster ions and negative ions on the reduced electric filed, which were not included in previous works investigating this type of discharge.

Chapter 5 presents a follow-up computational study, in which the model developed in Chapter 4 is extended to plasma-based N_2 fixation, to determine the minimum energy cost at atmospheric pressure under vibrational-translational non-equilibrium and chemical non-equilibrium conditions. We employ rate coefficients recently published in the Stellar database and show that the theoretical minimum of 0.2 MJ/(mol N) established in the 1980s cannot be achieved at atmospheric pressure. In addition, we demonstrate that vibrational-translational non-equilibrium cannot be exploited for reducing the energy cost for N_2 fixation. Instead, we present a novel effect – namely the thermal production of NO under chemical non-equilibrium – that may push the boundaries beyond thermodynamic equilibrium.

Finally, **Chapter 6** summarizes the work conducted in this thesis and presents a strategy for future improvement of plasma-based N_2 fixation, and gas conversion in general.

Samenvatting

Plasmagebaseerde gasconversie wint aan interesse als een veelbelovende technologie die kan bijdragen aan de groene transitie. Het doel van deze thesis is om een beter inzicht te ontwikkelen in de onderliggende processen van plasmagebaseerde N_2-fixatie naar NO en plasmagebaseerde CO_2-conversie. Ondanks het potentieel vertoont plasmagebaseerde gasconversie een beperkte energie-efficiëntie. Daarom is het essentieel om manieren te zoeken om voorbij het thermodynamisch evenwicht te gaan, en de mogelijke beperkingen van de technologie te begrijpen.

Hoofdstuk 1 onderzoekt de impact van CO_2-emissies op de opwarming van de aarde en het potentieel van plasmagebaseerde gasconversie om de chemische industrie te decarboniseren. We tonen aan dat plasmagebaseerde gasconversie een veelbelovende oplossing is, die processen zoals CO_2-splitsing en N_2-fixatie mogelijk maakt. Verder bespreken we verschillende plasmatypes en ontladingsmethoden met betrekking tot hun efficiëntie, en we geven een overzicht van de huidige stand van zaken op het gebied van plasmagebaseerde stikstofoxideproductie, wat het centrale onderwerp van dit werk is.

Hoofdstuk 2 presenteert een nieuw computationeel vloeistofdynamisch (CFD) plasmamodel, ontwikkeld voor N_2-plasma, om te onderzoeken hoe het kathode-emissiemechanisme de plasma-ontlading beïnvloedt in een gelijkstroomboog en om te bepalen welk ontwerp het meest geschikt is voor gasconversietoepassingen. Gelijkstroomontladingen behoren tot de meest onderzochte plasmatypes in de literatuur voor gasconversie. Ze kunnen bestaan in twee regimes: boog en gloed, afhankelijk van de emissiemechanismen op het kathode-oppervlak. Experimenteel onderzoek naar hoe deze verschillende regimes de plasmakolom beïnvloeden is schaars en moeilijk uit te voeren, omdat hiervoor een complex ontwerp nodig is om de kathode voldoende te koelen en zo een overgang naar een gloedontlading mogelijk te maken bij stromen hoger dan 100 mA. In dit hoofdstuk ontwikkelen we een nieuw CFD-plasmamodel dat de zone nabij de kathode simuleert door secundaire elektronenemissie en thermionische veldemissie (respectievelijk kenmerkend voor het gloed- en boogregime) te integreren. Het model toont aan dat boogontladingen efficiënter zullen zijn dan gloedontladingen voor gasconversietoepassingen.

Hoofdstuk 3 onderzoekt experimenteel de prestaties van N_2-fixatie in een gelijkstroomboogreactor, en meer specifiek het effect van verhoogde drukken in een roterende glijdende boogontlading. We tonen aan dat een lichte drukverhoging (van 0 tot 3 barg) de energiekosten verlaagt en de productie van NO en NO_2 verhoogt. Druk – een vaak over het hoofd geziene parameter in plasmagebaseerde gasconversietoepassingen – blijkt een van de belangrijkste variabelen te zijn bij het verbeteren van de resultaten van gasconversie.

Hoofdstuk 4 richt zich op CO_2-splitsing en presenteert een nieuw zes-temperaturen computationeel model voor gepulseerd CO_2-plasma, dat compatibel is met CFD-modellen zoals ontwikkeld in Hoofdstuk 2. CFD-simulaties van plasma-ontladingen met nadruk op vibratie-translatie-onevenwicht zijn zeldzaam of maken gebruik van benaderingen die ze ongeschikt maken voor reactorontwerp en voorspellende modellering. Traditioneel worden dergelijke processen gemodelleerd door een groot aantal reacties in rekening te brengen om de vibrationeel-geëxciteerde toestanden computationeel te beschrijven. In dit hoofdstuk presenteren we een nieuw plasmamodel met zes temperaturen dat deze beperkingen overwint door elke vibratiemodus te modelleren met energiebalansvergelijkingen in plaats van met afzonderlijke energietoestanden, wat de rekentijd aanzienlijk vermindert. We valideren het model met een lage-druk gepulseerde gloedontlading in CO_2 en vinden een goede overeenstemming tussen de experimentele metingen en de modelresultaten. Bovendien onthullen we het belang van clusterionen en negatieve ionen voor het gereduceerde elektrisch veld, die in eerdere studies over dit type ontlading niet werden meegenomen.

Hoofdstuk 5 presenteert een vervolgstudie, waarin het in Hoofdstuk 4 ontwikkelde model wordt uitgebreid naar plasmagebaseerde N_2-fixatie om de minimale energiekost bij atmosferische druk te bepalen onder vibratie-translatie-onevenwicht en chemisch onevenwicht. We gebruiken recent gepubliceerde reactiesnelheidscoëfficiënten uit de Stellar-database en tonen aan dat het theoretische minimum van 0,2 MJ/(mol N), gerapporteerd in de jaren 1980, niet haalbaar is bij atmosferische druk. Bovendien laten we zien dat vibratie-translatie-onevenwicht niet kan worden benut om de energiekosten van N_2-fixatie te verlagen. In plaats daarvan presenteren we een nieuw effect – namelijk de thermische productie van NO onder chemisch onevenwicht – dat de grenzen van het thermodynamisch evenwicht mogelijk kan verleggen.

Tot slot vat **Hoofdstuk 6** het werk in deze thesis samen en presenteert het een strategie voor toekomstige verbeteringen van plasmagebaseerde N_2-fixatie en gasconversie in het algemeen.

Acknowledgements

If I have seen further, it is by standing on the shoulders of giants.

Isaac Newton

Finally, the time came to finish another chapter in my life. Reaching this point has been a long journey, which started very long ago in a small town in Bulgaria. I wouldn't have been here and accomplished what I have, if it was not for the teachers that believed in me from the start, and gave me the support and the knowledge to push forward. So, I would first like to thank Nadezhda Tsocheva and Svilen Rusev, who taught me from a very young age to be critical, and gave me the tools to pave my own path.

I want to thank Todor for introducing me to the field of plasma and being my very close friend throughout this journey. I want to thank doc. Benova for giving me the knowledge and opportunities to develop my skills, and most importantly allowing me to be myself. Without both of you, I would have never reached where I am now, so I am eternally grateful. I want to thank Stanimir, not only for developing me as a scientist, but also for the incredible discussions and friendship that resulted from this. I will never forget our long and long meetings, discussing problems of science but also of life.

Arriving in Belgium came with its difficulties. I am 100 % sure that, if it wasn't for Georgi and Anja, I would have lost it the first year. I am very grateful for your help! I want to thank Kevin and Hamid for welcoming me in the beginning and being there when I needed them.

Colin, my Irish brother, thank you for always being there for me, always ready to oppose me and expand my field of view. Josh, my English brother, for always being ready to help and always keeping the mood cheerful. I want to thank my Belgian sister, Rani, for showing me the Belgian way, bringing order to my messy mind and being there every morning for the "what documentary I watched last night". I also want to thank my partner, Sarah, for supporting me, bringing joy to my grey life and being there for me, while being exposed to the worst part of my frustrations.

I want to thank Yury, for introducing me to craft beer, always being critical and always bringing the good times with him. Omario, for bringing the smile to the office and supporting my offensive towards certain cuisines and culture. Pepijn, for always being the voice of reason at lunch. I want to thank Mahdi, for being such a good friend and introducing me to the Persian cuisine. I want to thank Callie, for always bringing the good vibes and showing me how to be a more balanced person.

I want to thank everyone from PLASMANT, for handling my difficult personality: Robin, Joran, Mac, Hugo, Sara, Elli, Ed, Cedric, Igor, Greg, Stijn, Helder, Rubén, Stein, Vojta, Ata,

Karen, Karel, Priyanka, Herman, Arne and Luc. Special thanks to Matthias, for helping me with the last chapter of the thesis and for always challenging my views.
I want to thank Annemie, for giving me the freedom and opportunities to develop as a researcher. I wouldn't be who I am now, without your exceptional guidance. Thanks to you, I not only become a better researcher, but also a better person. I am eternally grateful for all of your help! I hope that one day I can do at least 1 % of what you are doing on a daily basis.
I would have never made it, if it wasn't for my Bulgarian family – Plamen and Dayana. Thank you for being there for me for all these years, thank you for the long dinner calls, despite that I am away, and thank you for always supporting me. I want to thank Angel, for always cheering me up, being there for me and always helping me relax, making new memories every time I go back. I want to thank Yordan, for always believing in me, for the long conversations unravelling the philosophy of life and for the rakia and wine. Georgi (different Georgi from the one above) and Vasilena, for never forgetting about me, always calling and being there despite their busy schedules. Chavdar, for challenging the foundations of physics together with me and never missing the opportunity to discuss challenging topics over a bottle of rakia. I want to thank Georgi (third one, different from the ones above) for always believing in me and helping me since I was a child. I want to thank Nikola, for being my scientific mentor and friend since high school. You showed me the level of dedication needed in order to achieve my goals and always supported me!
Finally, I want to thank my mother Kornelia, for sacrificing so much in order to give me the opportunity to reach this point. Without you I wouldn't be the man I have become.
Благодаря ви! Thank you! Bedankt!

Table of contents

Chapter 1.

Introduction

This chapter is based on my previous publications (see publication list [1, 4, 5]). More specific introductions will be provided for each of the following chapters.

1.1 Anthropogenic effects of CO_2 emissions - Global warming

The overwhelming rise in CO_2 emissions has become one of the most pressing challenges of our time. Scientists have already been warning us about the hazardous effects of greenhouse gasses on the Earth's climate since 1986, when the measurements of CO_2 emission started [1]. Today we are already experiencing clear problems by observing more frequent extreme weather events, and the current climate models are predicting even more severe consequences, if the average temperature continues to rise with the same pace [2, 3]. Our planet is already 1.3 °C warmer than it was in the 19th century, and to keep the average temperature increase below 1.5 °C (as this is the number agreed upon in the Paris Agreement in 2015, which was signed by 194 states and the EU), emissions need to be reduced with 45% by 2030 and reach net zero by 2050 [4]. This led to the development of policies and to push towards green technologies, which should replace the current fossil fuel-based economy. Almost 10 years after this agreement, we can wonder what influence it has had already? Figure 1.1 presents the projected warming based on pledges and current policies, based on data gathered up to November 2024 [5].

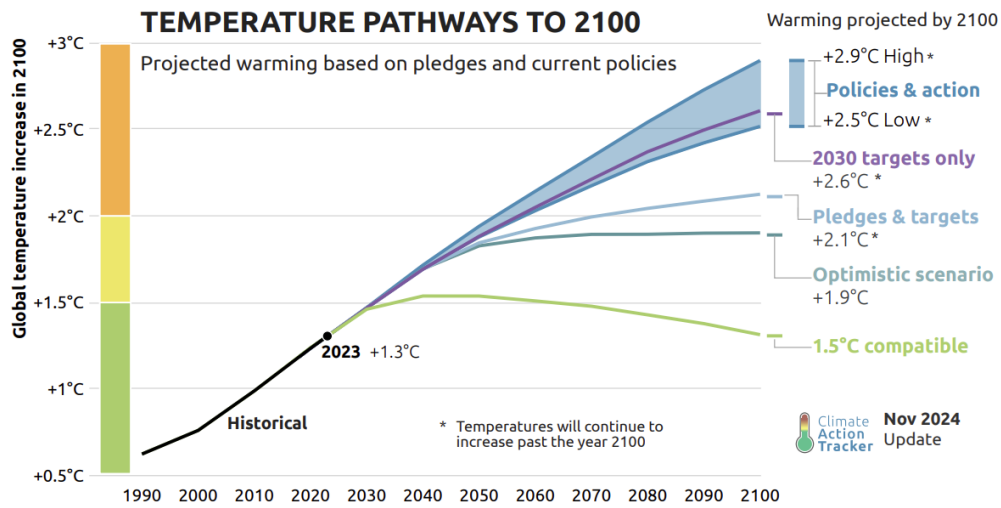

Figure 1.1. The projected warming based on pledges and current policies, based on data gathered up to November 2024, taken from [5]

We can see that despite the ambitious projects and catchy headlines in the newspapers, we are falling short from our goals. In fact, we cannot even satisfy the 2030 goal of

keeping the average temperatures below 1.5 °C. In the most optimistic scenario, the temperature will increase to 1.9 °C by 2100 and then reach a plateau, but in the most pessimistic one, it will rise up to 3 °C and it will even continue to rise beyond 2100. Despite the significant investments in green technology and development of environmental policies, we are not fulfilling the targets set in the Paris agreement. It is now more obvious than ever, that action is needed to circumvent the disastrous consequences, which come with climate change.

1.2 Decarbonization of the chemical industry

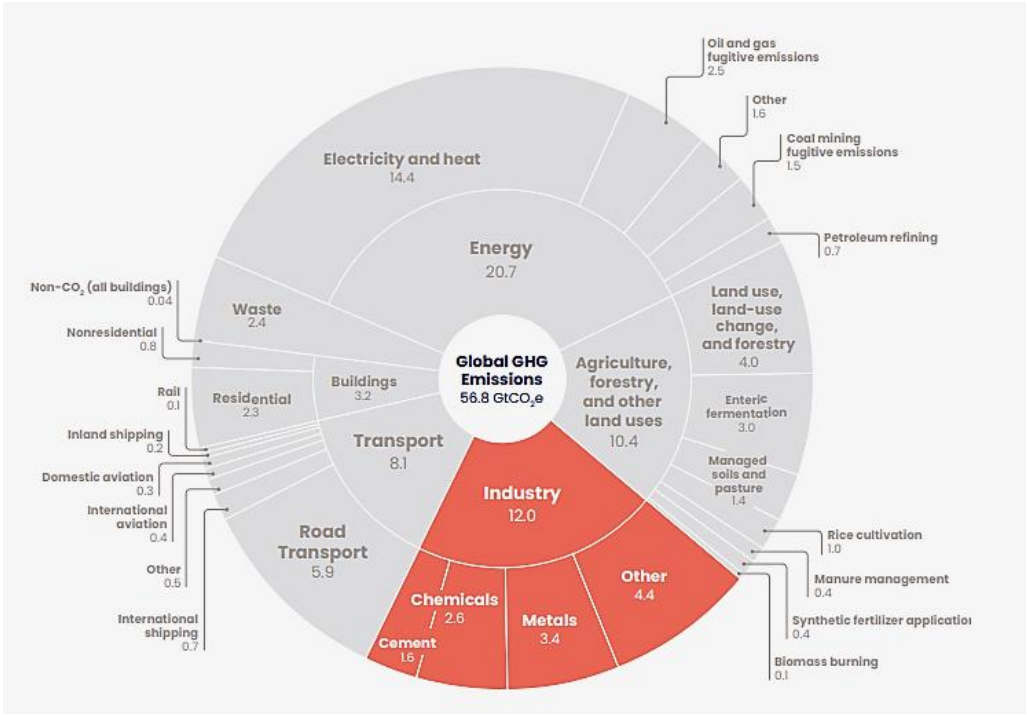

Figure 1.2. Shares of global greenhouse gas (GHG) emissions in 2021, presented in CO_2 equivalent units, taken from [6].

We can see in Figure 1.2 that the chemical industry emitted 2.6 $GtCO_2e$ in 2021, which is a significant portion of the global greenhouse gas (GHG) emissions. Since the 2000s, the total GHG emissions for chemical manufacturing have increased faster than any of the other sectors, which raises significant concerns in the feasibility of reaching the targets by 2050 [7]. The global demand of chemicals continues to grow, making the chemical industry the third-largest source of GHG emissions today [8]. In effect, the sector is considered the most difficult to electrify, due to a combination of factors,

including diverse end-uses, cost sensitivity, high-temperature processes, and continuous operational requirements [9]. The most promising strategy for reducing the GHG emissions has been electrification of the processes in combination with using renewable electricity. Unfortunately, since fossil fuel-based technology was used to optimize the industry, the share of electricity in the sector has been falling short of the targets, and in the current expected trend it will not reach net zero by 2050. Since most of the chemical plants are optimized based on centralized production, they require continuous and reliable supply of renewable electricity to operate without emitting GHG. The current supply of renewable electricity is intermittent, thus making it incompatible with the operational capabilities of the existing plants. As a result, there is no straightforward way of quickly decarbonizing the chemical industry. Because of this, new chemical reactions and manufacturing methods need to be explored, which are more compatible with renewable electricity, and less harmful for the environment.

In this regard, plasma-based conversion emerges as a versatile and promising technology. Particularly, plasma offers high process versatility, allowing for various types of reactions, including CO_2 splitting, N_2 fixation, and combinations with the conversion of other gases (*e.g.*, CH_4, H_2, H_2O) [10, 11]. This is further solidified by the large number of emerging start-ups, commercialising plasma-based gas conversion [12-15].

1.3 Electrifying the process of N_2 fixation

N_2 fixation (NF) is the process of transforming chemically inert atmospheric N_2 into accessible N_2, and is one of the most important tasks of the chemical industry. The process of producing N_2-based fertilizers is paramount for ensuring the amount of food required to meet the demands of the increasing world's population. Currently, most N_2-based fertilizers are produced by the Haber-Bosch (HB) process – one of the largest industrial chemical processes. However, the large-scale HB is very energy-intensive, consuming 1-2% of global energy annually - primarily in the form of fossil energy carriers [16]. While the most modern iteration of HB reduces CO_2 emissions through utilization and production of a combined urea/ammonium nitrate fertilizer (UAN), the process still releases over 300 Mt of CO_2 per year [17]. This contributes greatly to the global GHG emissions (i.e., industrial fossil fuel usage), adding to the detrimental effects of global warming. HB has been extensively optimized over the century-long period of its existence, leading to a very low energy consumption (EC) for NF into NH_3 (0.5 MJ/(mol N)) [18]. However, it is efficient only with the currently employed large-scale centralized

production sites and requires further distribution via fossil fuel-based transportation (which was not accounted for in the CO_2 production value stated above). The current geopolitical situation and the related fossil energy crisis renders HB unfavourable in the modern-day. Other, alternative technologies of NF are being actively and extensively researched. Among such technologies, plasma-based NF is highly attractive. Plasma-based NF is particularly interesting because (i) it operates at overall much more benign conditions compared to the HB's high temperature and pressure (700-1000 K, 200-400 bar), (ii) it can be quickly turned on and off, which enables integration with renewable resources, (iii) it can be decentralized in small-scale plants (removing the need for post-production transport), and (iv) it provides a much higher production rate (PR) than other investigated technologies (e.g. electrochemical NF) [19].

1.4 What is plasma?

The term "plasma" in physics defines a partially or fully ionized gas that possesses macroscopic quasi-neutrality and collective behavior. Since electrons and ions are always created in pairs, it means that there is never a net charge in the plasma, which makes it macroscopically quasi-neutral. The collective behavior arises since the movement of charges can locally generate electric fields and currents. These electric fields and currents can then influence the properties of the plasma away from the point of their generation, meaning the properties depend not only on the local condition in each point, but also on the regions further away from this point [20].

The presence of a large number of charged particles makes plasma electrically conductive, which determines its properties to interact with electromagnetic fields. To sustain ionization, laboratory-made plasmas are typically created by exposing a gas to an electric field. Since the electrons have higher mobility and smaller mass than the ions, they take most of the energy of the electric field. The electric field accelerates the free electrons in the gas and when they gain enough energy, a breakdown occurs. After breakdown, ionization in the plasma can be sustained by different mechanisms – direct electron impact, stepwise ionization, Penning ionization, associative ionization, *etc.* Besides charged particles, plasma comprises of atoms, excited states, and radicals, thus creating a highly reactive environment.

Plasma was first observed in a device called a Crookes tube in 1879 [21]. Crookes referred to the electric discharge he observed in a low-pressure air tube as "radiant

matter". The term "plasma" was introduced in 1928 by the scientists Irving Langmuir and Lewi Tonks, while studying low-temperature gas discharge plasma using probe methods [22, 23]. The reason for using this term was an analogy with blood plasma in the human body.

Since then, plasma has emerged as backbone for modern technological advances. The scientific field is typically driven by the large number of applications which plasma encompasses. The first commercial use of plasma devices even predates its name. In 1870, arc lamps, created by passing current between two carbon electrodes, were widely used for street lighting, until substituted by the incandescent lightbulb [24]. In 1903, Kristian Birkeland used plasma to produce nitric acid [25]. Plasma has revolutionized the heavy industry through the utilization of plasma welding, plasma cutting and plasma spraying technologies [26-28]. Probably the most important application of plasma up to now is in the semiconductor industry, where it is used to pattern circuits onto silicon wafers, creating the chips used in almost every device [29].

Plasma has become one of the most important and versatile technologies of the 20th and early 21st centuries, with applications ranging from television screens to space thrusters and nuclear fusion.

1.5 Plasma classification

Plasmas are typically classified based on their deviation from equilibrium, thus it is important to define the possible types of equilibrium. As mentioned above, plasma comprises of electrons, ions, neutrals (molecules, atoms, radicals) and excited states. The temperature of the plasma constituents might not be the same and typically this is used to classify the type of plasma.

1.5.1 Thermal equilibrium

In thermal equilibrium, all temperatures of the particles in the plasma – mainly electron temperature (T_e), vibrational temperature (T_v) and the gas temperature (T_g), are equal to each other and their respective distribution functions follow a Maxwell-Boltzmann distribution [30]. This condition is satisfied in plasmas which are fully ionized or are sustained by high power density (>10^{10} W/m^3). These plasmas are also typically very hot, reaching temperatures between 6000 and 20 000 K.

1.5.2 Non-thermal equilibrium

Non-thermal equilibrium is a state in a physical system where the different components have different temperatures or energy distributions. Because electrons are much lighter than the ions, the elastic energy transfer per collision is not enough to equilibrate the energy distribution function, within a few collisions, and thus, multiple collisions ($>10^3$) are required for equilibration [20, 30].

As mentioned earlier, the electrons are accelerated in the electric field, and collide with neutrals, leading to elastic scattering, excitation or ionization (or dissociation in case of molecules). This means that plasma party comprises of electronically excited states. Since excitation and ionization are inelastic collisions (i.e. the total kinetic energy of the system is not conserved) and the electrons are much lighter than the neutrals, the electron energy distribution function (EEDF) does not follow a Boltzmann distribution. As a result, plasmas in laboratory environments are capable of channeling nearly all of the energy of the applied electric field to electronically excited and vibrational states, while significantly less energy is dissipated in ionization and elastic scattering [31, 32]. Plasmas with such properties are typically “colder” (but still in a range of 300 K – 6000 K) and are characterized by higher T_e compared to T_g. It is exactly this property of the plasma that makes it so attractive for chemical applications, which benefit from very reactive environments at relatively low temperature.

1.5.3 Chemical non-equilibrium

Chemical non-equilibrium is a state where the forward and the reverse reactions are not balanced and there is a net change in the density of the species as a function of time. Typically, chemical non-equilibrium is a transient state and it describes how the species density evolves with time, before reaching equilibrium and the net change as a function of time is zero. In plasma it is nearly impossible to observe a perfect chemical equilibrium since there are strong temperature and density gradients [30]. These gradients drive transport of species and energy due to diffusion and conduction, which bring the system to a steady state of chemical non-equilibrium [33].

1.6 Types of plasma discharges

Since plasma discharges are created by an electric field, the way the electric field is applied determines their characteristics. Based on this, a second classification can be made.

1.6.1 Glow and arc discharges

Glow and arc discharges are created by applying direct current (DC) between two electrodes. The names “glow” and “arc” reflect the visual appearance of the discharge based on experiments in low pressure plasmas. Indeed, the “glow” is a uniform discharge, which fills the full cross-section of the tube in which it is created, while the “arc” represents a constricted filament filling only part of the cross section of the tube. A stricter definition of glow and arc can be found in the book of Raizer [34], where the classification is made based on the electron emission mechanisms on the cathode. Since the cathode is negatively charged, it repels the electrons from the discharge near the surface and an additional mechanism for charge creation has to arise in order to ensure current continuity. In glow discharges, this mechanism is secondary electron emission, where ions accelerated in the negative electric field collide with the surface of the cathode, resulting in electron emission. This leads to a creation of a large uniform “glow” across the surface of the cathode, which size is directly proportional to the applied current. In arc discharges, the emission comes from thermionic emission, field enhanced emission or the combination of both. As a result, since these effects are far more efficient compared to secondary electron emission, a small bright and constricted spot appears on the surface of the cathode. The spot is typically very hot and is the main reason for electrode erosion in high current arcs. The transition from an arc to a glow discharge happens as a function of the current and depends on the temperature of the cathode. Thus, any DC discharge can seemingly transition between both.

These types of discharges can operate as non-thermal and thermal plasma, depending on the applied current. Typically, glow discharges are observed when the current is low (< 1A) and thus, they are more likely to be non-thermal, while arc discharges are observed when the current is high (> 1A) and are more likely to be thermal. Despite this, non-thermal arc discharges do exist in the transition zones between both conditions.

1.6.2 Gliding arc discharges

The gliding arc discharge initially forms at the shortest distance between the electrodes and then moves along with the gas flow [35]. As the arc column length increases, the required voltage to sustain the plasma also rises. When the arc length exceeds a critical value, heat losses from the plasma column surpass the energy supplied by the power source, making it impossible to maintain thermodynamic equilibrium in the plasma. Consequently, the plasma undergoes a transition to a thermal non-equilibrium state. Following this transition, the gliding arc continues to evolve until the power source can no longer sustain it, at which point the cycle repeats. Gliding arcs are the easiest way of creating non-equilibrium transient discharges in atmospheric pressure [35].

1.6.3 Spark discharges

A spark plasma discharge is a type of electrical discharge characterized by a short-duration, high-intensity arc formed between two electrodes [36, 37]. Because of its short duration, it is typically operated in pulsed conditions, where the pulse width can vary from 1 ns to 100 µs [38]. This type of discharge is the closest to naturally occurring lightning, and the only difference between them is the scale. The discharge is typically in thermal equilibrium, but can be in chemical non-equilibrium because of its short lifetime. The properties of the discharge can vary significantly with applied power density, pulse width and frequency.

1.6.4 Dielectric barrier discharges

A dielectric barrier discharge (DBD) is a type of discharge in which one or both of the electrodes is covered by a dielectric (e.g. quartz) [39, 40]. A DBD prevents the creation of an arc or glow discharge by utilizing the insulating nature of the dielectric barrier. The operating principle of DBD is as follows: as the electric field reaches the breakdown voltage, a breakdown occurs. After breakdown - when the plasma reaches one of the electrodes - it builds up space charge, due to the dielectric barrier, that cancels the applied electric field, and at this moment the discharge stops. The created discharge is usually called a microdischarge. Microdischarges have very short lifetimes (few ns) and are characterized by a strong degree of thermal non-equilibrium (e.g. T_e = 15 000 K and T_g = 300 K). They are usually spread randomly across the dielectric surface and their number increases with the applied voltage. Since the space charge destroys the

microdischarge, an AC or DC-pulsed power supply is needed to sustain continuous creation of microdischarges.

1.6.5 Microwave discharges

In microwave discharges, the plasma is sustained by microwave fields with typical frequency of 915 MHz or 2.45 GHz [41]. They are created in dielectric tubes, filled with gas and placed in waveguide resonators. The sustaining wave can be either a standing surface wave or a travelling surface wave. These discharges are hot (e.g. 6000 K) and constricted at atmospheric pressure, experiencing thermal equilibrium with chemical non-equilibrium [42]. If they are sustained at low pressure (below 0.1 bar), they are usually diffuse and in a state of thermal non-equilibrium [40, 43].

1.7 State-of-the-art of plasma-based NF

Various pathways of NF by plasma have been studied, ranging from a direct HB alternative of plasma-catalytic N_2 reduction with H_2 [44,45], to plasma-electrochemical N_2 reduction and/or oxidation with H_2O, as demonstrated in recent reviews [46, 47, 48]. Nowadays, the most energy-efficient method of plasma-based NF is via oxidation to N_2 oxides (NO and NO_2), which can be either used as-is or converted to NH_3 via subsequent catalytic [49] or electrochemical reduction [50].

A variety of plasma reactors (and discharge types) have been applied for this purpose, from DBDs to thermal arc plasmas [47, 51]. One of the first industrial processes for fertilizer production was the plasma-based Birkeland-Eyde process, which utilized hydroelectric energy to drive NF into NO_x operating with oxygen-enriched air [25]. The most recent advances in plasma-based NO_x generation with the lowest reported EC are summarized in Table 1.1. DBD discharges, which have the highest state of thermal non-equilibrium, are typically the worst performing, which is why they are not listed in Table 1.1. One of the main difficulties with finding the optimal plasma setup is the reverse correlation between EC and NO_x yield (and production rate; PR). Extremely low EC (1.6 MJ/(mol N)) is often accompanied by a low PR (1 g/h) (see entry 9 in Table 1.1). To our knowledge, the best metrics in terms of low EC and high PR were obtained with the rotating gliding arc (RGA) plasma (entries 6, 7 and 8) and microwave (MW) plasma (entry 2).

Table 1.1 Overview of recent advances in plasma-based N_2 fixation via oxidation to NO_x, and their relevant energy consumption (EC) and production rate (PR) values.

Entry	Discharge type	N_2:O_2	EC (MJ/(mol N))	NO_x PR (g/h)	Reference
1	DC glow	4:1	2.8	1.9	52
2	Microwave (surface wave)	1:1	2.0	85.9	53
3	Three-level coupled rotating electrodes discharge	4:1	2.7	0.4	54
4	Low-current glow-type discharge	4:1	3.4	3.0	55
5	Pulsed gliding arc	1:1	4.8	<0.1	56
6	Rotating gliding arc	1:1	2.5	7.0	57
7	Rotating gliding arc (effusion nozzle)	1:1	2.1	7.4	58
8	Rotating gliding arc elevated pressure: 3 barg	1:1	1.8	68.9	59
9	Pulsed-spark discharge	1:1	1.6	0.96	60

RGA plasma reactor operation is more facile, but its NO_x production EC is somewhat higher when used without additionally designed parts, such as an effusion nozzle, although the EC can be reduced when operating at elevated pressure (entry 8, and see Chapter 3). Furthermore, arc plasmas are more versatile, with the energy efficiency of the power supply being typically higher compared to that of a MW plasma [30].

A recent techno-economic analysis by Rouwenhorst *et al.* compared plasma-based technologies with the HB-Ostwald process (in which the NH_3 produced by HB is further converted into NO_x by the Ostwald process [18]), suggesting that plasma-based fertilizer production could become competitive with HB-Ostwald if the plasma EC reaches

between 1 and 1.5 MJ/(mol N) [61]. Early plasma research on NF conducted in the 1980s showed potential for NO_x production at low EC (0.2 MJ/(mol N)) and high concentrations (15%), but this was at a pressure of 0.013 atm [62], making it unsuitable for industrial applications. Thus, in this thesis we aim to develop strategies, which can potentially bring the EC closer to 1.5 MJ/(mol N).

1.8 Objective of this work

The objective of this work is to improve the understanding of the underlying mechanisms driving plasma-based NF, in order to improve the EC and increase the NO concentration and PR. In addition, this thesis presents a new modelling approach, which makes it possible to extend the computationally heavy plasma chemistry models to multiple dimensions, so that predictive models can be used for designing more efficient plasma reactors, which are able to compete with the industrially accepted processes.

The thesis is structured into six chapters, after this Introduction chapter. Considering the variety of the investigated systems, each chapter includes a more specific introduction. The structure is as follows:

Chapter 2 presents a new 2D self-consistent computational fluid dynamics (CFD) model of a DC plasma in N_2, to investigate how the cathode emission mechanism (glow or arc) affects the radius of the plasma and its properties, which provides valuable information on which DC plasma mode (glow or arc) could be more useful for plasma-based NF.

Chapter 3 experimentally investigates NF in a rotating gliding arc (RGA) DC plasma reactor, and specifically how the EC and NO concentration and PR change as function of pressure (0-3 barg).

Chapter 4 develops a new modelling approach for describing the vibrational degrees of freedom in a plasma. It is in first instance developed for a CO_2 plasma. The model uses the average energy deposited in each of the vibrational modes of CO_2 (being the asymmetric stretch vibration, T_3, and the symmetric stretch and bending vibrations: $T_{1,2}$), as well as for CO and O_2, instead of calculating the populations of each excited state, which is computationally very expensive. This new model is very useful to be implemented in more-dimensional models, like developed in Chapter 2, to account for an accurate description of the vibrational levels with limited computation time. In addition, the model provides an expanded ion chemistry for CO_2 plasma, coupling the plasma conductivity with a circuit model and self-consistently calculating the electron temperature and the electron density.

Chapter 5 applies a simplified version of the newly developed model in Chapter 4 to an air plasma, where the most recent rate coefficients available to date are used, to redefine the minimum EC which plasma-based NF can achieve.
Finally, in **Chapter 6,** we summarize the overall conclusions and propose a new strategy for achieving energy-efficient NF in atmospheric pressure air plasma.

Chapter 2.

Simulation of glow and arc discharges in nitrogen: Effect of the cathode emission mechanisms

Experimental work demonstrated that low current DC N_2 discharges can exist in both glow and arc regimes at atmospheric pressure. However, modelling investigations of the positive column, including the influence of the cathode phenomena, are scarce. In this chapter, we developed a 2D axisymmetric model of a plasma discharge in flowing N_2 gas, studying the influence of two cathode emission mechanisms – thermionic field emission and secondary electron emission, on the cathode region and the positive column. We show that, for an inlet gas flow velocity of 1 m s^{-1} and current range of 80-160 mA, the cathode emission mechanism greatly affects the size and temperature of the cathode region, but does not significantly influence the discharge column at atmospheric pressure. We also demonstrate that the electron density balance is local and dominated by volume processes in the discharge column. With increasing flow velocity, discharge contraction is enhanced due to increased convective heat loss. The cross sectional area of the conductive region is strongly dependent on the gas velocity and heat conductivity of the gas. These findings are relevant for designing future DC plasma reactors for NF, and gas conversion more in general, since our results show that the glow discharge should be avoided and the arc mode should be promoted.

This chapter is based on:
Simulation of glow and arc discharges in nitrogen: effects of the cathode emission mechanisms.
I. Tsonev, J. Boothroyd, S. Kolev, A. Bogaerts,
Plasma Sources Science and Technology, 32(5), 054002, (2023).
https://doi.org/10.1088/1361-6595/acc96c

2.1 Introduction

In this chapter, we study a N_2 DC discharge, to obtain more insight in the plasma characteristics in both glow and arc regime, of interest for plasma-based NF. Specifically, we investigate the cathode emission processes sustaining arc and glow discharges, and how they affect the plasma behavior, including the cathode region, positive column, and volume contraction. The volume contraction of a DC discharge originates from nonlinearities in the electron production and loss rates [63], with the thermal instability due to gas heating making a major contribution in many discharges. The electron impact ionization frequency strongly depends on the reduced electric field. The reduced electric field is the ratio between the electric field and the neutral number density and is typically measured in Td, where 1 Td = 10^{-21} V·m^2. At a constant pressure, a spatially non-uniform gas temperature profile will significantly enhance the ionization processes in the high temperature region, which in turn will further increase the temperature, creating a positive feedback loop. Discharges balanced by diffusion processes tend to be less constricted, whereas those balanced by volume recombination are significantly more constricted. Furthermore, the effect of the boundary conditions (BCs) and gas flow dynamics can also influence the gas temperature cross section, thus resulting in stronger or weaker constriction [64].

Significant efforts have been made to explain the thermal instability phenomena in the bulk of the gas [63-74]. Specifically, Yu *et al.* investigated the chemical kinetics of N_2 in vibrationally excited plasma at high gas temperature [67]. They found that two regimes of operation exist based on the dominant recombination mechanisms. An S-shape dependence of the electron density as function of the electron temperature for constant gas temperature was attributed to the transition of glow discharges into arc discharges for air [68]. Akishev *et al.* investigated the basic processes sustaining constricted N_2 discharges using a combination of a 1D computational model and experiments [64]. The main charged particle creation pathway was identified as associative ionization between the electronically excited states of N_2. Prevosto *et al.* studied a similar system to the one investigated by Akishev [69]. They included the influence of the associative ionization of the atomic species, further improving the charged particle dynamics for higher currents, assuming a local balance of the plasma species. Naidis *et al.* developed a 2D air model, quantifying the degree of non-equilibrium and the effect of the gas flow across a wide current range [70]. A dynamic contraction model was developed by Shneider *et al.* [73, 74], revealing the time-dependent evolution of the thermal instability in air and N_2.

Despite the substantial efforts that have been made to explain the thermal instability phenomena in the bulk of the gas, a lot less work has been done to investigate the influence of the cathode on the positive column in low current, atmospheric pressure discharges. Fully coupled self-consistent models including the electrode effects are scarce, among others due to the computational demand of the calculations.

The phenomena of the cathode instability represent a change of the electron emission mechanism from the electrode. Glow discharges are, by definition, sustained via secondary electron emission, whereas arcs - by field emission, thermionic emission or the combined effect of both [63, 75]. To avoid computational complexities, the effects of the cathode region on the discharge column are often neglected, based on the premise that the cathode region is significantly smaller than the arc column [69, 72]. Alternative solutions employ boundary conditions or matching conditions to an analytical solution [76]. Baeva *et al.* incorporated a non-local thermodynamic equilibrium (NLTE)-sheath approach, imposing boundary conditions on the interface between the plasma column and the cathode sheath [77, 78]. Liang and Trelles simulated the cathode-plasma interaction by including an effective electrical conductivity on the boundaries [79]. Almeida *et al.* developed a 1D self-consistent model investigating the cathode attachment [80]. A fully self-consistent treatment of the cathode and anode attachments has been carried out for high current N_2 arcs [81] assuming that the main mechanism of emission from the cathode is thermionic emission. Kolev *et al.* investigated the effect of the cathode instability in a self-consistent argon model [82]. The model accounted for both thermionic-field emission and secondary electron emission, revealing that the cathode mechanisms do not influence the positive column. Nonetheless, a more complete model with minimal neglect of the physical phenomena at the cathode is required for many gas compositions, such as *e.g.* the aforementioned discharges in N_2, important for plasma-based NF.

Therefore, in this chapter, we developed a 2D two-temperature model in a laminar N_2 gas flow. The model includes the main ionization pathways determined by Prevosto and Akishev [64, 69]. The main novelty of our model compared to the ones mentioned above is the inclusion of the self-consistent computation of the cathode region. We compare the thermionic-field emission with the secondary electron emission in order to determine the influence of the cathode region on the positive column.

2.2 Model description

2.2.1 Model equations

We constructed a fluid plasma model with the drift-diffusion approximation, as employed in the Plasma Module of COMSOL Multiphysics 6.0 [83]. The electron energy distribution function (EEDF) is calculated using BOLSIG+ software. The electron impact cross-sections are then integrated over the distribution function and incorporated in the model.

The species considered in the model are $N_2(X^1\Sigma_g^+)$, $N_2(A^3\Sigma_u^+)$, $N_2(a'^1\Sigma_u^-)$, $N_2(B^3\Pi_g)$, $N_2(C^3\Pi_u)$, $N(^4S)$, $N(^2D)$, $N(^2P)$, N^+, N_2^+, N_3^+, N_4^+ and the electrons. The chemical reactions included in the model are listed in Appendix A1. Excitation of the vibrational degree of freedom (R2.2, Table A1) is assumed to proceed through the first 8 levels, and excitation to higher levels is neglected, as in [69].

For each species, the continuity equation is solved:

$$\frac{dn_s}{dt} + \nabla \cdot \boldsymbol{\Gamma}_s + (\boldsymbol{u}_g \cdot \nabla) n_s = R_s, \tag{2.1}$$

where n_s is the species density, $\boldsymbol{\Gamma}_s$ is the species flux, $\boldsymbol{u}_g$ is the gas velocity and R_s is the net rate of change, based on the reactions detailed in Appendix A1. The neutral species flux is given as:

$$\boldsymbol{\Gamma}_n = -D_n \nabla n_n, \tag{2.2}$$

where D_n is the diffusion coefficient of the neutral species in N_2, given in table A6 in Appendix A1, and n_n is the neutral number density.

For the charged species, the flux is expressed as:

$$\boldsymbol{\Gamma}_s = -D_s \nabla n_s + \frac{q_s}{|q_s|} n_s \mu_s \boldsymbol{E}, \tag{2.3}$$

where D_s, μ_s, and q_s are the diffusion coefficient, mobility and species' charge, respectively, and $\boldsymbol{E}$ is the electric field vector. The subscript "s" indicates either electrons or ions. The electron transport properties D_e and μ_e are calculated by BOLSIG+. The Einstein relation is used to calculate the ion mobility from the ion diffusivity, listed in table A6 in Appendix A1.

The electron energy balance equation is solved for obtaining the averaged electron energy $\bar{\varepsilon}_e$:

$$\frac{d(n_e \bar{\varepsilon}_e)}{dt} + \nabla \cdot \boldsymbol{\Gamma}_\varepsilon + \boldsymbol{E} \cdot \boldsymbol{\Gamma}_e + (\boldsymbol{u}_g \cdot \nabla) n_e \bar{\varepsilon}_e = Q_{bg} + S_{en}, \tag{2.4}$$

where $\boldsymbol{\Gamma}_\varepsilon$ is the electron energy flux and S_{en} is the average energy lost through electron collisions. An additional background power density Q_{bg} is used in order to reduce

gradients between the discharge column and the surrounding gas. This improves computational stability and reduces requirements on the mesh. Mesh convergence was ensured by gradually decreasing the size until there was no change in the output of the model. The final mesh consists of 30,000 unstructured quadrilateral elements. The background power density is kept low (10^5 W m^{-3}) such that it does not significantly influence the results. The electron energy flux is given by:

$$\boldsymbol{\Gamma}_{\varepsilon} = -D_{\varepsilon}\nabla n_{\mathrm{e}}\overline{\varepsilon}_{\mathrm{e}} - \mu_{\varepsilon} n_{\mathrm{e}}\overline{\varepsilon}_{\mathrm{e}}\boldsymbol{E}, \tag{2.5}$$

where D_{ε} and μ_{ε} are the electron energy diffusion coefficient and electron energy mobility, respectively. The Poisson equation is also solved, and coupled to the above system of equations. Thus, the electric field is determined self-consistently from the space charge density:

$$\nabla \cdot (\epsilon_0 \boldsymbol{E}) = -\nabla \cdot (\epsilon_0 \nabla V) = \textstyle\sum_{\mathrm{s}} q_{\mathrm{s}} n_{\mathrm{s}}, \tag{2.6}$$

where ϵ_0 is the vacuum permittivity and *V* is the electric potential. It is important to note that there is no special treatment of the ambipolar electric field in our model. The electric field entering equation (2.1) originates from the Poisson equation (2.6) and the externally connected circuit. The equality of the fluxes of ions and electrons is not implied, hence the losses are determined by the electric field vector, which is self-consistently computed.

The gas temperature is calculated using the energy balance equation, assuming the ion temperature is equal to the gas temperature:

$$\rho C_{\mathrm{p}} \frac{\partial T_{\mathrm{g}}}{\partial t} + \rho C_{\mathrm{p}} \boldsymbol{u}_{\mathrm{g}} \cdot \nabla T_{\mathrm{g}} - \nabla \cdot \left(k_{\mathrm{g}} \nabla T_{\mathrm{g}}\right) = Q_{\mathrm{g}} + N_2(X) \frac{e_v - e_v(T_g)}{\tau_{VT}}, \tag{2.7}$$

where ρ is the gas density, C_{p} is the heat capacity at constant pressure, k_{g} is the thermal conductivity and Q_{g} is the gas heating released from the reactions in the plasma and the Joule heating of the electrons, $N_2(X)\frac{e_v - e_v(T_g)}{\tau_{VT}}$ is the heating due to vibrational-translation (V-T) relaxation, $e_v(T_g)$ is the equilibrium value of the mean vibrational energy and τ_{VT} is the V-T relaxation time calculated from the expressions in [69]. Estimations of the effect of Joule heating resulting from ion currents resulted in negligible differences in the temperature in the positive column and a small effect near the cathode region. In order to improve the computational stability of the problem, the term was neglected from the calculations.

In addition to the gas temperature balance equation, the vibrational energy balance equation for $N_2(X)$ is also solved:

$$N_2(X)\frac{de_v}{dt} + \nabla \cdot \left(N_2(X) D_{\mathrm{N_2}} \nabla e_v\right) + \boldsymbol{u}_{\mathrm{g}} \cdot \nabla e_{\mathrm{v}} = Q_{e_v} - N_2(X)\frac{e_v - e_v(T)}{\tau_{VT}} \tag{2.8}$$

where e_v is the mean vibrational energy, and Q_{e_v} stands for the heating and cooling rate of the vibrational degrees of freedom due to Joule heating and reactions in the plasma. This is the general form of the vibrational energy balance equation. In Chapter 4 and 5, we will solve the same equation for a multi-temperature system using a global model, i.e. conductive energy loss (second term on the left-hand side) and convective energy losses (third term on the left-hand side) will be a globally-averaged values. The mean vibrational energy is related to the vibrational temperature with

$$e_v(T_v) = \frac{\hbar\omega}{\exp\left(\frac{\hbar\omega}{kT_v}\right) - 1} \tag{2.9}$$

where T_v is the vibrational temperature and $\hbar\omega$ is the vibrational quanta of the N_2 molecule. The vibrational distribution function is assumed to follow the analytical description as in [64, 69] given by:

$$\left.\begin{aligned} N_2(X,v) &= N_2(X,0)exp\left(-v\frac{\hbar\omega}{kT_v}\right), 0 < v \le v_1; \\ N_2(X,v) &= N_2(X,v=v_1)\frac{v_1+1}{v+1}, v_1 < v \le v_2 \\ N_2(X,v) &= N_2(X,v=v_2)exp\left(-(v-v_2)\frac{\hbar\omega}{kT_g}\right), v > v_2 \\ v_1 &= 9, v_2 = v_1 + (35-v_1)exp\left(-\frac{T_g - 300}{3000}\right) \end{aligned}\right\} \tag{2.10}$$

The solution for the gas flow velocity is obtained from the Navier-Stokes equations:

$$\rho\frac{\partial \boldsymbol{u}_g}{\partial t} + \rho(\boldsymbol{u}_g.\nabla)\boldsymbol{u}_g = \nabla.\left[-p\boldsymbol{I} + \mu_g(\nabla.\boldsymbol{u}_g + (\nabla.\boldsymbol{u}_g)^T) - \frac{2}{3}\mu_g(\nabla\cdot\boldsymbol{u}_g)\boldsymbol{I}\right] \tag{2.11}$$

$$\frac{\partial\rho}{\partial t} + \nabla\cdot(\rho\boldsymbol{u}_g) = 0 \tag{2.12}$$

Where $\boldsymbol{I}$ is the identity matrix, p is the gas pressure, μ_g is the dynamic viscosity (which is a function of temperature) and the superscript T identifies a tensor operation. The pressure is assumed to be close to constant at 1 atm and thus, the gas density ρ is assumed to be a function of gas temperature only following the ideal gas law. The transport properties μ_g, C_p and k_g are taken as tabulated data from [30].

2.2.2 Boundary conditions

The model is solved in an axisymmetric geometry comprising of two hemispherical electrodes ($r_{\text{electrode}}$ = 0.2 cm) separated by a discharge gap of 1.6 cm placed in a cylindrical tube (r_{tube} = 2 cm), presented in Figure 2.1. The bottom electrode (AB) is chosen to be the cathode, where a negative voltage is supplied through a ballast resistor connected to a voltage source. The ballast resistor was chosen as 1 MΩ and the applied voltage was varied to control the current.

The boundary condition on the cathode for the electron density balance equation (2.1) is given as:

$$\mathbf{n} \cdot \boldsymbol{\Gamma}_{\mathrm{e}} = \frac{1}{2} v_{\mathrm{e,th}} n_{\mathrm{e}} - \left(\sum \gamma_{\mathrm{i}} \left(\boldsymbol{\Gamma}_{\mathrm{i}} \cdot \mathbf{n} \right) + \boldsymbol{\Gamma}_{\mathrm{t}} \cdot \mathbf{n} \right), \tag{2.13}$$

where $v_{\mathrm{e,th}} = \sqrt{\frac{8 k_{\mathrm{B}} T_{\mathrm{e}}}{\pi m_{\mathrm{e}}}}$ is the electron thermal velocity, $\boldsymbol{\Gamma}_{\mathrm{i}} \cdot \mathbf{n}$ is the ion flux normal to the cathode and γ_{i} is the secondary electron emission coefficient for each ion. It is important to note that the secondary electron emission coefficients are not well known for these systems and are often calculated as fitting parameters of a specific experiment. The secondary electron emission coefficients in this chapter were taken from [84] as $\gamma_{\mathrm{i}} = 0.032$ and assumed the same for the four different ions. $\boldsymbol{\Gamma}_{\mathrm{t}}$ is the electron flux due to field-enhanced thermionic emission, taken from [75]. To distinguish between the arc and glow case, the thermionic emission flux ($\boldsymbol{\Gamma}_{\mathrm{t}}$ in equation 2.13) is only included when considering the arc case, whereas the secondary electron emission flux ($\boldsymbol{\Gamma}_{\mathrm{i}}$ in equation 2.13) is only calculated in the glow case:

$$\boldsymbol{\Gamma}_{\mathrm{t}} \approx \left(\mathrm{A_T} {T_{\mathrm{C}}}^2 + \mathrm{A_F} {\boldsymbol{E}_{\mathrm{C}}}^x \right) \exp\left[- \left(\frac{{T_{\mathrm{C}}}^2}{\mathrm{B_T}} + \frac{{\boldsymbol{E}_{\mathrm{C}}}^2}{\mathrm{B_F}} \right)^{-1/2} \right]. \tag{2.14}$$

Equation 2.14 accounts for the combined effect of the thermionic and field emission on the electron emission. Although our model assumes a cold cathode ($T_{\mathrm{C}} = 300\ K$), and thus thermionic emission is negligible, we keep the more general expression (2.14) to allow the future use of our model in more diverse cases. Equation (2-14) has a rather complicated nature and a detailed discussion regarding the exact derivation of the constants is outside the scope of this work. The coefficients $\mathrm{A_T}$, $\mathrm{A_F}$, $\mathrm{B_T}$, $\mathrm{B_F}$ and *x* are separate functions of the cathode material work function W_{f}, with *x* being a factor close to unity. $\mathrm{A_T}$ (A m^{-2} K^{-2}) and $\mathrm{A_F}$ (AV^{-x} m^{x-2}) are the pre-exponential factors in the Richardson-Dushman and Fowler-Nordheim formula, respectively. $\mathrm{B_T}$ (K^{-2}) and $\mathrm{B_F}$ (V^{-2} m^{-2}) can be approximated as exponential factors in both formulae. To account for the

surface roughness (which can amplify the electric field through sharp edges in microprotrusions) an effective electric field is defined as $\boldsymbol{E}_{\mathrm{C}} = FEF \times (\boldsymbol{n} \cdot \boldsymbol{E})$, where FEF is the field enhancement factor accounting for amplification of the electric field. This parameter is a similar fitting parameter to γ_{i}. In [85] a FEF value of 55 is given for a smooth surface. As the purpose of our model is to compare the effects of the cathode phenomena for conditions that will create an arc, we have chosen a FEF factor of 200, which relates to a relatively rough surface without special conditioning. The work function used in our work is chosen to be $W_{\mathrm{f}} = 4.36$ eV, which corresponds to Mo [86]. The boundary condition for the electron energy balance equation (2.4) on the cathode is given as:

$$\boldsymbol{n} \cdot \boldsymbol{\Gamma}_{\varepsilon} = \frac{5}{6} v_{\mathrm{e,th}} n_{\varepsilon} - \left(\sum \gamma_{\mathrm{i}} \epsilon_{\mathrm{i}} \left(\boldsymbol{\Gamma}_{\mathrm{i}} \cdot \boldsymbol{n} \right) + \epsilon_{\mathrm{t}} (\boldsymbol{\Gamma}_{\mathrm{t}} \cdot \boldsymbol{n}) \right), \tag{2.15}$$

where ϵ_{i} is the average energy of secondary electron emission, given as $\epsilon_{\mathrm{i}} = \varepsilon_{\mathrm{i}} - 2W_{\mathrm{f}}$, in which ε_{i} is the ionization energy of the bombarding species and W_{f} is the work function of the material. Furthermore, ϵ_{t} is the average energy of the electrons emitted by field-enhanced thermionic emission. Although the average energy of electron emission has to be a distribution function, for the sake of numerical stability, we have chosen a low constant value of 0.02 eV for ϵ_{t}.

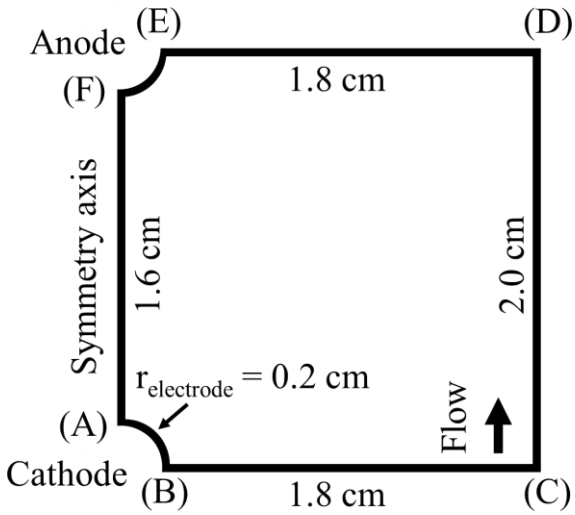

Figure 2.1. Description of the computational domain.

The boundary conditions for the ions are the same for the cathode and the anode, given as:

$$\boldsymbol{n}\cdot\boldsymbol{\Gamma}_{\mathrm{i}} = n_{\mathrm{i}}K_{\mathrm{i,surf}} + max\left(\frac{q_{\mathrm{s}}}{|q_{\mathrm{s}}|}\frac{D_{\mathrm{i}}e}{k_{\mathrm{B}}T}n_{\mathrm{i}}\boldsymbol{E}\cdot\boldsymbol{n}, 0\right) \tag{2.16}$$

The expression $K_{\mathrm{i,surf}} = \left(\frac{\gamma_{\mathrm{s}}}{1-\gamma_{\mathrm{s}}/2}\right)\frac{1}{4}\sqrt{\frac{8RT_{\mathrm{g}}}{\pi M_{\mathrm{s}}}}$ where γ_{s} is the sticking coefficient and M_{s} is the species mass, taken from [87], with all surface reactions employing a sticking coefficient of 1. In order to get an adequate comparison between the glow and the arc regime, the temperature of the cathode and the anode was kept constant at 300 K. The boundary condition (BC) (see Figure 2.1) was chosen as an inlet boundary condition with a given parabolic gas velocity profile, which has a maximum in the middle of the boundary, giving a fully developed flow profile. The specified velocity u_{g_0} is then the average velocity on the boundary. The outlet boundary condition for boundary (DE) is given as:

$$\left[-\mathrm{p}\boldsymbol{I} + \mu_{\mathrm{g}}\left(\nabla\cdot\boldsymbol{u}_{\mathrm{g}} + \left(\nabla\cdot\boldsymbol{u}_{\mathrm{g}}\right)^{T}\right) - \frac{2}{3}\mu_{\mathrm{g}}(\nabla\cdot\boldsymbol{u}_{\mathrm{g}})\boldsymbol{I}\right]\boldsymbol{n} = \mathrm{p}_0\boldsymbol{n} \tag{2.17}$$

The rest of the boundary conditions are listed in table 2.1, with indication to Figure 2.1.

Table 2.1. Boundary conditions

	n_e	n_i	n_n	V	$\overline{\varepsilon}_e$	T_g	u_g	T_v
(AB)	(2.13)	(2.16)	$\boldsymbol{n}\cdot\boldsymbol{\Gamma}_n = n_i K_{n,surf}$	$V = V_c$	(2.15)	$T_g = 300\text{K}$	$u_g = 0$	T_v = 300K
(BC)			$\boldsymbol{n}\cdot\alpha = 0, (\alpha = \boldsymbol{\Gamma}_e, \boldsymbol{\Gamma}_i, \boldsymbol{\Gamma}_n, -\nabla V, \boldsymbol{\Gamma}_\varepsilon)$			$T_g = 300\text{K}$	$u_g = u_{g_0}$	T_v = 300K
(CD)			$\boldsymbol{n}\cdot\alpha = 0, (\alpha = \boldsymbol{\Gamma}_e, \boldsymbol{\Gamma}_i, \boldsymbol{\Gamma}_n, -\nabla V, \boldsymbol{\Gamma}_\varepsilon)$			$T_g = 300\text{K}$	$u_g = 0$	T_v = 300K
(DE)			$\boldsymbol{n}\cdot\alpha = 0, (\alpha = \boldsymbol{\Gamma}_e, \boldsymbol{\Gamma}_i, \boldsymbol{\Gamma}_n, -\nabla V, \boldsymbol{\Gamma}_\varepsilon)$			$\boldsymbol{n}\cdot \text{k}\nabla T_g = 0$	(2.17)	$\boldsymbol{n}\cdot \text{k}\nabla T_v = 0$
(EF)	$\boldsymbol{n}\cdot\boldsymbol{\Gamma}_e = \frac{1}{2} v_{e,th} n_e$	(2.16)	$\boldsymbol{n}\cdot\boldsymbol{\Gamma}_n = n_i K_{n,surf}$	$V = 0$	$\boldsymbol{n}\cdot\boldsymbol{\Gamma}_\varepsilon = \frac{5}{6} v_{e,th} n_e$	$T_g = 300\text{K}$	$u_g = 0$	T_v = 300K

The choice of the boundary conditions on (CD) was evaluated to ensure the wall is not influencing the plasma. To test this condition, the position of the wall was varied at r = 2, 4 and 6 cm. The results showed no influence to the gas temperature and electron density, demonstrating that the gas flow is strong enough to insulate the plasma from the wall. The model is axially symmetric, meaning that the gradients in ϕ are 0 and the radial divergence has the form $\frac{1}{r}\cdot\frac{d(r\cdot\boldsymbol{\Gamma}_r)}{dr}$.

2.3 Results and discussion

We solved our model for three different current values (80, 120 and 160 mA) and a flow velocity of 1 m s^{-1}. For the 80 mA case, the flow conditions were expanded to 1, 2 and 4 m s^{-1}. Each of the current values for a velocity of 1 m s^{-1} were solved either with field-enhanced thermionic emission (arc) or secondary electron emission (glow) boundary condition on the cathode. We used a time-dependent solver until reaching steady-state. To aid in the following discussion, we define the radius of the plasma column as follows:

$$r_\beta = \sqrt{\frac{\int \beta ds}{\pi Max(\beta)}}, \tag{2.18}$$

where β is either T_g or the total current density j. In order to evaluate the radius and area of the discharge, the current density is chosen as a more universal parameter, rather than the electron density. It is important to note however that the current density profile coincides with the electron density profile in the positive column.

In the following, we will start with a discussion on the cathode region of both types of discharges, followed by the positive column, in both cases for different electric currents, and finally we will investigate the effect of the gas flow velocity on the plasma behavior in the positive column.

2.3.1 Cathode region

In Figure 2.2 the axial variation (r = 0) of several quantities in the cathode region for the arc and the glow case are presented. The results are plotted as a logarithmic function of z in order to highlight the deviations of the plasma parameters in the cathode layer. A non-quasineutral layer is observed for both the glow and arc case. For the case of electron supply by field emission and thus the arc discharge (Figure 2.2a)), the size of the non-quasineutral cathode layer is in the order of 10^{-4} cm. The ion and electron density are within the same order of magnitude within this layer, owing to the high efficiency of electron emission.

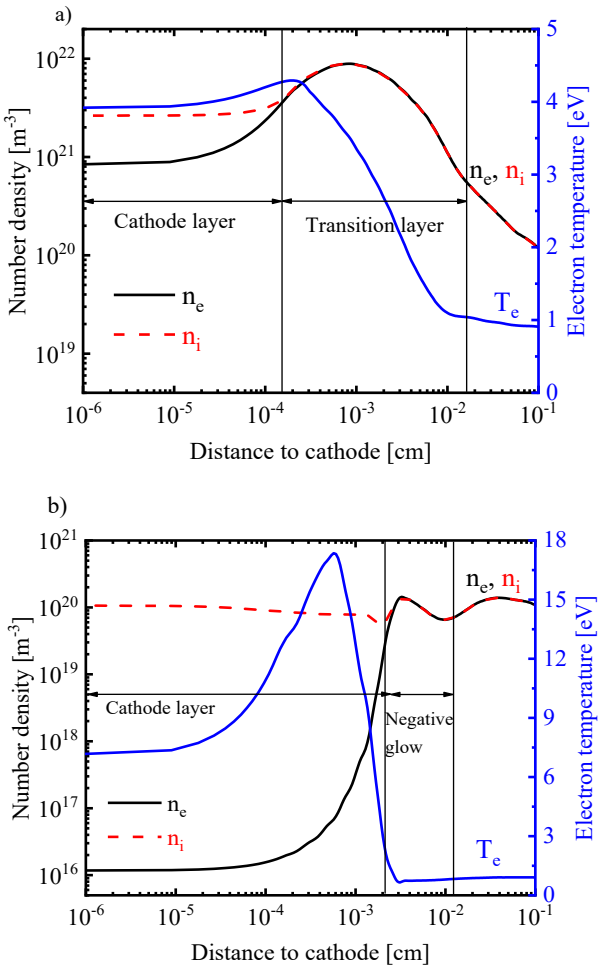

Figure 2.2. Axial profile of the total positive ion density, electron density and electron temperature in the near cathode region, for a) the arc and b) glow regime, at the symmetry axis (r = 0), at I = 80 mA and $u_{g_0} = 1\ m\ s^{-1}$.

The high value of the electron temperature observed in both cases (arc and glow) is attributed to the acceleration of electrons in the high space charge field created by the difference between the electron and ion densities. For the arc regime (Figure 2a)) $T_e \cong 3.8$ eV in the cathode region, while for the glow case (Figure 2.2b)) $T_e \approx 9 - 17$ eV. In the latter case, when the cathode emission mechanism is changed to secondary electron emission, the efficiency of electron emission from the surface is greatly reduced. Therefore, the electron density in the vicinity of the cathode surface becomes

significantly lower than the ion density, and the resulting difference in the opposing charges leads to a substantially stronger electric field and thus a much higher T_e compared to the arc regime. The size of the space charge imbalance layer is also considerably larger than in the arc regime: above 10^{-3} cm. Beyond the space charge imbalance layer, we can define the negative glow in the glow regime, and a transitional layer in the arc regime (as indicated in Figure 2.2).

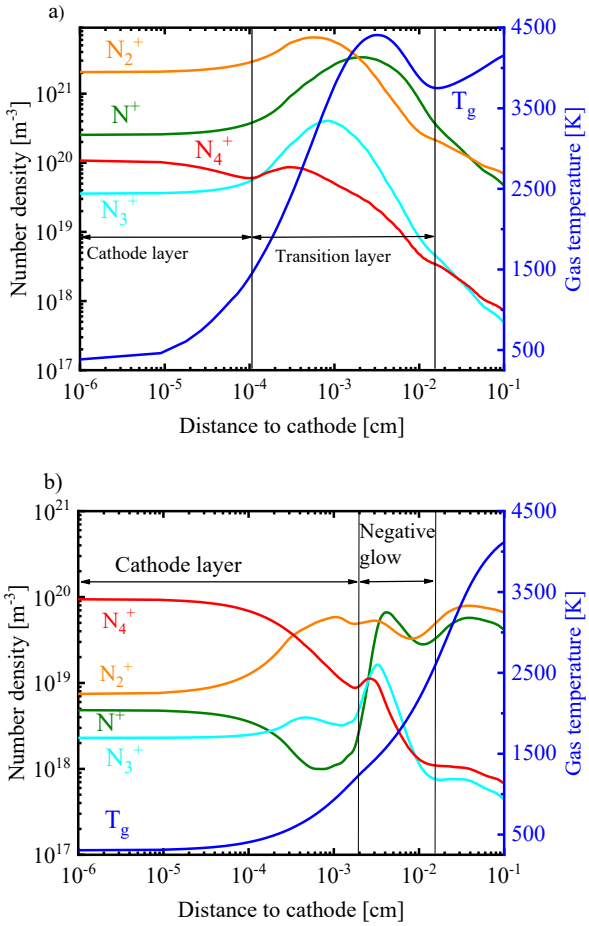

Figure 2.3. Axial profile of the various positive ion densities and the gas temperature in the near cathode region, for a) the arc and b) glow regime, at the symmetry axis (r = 0), at I = 80 mA and $u_{g_0} = 1$ ms^{-1}.

Figure 2.3 represents the axial density profiles of the various positive ions, as well as the gas temperature, for both emission mechanisms, *i.e.* the arc (a) and glow (b) regime. In the arc case, the dominant ion in the cathode layer is N_2^+ (Figure 2.3 a)), whereas in the glow case (Figure 2.3 b)) the dominant ion changes to N_4^+. The change in the dominant

ion is due to the larger increase in gas temperature close to the wall in the arc compared to the glow regime. Indeed, the maximum gas temperature and electron density in the arc regime is reached much closer to the wall (within the transitional layer), while in the glow regime, no maximum gas temperature or electron density is observed in the negative glow region, and the gas temperature rises steadily as a function of axial position towards the positive column.

As shown in Figure 2.2, the electron density in the vicinity of the cathode is significantly larger in the arc than in the glow regime. There are enough electrons to create a conductive connection between the positive column and the electrodes, and hence the electric potential drop across the non-quasineutral layer in the arc regime is rather small (*ca.* 15 V, see Figure 2.4; inset). The electron density in the glow regime is significantly lower, and thus, the electric field has to be much higher, for the plasma to sustain the current in this area, *i.e.* to accelerate the ions, which provide the same total current. This results in a very steep and very large voltage drop across the non-quasineutral layer, of 300 V (see Figure 2.4). However, even though the mechanism of electron emission differs for the arc and glow regimes, we can see in Figure 2.4 that the electric potential across the positive column sustains a linear dependence beyond the near-cathode region. In addition to this, the differences in the electric potential (and thus in electric field) in the positive column are small.

Here we should stress that the additional voltage at the cathode layer in the glow discharge means additional deposited power, which in this case is significant and in the same order as the rest of the discharge, *i.e. ca.* 24 W for 80 mA current, while the total power is 56 W. Due to the significant ion current near the cathode in the glow regime, the gas is additionally heated by the ions. Despite that, our calculations suggest that the gas temperature in the cathode fall of the glow discharge is only slightly elevated (see Figure 2.3b)), which is due to the intense cooling from the cathode, assumed to be at 300 K in our configuration. The gas cooling is effective due to the large surface area of the cathode region in the glow discharge and the small distance to the cathode surface. If the cathode is not cooled, the power deposited there could be sufficient for considerable gas and cathode heating and transition to an arc.

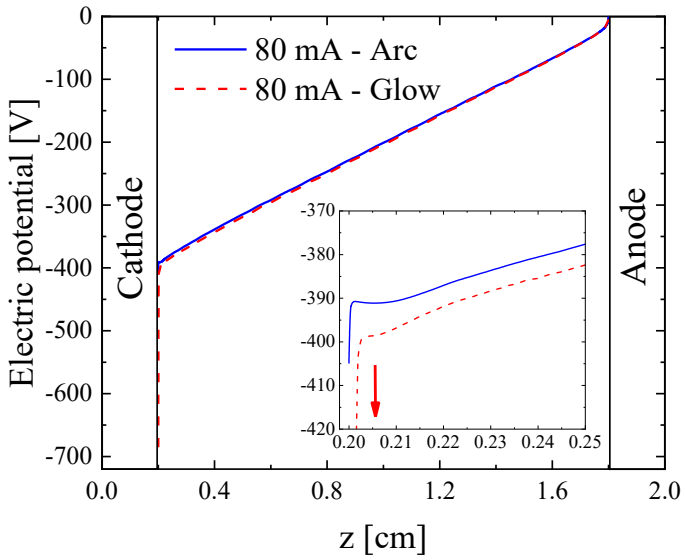

Figure 2.4. Axial profile of the electric potential across the discharge, for the arc and the glow case at r = 0, for I = 80 mA and $u_{g_0} = 1$ m s^{-1}. The radius of the cathode and anode is 0.2 cm (placed at z = 0 and 2 cm, respectively).

Figure 2.5 illustrates the 2D electron density profiles in the arc and glow regime for different currents. The cathode region looks clearly different in both regimes, for all currents investigated, *i.e.* it is characterized by a very high electron density, but confined in a very small region in the arc regime, while the electron density profile is quite wide with much lower values in the glow regime. Moreover, increasing the discharge current leads to qualitatively different behavior in the glow and the arc in the near-cathode region. In the glow regime, the cathode region is sustained by secondary electron emission initiated by the ion flux normal to the cathode surface. Because of this, increasing the current does not lead to more electron emission, but the current density is preserved and the cathode region enlarges radially. This effect is clearly observed in Figure 2.5. The area of the cathode region determined from the current density increases from 0.55×10^{-2} cm^2 to 1.2×10^{-2} cm^2 and is directly proportional to the current, following the well-known fact that the current density at the cathode surface in normal glow discharges remains constant. In the arc regime, increasing the current results in even stronger field-enhanced thermionic emission. In contrast to the glow regime, the current density in the arc cathode region increases upon increasing current. The area of the arc cathode region determined from the current density remains approximately constant as

a function of the current, at a value as small as 7.07×10^{-6} cm^2, which corresponds to a radius of 1.5×10^{-3} cm. As mentioned above, this results in almost two orders of magnitude higher electron densities (see Figure 2.5).

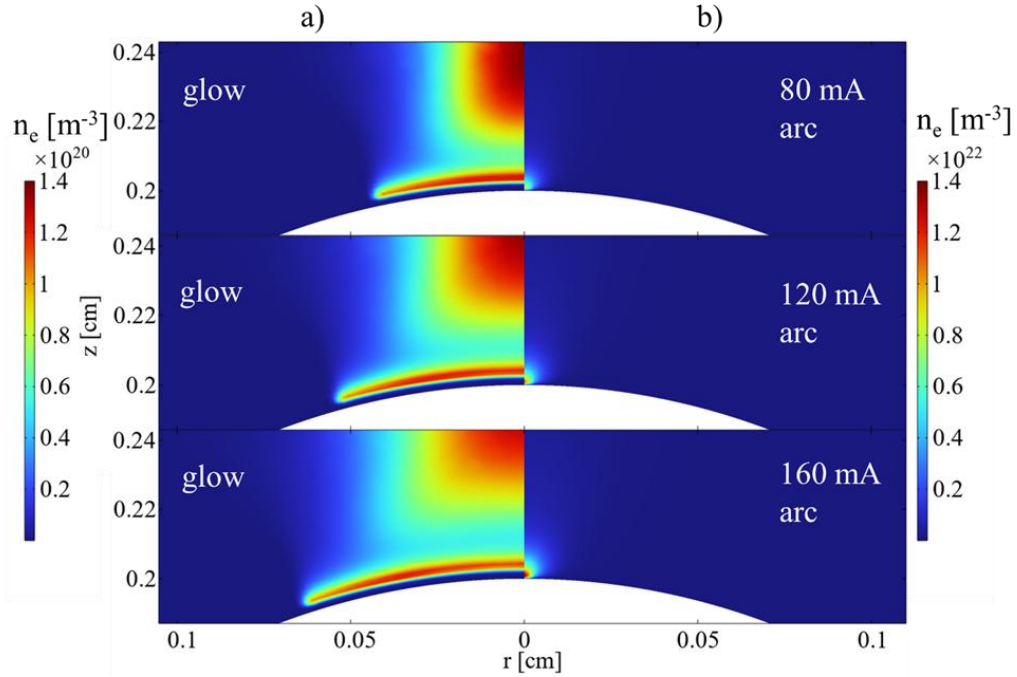

Figure 2.5. 2D profiles of the electron density at three different currents, for a) the glow and b) the arc regime, for a gas velocity $u_{g_0} = 1$ ms^{-1}.

The significantly higher electron densities in the arc compared to the glow give rise to an increase in the vibrational temperature near the electrode. The axial profile of the vibrational temperature for 80 mA and $u_{g_0} = 1$ ms^{-1} in the near cathode region is presented in Figure 2.6. Within the glow, the gas temperature and vibrational temperature are nearly in equilibrium, because the electron density in the negative glow is nearly the same as in the positive column. This results in a smooth transition between the near cathode region and the positive column, leading to vibrational-translational (V-T) equilibrium in the whole region. In contrast, in the arc spot, the electron density experiences a maximum (see Figure 2.2 a)) and a sharp decline towards the positive column. Within the high electron density region, electron impact vibrational excitation (R2.2 in Table A1) deposits a significant amount of energy into the vibrational degrees of freedom, which do not have enough time to relax to the translational degrees of

freedom. As a result, a maximum of the vibrational temperature is observed in the high electron density region (Figure 2.6).

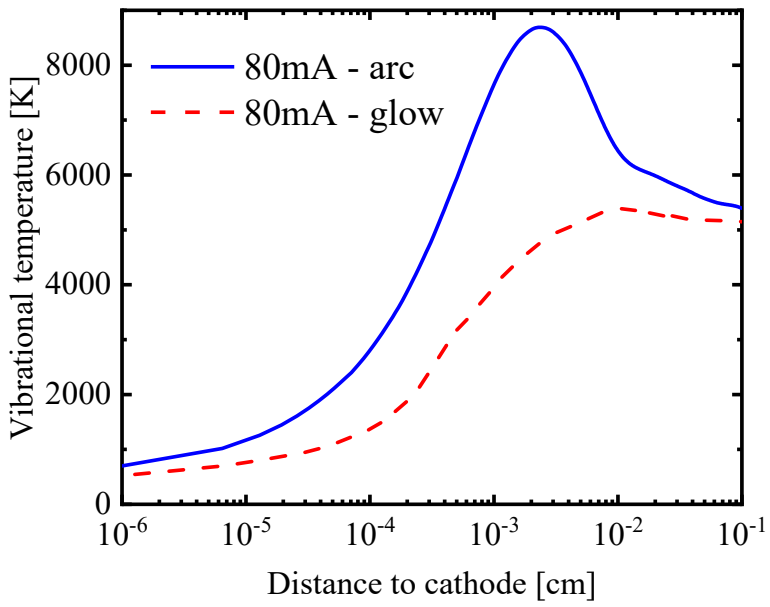

Figure 2.6. Axial profile of the vibrational temperature for 80 mA and $u_{g_0} = 1\ ms^{-1}$ in the near cathode region.

2.3.2 Positive column

The key difference between the glow and the arc cathode region identified in the previous subsection is the significantly higher electron density in the arc regime at the discharge axis. This effect enhances the vibrational heating, leading to a vibrational temperature much higher in the arc spot than in the glow, as shown in Figure 2.6 above. In Figure 2.7, the axial and radial dependence of the gas temperature, at the three different currents for both the glow and arc regime, are presented. Within the positive column, the vibrational and gas temperature are in near equilibrium with each other, thus the vibrational temperature is not shown in Figure 2.7. The contracted nature of the plasma within the investigated current range results in high gas temperatures ($\approx 4700\ K$) and negligible differences between the arc and glow discharge. In the axial direction, there is no strong gradient of gas temperature, resulting in a nearly constant axial distribution. The only differences observed between the glow and the arc are in the

near cathode region, where the arc exhibits an increase in gas temperature with rising vibrational temperature, as shown in Figure 2.7 a). This leads to strong V-T non-equilibrium in the arc spot, as mentioned in previous section.

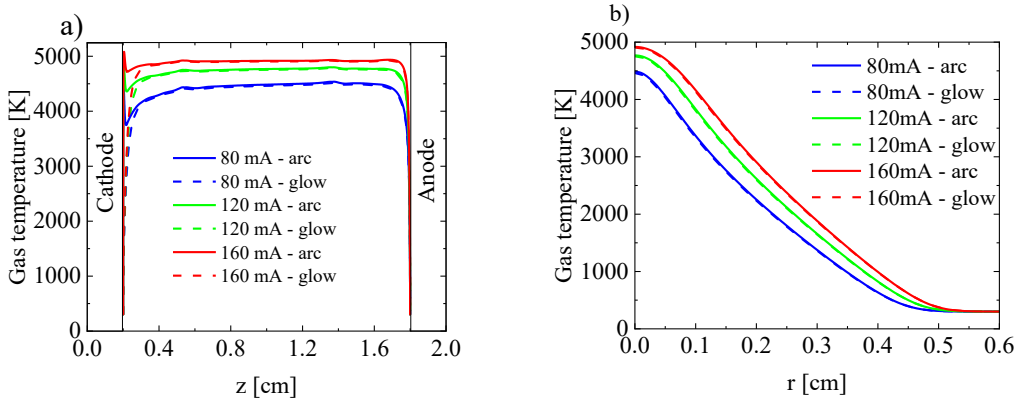

Figure 2.7. Gas temperature at three different currents, for both glow and arc regime, in a) the axial direction (at r = 0, where $r_{cathode}$ and r_{anode} = 0.2 cm, placed at z = 0 and 2 cm) and b) the radial direction (at z = 1 cm), for $u_{g_0} = 1\ m\ s^{-1}$.

The radial temperature distribution at the three different currents (at z = 1 cm) is presented in Figure 2.7b). Upon increasing the current from 80 mA to 160 mA, the radius of the region with elevated gas temperature increases by 12.5 % (from 0.24 cm to 0.27 cm), while the cross section increases with 27 % (from 0.18 cm^2 to 0.23 cm^2).

The heating and cooling rates in the positive column for 80 mA and z = 1 cm are presented for the arc regime in Figure 2.8. Due to similarities between the glow and arc column, only the result for the arc is shown. The heat conductivity (black curve) transports the energy radially from the middle of the column towards the side, until the convective heat transfer (red curve) stops the expansion. As function of the current, there is an increase in the gas temperature, which can be seen in Figure 2.7. The maximum gas temperature increases by 433 K, from 4483 K to 4916 K. The radial distribution of the temperature is then determined by the balance between the heat conductivity and the convective heat losses. Our analysis shows that the radial conductive component has the largest contribution to the loss mechanisms in the plasma column, while the dominant heating process is V-T relaxation, with the largest contribution to the gain mechanisms.

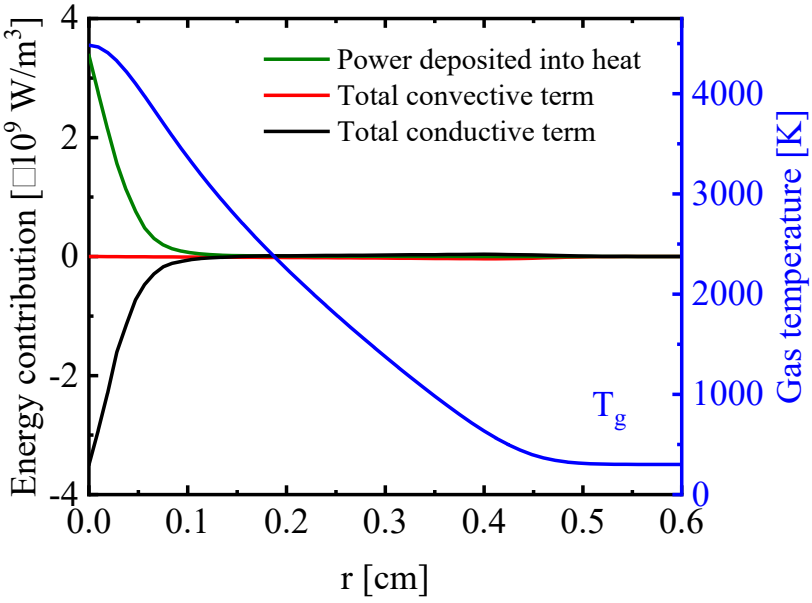

Figure 2.8. Heat balance in the positive column for 80 mA, arc regime, z = 1 cm and u_{g_0} = 1 m s^{-1}.

As indicated in [64], this effect insulates the plasma from the wall, acting as a virtual cold wall. It is then logical that at a constant gas flow velocity, the positive column expands upon increasing current. The expansion of the positive column can also be seen in the radial electron density profile. The radial dependence of the electron density at three different currents, for the glow and the arc regime, at z = 1 cm and $u_{g_0} = 1$ m s^{-1}, is presented in Figure 2.9. Similar as in Figure 2.7, because of the contracted nature of the plasma, no differences are observed in the electron density between the glow and arc. Upon rising current from 80 to 160 mA, the electron density in the positive column experiences a small increase, from 5.8×10^{19} m^{-3} to 6.5×10^{19} m^{-3}.

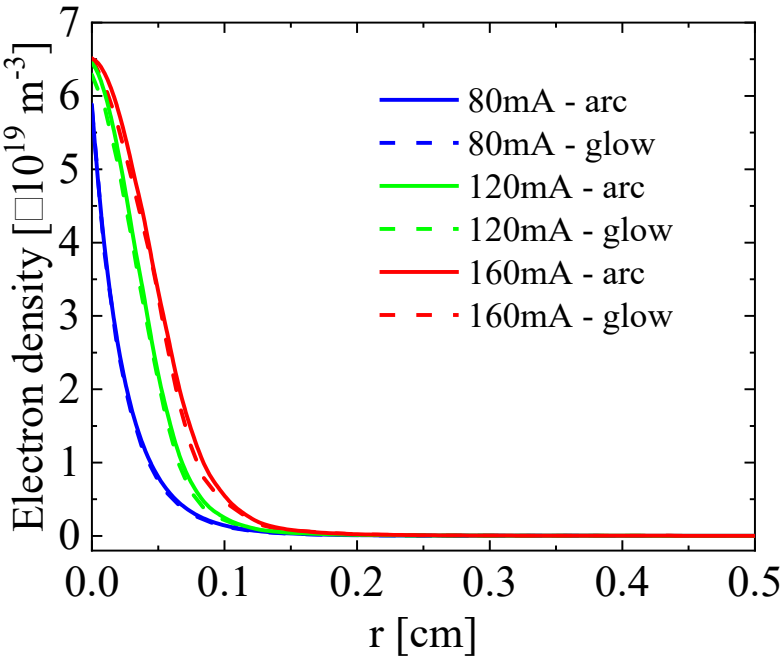

Figure 2.9. Radial dependence of the electron density at three different currents, for the glow and the arc regime, at z = 1 cm, $u_{g_0} = 1$ m s^{-1}.

Generally speaking, our results show that in the positive column and the anode region, the differences in all quantities between the arc and the glow regime amount to negligible values. This effect is highlighted in Figure 2.10, where 2D distributions of the electron density of the arc and glow case are compared to each other. Although the glow cathode region covers a significantly larger area than the arc cathode region, this does not translate to a larger area of the positive column. It is important to note that these results are not universal: they depend strongly on the chemistry and probably on the boundary conditions and the cathode properties.

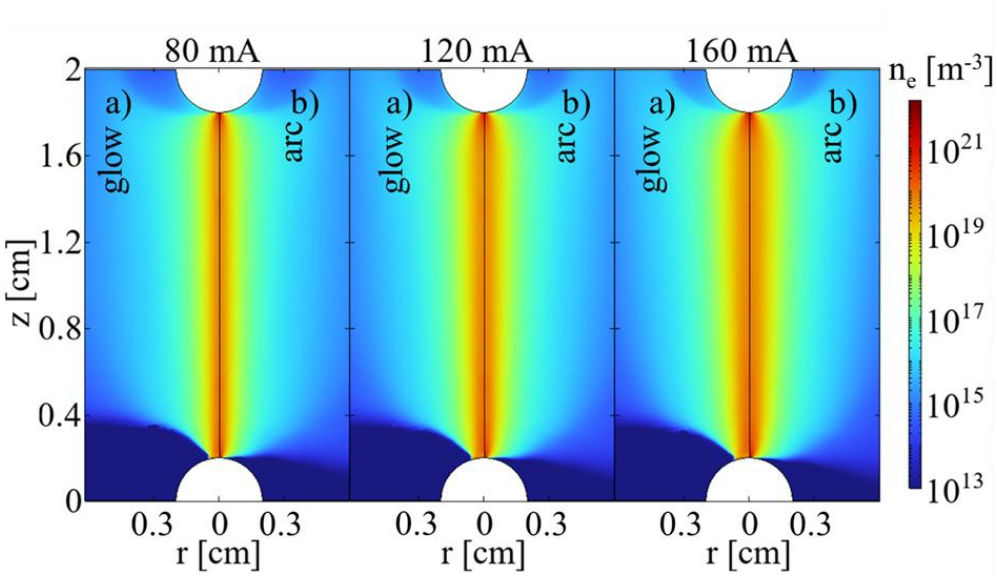

Figure 2.10. 2D electron density profile, at three different currents, for the arc (a) and glow (b) regime, at $u_{g_0} = 1\ m\ s^{-1}$.

Upon increasing the current from 80 to 160 mA, the radius of the current density profile increases by 64 % (from 3.8×10^{-2} cm to 6.3×10^{-2} cm), while the cross section rises by 167 % (from 4.5×10^{-3} cm^2 to 1.2×10^{-2} cm^2). The electron density balance was determined by analyzing equation (2-1). In Figure 2.11, the total rates of production and destruction, as well as the rate of flux losses and the rate of gas convection losses, determining the electron density balance, are presented for the arc regime at 80 mA and z = 1 cm. As previously stated, due to the negligible differences in the glow and arc column, only the result for the arc is shown. The electron density balance is determined to be local and the diffusive, migrative and gas convective fluxes have a negligible contribution (see Figure 2.11). The absolute value of the loss terms was taken in order to make the comparison between the dominant terms.

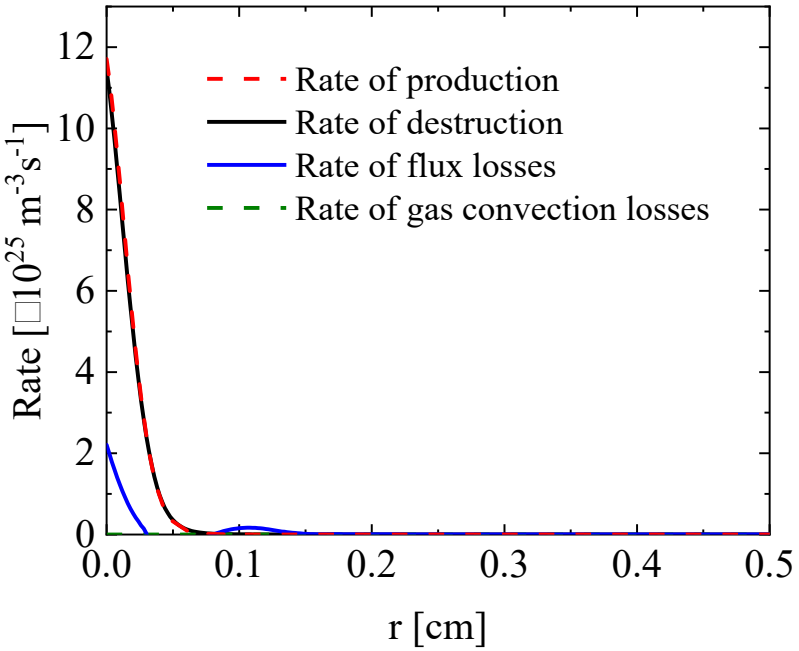

Figure 2.11. Production and destruction rates determining the electron density profile, for the arc regime, at I = 80 mA, u_{g_0} = 1 m s^{-1}, and z = 1 cm. The glow regime has a similar radial profile, thus only the result for the arc is presented here.

Our reaction analysis reveals that the dominant mechanism of electron production, for both arc and glow regime, is Penning and associative ionization (R2.28, R2.29, R2.30 - table A3)

R2.28 $N_2\left(a'^1\Sigma_u^-\right) + N_2\left(a'^1\Sigma_u^-\right) \rightarrow N_4^+ + e,$

R2.29 $N_2(A^3\Sigma_u^+) + N_2\left(a'^1\Sigma_u^-\right) \rightarrow N_2^+ + N_2 + e,$

R2.30 $N_2\left(a'^1\Sigma_u^-\right) + N_2\left(a'^1\Sigma_u^-\right) \rightarrow N_2^+ + N_2 + e,$

which is balanced by dissociative recombination (R2.32 - table A4). The electronically excited $N_2(A^3\Sigma_u^+)$ and $N_2\left(a'^1\Sigma_u^-\right)$ are produced primarily from quenching of the electronically excited $N_2\left(B^3\Pi_g\right)$ and $N_2(C^3\Pi_u)$ states. Further analysis of the production and loss processes for the positive ions and excited states reveals that they are also locally balanced. The radial distribution of the various ion densities for the same conditions is presented in Figure 2.12. It is clear that the dominant positive ion is N_2^+ throughout most of the positive column. Near the edges of the current-conductive

region, where the gas temperature is lower, N_3^+ becomes the dominant ion. This is attributed to the charge exchange reaction (R2.19 – table A1), which is also the reason for the change in the dominant ion near the cathode surface. The density profile of the atomic ions N^+ closely follows that of N_2^+. Upon increasing current, the density of N^+ approaches the density of N_2^+, as also found in [69].

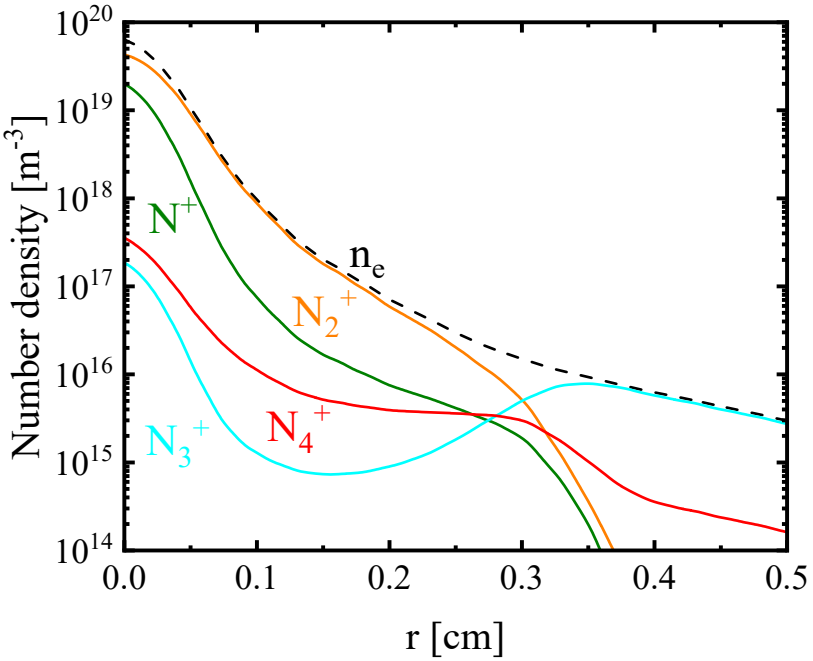

Figure 2.12. Radial distribution of the various ion densities, as well as the electron density, for z = 1 cm, I = 80 mA, u_{g_0} = 1 m s^{-1}, in the arc regime. Due to similarities between the glow and arc column, only the result for the arc is shown here.

2.3.3 Effect of the gas flow rate

In section 2.3.2 we demonstrated that the cathode region, and hence the electron emission mechanism, has no significant effect on the positive column. To investigate the effect of the gas flow rate on the discharge, we chose a single current condition (80 mA) and a single electron emission mechanism, *i.e.* thermionic field emission, hence reflecting the arc regime. We varied the inlet flow velocities as 1, 2 and 4 m s^{-1}. The 2D velocity distributions are shown in Figure 2.13.

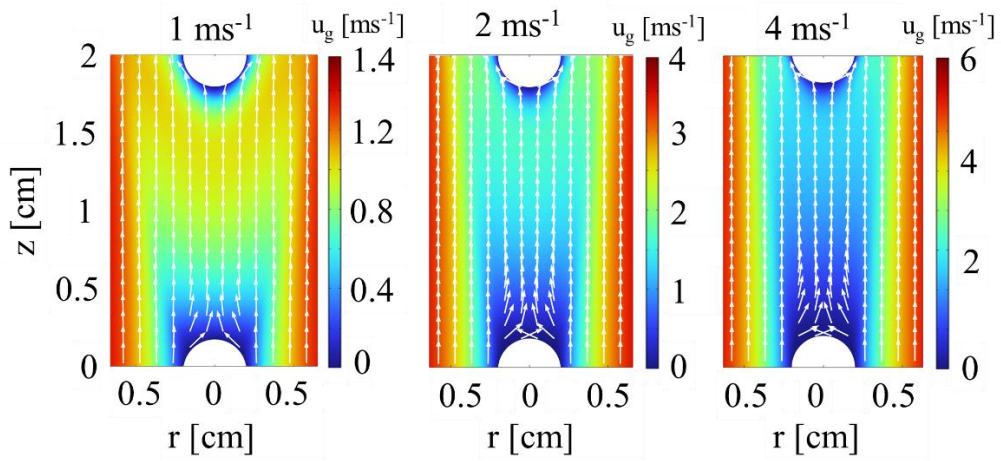

Figure 2.13. 2D distribution of the gas velocity magnitude, at three different inlet flow velocities, for I = 80 mA, in the arc regime. The white arrows show the velocity direction.

We can see that the cathode is effectively shielded by the high velocity region of the flow. A velocity gradient is present in both axial and radial direction. As the flow velocity rises to 4 m s^{-1}, a small recirculation zone appears above the cathode surface. The velocity in the recirculation zone is rather low and has no significant effect on the arc properties near the cathode.

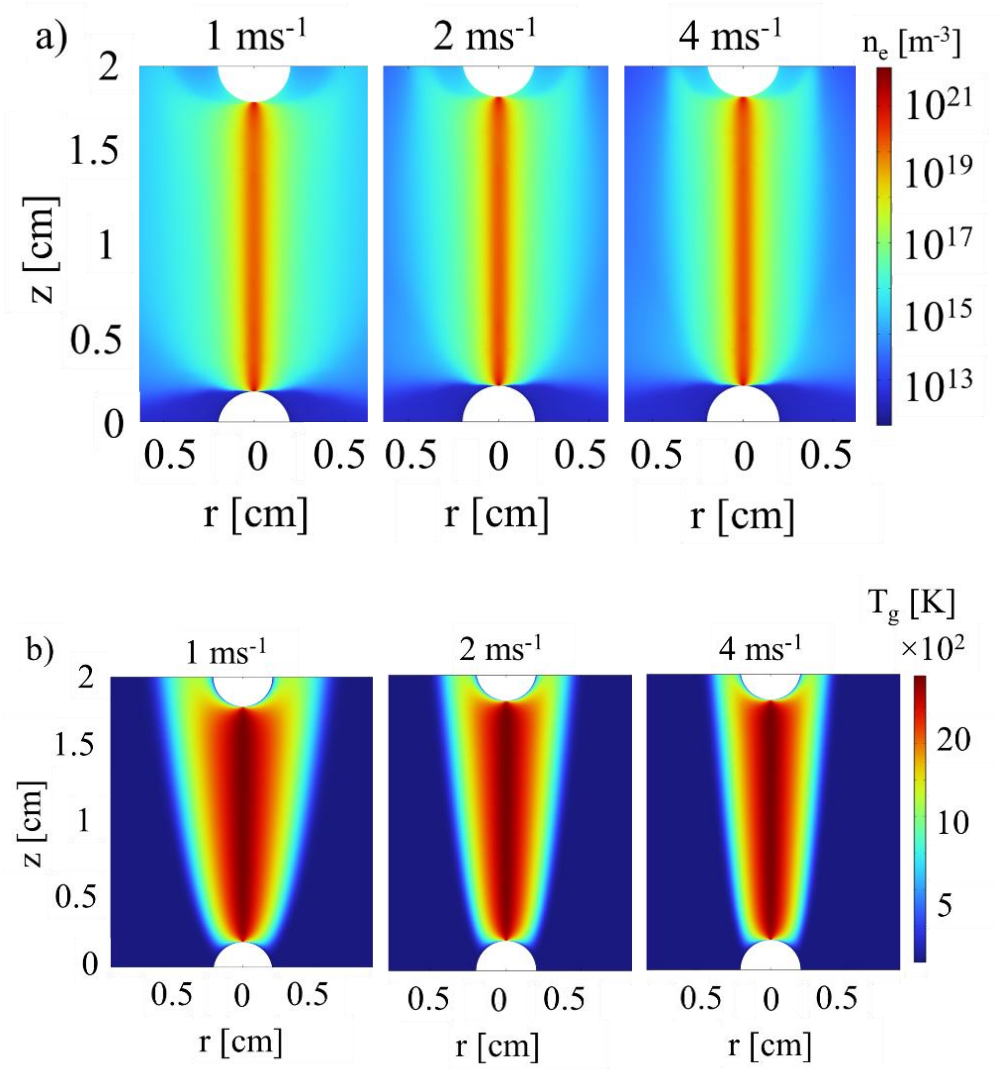

Figure 2.14. 2D profiles of a) electron density and b) gas temperature, at three different inlet flow velocities, for I = 80 mA in the arc regime.

In Figure 2.14, the electron density and gas temperature profiles at the three different gas flow velocities are presented. In section 2.3.2, we already demonstrated, in agreement with [64], that the gas flow effectively insulates the arc from the walls through convective heat transfer in the axial direction. The increased axial cooling upon higher gas flow rate leads to further contraction of the area of the elevated gas temperature. The radius reduces by 37.5 % (from 0.22 to 0.16 cm) between 1 and 4 m s^{-}

[1] (see Figure 2.14a)), and the cross section area reduces by 87.5 % (from 0.15 to 0.08 cm^2). The arc radius defined from the current density profile changes from 3.8×10^{-2} cm to 3.3×10^{-2} cm, corresponding to a 15 % decrease, and the cross section area drops by 32 % (from 4.5×10^{-3} to 3.4×10^{-3} cm^2). The radial temperature gradient also becomes significantly steeper upon higher gas flow velocity, which further enhances the cooling of the arc due to heat conduction and results in slightly lower temperatures in the center of the positive column. The radial profiles of gas temperature and electron density at three different gas flow velocities, for z = 1 cm, are shown in Figure 2.15. It is interesting to see that the increase in the gas flow velocity does not influence the core of the positive column. The effects of the gas flow are primarily on the periphery of the plasma, indicating the electrodes are shielding the column from the gas flow. This leads to a reduction in the radial size of the positive column without significantly affecting the core. A constant V-T non-equilibrium of ~600 K is observed in the middle of the positive column where the electron density has it highest values (Figure 2.15 a)). The electron density also does not experience a significant change in its maximum value as a function of the gas flow (Figure 2.15 (b))

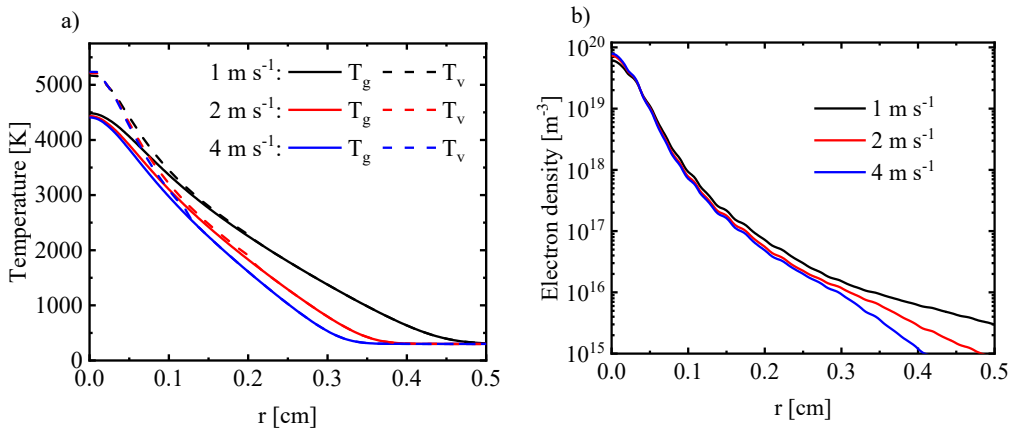

Figure 2.15. Radial distribution for a) the gas and vibrational temperature and b) the electron density, at three different gas flow velocities, for z = 1 cm.

The dominant ion remains N_2^+ with an increasing population of N^+ upon higher flow velocities. Naturally, as the plasma is cooled down, a higher voltage is required to sustain the discharge because of the lower gas temperature of the positive column. Because the electrodes are protecting the plasma main conductive channel, increasing the velocity does not lead to significant increase in the burning voltage, from 405 V at 1 m s^{-1} to 412 V at 4 m s^{-1}.

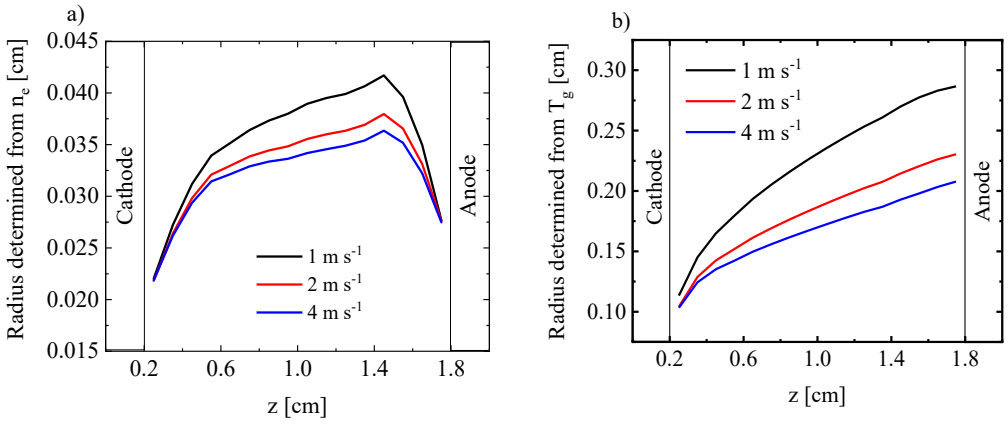

Figure 2.16. Axial profile at r = 0 of the arc radius defined from the current density profile a) and from the gas temperature profile b) for I = 80 mA.

Figure 2.16 shows the axial profile at r = 0 for the radius of the arc defined from the current density *j* and the gas temperature T_g. The strong coupling between the gas temperature and the electron density is observed as a function of the axial position. Following the discussion in the previous section, the radius of the region with elevated temperature is defined by the balance between the convective and conductive components, meaning that there is a strong connection between the gas velocity and the gas temperature. The electron density balance was determined to be local, indicating the radius of the current density profile depends strongly on the gas temperature profile and indirectly on the gas velocity distribution. The gas entering the domain from the cathode towards the anode is at 300 K and gradually heats up along the axial direction. The axial transport of heated gas leads to a less steep temperature gradient in the radial direction as a function of the axial position, which in turn results in expansion of the arc. This effect is highlighted in Figure 2.16 b) where the gas temperature radius increases as a function of the axial position for any flow rate, together with the current density profile (Figure 2.16 a)).

2.4 Conclusions

We developed a fully self-consistent model of a N_2 plasma at atmospheric pressure, including the cold cathode emission processes, which allows us to model the cathode region next to the positive column. Specifically, we compared thermionic-field emission with secondary electron emission, in order to determine the influence of the cathode region on the positive column, for both arc and glow regime, respectively. Hence, our

model investigates the possibility of instabilities arising from the cathode emission phenomena sustaining arc and glow discharges. The results show that, for a constant gas flow velocity of 1 m s^{-1} and electric currents of 80, 120, and 160 mA, the electron emission mechanism affects the size and temperature of the cathode region, which is hot and very constricted for the arc regime, while colder and more spread out (especially upon higher currents) for the glow regime. However, this different cathode region behavior does not significantly influence the positive column at atmospheric pressure. Our model also reveals that the electron density balance is local and the electron migration and diffusion are negligible at the investigated conditions. Furthermore, the contraction of the positive column and its properties are mainly determined by the balance between conductive and convective heat transport. Finally, our model predicts that increasing the gas flow velocity does not significantly influence the peak gas temperature, and the resulting contraction weakly influences the electron density.

Finally, it is worth to mention that in order to validate our model, we performed a comparison with the experimental data modelled in [64, 69] and the results are presented in Appendix A2. Although we are using the same kinetic scheme, we observe nearly an order of magnitude higher electron density compared to the results in [69]. When comparing to the results from [64], very good agreement is reached for the gas temperature, but deviation of the vibrational temperature is observed as a function of the current. Nevertheless, the aim of our work was different, i.e., to study the effect of the cathode emission on the positive column, and the possible differences between glow and arc regime, where we find no differences. We believe this claim is still valid, despite the limitations of our model to reproduce the experiments of [64, 69]. However, in view of the above discrepancy, our claim should still be validated by experiments, before drawing final conclusions. Fortunately, two years after our model was published, our claim was validated by experiments performed by Li *et al.* [88]. Their experiment showed that the EC for NF improves when the discharge regime changes from glow to an arc, while there was no change in the NO concentration.

Our calculations inspire optimism on the possibility of creating extended gas discharge systems with a large area sectioned cathodes, that can generate plasmas in large volumes, regardless of the mode of the cathode layer on the cathode sections. Furthermore, an important conclusion of our model, in terms of gas conversion applications, is that, due to the additional power deposited for sustaining the glow discharge, this mode will not be beneficial for gas conversion applications, and the arc mode should be promoted for more energy-efficient conversions.

Chapter 3.

Nitrogen fixation by an arc plasma at elevated pressure to increase the energy efficiency and production rate of NO_x

As mentioned in the Introduction, plasma-based NF for fertilizer production is an attractive alternative to fossil fuel-based industrial processes. However, many factors hinder its widespread applicability, e.g., the commonly observed inverse correlation between energy consumption (EC) and production rates (PR), or the necessity to enhance the selectivity towards NO_2, i.e., the desired product for a more facile formation of nitrate-based fertilizers. In Chapter 2, we found that arc discharges should be the most efficient for gas conversion. In this chapter, we investigate the use of a rotating gliding arc plasma for NF at elevated pressures (up to 3 barg), at different feed gas flow rates and composition. Our results demonstrate a dramatic increase in the amount of NO_x produced as a function of increasing pressure, with a record-low EC of 1.8 MJ/(mol N), while yielding a high PR of 69 g/h and a high selectivity (94%) of NO_2. We ascribe this improvement to the enhanced thermal Zeldovich mechanism, and an increased rate of NO oxidation compared to the back reaction of NO with atomic oxygen, due to the elevated pressure.

This chapter is based on:
Nitrogen fixation by an arc plasma at elevated pressure to increase the energy efficiency and production rate of NO_x
I. Tsonev*, C. O'Modhrain*, A. Bogaerts, Y. Gorbanev (* = shared first author)
ACS Sustainable Chemistry & Engineering, 11(5), 1888-1897, (2023)
https://doi.org/10.1021/acssuschemeng.2c06357

3.1 Introduction

One of the key appeals of plasma-based NF, and other plasma-based gas conversion processes is their operation at atmospheric pressure, as opposed to high-pressures required for HB. However, it is interesting to investigate the performance of plasma-based NF at somewhat elevated pressures as well. Indeed, elevated pressures of several bar can be easily achieved with a simple needle valve, and the created backpressure does not require special feed gas flow equipment outside of standard mass flow controllers (MFCs).

Fundamental phenomena of high-pressure plasmas in a variety of gases have been extensively studied, both experimentally and theoretically, including high pressure arc discharges [76,89,90]. However, the reports focusing on applications of elevated pressure plasma to gas conversion are scarce. Several works involving CO_2 splitting in DBD reactors at elevated pressure have been carried out [91,92], in addition to hydrocarbon synthesis from syngas using high-pressure arcs [93]. The importance of plasmas above atmospheric pressure is also highlighted in the latest low temperature plasma roadmap [94]. To the best of our knowledge, to date there have been no published works dedicated to studying plasma-based NF into NO_x at elevated pressure.

In this chapter, we investigate the use of the RGA plasma reactor, previously used by our group for NF at atmospheric pressure [57, 58]. We conducted experiments at elevated pressures (1-3 barg, i.e., ca. 2-4 atm), at different feed gas flow rates (4, 8 and 12 Ln/min) and compositions (air - N_2:O_2 4:1, and oxygen-enriched air - N_2:O_2 1:1). We observed dramatic improvements in NO_x yield, PR and EC upon rising pressure, as well as a change in the NO_x product distribution with a shift towards NO_2.

3.2 Description of the experimental setup

The feed gas flow (N_2:O_2 of 4:1 or 1:1, total flow rate 4, 8, or 12 Ln/min) was supplied using mass flow controllers (MFC, Bronkhorst F-210CV) connected to N_2 and O_2 gas cylinders (both 99.999%, Praxair). The feed gases N_2 and O_2 were mixed using a T-connector, and introduced into the RGA plasma reactor (Figure 3.1). The reactor comprised the main part (consisting of a spark plug and the immediate surroundings) and the long reactor body (stainless steel). A detailed description of the reactor itself is shown in Figure B1 in Appendix B.

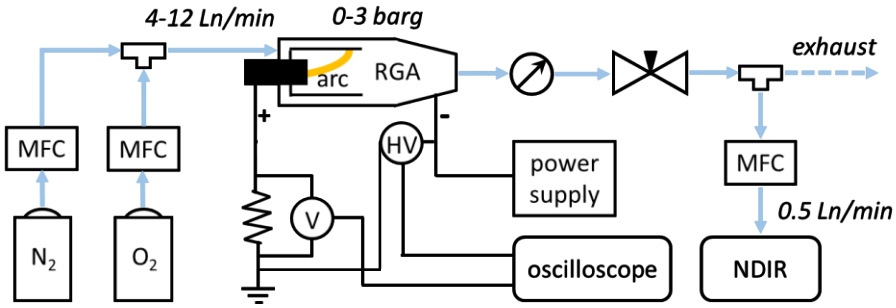

Figure 3.1. Schematic representation of the RGA plasma setup for NO_x production, with an illustrated high-temperature arc inside the RGA reactor.

The outlet of the plasma reactor was connected to a manometer (Keller LEO2) and a needle valve, which allowed monitoring and varying the pressure inside the reactor, respectively. Details on the pressure and mass flow rate are found in Appendix B, section B1 and Figure B2.

The discharge was driven by a high-voltage current-controlled DC power supply unit (PSU; Technix SR12KV-10KW). The electrical characteristics were monitored with a digital oscilloscope (Keysight InfiniiVision DSOX1102A) using a high voltage probe (Tektronix P6015A). The voltage over a shunt resistor (2 Ω) was measured as shown in Figure 3.1, to estimate the current values. The reactor was positioned on a wooden surface, and the only path of the current to ground was through the shunt resistor. The sample rates used in the presented data were 10 MSa/s on a 5 ms timescale. In order to determine the accuracy of the data, we varied the sampling rate between 10 MSa/s (5 ms) and 1 MSa/s (50 ms), and observed no significant changes in the average voltage, average current, and the average power. The power measurements conducted in this way have an uncertainty of about 20 %.

The total power consumption (defined from the plug power, i.e., the energy used by the PSU) was measured using a three-phase power meter (Chauvin Arnoix MEMO TD80). The temperature of the outer walls of the RGA plasma reactor was measured with an IR thermal imaging camera (Bosch GTC 600 C, -20 to 600 ^{o}C, accuracy ±0.1 ^{o}C).

The concentration of the produced NO_x in the gas outlet from the RGA reactor was analysed with a non-dispersive infrared (NDIR) sensor (Emerson, Rosemount X-stream Enhanced XEGP Continuous Gas Analyzer) as described in section B2 in Appendix B.

The calculation of the plasma power, EC and NO_x PR is detailed in section B3 in Appendix B. Each experiment was conducted in triplicate. The error bars represent standard deviations between the obtained values. We note that in some cases the error bars are too small to be visible on the graphs, but they are present for every datapoint.

3.3 Results and discussion

We investigated the performance of our reactor for two different feed gas ratios, i.e., N_2:O_2 of 4:1 and 1:1. Each mixture was examined at feed gas flow rates of 4, 8 and 12 Ln/min. A current-controlled PSU was used, i.e., we were able to vary the current value, while the voltage varied in response. At a constant current, the power deposition into the plasma increases upon rising pressure, indicating that the average voltage increases. Under all conditions studied, we observed formation of NO_x. We report NO_x concentration, plasma power, EC and PR as a function of the supplied current. We specifically note that we present the data as a function of the PSU-supplied current for clarity and consistency. The values of the plasma-deposited current varied from the PSU-supplied current. The plasma-deposited current values were calculated as shown in section B3 in Appendix B, and these values were implemented in the calculations of the plasma power and EC.

3.3.1 Production of NO_x from air (N_2:O_2 mixture 4:1)

The results for N_2:O_2 4:1 at a flow rate of 4 Ln/min and 12 Ln/min are shown in Figures 3.2a-b and 3.3a, and Figures 3.2c-d and 3.3b, respectively. We observed two distinct modes of plasma operation, characterized as restrike and takeover modes [95,96]. These two modes occur as a function of increasing current, and are typically discriminated by a decreasing level of voltage fluctuations. The restrike mode is characterized by repeated ignition and extinguishing of the arc, resulting in large voltage fluctuations. The takeover mode occurs at higher current, resulting in quasi-regular arc movement and quasi-periodic voltage fluctuations with lower amplitude compared to

the restrike mode. The differences in the current and voltage waveforms of the two modes are shown in Appendix B (Figure B3).

In all experiments, we examined only the conditions which allowed the takeover mode. For example, at 0 barg and 4 L/min, this mode of operation could only be achieved at a minimal PSU current of 500 mA (Figure 3.2a). The restrike mode was avoided because it produces electromagnetic interference, affecting the analytical equipment and presenting potential hazards.

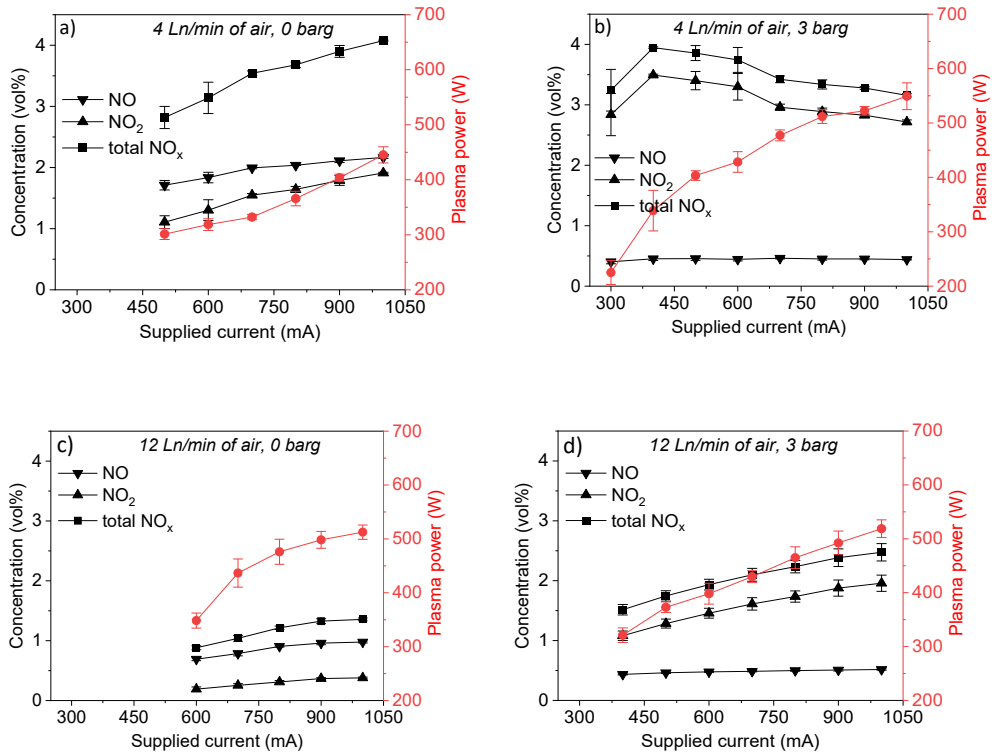

Figure 3.2. Concentration of produced NO_x and plasma power with N_2:O_2 = 4:1, for different gas flow rates, as a function of the PSU current: (a) 4 Ln/min, 0 barg; (b) 4 Ln/min, 3 barg (c); 12 Ln/min, 0 barg; (d) 12 Ln/min, 3 barg. The results are presented for conditions which produced the stable takeover discharge mode (see text).

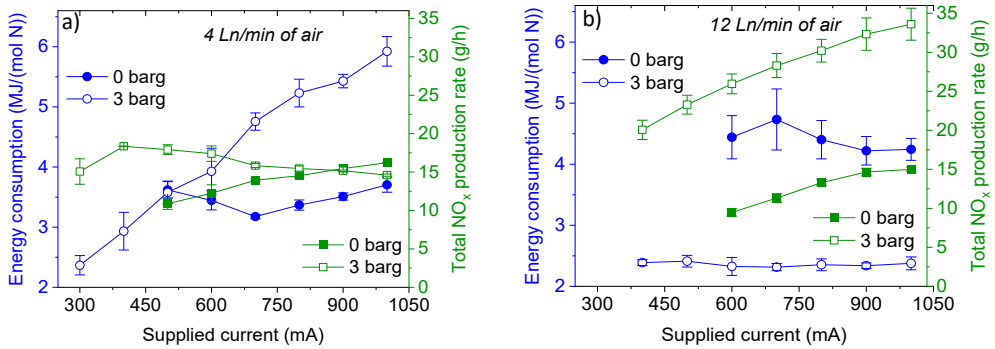

Figure 3.3. Energy consumption and total NO_x production rate with N_2:O_2 = 4:1, at 0 and 3 barg, for 4 Ln/min (a) and 12 Ln/min (b). The results are presented for conditions which produced the stable takeover discharge mode (see text).

It is generally accepted in plasma-based NF that NO_x production occurs via dissociation of N_2 and O_2 into N and O, followed by the Zeldovich reactions, as shown in simplified reactions R3.1-R3.6 [97, 98]. In general, in plasmas these reactions can either be thermally of vibrationally promoted, depending on the species present.

R3.1	$O_2 \rightleftharpoons 2O$
R3.2	$N_2 \rightleftharpoons 2N$
R3.3	$N_2 + O \rightleftharpoons N+NO$
R3.4	$O_2 + N \rightleftharpoons NO+O$
R3.5	$NO + O \rightleftharpoons NO_2$
R3.6	$2NO + O_2 \rightarrow 2NO_2$

First, we studied NO_x production at 4 Ln/min feed gas flow rate. At 0 barg, a gradual rise of the plasma-deposited power by ca 1.5 times (from 300 to 445 W), as a consequence of increasing the supplied current (from 500 to 1000 mA) yields a higher amount of NO_x produced, by a factor of 1.6, i.e., from 2.8 to 4.1 vol% (Figure 3.2a), the latter corresponding to the highest PR of 16.2 g/h (Figure 3.3a). These closely proportional changes of NO_x concentration and power lead to a relatively constant EC, around 3.5 MJ/(mol N) (Figure 3.3a). It is worth noting that PR is governed by two factors: the total NO_x concentration, and the product ratio of NO:NO_2 (see eq. B6 in Appendix B). In this particular case, the higher plasma-deposited power did not affect the product distribution, which remained within NO:NO_2 of 1.5:1 - 1:1 (Figure 3.2a), hence the direct proportionality between total NO_x concentration and PR.

In order to highlight the increased performance at elevated pressures, a comparison of PR and EC must be done at the same power. As mentioned above, we used a current-controlled PSU, hence we did not have a direct control of power. Therefore, we compare the closest power values at different pressures. At 0 barg and 900 mA PSU-supplied current, the recorded power was ca. 400 W (Figure 3.2a). These conditions produced 3.9 vol% NO_x at a corresponding PR of 15.5 g/h and EC of 3.5 MJ/(mol N) (Table B1 in Appendix B shows the comprehensive comparison between different conditions with the closest power values). In contrast, at 2 barg, 400 W of plasma-deposited power was achieved with a lower PSU-supplied current of 600 mA (Figure B4b). This resulted in a higher PR (17.9 g/h) at the same power, and a lower EC of 3.3 MJ/(mol N). However, further rising the pressure to 3 barg at 400 W leads to an increase in EC back to 3.5 MJ/(mol N).

At 3 barg and 4 Ln/min (Figure 3.2b), the NO_x production does not rise proportionally as a function of the plasma-deposited power. As a result, the EC increases dramatically, from 2.4 MJ/(mol N) at 300 mA, to 5.9 MJ/(mol N) at 1 A (Figure 3.3a). A drop in PR from 18.3 g/h to 14.6 g/h is also observed (Figure 3.3a).

As mentioned earlier, at a constant current we observe that the power deposited into the plasma increases upon increasing pressure. This suggests that the voltage increases as function of rising pressure. For example, following the conditions in Figure 3.2 above, with the flow rate of air of 4 Ln/min and the PSU supplied current value of ca. 500 mA, at 0 barg the average voltage is 578 V, yielding a power value of 295 W. At 3 barg, the voltage is 736 V, and the power 383 W. Similarly, the values for 12 Ln/min (at ca. 600 mA) are 572 V and 355 W, and 668 V and 414 W at 0 and 3 barg, respectively.

The effect of increasing pressure, however, results in a shift of the product distribution, yielding a higher selectivity of NO_2. The NO:NO_2 ratio changes from around 1:1 at 0 barg to 1:6 at 3 barg. This shift in product ratio is advantageous because higher NO_2 selectivity is beneficial for the nitrate fertilizer-aimed NF: NO_2 is more easily absorbed in aqueous washers, thus facilitating the process of NO_3^- accumulation in liquid [49, 99].

Noteworthy, at elevated pressure, plasma is sustained in the takeover mode at lower currents. For example, with 4 Ln/min, 0 and 3 barg, we observe the takeover mode at 500 and 300 mA, respectively (Figure 4.2a-b). It is at these lower currents (300-400 mA) that the lowest EC, at the highest PR, are observed for 4 Ln/min: ca. 2.4 MJ/(mol N) and 16 g/h, respectively, at 3 barg (Figure 3.3a). The NO_x concentration, EC and PR for 4 Ln/min, 1 and 2 barg are shown in Figure 3.4 and 3.5. This effect may be explained by

the change in size of the cold gas boundary layer, pushing the attachment point of the arc on the cathode (i.e., where the arc is attached to the reactor wall).

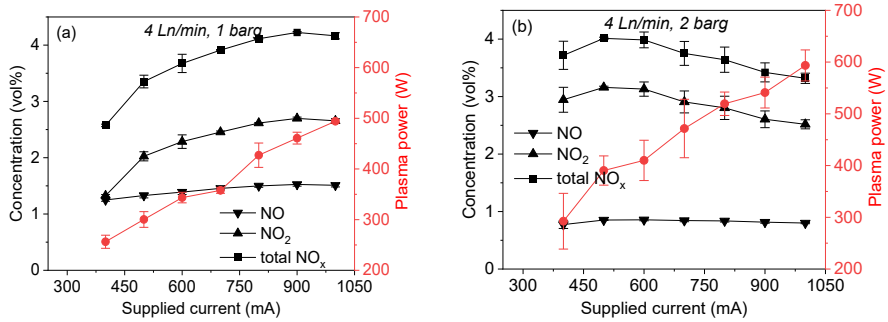

Figure 3.4. Concentration of produced NO_x and plasma power with N_2:O_2 = 4:1, at 4 Ln/min, 1 barg (a) and 2 barg (b) as a function of the current supplied by the PSU. The results are presented for conditions which produced the stable takeover discharge mode.

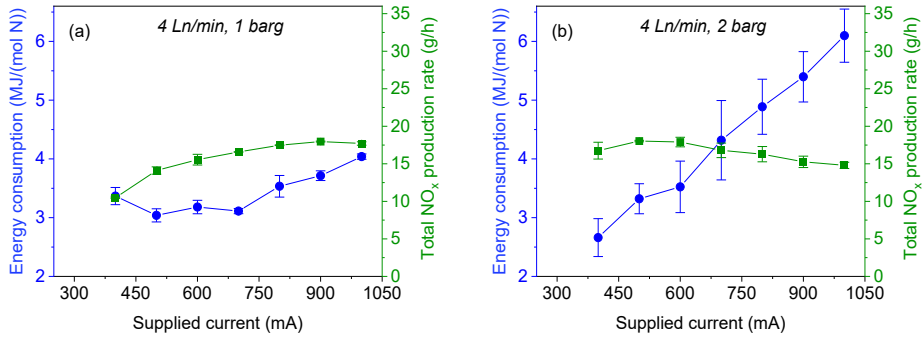

Figure 3.5. Energy consumption and total NO_x production rate with N_2:O_2 = 4:1, at 4 Ln/min, 1 barg (a) and 2 barg (b) as a function of the current supplied by the PSU. The results are presented for conditions which produced the stable takeover discharge mode.

Two forces influence the attachment point: the drag force resulting from the gas flow, and the electromagnetic force resulting from the movement of charged particles. The increased pressure leads to a higher temperature in the reactor (see section 3.3.2 on Mechanistic considerations below), which in turn reduces the size of the cold gas boundary layer and its effect on the attachment point. The drag force resulting from the gas flow can no longer extend the arc to a point in which restrike can occur, and the more stable takeover mode is achieved [100]. Furthermore, the reduced velocity results in a reduced swirl intensity, and the arc experiences reduced contracting force. This leads to thickening of the arc column, and contributes to a more stabilized arc.

At 0 barg, the results for 8 and 12 Ln/min follow similar trends to one another. The Figures relating to the 8 Ln/min are presented in Figure 3.6 and 3.7.

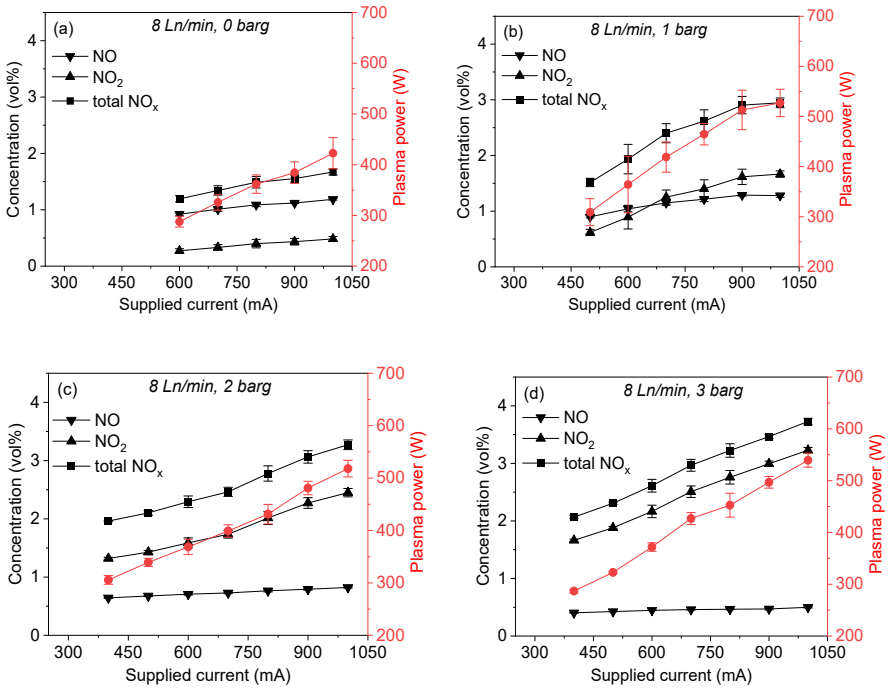

Figure 3.6. Concentration of the produced NO_x and plasma power with N_2:O_2 = 4:1, at 8 Ln/min, 0 barg (a), 1 barg (b), 2 barg (c) and 3 barg (d) as a function of the current supplied by the PSU. The results are presented for conditions which produced the stable takeover discharge mode.

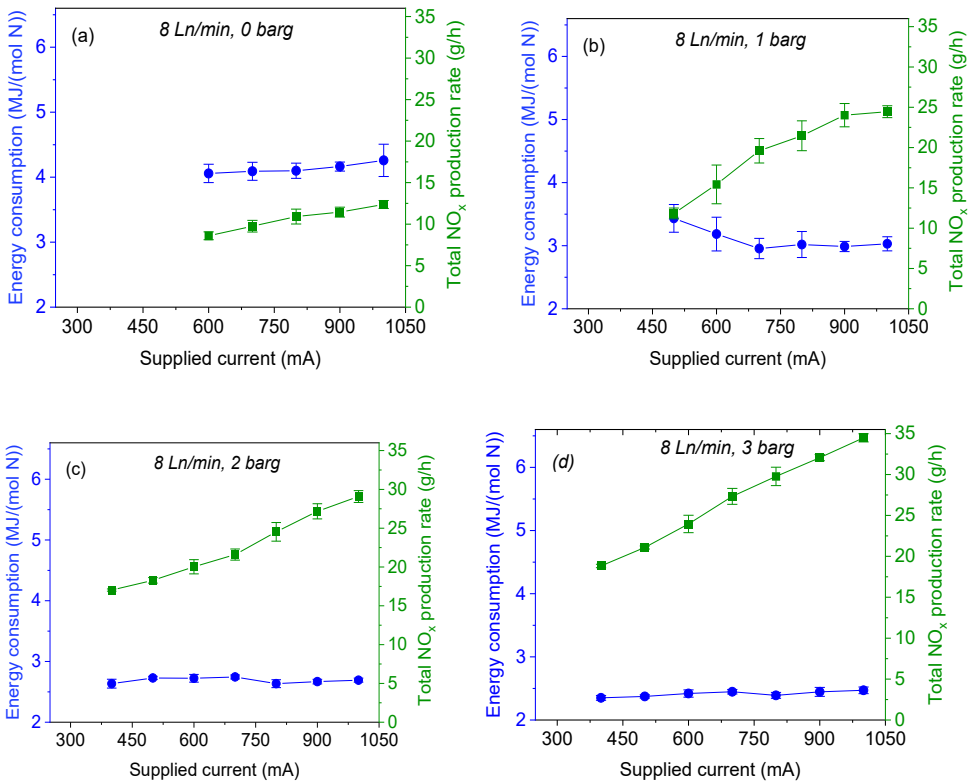

Figure 3.7. Energy consumption and total NO_x production rate with N_2:O_2 = 4:1, at 8 Ln/min, 0 barg (a), 1 barg (b), 2 barg (c) and 3 barg (d) as a function of the current supplied by the PSU. The results are presented for conditions which produced the stable takeover discharge mode.

With 12 Ln/min, at 0 barg the maximal amount of NO_x produced is 1.4 vol% at a deposited power of 515 W (1000 mA supplied current) (Figure 3.2c). The power increases by a factor of 1.6 (from 350 W to 515 W) as a function of the supplied current (from 600 mA to 1000 mA), while the total NO_x concentration is clearly lower than at 4 Ln/min. This results in a higher EC (4.2-4.7 MJ/(mol N)) and lower PR (9.5-15 g/h) for all applied currents at 12 Ln/min and 0 barg (Figure 3b). Compared to 4 Ln/min, the NO:NO_2 ratio shifts towards NO, and constitutes 3:1-4:1 at all current values (Figure 3.2c).

At 3 barg, with 8 and 12 Ln/min, the drop in NO_x concentration and PR (as seen for 4 Ln/min) at higher currents is not observed (Figures 3.6-3.9 and Figure 3.2d).

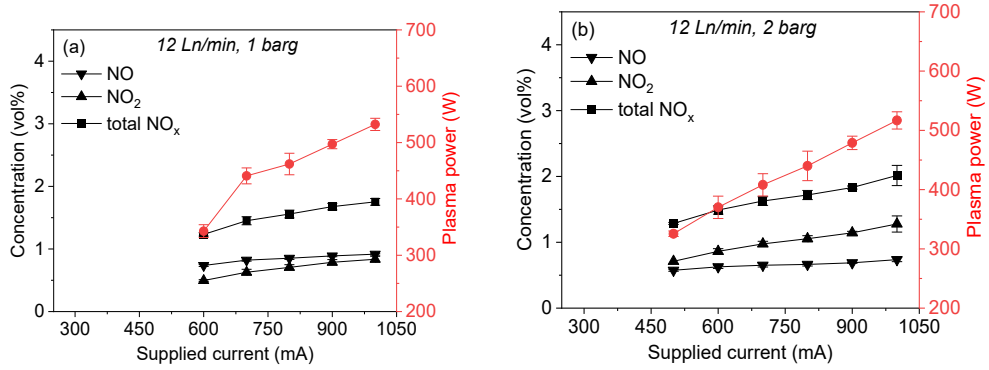

Figure 3.8. Concentration of produced NO_x and plasma power with N_2:O_2 = 4:1, at 12 Ln/min, 1 barg (a) and 2 barg (b) as a function of the current supplied by the PSU. The results are presented for conditions which produced the stable takeover discharge mode.

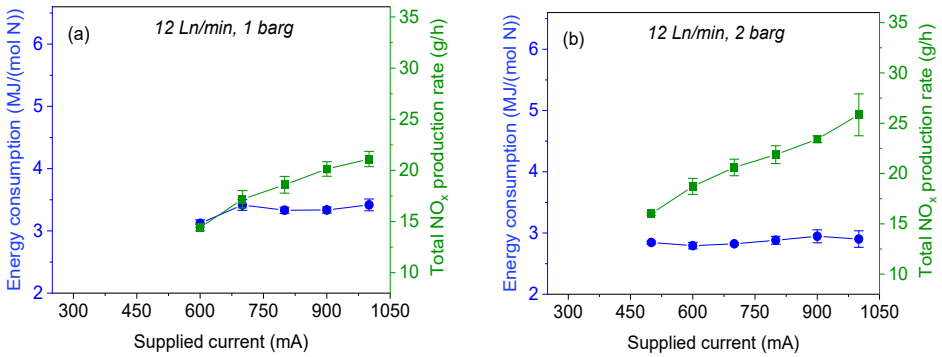

Figure 3.9. Energy consumption and total NO_x production rate with N_2:O_2 = 4:1, at 12 Ln/min, 1 barg (a) and 2 barg (b) as a function of the current supplied by the PSU. The results are presented for conditions which produced the stable takeover discharge mode.

Instead, the NO_x concentration and power values continue to rise proportionally, resulting in a relatively constant EC at all current values (Figure 3.3b). While the EC remains constant, the higher NO_x concentration yields a rise in PR from 20 to 34 g/h as a function of increasing current. This higher PR is also linked to the shift in product distribution towards NO_2. Indeed, the NO:NO_2 ratio of 1:2 at 400 mA rises to 1:4 at 1000 mA.

The main difference between lower flow rate (4 Ln/min) and higher ones (8 and 12 Ln/min) is that with higher flow rates, at constant power and elevated pressure, both the PR and EC improve more than two-fold. For example, with 12 Ln/min and 430 W, the

PR and EC change from 11 g/h and 4.7 MJ/(mol N) at 0 barg to 28 g/h and 2.3 MJ/(mol N) at 3 barg (see Table B1).

Taken together, our results indicate that elevated pressure (up to 3 barg) can be highly beneficial for the energy and production efficiency values of plasma-based NO_x generation. To date, the unmodified RGA reactor (i.e., without an effusion nozzle [58]) used in this study was able to produce 4.1 vol% NO_x from air (with 60% NO_2 selectivity) at an EC of 3.0 MJ/(mol N), and a PR of ca. 9 g/h [57]. In our new experiments, the optimal condition for NO_x production with N_2:O_2 of 4:1 is at 12 Ln/min, 3 barg, 900 mA PSU current. These conditions yield 2.4 vol% NO_x (with 80% NO_2), 2.3 MJ/(mol N) EC, and 32 g/h PR (Figure 3.2d, Figure 3.3b).

Furthermore, besides the plasma-based EC, we also evaluated the plug-to-NO_x EC, based on the total energy consumption of the power supply, defined by the measured plug power. This is an often overlooked metric in the plasma research community, and rarely reported in literature [101], although any application-related discussion should include this metric, alongside the commonly used plasma-based EC. For the aforementioned optimal plasma-based EC conditions, the plug-to-NO_x EC is 7 MJ/(mol N). Lower values (5.4 MJ/(mol N)) are obtained at 400 mA PSU, but they correspond to lower PR and higher plasma-based EC (see Table B2 for all values of plug power and plug-to-NO_x EC).

3.3.2 Mechanistic considerations

We hypothesize the reasons behind the more efficient production of NO_x at elevated pressure to be (i) elevated gas temperature and (ii) increased rate of NO_2 production, meaning a reduced significance of the back reactions which lead to loss of NO (back reactions in R3.3 and R3.4). Plasmas in which the electron temperature is higher than the gas temperature are characterized as non-equilibrium, while they are in equilibrium when the electron and gas temperatures are equal to each other [102]. Naidis *et al.*[70] estimated that at currents around 200 mA, the plasma is in near-local thermodynamic equilibrium (LTE) conditions: both the electric field and the gas temperature predicted by the non-LTE model are in good agreement with the LTE model for currents above 200 mA, indicating that the non-equilibrium effects do no significantly influence the conductivity and the heat balance within the plasma. In our work, we investigate currents >200 mA at elevated pressure, hence we infer the arc in the RGA reactor is close to thermodynamic equilibrium. In our considerations below we assume that the electron, vibrational and gas temperature are in equilibrium and the electron processes

do not influence the production of NO directly. While this is likely the case, and the thermal Zeldovich mechanism dominates the overall process, we acknowledge that some part of the observed effect may be due to non-equilibrium phenomena [97].

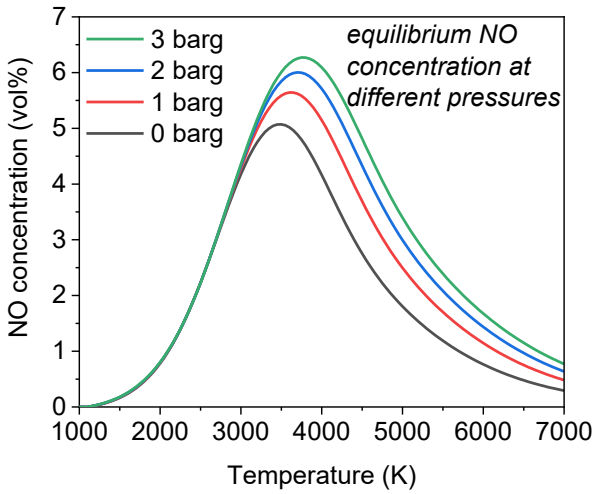

Figure 3.10. Equilibrium concentration of NO as a function of temperature at different pressures (0-3 barg).

Thermodynamic equilibrium composition calculations performed by D'Angola *et al.*[103] as a function of pressure and temperature were used to support our hypothesis. The details of calculating the presented data can be found in Appendix B (section B4, and Table B3). Figure 3.10 shows the equilibrium concentration of NO as a function of temperature for different pressures. Below 3000 K, there is no change in the NO concentration for different pressures. Above 3000 K, the concentration reaches a peak and then gradually drops upon increasing temperature. The maximal NO concentration rises from 5 vol% at 0 barg to 6.3 vol% at 3 barg. The maximal concentration peak also shifts towards a higher temperature: from 3500 K at 0 barg to 3800 K at 3 barg. At any given temperature, the NO concentration after the peak (on the right slope) is higher at elevated pressures.

With increasing pressure, we experimentally observe a higher plasma-deposited power and a lower flow velocity (due to the constant mass flow rate). This increased power, and higher residence time (i.e., lower velocity) both lead to higher temperatures inside the plasma arc, which in turn lead to higher concentrations of NO as a function of pressure. We note that the concentration of NO discussed here is the NO produced by

the plasma, and not the final concentration of NO measured downstream, because this plasma-produced NO is further oxidized into NO_2 (see below).

Figure 3.10 also suggests that the NO concentration can drop when the temperature exceeds the optimal value at the specified pressure, as seen on the right slope, after the peak value. We believe this effect was observed in our experimental results, specifically at 4 Ln/min, 2 and 3 barg (Figure 3.4, Figure 3.2b). At 3 barg, the initial rise of the downstream NO_x concentration from 3.2 to 3.9 vol% is followed by a drop back to 3.2 vol%. This drop in the concentration coincides with the condition with the longest residence time and the highest power. This leads to exceeding the optimal temperature, and heating of the plasma beyond 3800 K, and hence lower concentration of the plasma-produced NO. Although the temperature could not be monitored directly, we measured the temperature of the outer walls with an IR camera. At 4 Ln/min, we measured temperature values of 500, 540, 580 ^{o}C at 0, 1, and 2 barg, respectively. The temperature recorded at 3 barg was >600 ^{o}C (an exact measurement could not be taken due to the camera limits). This provides evidence for the temperature increase inside the reactor at elevated pressures. We note, however, that these results cannot be used to directly estimate the temperature inside the reactor, and are used qualitatively, exclusively to confirm the rising trend of temperature as a function of rising pressure.

It is important to note that the equilibrium composition cannot explain by itself the high concentrations measured at the outlet of the reactor. The recombination reactions along the gradual temperature drop in the reactor after the plasma partly destroy the created NO coming from the active plasma zone via the back reactions (see R3.3, R3.4) [58]. This is also seen in our experimental results, where the maximal NO_x concentration obtained is 4.2 vol% at 4 Ln/min and 1 barg (Figure 3.4a), while the maximal theoretical equilibrium concentration is 5.6 vol% at 1 barg (Figure 3.10). We believe that the higher pressure benefits the NO production by limiting the pressure-independent rate coefficient of the recombination reaction (back reaction of R3.4) and by increasing the pressure-dependent rate coefficient of the oxidation reaction (R3.5). In Figure 3.11, the dependence of the reaction rate coefficients for the back reaction of R3.4 and forward reaction of R3.5 are compared as a function of temperature for different pressures. The values were taken from Baulch *et al.*[104] and details about the pressure dependence of R3.5 can be found in Appendix B (section B5).

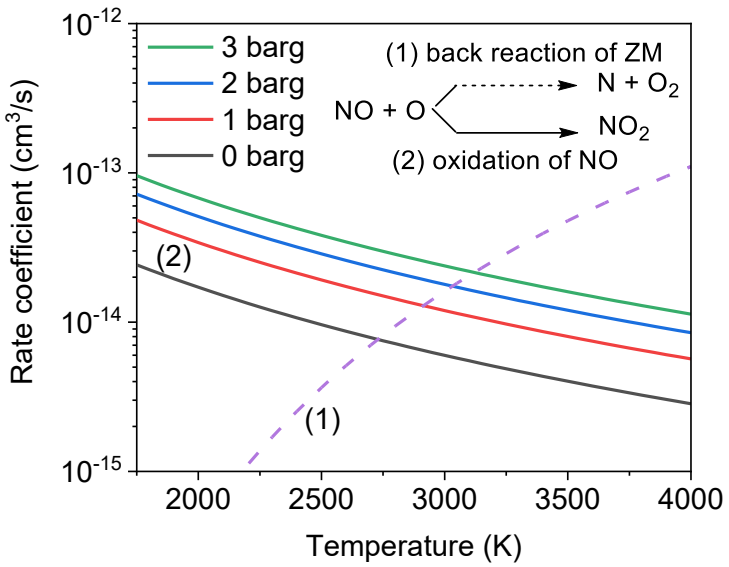

Figure 3.11. Rate coefficients of the pressure-independent back reaction of R3.4 and the pressure-dependent forward reaction of R3.5 as a function of temperature.

In the low temperature region (<2500 K) the oxidation of NO to NO_2 will be dominant (R3.5), while in the high temperature region (>3000 K) the back reaction of R3.4 dominates. At 0 barg, the rate constant of the reaction between NO and O (back reaction R3.4) is equal to the oxidation rate constant at 2700 K, while at 3 barg this intersection occurs at 3100 K. This suggests that in our experiments, the temperature in the post-plasma compartment of the reactor is below 3100 K, where reaction R3.5 and the back reaction of R3.4 occur. The RGA reactor operates without an active quenching system, which means the temperature drop inside the reactor after the plasma is gradual, because the energy is primarily lost due to heat transfer with the walls. Following this, with increasing pressure, more NO is oxidized into NO_2 along the temperature gradient due to R3.5. Although we believe this to be the main mechanism behind increased NO_x production, it cannot be conclusively proven using our current experimental setup.

In all of the experiments performed under elevated pressure, we observe significant NO_2 formation (i.e., high NO_2 selectivity), which could be explained by other oxidation reactions. Specifically, reaction R3.6 could be responsible for the oxidation of NO in the even lower temperature compartment of the reactor, close to the exhaust [56], because

R3.6 is reported within 273-600 K [104]. Future work involving a computational fluid dynamics model is required to evaluate this mechanism.

3.3.3 Production of NO_x from oxygen-enriched air (N_2:O_2 mixture of 1:1)

Literature reports, including our previous works with the RGA plasma reactor, show that the lowest EC is achieved with the feed gas N_2:O_2 ratio of 1:1 (e.g., entries 2, 5-9 in Table 1.1). Obtaining such mixtures is possible for example, via pressure swing adsorption technology, and the evident increase in efficiency presents a clear interest for industrial applications [53, 57, 105]. We investigated the performance of our plasma system at 4-12 Ln/min, 0-3 barg, with the N_2:O_2 feed gas ratio of 1:1.

Interestingly, the higher oxygen content in the feed gas results in a less stable discharge, only enabling the takeover mode at higher PSU supplied currents. This is most apparent at 12 Ln/min, where even at 3 barg, the plasma could only be sustained at a supplied current above 800 mA (Figure 3.12b). To our knowledge, the fundamental aspects of the attachment mechanisms in low current oxygen-enriched arcs have not been investigated in literature. A separate fundamental investigation of this effect is needed in order to explain the instability of the arc.

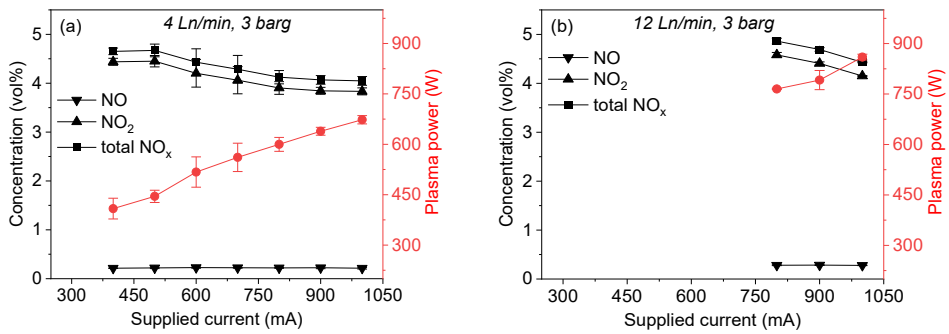

Figure 3.12. Concentration of produced NO_x and plasma power with N_2:O_2 1:1, 3 barg, with 4 Ln/min (a) and 12 Ln/min (b) as a function of the current supplied by the PSU. The results are presented for conditions which produced the stable takeover discharge mode (see text).

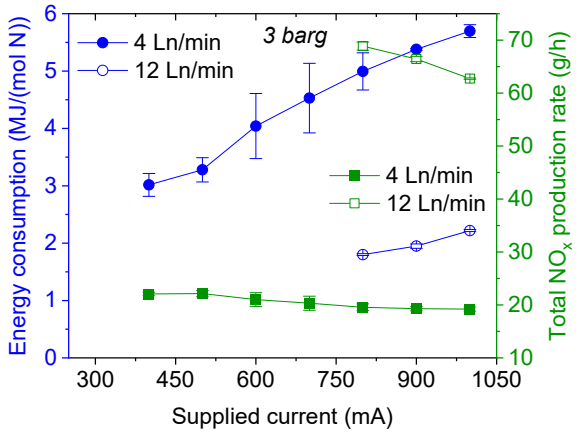

Figure 3.13. Energy consumption and total NO_x production rate with N_2:O_2 1:1, 3 barg, 4 and 12 Ln/min. The results are presented for conditions which produced the stable takeover discharge mode (see text).

With 4 Ln/min at 0 barg, the trends of NO_x concentration, EC and PR resemble those observed with the 4:1 ratio (see Figure 3.14 and 3.15).

The proportional increase in power and NO_x concentration result in the EC remaining relatively constant (around 4 MJ/(mol N)) as a function of the current. However, the drop in NO_x concentration at high current values starts already at 1 barg (Figure 3.14b), and not at 2 barg, as is the case for 4 Ln/min with the 4:1 N_2:O_2 ratio (Figure 3.4b). This indicates that already at these conditions we pass the optimal temperature giving rise to the peak production of NO (similar to that in Figure 3.10 for N_2:O_2 4:1). Another important difference is that higher O_2 content of the feed gas results in a higher plasma-deposited power for the same current and pressure. We speculate that this higher power results in higher temperature. Although equilibrium compositions of N_2:O_2 mixtures are semi-qualitatively described in literature[103,106], the quantitative data is not readily available. However, Ghorui *et al.* showed that the variation of the gas composition as a function of temperature for the 1:1 N_2:O_2 ratio follows a similar trend to that of 4:1 [106]. Therefore, we believe the explanations given in the previous section are applicable here, albeit we do not know at which temperature the maximal NO concentration is achieved. Further investigation into the nature of this process would require a detailed chemical kinetic model, which was outside the scope of this work. At 3 barg and 4 Ln/min, the NO_x production is further limited, giving a dramatic increase in EC (from 3.0 to 5.7 MJ/(mol N)) upon rising current from 400 to 1000 mA (Figure 3.13), similarly to the N_2:O_2 4:1 case.

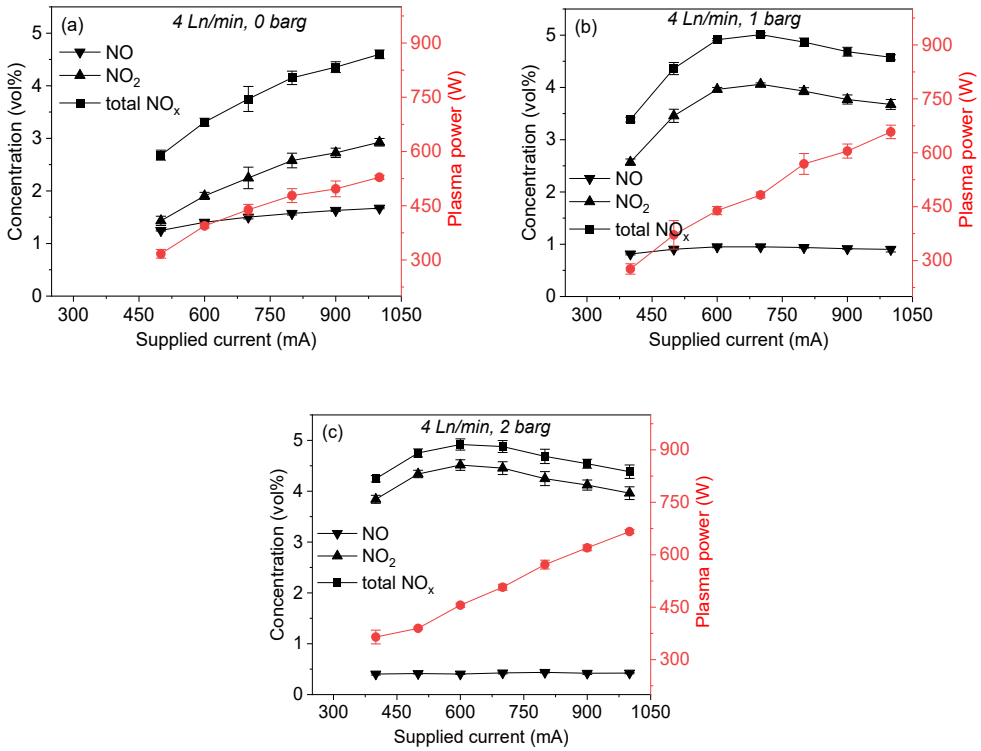

Figure 3.14. Concentration of produced NO_x and plasma power with N_2:O_2 = 1:1, at 4 Ln/min, 0 barg (a), 1 barg (b), and 2 barg (c) as a function of the current supplied by the PSU. The results are presented for conditions which produced the stable takeover discharge mode.

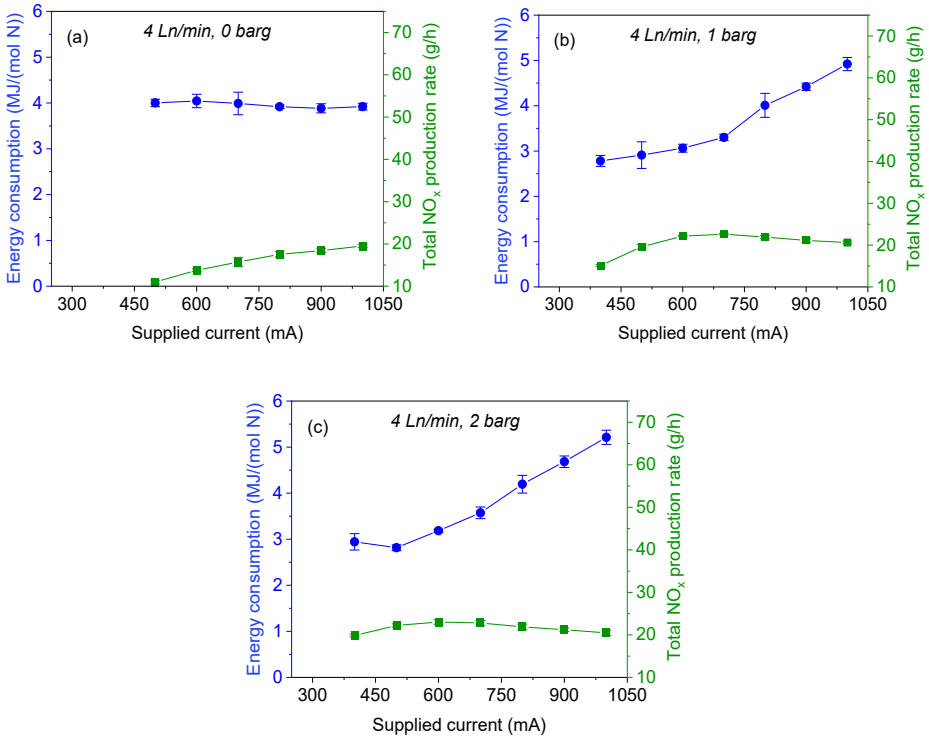

Figure 3.15. Energy consumption and total NO_x production rate with N_2:O_2 = 1:1, at 4 Ln/min, 0 barg (a), 1 barg (b), and 2 barg (c) as a function of the current supplied by the PSU. The results are presented for conditions which produced the stable takeover discharge mode.

With 4 Ln/min, at the near constant power of 440 W, the EC as a function of pressure first decreases (from 4.0 to 3.1 MJ/(mol N), between 0 and 2 barg), and then slightly increases (to 3.3 MJ/(mol N) at 3 barg), while the PR increases (see Table B1), in line with the 4:1 case.

With 8 Ln/min and the N_2:O_2 ratio of 1:1, the trends are once again similar to the 4:1 ratio (Figure 3.16, 3.17). However, with 12 Ln/min, a higher current leads to a lower NO_x concentration (and PR) at all studied pressures (Figure 3.12b and 3.13; see also Figure 3.18, 3.19). This results in the EC rising from 1.8 to 2.2 MJ/(mol N) (Figure 3.13). Nonetheless, the performance still improves upon the values obtained at 4 Ln/min, reaching an EC as low as 1.8 MJ/(mol N) with a corresponding PR of 69 g/h at a power of 860 W (supplied current of 800 mA), with an NO:NO_2 ratio of 1:21. Importantly, the NO_2 selectivity is much higher with the N_2:O_2 ratio of 1:1 than with 4:1, under all investigated

conditions, likely due to the increased amount of oxygen available for oxidation. Moreover, at 3 barg the NO_2 selectivity is relatively independent of the gas flow rate in all experiments. This further demonstrates the advantage of using an oxygen-enriched air mixture for the purpose of plasma-based NF.

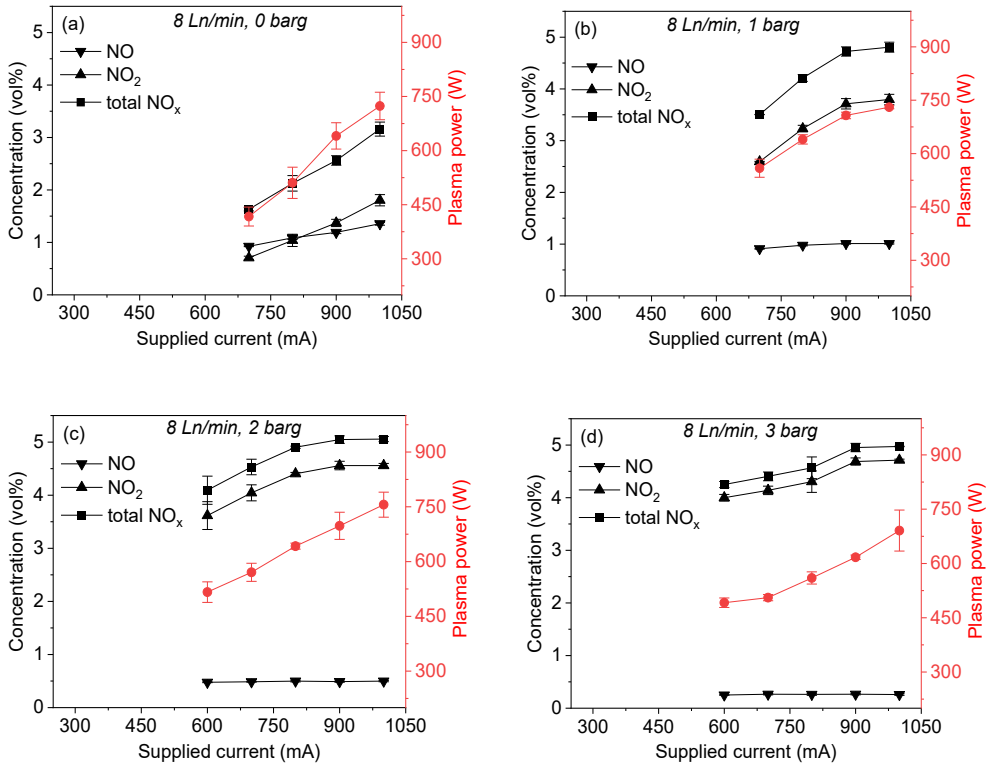

Figure 3.16. Concentration of produced NO_x and plasma power with N_2:O_2 = 1:1, at 8 Ln/min, 0 barg (a), 1 barg (b), 2 barg (c), and 3 barg (d) as a function of the current supplied by the PSU. The results are presented for conditions which produced the stable takeover discharge mode.

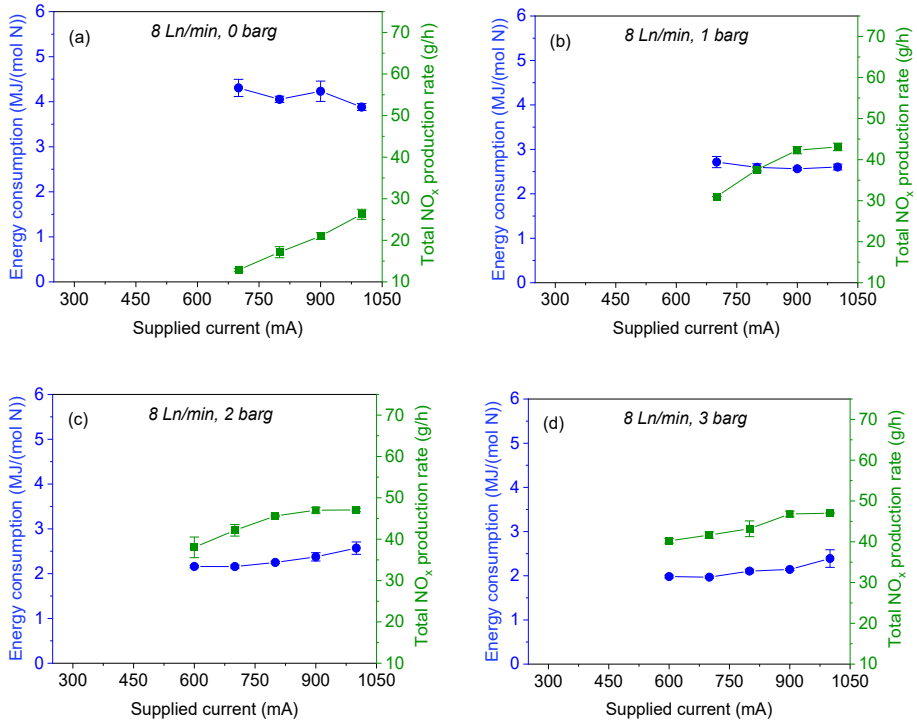

Figure 3.17. Energy consumption and total NO_x production rate with N_2:O_2 = 1:1, at 8 Ln/min, 0 barg (a), 1 barg (b), 2 barg (c), and 3 barg (d) as a function of the current supplied by the PSU. The results are presented for conditions which produced the stable takeover discharge mode.

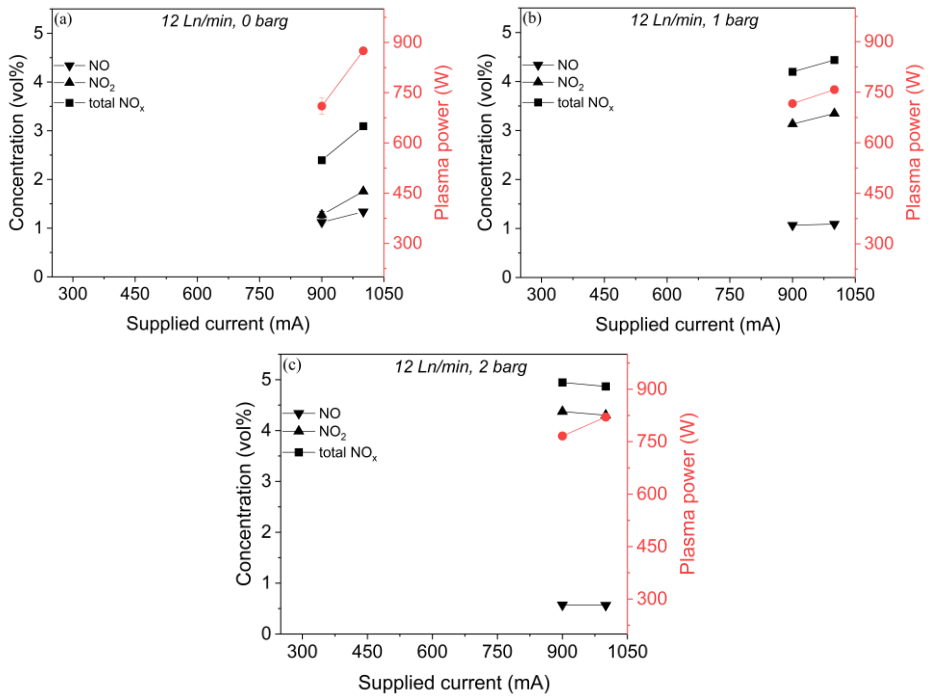

Figure 3.18. Concentration of produced NO_x and plasma power with N_2:O_2 = 1:1, at 12 Ln/min, 0 barg (a), 1 barg (b), and 2 barg (c) as a function of the current supplied by the PSU. The results are presented for conditions which produced the stable takeover discharge mode.

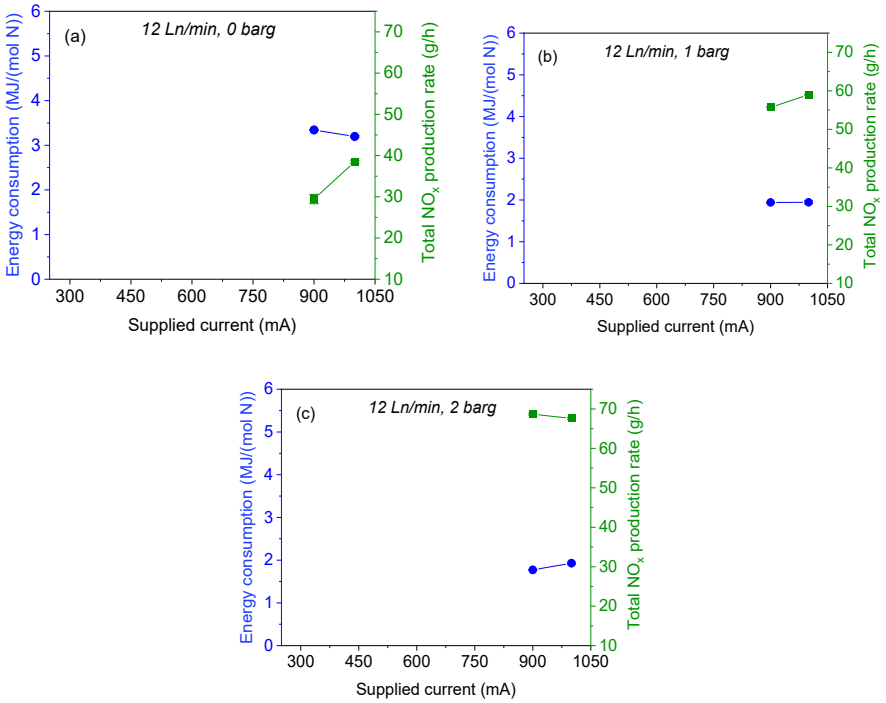

Figure 3.19. Energy consumption and total NO_x production rate with N_2:O_2 = 1:1, at 12 Ln/min, 0 barg (a), 1 barg (b) and 2 barg (c) as a function of the current supplied by the PSU. The results are presented for conditions which produced the stable takeover discharge mode.

The most promising results are obtained at 12 Ln/min, 3 barg – similar to the 4:1 ratio of N_2:O_2. For this 1:1 case, we were able to generate 4.9 vol% NO_x (almost exclusively NO_2) (Figure 3.12b), with an EC of merely 1.8 MJ/(mol N) at a high PR of 69 g/h (Figure 3.13). At close power values, this corresponds to a rise in PR and a reduction in EC by a factor of 2.3 and 1.8, respectively, compared to 0 barg. Furthermore, the corresponding plug-to-NO_x EC was as low as 3.7 MJ/(mol N). This is up to two orders of magnitude lower than other competing plasma-based NF technologies, e.g. reported recently by Attri *et al.*[101]. Additional comparison of this value with literature is difficult due to the common lack of the plug-to-NO_x EC reporting.

3.4 Conclusions

We studied the production of NO_x in an RGA plasma reactor as a function of the supplied current, feed gas flow rate and ratio, at elevated pressure (0-3 barg). At N_2:O_2 ratio of 4:1 (mimicking dry air), and a feed gas flow rate of 4 Ln/min, we observed an initial improvement of process performance as a function of pressure, i.e., from 0 to 2 barg,

the PR increases by ca. 15% and the EC is reduced by 6% at ca. 400 W. Further increasing the pressure to 3 barg, however, yields lower NO_x concentration, which is attributed to surpassing the thermal equilibrium peak of NO production. Nevertheless, at higher flow rates (8 and 12 Ln/min), we believe we do not surpass the optimal condition for production of NO, which results in an improvement as a function of pressure, even beyond 2 barg. At 12 Ln/min, we observe a rise in PR and a drop in EC by factors of 2.5 and 2, respectively, between 0 and 3 barg and near constant power of 440 W.

We attribute the improvement in EC and PR upon rising pressure to the synergetic effect between the higher equilibrium NO concentration and the oxidation of NO by O to NO_2. We believe that oxidation limits recombination of NO with O (into N and O_2), thus providing a higher NO_x concentration extracted from the post-plasma compartment of the reactor.

The high selectivity towards NO_2, which is beneficial for effective utilization of fixated N_2, is also a result of elevated pressure in all three temperature regions of the plasma reactor. Besides favouring the oxidation of NO (formed in the plasma arc, i.e. the highest temperature) with O into NO_2 in the colder post-plasma region, higher pressure also increases the rate of NO oxidation by O_2 in the reactor compartment remote from plasma, with temperatures reaching several hundred degrees.

Under optimized conditions (N_2:O_2 ratio of 1:1, with 12 Ln/min, 3 barg, PSU current of 800 mA) our obtained EC of 1.8 MJ/(mol N) is, to our knowledge, the lowest value of plasma-based EC for NO_x generation with high PR (>50 g/h), reported to date in literature. However, the total energy efficiency of the process, defined by the plug-to-NO_x EC, is merely 3.7 MJ/(mol N) in our system.

Our work identifies pressure as an important parameter to enhance the plasma NF performance, which is often overlooked by researchers. In general, plasma operation at slightly elevated pressures does not require equipment different from that used at atmospheric pressure but improves the process, making plasma-based NF an even more appealing auxiliary technology for industrial applications.

Chapter 4.

Simulation of a pulsed CO_2 plasma based on a six-temperature energy approach

This chapter focuses on CO_2 plasma, instead of N_2 or air plasma, but the modeling approach developed in this chapter is of general interest for plasma-based gas conversion to study V-T non-equilibrium (reported to be the most efficient gas conversion mechanism), and is therefore also applicable to air plasmas, as will be demonstrated in next chapter. Recent time-resolved measurements of gas and vibrational temperatures in pulsed glow discharges have fostered the development and validation of detailed kinetic models to understand the underlying heating dynamics. The models published so far have been successful in identifying the fundamental processes underlying vibrational and gas heating in pure CO_2 discharges; however, this has come at the cost of including vibrational kinetics with thousands of reactions. This makes these models not compatible with self-consistent computational fluid dynamics (CFD) codes, like the one described in Chapter 2, which are needed to develop new plasma reactors operating at high pressures or with complex flow patterns, and to capture the relevant dynamics in multiple dimensions. In this chapter, we solved separate energy balance equations for the asymmetric and symmetric vibrational modes of CO_2, as well as for the vibrational modes of CO and O_2, the gas temperature, and the electron temperature, making it a six-temperature (6T) plasma model. This eliminates the need to include a vast array of vibrational levels as separate species, drastically reducing the number of reactions in the model. The model is compared with experimental measurements conducted in a pulsed CO_2 glow discharge at 6.7 mbar. Excellent agreement is observed for the temporal evolution of the vibrational and gas temperatures, confirming that our approach is suitable for modeling systems under significant non-equilibrium conditions, paving the way for coupling detailed CO_2/CO/O_2/O kinetics with CFD codes.
This chapter is based on:

Simulation of a pulsed CO2 plasma based on a six-temperature energy approach
I.Tsonev[1]*, O. Biondo*, A. Bogaerts (* = shared first author)
Plasma Sources Science Technology, 34, 015014, (2025)
https://doi.org/10.1088/1361-6595/adad14

4.1 Introduction

A key factor in improving energy efficiency of plasma-based gas conversion is identifying the fundamental processes underlying the conversion, especially those leading to splitting with minimal energy consumption, and optimizing the reactor design accordingly. For decades, research suggested that the potential of plasma technology lies in the ability to selectively excite the asymmetric streching mode of the CO_2 molecule, which is believed to lower the activation energy for CO_2 dissociation and thereby increase the energy efficiency of the process [40]. However, uncertanties remain regarding the utilization of the asymmetric streching mode as an efficient dissociation mechanism. The main reason for this is the lack of detailed experimental data of the temporal dynamics of its excitation, along with that of the dissociation products of CO_2, *i.e.,* CO and O_2.

Indeed, time-resolved vibrational temperature profiles are crucial to validate the existing kinetic models. Only recently, glow discharge reactors with power pulsing have been developed for this purpose [107,108]. Specifically, Rivallan *et al*. [107] investigated the temporal evolution at the microsecond timescale of the infrared spectra in the range of 4000-1200 cm^{-1} with a Fourier-transform infrared (FTIR) spectrometer during the active phase of an air-CO_2 discharge, in the 1-15 mbar range. The analysis indicated that the recorded spectra were greatly affected by the discharge in the 2400-2200 cm^{-1} region, where the asymmetric stretching mode of CO_2 falls. Subsequently, Klarenaar *et al*. [108] extended the time-resolved analysis to the densities of the levels of the symmetric stretching and bending modes of CO_2, which are strongly coupled into one effective vibrational mode due to Fermi resonance [109]. In addition, the authors introduced the measurements of the vibrational levels of CO, produced in the discharge, as well as the rotational temperature, which can be assumed in equilibrium with the translational temperature due to the extremely fast rates of rotational relaxation for CO_2 [110,111]. Therefore, Klarenaar *et al*. [108] were able to monitor the temporal evolution of four different temperatures, namely the temperature of the asymmetric stretching mode (T_3), the symmetric levels of CO_2 (*i.e.* coupled symmetric stretching and bending modes, T_{12}), CO vibrations (T_{CO}) and the gas (T_g), in a CO_2 discharge at 6.7 mbar and an applied current of 50 mA. The accuracy of the time-dependent measurements of T_g by means of FTIR spectroscopy was later confirmed with rotational Raman spectroscopy [112], which enabled also spatially resolved measurements, confirming the hypothesis that T_g is constant along the line-of-sight of the FTIR measurements. Similarly, Klarenaar *et al*. [112] validated the vibrational temperatures measured by [108], relating the rotational

Raman spectra of CO_2 to the vibrational temperatures through the vibrationally averaged nuclear degeneracies [113]. The comparison between FTIR and rotational Raman spectroscopies was further continued in [114], with a focus on the excitation of the asymmetric stretching mode within the range of 1.3-6.7 mbar and a discharge current of 10-50 mA. More recently, Damen *et al*. [115] performed time-resolved measurements of the vibrational and rotational temperatures with the same reactor of [108, 112, 114] but with quantum cascade laser (QCL) spectroscopy as diagnostic tool. Compared to FTIR, QCL spectroscopy allows measurements with a smaller instrumental broadening and higher temporal resolution. On the other hand, the asymmetric strecthing mode is not Raman active and therefore T_3 cannot be inferred directly from rotational Raman spectroscopy. Moreover, Damen and co-authors investigated the effect of N_2 [115] and H_2O [116] addition to the vibrational kinetics of CO_2 and its dissociation, while the influence of O_2 was studied by Vervloedt *et al*. [117] in the same pulsed glow discharge setup.

The extensive characterization of the temporal evolution of vibrational temperatures in pulsed glow discharges provides the ideal framework for benchmarking global kinetic models. The high homogeneity of the positive column of a glow discharge [63] allows for the capture of the main kinetic phenomena without relying on numerous approximations for multi-dimensional processes, such as heat transfer to reactor walls and fluid dynamics. Additionally, power pulsing facilitates the study of vibrational excitation and relaxation, which would otherwise quickly reach a steady state and equilibrate with the other degrees of freedom in continuous-mode discharges.

Global kinetic models, also called zero-dimensional (0D) chemical kinetics models, are the computational tool of choice for describing detailed plasma chemistry in complex gas mixtures. These models are particularly useful for studying molecular discharges where multiple products are formed through dissociation and recombination reactions. Moreover, 0D models are quick to develop and execute, allowing them to be complemented with the solution of the electron Boltzmann equation and detailed vibrational kinetics without significantly increasing computational time and effort [118, 119]. In this context, state-to-state (STS) models have been developed to simulate the time-dependent evolution of the densities of numerous vibrational states, which are treated as individual chemical species. Thus, for each individual state, a continuity equation is solved, with production and loss terms determined by reaction rates.

Specific to CO_2, pioneering works on the development of STS models are [120, 121]. Thanks to the detailed scheme for the vibrational chemistry of CO_2, Kozák and Bogaerts [121] demonstrated that conversion could be improved in microwave discharges

through stepwise excitation of the asymmetric stretching mode (also known as the ladder-climbing mechanism) [40, 122]. This is due to favorable conditions for electron-impact excitation of the low vibrational energy levels and fast vibration-vibration relaxation towards the higher levels, closer to the dissociation limit of the molecule. In contrast, it was also reported in [121] that plasma with strong non-equilibrium between electrons and heavy particles, such as dielectric barrier discharges (DBDs), promote dissociation through channels with much higher energy thresholds than the ladder-climbing mechanism, such as electronic excitation, thereby reducing the associated energy efficiency. These findings motivated further developments of STS 0D models, focusing on vibrational excitation in plasmas with mild deviations from equilibrium [123-125]. In these plasmas, also known as "warm" plasmas, the electron temperature typically exceeds the vibrational temperatures, which are higher than the gas temperature. The STS 0D models developed up to now suggested that the ladder-climbing mechanism can have a beneficial effect on the reactor performance.

Notwithstanding the remarkable effort, the aforementioned detailed STS 0D models lack direct validation with experimental results. This can be ascribed to a fundamental feature often observed in "warm" plasmas, distinguishing them from the low-pressure glow discharges studied by Rivallan *et al.* [107] and Klarenaar *et al*. [108]. This feature is the high degree of spatial inhomogeneity, especially in the radial direction, which is further enhanced by stabilizing swirling flows and microwave absorption patterns in microwave discharges [42]. Due to these complications, direct comparison between experiments and STS 0D models is not possible. Instead, the models can only provide insights that can be linked to certain experimental trends. Thus, while helpful in identifying mechanisms underlying reactor performance *a posteriori*, after the experiments are done, they are not ideal for steering the design of new and improved reactors. This limitation arises because the predictive power of a model scales with the range of conditions for which it can accurately capture experimental trends.

As "warm" plasmas cannot be used for the validation of 0D models, the N-PRiME group focused on modeling of the low-pressure pulsed glow discharge developed by Klarenaar *et al*. [108]. Particular attention was paid to the "single-pulse" measurement, where a sufficiently high gas flow rate and inter-pulse time were set to ensure full evacuation of the exhaust and replacement with fresh feed gas before the subsequent pulse. These conditions enable to isolate the vibrational kinetics of CO_2 and its potential effects on dissociation without interference from the dissociation products.

The first modelling effort from the N-PRiME group on the "single-pulse" measurement led to two separate contributions, in which the authors modelled the afterglow

dynamics [126] and the active phase of the discharge [127]. In the former, they validated a set of vibration-translation (V-T) and vibration-vibration (V-V) energy transfers under plasma-off conditions, where electron kinetics do not play a role and the dynamics are dominated by relaxation processes. In the latter, they added a set of electron impact processes for vibrational excitation and de-excitation. Overall, the model successfully captured the experimental trends for T_3 and T_{12}, although the experimental T_g profile was used as input parameter. Subsequently, Silva *et al*. [128] extended the validation of the kinetic scheme of [126, 127] with the self-consistent calculation of T_g in the afterglow of the "single-pulse" measurement of [108]. This confirmed the validity of their vibrational scheme, providing a new reference model for continuing the construction of a fully self-consistent model.

Along with the efforts of the N-PRiME group, two STS 0D models were separately developed for the purpose of reproducing the "single-pulse" measurement of [108]. Kotov [129] employed a reduced vibrational scheme, previously constructed and tested in [130], which included all levels up to the dissociation limit by grouping them into fewer effective levels. The author was able to qualitatively reproduce the experimental vibrational temperature profiles, although they were overall overestimated. Kotov attributed this discrepancy to the lack of self-consistency of their model, particularly regarding the electron kinetics. Nearly at the same time, Pietanza *et al*. [131] simulated some features of the "single-pulse" experiment with their model, which involved a self-consistent calculation of the electron, vibrational, and heavy particle kinetics. Overall, they obtained good agreement with experiments in terms of vibrational temperatures up to 1 ms, but overestimated the profiles beyond that point. Within the same time frame, the computed electron density was in good agreement with previous estimations [127], but was also overestimated later on. The authors suggested that including some electron loss mechanisms and more symmetric levels of CO_2 could improve the agreement and make the model more complete. These two independent modelling studies underlined the importance of the electron kinetics. Pietanza *et al*. [131] particularly demonstrated that capturing the transient behavior of electron kinetics is essential for a full understanding of the mechanisms underlying the "single-pulse" measurement.

In this regard, Biondo *et al*. [132] attempted a self-consistent calculation of the electron density, along with the estimation of the temporal evolution of the reduced electric field (E/N) from the power profile; the latter was obtained from the current profile and a fixed voltage from [108]. Compared to Pietanza *et al*. [131], Biondo *et al*. [132] observed that E/N should be higher than *ca*. 94 Td throughout the "single-pulse" experiment in order

to sustain the discharge, in contrast to previous estimations [108, 127]. However, since the voltage profile was not provided for the "single-pulse" experiment, the authors decided to test two extreme cases, *i.e.* 55 Td (as previous estimations) and 90 Td constant throughout the pulse-on time. By including the solution of the gas heat balance equation, Biondo *et al*. [132] could capture the temporal evolution of T_g, together with that of T_{12} and T_3, thereby validating their kinetic scheme for gas heating. Particularly, they found that relaxation of electronic states is necessary to obtain good agreement with the experiments at 90 Td, while at lower E/N, the gas heating is underestimated. Therefore, this study confirmed that electron kinetics play a critical role in defining the dynamics of gas heating.

Notwithstanding the high degree of self-consistency reached by this joint effort between the N-PRiME and PLASMANT groups [132], reproducing the "single-pulse" experiment of Klarenaar *et al*. [108] required *ca*. 14000 individual reactions. This extensive kinetic model would not be compatible with a self-consistent computational fluid dynamics (CFD) model, which is needed to develop new plasma reactors, operating at high pressures or with complex flow patterns, to capture the relevant dynamics.

The drawback of extensive kinetic schemes is intrinsic of the STS approach, which requires a state-resolved set of reactions. An alternative approach to avoid computationally expensive reaction sets can be found in the field of laser modelling, as detailed in the book of Smith and Thomson [133]. In this approach, here referred to as the "energy approach", the solution of the vibrational densities from individual continuity equations (STS approach) is replaced with the solution of only a few energy balance equations, i.e., one for each vibrational manifold. This dramatically reduces the number of chemical species in the model, potentially enabling the coupling of chemical kinetics with multi-physics (CFD) models.

One of the first applications of the energy approach in the context of non-equilibrium CO_2 reactive flows was presented by Kustova and Naghibeda [134]. Their model included multiple CO_2 vibrational modes and the corresponding main energy transitions, while being sufficiently simple and suitable for engineering applications. The authors used the model to obtain non-equilibrium transport coefficients for CFD codes and compared their results with available literature data. Subsequently, Kustova *et al*. [135] introduced the energy approach to strong non-equilibrium CO_2 flows, to study the structure of shock waves created during Mars atmospheric entry. They developed a three-temperature (T_3, T_{12} and T_g) model capable of capturing the effects of V-V inter-mode relaxation on bulk viscosity, essential to achieve reasonable solutions in shock wave studies.

Recently, Kunova *et al*. [136] made significant efforts to extend and validate the theory underlying the energy approach. A comparison between the STS and energy approach revealed that one can model the vibrational modes of CO_2 and significantly improve the computational cost without any loss of accuracy, thus allowing an efficient implementation into CFD codes. Later, Kustova and Mekhonoshina [137] employed the three-temperature model of [135] to investigate different theories for the calculation of the transition probabilities of intra- and inter-mode vibrational energy transfer. The authors validated the resulting relaxation times against experimental values available in the literature, recommending the use of the forced harmonic oscillator (FHO) model [138] for non-equilibrium flow simulations.

In this chapter, we make use of the experimental framework provided by Klarenaar *et al*. [108] and the solid computational foundations developed by the PLASMANT [121, 123-125, 132], N-PRiME [126,127, 128, 132] and Saint Petersburg [135-137] groups, to develop a fully self-consistent model capable of reproducing the single-pulse measurement. Particularly, we implement the energy approach in a kinetic plasma model that solves the electron energy balance equation for the electron temperature (T_e), separate vibrational energy balance equations for the asymmetric (T_3) and symmetric ($T_{1,2}$) modes of CO_2, as well as for the vibrational modes of CO (T_{CO}) and O_2 (T_{O2}), and the gas temperature (T_g) balance equation, making it a six-temperature (6T) plasma model. The two-term Boltzmann equation is used to determine the electron energy distribution function (EEDF) and the electron density (n_e) is calculated assuming quasi-neutrality. The successful comparison of the outcome of our model with the single-pulse experiment confirms the mechanisms for gas heating in pure CO_2 discharges proposed by Biondo *et al*.[36]. Furthermore, this study reveals the dynamic behavior of the electron and ion kinetics, while achieving reasonable agreement with the experimental current profile.

Overall, we achieve satisfactory agreement (within 10 %) between our model and the experiments. This confirms that the energy approach is suitable for modelling systems under non-equilibrium conditions, opening up to the coupling of a detailed $CO_2/CO/O_2/O$ kinetics with CFD codes for plasma reactor design and optimization.

4.2 Computational framework

Our 6-T model is developed and executed in COMSOL Multiphysics® 6.2 [83]. The EEDF is computed self-consistently using the Boltzman solver integrated in the Plasma Module. The rate coefficients of electron-impact reactions are obtained from the integration of

the corresponding cross sections over the EEDF. In our model, we include the cross sections for elastic scattering, excitation, ionization and attachment for CO_2 and its dissociation products (CO, O_2, O), whereas for C we only account for elastic scattering. The cross sections are taken from the LXCat database and detailed information on the included processes and references is given in Appendix C1.

4.2.1 Species included in the model

The species considered in this model are listed in Table 4.1, and they include 20 neutral species and 18 charged particles.

Table 4.1. Species included in the model

Neutral species *
$CO_2(X^1\Sigma_g^+)$, $CO_2(e_1)$, $CO_2(e_2)$, $CO(X^1\Sigma_g^+)$, $CO(a^3\Pi)$, $CO(a'^3\Sigma^+)$, $CO(A^1\Pi)$, $CO(b^3\Sigma^+)$, $CO(B^1\Sigma^+)$, $CO(C^1\Sigma^+)$, $CO(E^1\Sigma^+)$, $O_2(X^1\Sigma_g^+)$, $O_2(a^1\Delta_g)$, $O_2(b^1\Sigma_g^+)$, $O_2(A^3\Sigma_u^+$, $C^3\Delta_u$, $c^1\Sigma_u^-)$, $O(^3P)$, $O(^1D)$, $O(^1S)$, O_3, C
Charged species
CO_2^+, CO^+, O_2^+, O^+, O_3^+, O_4^+, C^+, $C_2O_2^+$, $C_2O_3^+$, $C_2O_4^+$, CO_4^+, O^-, O_2^-, O_3^-, O_4^-, CO_3^-, CO_4^- and electrons.

*For the specific nomenclature of the electronically excited levels, we refer to the LXCat database, from which electron-impact excitation to the listed electronically excited states is taken.

Among the neutral species in the model, two lumped electronic states of CO_2 are included. While the exact composition of these two states is not fully known, there is general consensus about the electronic states present in the energy range between 7 and 10 eV, corresponding to $CO_2(e_1)$, and above 10 eV, corresponding to $CO_2(e_2)$. Both lumped states contain dissociative and radiative states, and some contributing to fast gas heating through collisional quenching [132]. Further details can be found in the work of Pietanza *et al.* [139], which summarizes the relevant literature.

The extensive description of the ion kinetics is of utmost importance to accurately compute the time evolution of the plasma parameters, such as E/N. This is supported by previous modelling studies on low-pressure plasmas and lasers in molecular gases [140-142]. In this regard, it is essential to include ambipolar diffusion losses to the walls, which represent the dominant sink of charged particles in the positive column of glow discharges [143, 144]. In our model, the diffusion of charged particles to the walls is described by classical ambipolar diffusion in the presence of negative ions [145]. The mobility of each ion for calculating the corresponding diffusion coefficient is taken from [146], when available, or assumed from similar ions.

4.2.2 Species continuity equations

For each species except the electrons, the continuity equation is solved:

$$\rho_p \frac{dw_s}{dt} = mflow_{in} - mflow_{out} + R_s + R_{surf} \quad (4.1)$$

where ρ_p is the mass density, and w_s is the mass fraction of species s. $mflow_{in}$ is the mass flow feed, $mflow_{out}$ is the outlet flow and R_s and R_{surf} are the net rate of change of the species density, based on the gas phase and surface phase reactions, presented in detail in Appendix C1. The pressure in the simulation is kept constant by adjusting the outflow feed. The electron density is computed assuming quasi-neutrality.

The number densities of the vibrational states of CO_2, CO and O_2 are calculated assuming a Boltzmann distribution through the partition function Z. While this assumption is reasonable for the conditions in this study, limitations may arise under conditions for which a non-Boltzmann or Treanor distributions occur. In such cases, our model cannot capture deviations from Boltzmann distributions. However, this limitation does not introduce significant uncertainty on the computed temperature profiles, as the vibrational densities of higher levels in non-equilibrium are either low [121] or exhibit only moderate deviations from a Boltzmann distribution [147].

The partition functions for CO_2, CO and O_2 are presented in equations (4.2a), (4.2b) and (4.2c), respectively.

$$n_{vib,\,CO_2}(i_1,i_2,i_3) = \frac{n_{CO2}*(i_2+1)}{Z_{CO2}(T_{12},T_3)} \exp\left(-\frac{i_1\varepsilon_{100}}{k_B T_{12}} - \frac{i_2\varepsilon_{010}}{k_B T_{12}} - \frac{i_3\varepsilon_{001}}{k_B T_3}\right) \quad (4.2a)$$

$$n_{vib,\,CO}(i_{CO}) = \frac{n_{CO}}{Z_{CO}(T_{CO})} \exp\left(-\frac{i_{CO}\varepsilon_{CO}}{k_B T_{CO}}\right) \quad (4.2b)$$

$$n_{vib,\,O_2}(i_{O2}) = \frac{n_{O2}}{Z_{O2}(T_{O2})} \exp\left(-\frac{i_{O2}\varepsilon_{O2}}{k_B T_{O2}}\right) \quad (4.2c)$$

where n_{vib} is the vibrational number density as a function of i_1, i_2, i_3, i_{CO} and i_{O2}, which are the quantum numbers of the symmetric stretching and bending mode, the asymmetric stretching of CO_2, and of CO and O_2, respectively. n_{CO2}, n_{CO}, n_{O2} and Z_{CO2}, Z_{CO}, Z_{O2} are the total number densities and partition functions of CO_2, CO and O_2, respectively. ε_1, ε_2, ε_3, ε_{CO} and ε_{O2} are the energies of the first state of the symmetric stretching, bending mode and asymmetric stretching of CO_2, and of CO and O_2, respectively, and k_B is the Boltzmann constant.

Z_{CO2} is obtained by summation over all vibrational states below the dissociation threshold as follows:

$$Z_{CO2}(T_{12}, T_3) = \sum_{(i_1,i_2,i_3)} (i_2+1) \exp\left(-\frac{i_1\varepsilon_{100}}{k_B T_{12}} - \frac{i_2\varepsilon_{010}}{k_B T_{12}} - \frac{i_3\varepsilon_{001}}{k_B T_3}\right). \quad (4.3)$$

In equations (4.2a) and (4.3), the statistical weight s_{i_1,i_2,i_3} is taken into account as i_2+1. Z_{CO} and Z_{O2} are computed analogously to equation (4.3).
The energy of the vibrational modes as a function of temperature was calculated as:

$$E_{T_{1,2}}(T_{12}) = \sum_{i_1 i_2 i_3} (i_1\varepsilon_{100}+i_2\varepsilon_{010})n_{vib}(i_1,i_2,i_3) \quad (4.4a)$$

$$E_{T_3}(T_3) = \sum_{i_1 i_2 i_3} (i_3\varepsilon_{001})n_{vib}(i_1,i_2,i_3) \quad (4.4b)$$

$$E_{T_{CO,O_2}}(T_{CO,O_2}) = \sum_{i_{CO,O_2}} (i_{CO,O_2}\varepsilon_{CO,O_2})n_{vib,\,CO,O_2}(i_{CO,O_2}) \quad (4.4c)$$

The heat capacity per molecule of the vibrational degrees of freedom C_{p,T_v} is calculated as the derivative of the vibrational energy (from Eqs (4a-c)) with respect to the vibrational temperature:

$$C_{p,T_v} = \frac{dE_{vib}(T_v)}{dT_v} \quad (4.5)$$

4.2.3 Modelling the electrical circuit

Klarenaar *et al.* [108] did not report on the time evolution of the voltage during the single-pulse experiment. The measurement of the voltage is critical to calculate the power input as a function of time for the simulation. In effect, Damen *et al.* [115] showed that the voltage cannot be assumed constant and presents a significant spike at the onset of the pulse, in order to ionize the gas. Therefore, we couple the Plasma Module with the Electrical Circuit interface to compute the power, using the experimental current profile as a current source. To do so, the plasma is assumed a resistor in a circuit connected to a ballast resistor (50 kΩ) in series, with a capacitor (10 pF) in parallel. Thus, the plasma resistance is obtained from:

$$R = \frac{L_{plasma}}{(n_e\mu_e q_e)\pi R_{plasma}^2} \quad (4.6)$$

where n_e is the electron density, μ_e the electron mobility, and q_e the elementary charge. The voltage is then estimated based on R. Experimentally, Klarenaar *et al.* [*108*] used a voltage-regulated power supply instead of a current source. Moreover, we note that the ballast resistance used is not large enough to provide a constant current of 50 mA. Consequently, the plasma resistance together with the ballast resistance determines the current passing through the system. Therefore, we choose to use the experimentally

reported current source as an input to the simulation in order to avoid numerical instabilities during the solution.

4.2.4 Energy balance equations

The electron energy balance equation is solved to obtain the average electron energy $\bar{\varepsilon}_e$:

$$\frac{d(n_e\bar{\varepsilon}_e)}{dt} = S_{en} + Q_{circuit} \quad (4.7)$$

where n_e is the electron density, S_{en} is the average energy lost per collision and $Q_{circuit}$ is the deposited power, computed with Ohm's law.

Each of the vibrational temperatures included in this model (T_{12}, T_3, T_{CO} and T_{O2}) are calculated through separate energy balance equations. This model represents an evolution of the state-to-state approach. In Chapter 2 we showed how this approach can be applied to a multi-dimensional model, while in this chapter we are showing the applicability of the approach in a multi-temperature system with a global model. While we still use individual excitation and relaxation rates, these are employed to calculate the energy production or loss rates associated with each transition (then summed to give the total energy rates), rather than the vibrational density. The latter, on the other hand, is calculated from the partition function by assuming a Boltzmann distribution within each manifold, as described earlier in Section 4.2.2. We note that loss and gain in the vibrational energy balance equations due to chemical reactions are not included, as these reactions are orders of magnitude slower than vibrational relaxation for the conditions studied (see Figure C.1 in the Appendix). However, chemical-vibrational coupling should be accounted for to improve accuracy when chemical kinetics play a larger role, such as for the multi-pulse experiment by Damen *et al*. [115]. Future developments will therefore incorporate this coupling as described in [148, 149]. For T_{12}, the energy balance equation takes the form of:

$$n_{CO_2} \cdot \frac{de_{v,T_{12}}}{dt} = Q_{eV} + Q_{VVT} - Q_{VT_{12}} - Q_{condT_{12}} - Q_{feedT_{12}} \quad (4.8)$$

where $e_{v,T_{12}}$ is the energy deposited into the symmetric levels of CO_2, Q_{eV} is the energy deposited through collisions with electrons, i.e., the net energy due to superelastic collisions, Q_{VVT} includes the energy transferred from the asymmetric stretching mode to the symmetric levels through intra-molecular vibration-vibration-translation (V-V-T) relaxation, but also inter-molecular V-V-T relaxation between T_{O2} and T_{12}. The rate coefficients used in this chapter are presented in Appendix C2. V-V-T relaxation differs from V-V relaxation because the energy of the initial vibrational levels does not coincide with that of the final levels, and therefore part of the vibrational energy is lost to

translational degrees of freedom[132]. The latter part is not included in Q_{VVT} in (4.8), but it will be included in the energy balance equations of T_3, T_{O2} and T_g.

$Q_{condT_{12}}$ is the energy transfer to the walls due to conduction:

$$Q_{condT_{12}} = 8 \cdot C_{p,T_{12}}(T_{12}) \cdot D_{CO_2}(T_g) \cdot \frac{T_{12}\text{-}T_{12,wall}}{R^2} \tag{4.9}$$

where $C_{p,T_{12}}$ is the heat capacity of the symmetric levels of CO_2 at constant pressure, D_{CO_2} is the diffusion coefficient of CO_2, $T_{12,wall}$ is the temperature of the symmetric levels at the reactor walls, and R is the reactor radius. The factor 8 appears because of averaging over the cross section of the reactor, indicating that the equation is an energy balance equation for the average temperature in the plasma. If the averaging is not performed, the factor changes to 4, which then represents the centerline temperature in the reactor assuming a parabolic temperature profile [150]. More details about the choice of this factor will be given in section 4.3.1. The conduction term (eq. 4.9) has the same form for all of the vibrational energy balance equations. This term does not include vibrational deactivation due to collisions with the reactor walls, as it was shown earlier that this cooling process is only appreciable for pressure well below 6.7 mbar [151].

Along with conduction, convective cooling due to the feed gas, Q_{feed}, is included in the energy balance equation (eq. 4.8):

$$Q_{feedT_{12}} = \dot{m} \cdot w_{CO_2} \cdot \frac{H_{T_{12}}(T_{12,feed}) - H_{T_{12}}(T_{12})}{M_{CO_2} \cdot V_r} \tag{4.10}$$

where $\dot{m}$ is the mass flow feed (kg/s), w_{CO_2} and M_{CO_2} are the feed mass fraction and the molar mass of CO_2, $H_{T_{12}}$ is the energy stored in the symmetric levels of CO_2 and V_r is the reactor volume. The convection term (eq. 4.10) has the same form for all of the vibrational and gas energy balance equations.

The energy balance equation for T_3 is similar to that of T_{12}:

$$n_{CO_2} \cdot \frac{de_{v,T_3}}{dt} = Q_{eV} - Q_{VVT} - Q_{VT_3} - Q_{condT_3} - Q_{feedT_3} \tag{4.11}$$

In this case Q_{VVT} is a loss term, containing intra-molecular V-V-T relaxation analogously to T_{12}, and inter-molecular V-V-T relaxation with CO and O_2. More details on the terms of eq. 4.11 are given in the Appendix C2.

The energy balance equation for T_{CO} is defined as follows:

$$n_{CO} \cdot \frac{de_{v,T_{CO}}}{dt} = Q_{eV} + Q_{VVT_{CO_2}} - Q_{VT_{CO}} - Q_{VVT_{O_2}} - Q_{condT_{CO}} - Q_{feed_{CO}} \tag{4.12}$$

$Q_{VVT_{CO_2}}$ is the energy transferred from T_3, included as $-Q_{VVT}$ in eq. 4.11, whereas $Q_{VVT_{O_2}}$ represents a loss term for the energy transferred to T_{O2} via $CO(i_{CO}) + O_2 \leftrightharpoons CO + O_2(i_{O2})$, with a rate coefficient of $1.66 \times 10^{24} \left[\frac{cm^3}{s}\right] \cdot e^{41 - 306 \cdot T_g^{-1/3} + 1126 \cdot T_g^{-2/3}}$ taken from

[152]. $Q_{VT_{CO}}$ involves only one type of transition, $CO(i_{CO}) + M \leftrightharpoons CO(i_{CO}-1) + M$. The rate coefficient for this transition with M = CO_2, CO and O_2 is taken from [153, 154], whereas the rate coefficient with M = O is $5.3 \times 10^{13} \left[\frac{cm^3}{s}\right] \cdot \sqrt{T_g} \cdot e^{-1600[K]/T_g}$ [58].

The last vibrational energy balance equation is that for T_{O2}:

$$n_{O_2} \cdot \frac{de_{v,T_{O_2}}}{dt} = Q_{eV} + Q_{VVT_{CO}} + Q_{VVT_{T3}} - Q_{VT_{O_2}} - Q_{VVT_{T12}} - Q_{condT_{O_2}} - Q_{feed_{O_2}} \quad (4.13)$$

Even in this case, Q_{VVT} is split in multiple terms: two positive terms, $Q_{VVT_{CO}}$ and $Q_{VVT_{T3}}$, representing the transfer of heat from T_{CO} and T_3, respectively, and a loss term, $Q_{VVT_{T12}}$, for the transfer of energy to T_{12}. These terms are described above. V-T relaxation of O_2, $Q_{VT_{O_2}}$, is taken from the survey of Blauer and Nickerson [152]. All the other terms in (4.13) are similar to the previous equations.

Finally, we also solve the energy balance equation of T_g:

$$\rho C_p \frac{dT_g}{dt} = Q_{VT} + Q_{VVT} + Q_g - Q_{condT_g} - Q_{feedT_g} \quad (4.14)$$

where ρ is the gas density, C_p is the mixture-averaged gas heat capacity, subtracted of the heat capacity of the vibrational manifolds (see eq. (4.8-4.13)) at thermal equlibrium, i.e., for the vibrational temperatures equal to T_g, Q_g is the heat released from the reactions in the plasma and the Joule heating of the electrons. In contrast to the conduction term in the vibrational energy balance equations, Q_{condT_g} uses the thermal conductivity k_g instead of the product $C_p \cdot D_m(T_g)$. k_g is the mixture-averaged thermal conductivity, calculated as:

$$k_g = 0.5 \left(\sum_i x_m k_m + \frac{1}{\sum_m x_m / k_m} \right) \quad (4.15)$$

where x_m is the molar fraction of species m, and k_m is the thermal conductivity of species m. k_m is net of the vibrational contributions to the thermal conductivity, which are included in eq. (4.8 and 4.11-4.13). In order to include only the translational and rotational contributions for the molecules for which separate vibrational energy balance equations exist, we introduce the following calculation from Thomson [155], a specific form of the Eucken formula [156], which considers only translational and rotational degrees of freedom:

$$k_m = \frac{15}{4} \eta_m ((k_B * N_A)/M_m))(1 + \frac{4}{15}) \quad (4.16)$$

with m = CO_2, CO or O_2, and η_m and M_m being the corresponding viscosity and molar mass. η_m (in Pa × s) is calculated as [157, 158]:

$$\eta_m = 2.669e^{-6} \frac{\sqrt{T_g M_m \times 10^3}}{\sigma_m^2 \Omega_D} \quad (4.17)$$

where σ_m is the characteristic length of the Lennard-Jones potential, and Ω_D is the collision integral [87].

The mixture-averaged diffusion coefficient D_m for the species m is given as:

$$D_m = \frac{1-w_m}{\sum_{i \neq m} \frac{x_m}{D_{i,m}}} \quad (4.18)$$

where w_m is the mass fraction of species m. The binary diffusion coefficient $D_{i,m}$ is calculated based on the expression from [33, 87, 159]. For the charged particles, the diffusion coefficient is calculated from their mobility, taken from [146] or assumed from similar ions, based on the Einstein's relation. Heat capacity, enthalpy and entropy as function of temperature for each species are taken from the NASA polynomials [160, 161]. In the computation of T_g, the heat capacity of molecular species with separate vibrational energy balance equations is subtracted from the corresponding vibrational contributions, as described above. For cluster ions, namely $C_2O_2^+$, $C_2O_3^+$, $C_2O_4^+$, CO_4^+ and CO_4^-, the heat capacity is neglected, because their low concentrations do not affect the computations, while enthalpy and entropy are taken from [162, 163] without temperature dependence, with a constant value at ca. 300 K, depending on the source measurement. The uncertainty that this approximation brings to the computations is very small due to the low concentrations of these species and the narrow temperature range of this study. The thermal conductivity of CO_2 calculated in this way was compared to the thermal conductivity as a function of temperature available in literature and the agreement was within 5 %.

We must point out that, for each of the above balance equations, we have checked that the energy is conserved, because the time-dependent term at the left-hand side is equal (but opposite sign) to the sum of all heating terms (see Figures 4.3-4.5 below).

4.3 Results and discussion

The experimental conditions investigated in this study correspond to the single-pulse measurement of Klarenaar *et al.* [108]. The pressure is kept constant at 6.7 mbar and the feed flow rate is 166 sccm. The pulse-on time is 5 ms, with a current of 50 mA. The plasma length and radius are 17 and 1 cm, respectively. Our model represents the first fully self-consistent model describing the single-pulse experiment of Klarenaar *et al*.

[108], starting from the experimental current profile as input parameter, without the need to assume a priori electron density or temperature, or E/N. To achieve such degree of self-consistency, our model includes the electrical circuit, the ion kinetics, the electron temperature and the vibrational and gas temperature balance equations, in contrast to the existing models, which use the electron density profile or gas temperature profile as input to the simulations. Moreover, using energy balance equations instead of the STS description of the vibrational kinetics drastically reduces the number of reactions, making this kinetic model suitable for later implementation in CFD models.

4.3.1 Temperature evolutions and comparison with experiments

Figure 4.1 compares the calculated temporal profiles of the various temperatures with the experimental results.

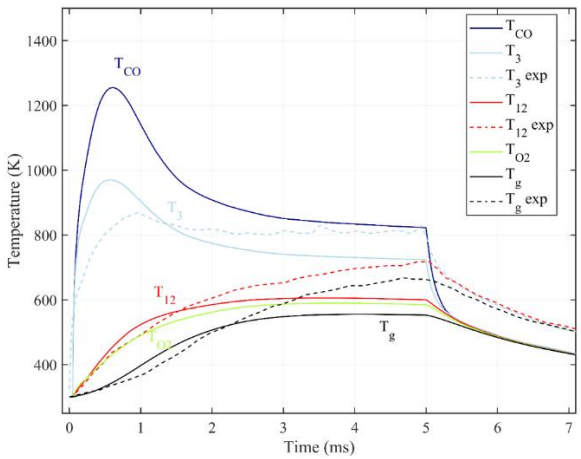

Figure 4.1. Calculated (solid lines) and experimental (dashed, when available) temperature profiles for the single-pulse experiment of [108].

Overall, we reach satisfactory agreement (within 10%) between calculated and experimental temperature profiles during the first part of the pulse. However, significant deviations arise for the second part of the pulse, especially for T_g and the closely related T_{12} and T_{O2} profiles. This can be ascribed to the way heat losses to the walls are accounted for in the model. Particularly, eq. (4.9) in section 4.2.4 describes heat conduction averaged over the tube radius, with a factor 8 in front of the conduction term. This is ideal for comparing the computed profiles with radially averaged experimental temperatures. However, Klarenaar *et al*. [108] measured the temperatures at the center of the tube radius; thus, the factor 8 in front of the conduction term (cf. eq. (4.9) above) has to be replaced by a factor 4, when calculating the gas temprature in

the center of the reactor [150]. Figure 4.2 presents calculated (solid lines) and experimental (dashed, when available) temperature profiles for the single-pulse experiment of [108] using the heat balance equation for the center of the reactor, allowing a more correct comparison with the experiment.

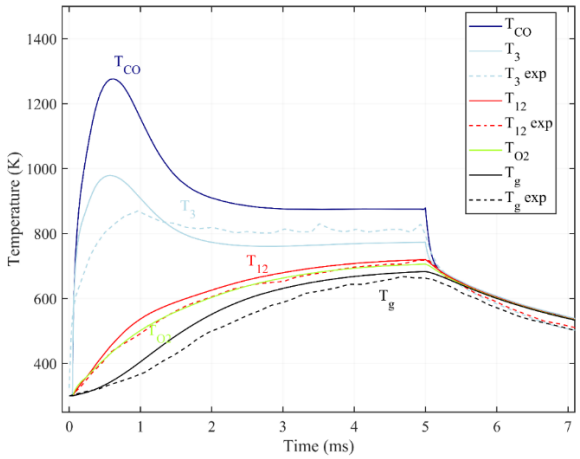

Figure 4.2 Calculated (solid lines) and experimental (dashed, when available) temperature profiles for the single-pulse experiment of [108] using the heat balance equation for the center of the reactor, needed to compare with the experiment.

Compared to Figure 4.1, Figure 4.2 shows improved agreement between the computed and experimental temperature profiles, especially in the second part of the pulse for T_{12} and T_g, which were earlier strongly underestimated. The difference between Figure 4.1 and 4.2 is a consequence of the strong dependence of T_{12} and T_g on the conduction term, as the corresponding degrees of freedom have a high heat capacity and transfer a substantial amount of energy to the walls through conduction. This underscores the critical importance of accurately understanding the shape of the temperature profile when applying the energy approach in modeling non-equilibrium conditions.

By examining the temporal profiles, we observe that T_{CO} closely follows the profile of T_3 and remains elevated throughout the entire duration of the pulse. Due to the low degree of dissociation and vibrational non-equilibrium, we do not account for dissociation processes occurring through high vibrational levels of the asymmetric stretching mode (T_3), known as the "ladder-climbing mechanism" [40, 121]. Nevertheless, our results indicate that, under these conditions, the excitation of T_{CO} is likely to promote CO + O recombination back to CO_2. This effect was briefly mentioned by Rusanov *et al*. [62], who estimated that when $T_{CO} \cong T_3$, the forward and reverse rate of dissociation equilibrate, reducing the overall energy efficiency by 30%. In our study, $T_{CO} > T_3$, suggesting that the

recombination might be favored over dissociation. Indeed, the vibrationally enhanced reverse reaction is often overlooked in literature due to the additional complexity it introduces into the system. Our results highlight the necessity of including the vibrational energy balance of the products, along with that of the feed components, to correctly describe the dynamics of the system.
In the next section, we delve deeper into the individual energy balance equations to reconstruct the heating dynamics. From now on, only the results for the centerline temperatures, with a factor 4 in the conduction terms, are presented.

4.3.2 Heating dynamics of the gas and vibrational modes

Given the reasonable agreement for the temperature profiles, we can now examine the gas heating dynamics by looking at the individual energy balances. The energy balance of T_3 is presented in Figure 4.3.

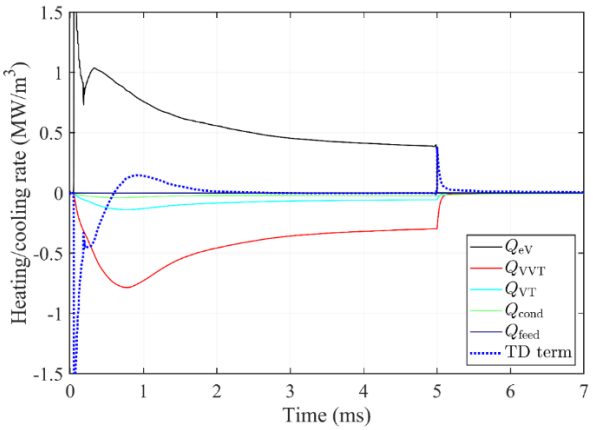

Figure 4.3 Contributions to the energy balance of T_3, see eq. (4.11), including the time-dependent (TD) term of the left-hand side, which is equal (but opposite sign) to the sum of all other terms (at the right-hand side), showing that the total energy is conserved.

Figure 4.3 indicates that T_3 is exclusively heated by electron-impact excitation (QeV), whereas the dominant cooling mechanism is V-V-T relaxation to T_{12}. V-T relaxation and heat conduction to the walls play a minor role. Due to the low heat capacity, T_3 is significantly higher than T_{12} (cf. Figure 4.2 above). The lower heat capacity also implies that the energy conduction towards the walls is reduced, assuming a parabolic dependence of the vibrational temperature profile. The same analysis is performed for T_{12} in Figure 4.4.

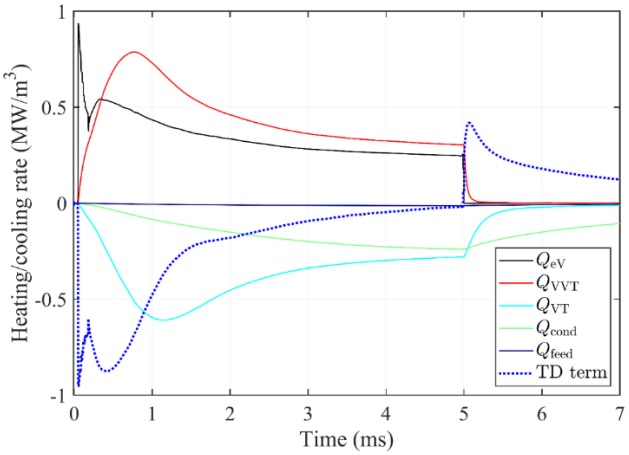

Figure 4.4. Contributions to the energy balance of T_{12}, see eq. (4.8), including the time-dependent (TD) term of the left-hand side, which is equal (but opposite sign) to the sum of all other terms (at the right-hand side), showing that the total energy is conserved.

The dominant cooling mechanism for T_3 (i.e., Q_{VVT}) is an important heating channel for T_{12}, in line with the modelling results of Biondo *et al*. [132], who showed that V-V-T relaxation is responsible for coupling the asymmetric and symmetric levels of CO_2. Equally important is electron-impact excitation, which constitutes approximately half of the heating rate for T_{12}. V-T relaxation is the primary cooling pathway, as also reported in previous studies (*e.g.*, [128,132]). However, heat conduction to the walls becomes as important in the second part of the pulse, and is the dominant cooling mechanism in the afterglow. This is consistent with what was described by Thomson *et al*. [155], indicating that the vibrational component of the thermal conductivity is responsible for nearly 30% of the total energy flux in CO_2. Thus, the use of the energy approach requires a careful description of the vibrational thermal conductivity in the energy balance equations.

The fact that the rates of V-T relaxation and heat conduction to the walls are comparable is a strikingly different result from previous modelling work, due to the distinct approach used here. Specifically, in many state-to-state modelling studies, such as those by Vermeiren and Bogaerts [164], Silva *et al*. [128], and follow-up works, the energy balance equation for T_g includes vibrational contributions to the heat capacity and thermal conductivity, assuming $T_{vib} = T_g$. The non-equilibrium vibrational contributions are thus either neglected or treated as wall deactivation [128]. In contrast, the energy approach allows for a more accurate description of the heating dynamics compared to these implementations of the state-to-state approach. However, a state-to-state approach can

achieve a similar level of accuracy if only translational and rotational contributions are included in the T_g balance equation, as demonstrated by Nagnibeda and Kustova [165]. Thus, the difference does not lie in the state-to-state approach itself, but in the proper treatment of the approximations made when applying it.

The energy balance for T_{CO} and T_{O2} are not shown because of the very low dissociation degree (ca. 0.4%). Thus, the last energy balance to examine is that of T_g, which is shown in Figure 4.5.

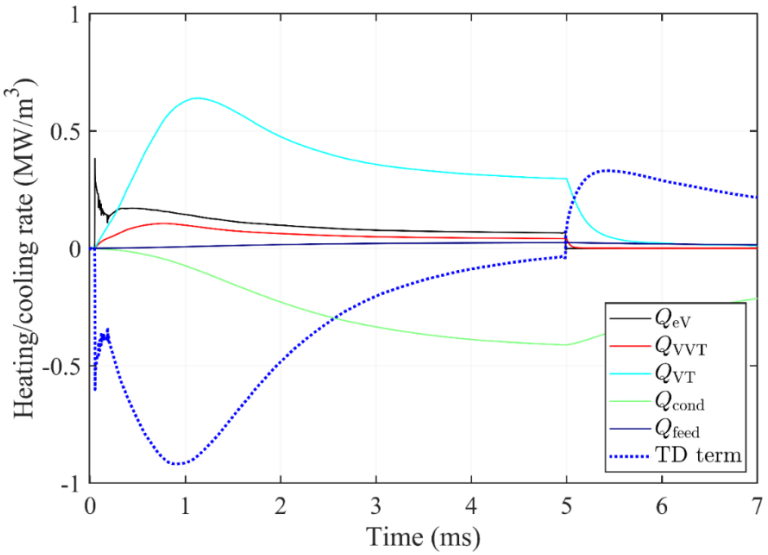

Figure 4.5. Contributions to the energy balance of T_g, see eq. (4.14), including the time-dependent (TD) term of the left-hand side, which is equal (but opposite sign) to the sum of all other terms (at the right-hand side), showing that the total energy is conserved.

Figure 4.5 indicates that V-T relaxation is an important pathway of gas heating, becoming the dominant mechanism in the afterglow, but it is not sufficient to describe the overall heating dynamics. Indeed, fast gas heating from reactions (Q_g), especially relaxation of electronic states, is responsible for the elevation of T_g during the first millisecond in the pulse, triggering V-T relaxation as a second heating mechanism. The electronic states contributing the most to fast gas heating are $CO_2(e_1)$, $CO_2(e_2)$ and $CO(a^3\Pi)$. The other electronic states have minimal contributions to the heating dynamics. Despite this, we believe that their inclusion is important in view of extending the validity of this model over a wider range of experimental conditions in the future, including conditions leading to higher CO_2 dissociation degrees. These findings agree well with the observations of

Biondo *et al*. [132], who showed that an E/N of more than 90 Td is needed to sustain the discharge, triggering electronic excitation and relaxation, and to achieve a good agreement with measured T_g. Nevertheless, Biondo *et al*. [132] were not able to perform a self-consistent calculation of the electron kinetics and E/N, and had to rely on a constant, estimated E/N of 94 Td for their simulations.

In our study, we go beyond the foundation laid by [132], by incorporating the electrical circuit in our model, with a current source of 50 mA as given by the experimental benchmark [108]. The corresponding calculation results are presented in the next section.

4.3.3. Electrical characterization: E/N, electrical current and T_e

As we include the electrical circuit in our model, we are able to self-consistently calculate E/N, T_e and current profiles, as shown in Figure 4.6.

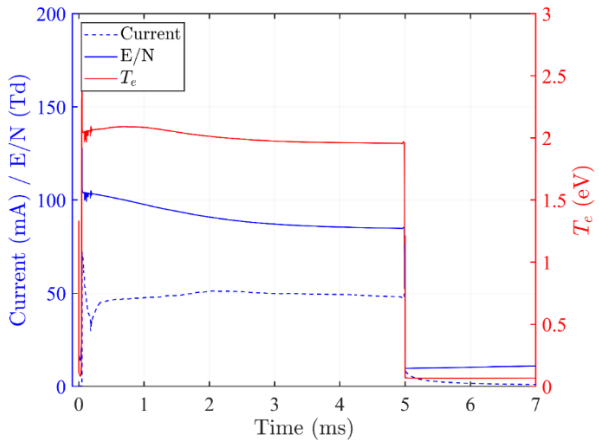

Figure 4.6. Current, reduced electric field (E/N) and electron temperature (T_e) calculated by our model for the single-pulse experiment of [108].

We can see that in the beginning of the pulse, where the electron density is low and the plasma resistivity high, the reduced electric field has a value of nearly 120 Td. As the electron density and the plasma conductivity are increasing, the electric field needed to sustain the discharge is reduced. As a result, the value of E/N gradually drops to 94 Td towards the end of the pulse. Figure 4.6 confirms that the discharge is sustained at E/N > 90 Td, in line with the findings of [132], corresponding to T_e > 2 eV. To achieve this, the inclusion of ambipolar diffusion of positive ions and electrons to the reactor walls is essential. Without it, the computed plasma parameters, such as reduced electric field,

electron temperature and density, become unrealistic shortly after the breakdown, which also makes the simulations challenging to solve.

4.3.4. Ion kinetics

In order to calculate the plasma properties of Figure 4.6 in a self-consistent manner, our model includes a detailed description of the ion kinetics. This is necessary to predict the correct electron density, which is very similar to the one estimated in [127], although achieved at a higher E/N. Figure 4.7 shows the time evolution of the number densities of the main ions and the electrons.

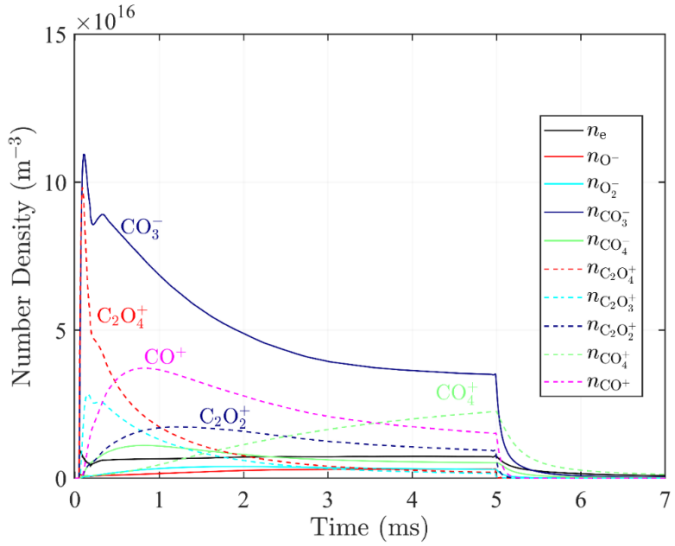

Figure 4.7. Time evolution of the electron and dominant ion number densities.

Including a complete set of ion kinetics reveals that the dominant negative ion during the pulse is CO_3^-, which has a much higher density than the electrons. It results from dissociative electron attachment to CO_2 forming O^-, and subsequent recombination of O^- with CO_2 to form the stable CO_3^- ion [166]. In fact, electron detachment from this ion has a high energy threshold [167], and thus the ion is only efficiently lost via ion-ion recombination and collisional detachment with O atoms and CO. Despite its importance, the corresponding chemistry is not well understood and is often omitted in CO_2 plasma modeling. For instance, Naidis and Babaeva [168] did not include CO_3^- in their work, when modelling similar experiments (same pressure but lower mass flow rate, with higher pulse repetition rate) [108]. Their conclusion was that CO_3^- is not formed, because O^- is effectively quenched through collisions with CO. However, our model shows that

quenching upon collision with CO is not effective enough to remove the ion, due to the low dissociation degree in the single-pulse experiment. The second important negative ion is CO_4^-, originating from a clustering reaction between O_2^- and CO_2 [142], but its density is much lower than for CO_3^-, and comparable to or even slightly higher than n_e. As a result of the high negative ion densities, the electrons are lost primarily by attachment reactions, rather through ambipolar diffusion. This effect increases the reduced electric field until a sufficient amount of CO is produced.

The dominant positive ions are a result of clustering reactions as well, and subsequent charge transfer reactions. Initially, $C_2O_4^+$ is formed from $CO_2^+ + 2CO_2 \longrightarrow C_2O_4^+ + CO_2$ [169]. Then, $C_2O_4^+$ reacts with CO, originating from the dissociation of CO_2, to produce $C_2O_3^+$ and CO_2. As the O_2 concentration builds up during the pulse, $C_2O_4^+$ is converted to CO_4^+ through $C_2O_4^+ + O_2 + CO_2 \longrightarrow CO_4^+ + 2CO_2$ [170]. Thus, CO_4^+ becomes the dominant positive ion in the second part of the pulse and in the afterglow.

4.4 Conclusions

Fully self-consistent modeling of gas conversion plasmas can unlock the potential of plasma-based gas conversion for the electrification of fossil fuel-based sectors, such as the chemical industry. However, the road ahead for fully self-consistent (and predictive) models is still very long, due to the multitude of physical phenomena that need to be thoroughly considered and captured, *e.g.*, fluid dynamics, heat transfer, chemical kinetics, and the interplay between them.

In this chapter, we focus on the kinetics underlying vibrational and gas heating, specifically in a pulsed CO_2 glow discharge, operated at low pressure. This type of discharge represents the ideal case to validate a kinetic scheme due to the homogeneity of the plasma. Moreover, pulsing enables to capture the transient behavior of the electron kinetics and the relaxation of excited species, and compare them with global computations.

Starting from the foundations laid by previous modelling efforts, we constructed a fully self-consistent kinetic model based on an energy approach, with separate energy balance equations for the vibrational temperatures of CO_2 (both asymmetric and symmetric modes), CO and O_2, the gas temperature, and the electron temperature. The latter is a particularly innovative aspect, introduced for the first time by our model. In fact, the models published so far have failed to include a fully self-consistent description of the electron kinetics using the experimental current as an input parameter. We were able to achieve this by coupling the plasma to an electrical circuit and resolving the

extensive ion chemistry, which is rarely considered in recent literature. This is possible by the drastic reduction in the number of reactions within the model, achieved by replacing the detailed, state-to-state vibrational kinetics with the energy approach. Therefore, these represent additional innovative features of our model.

Comparison with the temporal evolution of the measured temperature profiles shows satisfactory agreement (within 10 %), indicating that our model includes all the relevant kinetics, at least for the single-pulse experiment, where the dissociation degree is limited and all dissociation products are evacuated before the subsequent pulse. Therefore, we can consider our model to be validated for CO_2 discharges at low pressure and low excitation, for which the dissociation degree of CO_2 is smaller than 1%. Hence, the simulation outcome can be used to infer the underlying dynamics, confirming the importance of vibrational-vibrational relaxation, coupling the asymmetric and symmetric levels of CO_2. Moreover, our study highlights the important role of vibrational energy transfer to the walls for an accurate description of the gas heating.

Furthermore, our study reveals the importance of CO_3^- in describing the dynamics of the system. Due to the low dissociation degree, CO_3^- is efficiently produced, which results in an increase of the reduced electric field, needed to sustain the specified current. The CO_3^- density is an order of magnintude higher than the electron density, as a result of significant electron losses due to attachment reactions. The detailed description of the formation and destruction of positive and negative ions, as well as their interactions with electrons and neutrals, allows us to self-consistently simulate the behavior of the reduced electric field, eliminating significant assumptions previously necessary for modelling transient discharges.

Notwithstanding the successful results of this study, our model is still limited to conditions that are far from appealing for industrial application, namely atmospheric (or higher) pressure and high CO_2 conversion. The next step towards such conditions is to compare our model with experiments where the effects of dissociation products are significant, such as the multi-pulse experiment by Damen *et al* [115]. This experiment presents conditions with more prominent gas heating and higher fractions of species with high thermal conductivity (e.g., O and O_2). In doing so, we anticipate that the model will require a more detailed description of radial heat losses to the reactor walls. Additionally, the model will need to include the dependence of chemical reactions on all six temperatures for a more accurate description of dissociation and recombination dynamics, as previously presented by Kosareva *et al.* [149]. For these reasons, incorporating the validated chemical kinetics from this study into a 1D radial model will

be a necessary step towards self-consistent CFD modeling of CO_2 discharges, for reactor optimization and design.

While this chapter was focused on modeling a CO_2 plasma, the same modeling approach can also be applied to air plasmas used for NF, as demonstrated in the next chapter.

Chapter 5.

Re-defining the minimum energy cost for nitrogen fixation into NO in atmospheric pressure air plasma

The formation of NO in N_2-O_2 plasmas predominantly follows the Zeldovich mechanism, which can be enhanced through vibrational-translational (VT) non-equilibrium, where overpopulated vibrational states of N_2 reduce the reaction energy barrier. In Chapter 1, we showed that early research by Rusanov *et al.* suggested an exceptionally low energy cost (EC) of 0.2 MJ/(mol N) at low pressure, attributed to the vibrationally-enhanced Zeldovich mechanism. In this chapter, we re-evaluate the theoretical minimum EC for NF into NO, in atmospheric pressure air plasmas, more suitable for industrial applications. We used a new global model, similar to the one developed in Chapter 4, incorporating recent VT relaxation rate coefficients and updated reaction kinetics from the Stellar database. Our model simulates both steady state and transient conditions to determine optimal parameters for NF at VT non-equilibrium. Our results indicate that a minimum steady state EC of 2.09 MJ/mol is achievable at a gas temperature of 3100 K and a vibrational temperature for N_2 of 6000 K. Our transient simulations suggest an even lower limit of 1.82 MJ/mol if VT non-equilibrium can be sustained, but when taking into account the energy needed to sustain this VT non-equilibrium, this value is unrealistic. Hence, when accounting for relaxation of the vibrational states, in real conditions, e.g., ns-pulsed excitation, we obtain a minimum EC of 2.17 MJ/mol, where NO is actually formed due to chemical non-equilibrium but (VT) thermal equilibrium, suggesting a new pathway towards optimizing plasma-based NF with ns-pulsed plasmas. Thus, overall we define 1.82 MJ/mol as the theoretical minimum EC for NF into NO in atmospheric pressure air plasmas when VT non-equilibrium can be sustained at limited cost, and 2.17 MJ/mol in more realistic conditions, where VT non-equilibrium is imposed (e.g., ns-pulsed plasmas) but VT relaxation occurs.

This chapter will be submitted for publication soon.

5.1 Introduction

As stated in Chapter 1 and Chapter 3, plasma technology is promising for sustainable NF into NO_x, i.e., for fertilizer production, due to its compatibility with renewable electricity [61]. Rouwenhorst *et al.* estimated that in order for plasma to be competitive with current technology (i.e., Haber-Bosch followed by Ostwald), the EC for NO production should be between 1 – 1.5 MJ/(mol N)[61].

The NO formation process in plasmas typically proceeds by the Zeldovich mechanism, i.e.,

$O_2 + N \rightleftharpoons NO+O$

$N_2 + O \rightleftharpoons NO+N$

Enhancing the Zeldovich mechanism through vibrational-translational (VT) non-equilibrium has been the focus of plasma-based NF research in the past 10 years (e.g., [11, 18, 47, 171]). Indeed, VT non-equilibrium means that the N_2 vibrational states are overpopulated compared to a Boltzmann distribution at the gas temperature, and these vibrational states reduce the energy barrier for the Zeldovich mechanism.

The efforts on promoting VT non-equilibrium in plasmas were inspired by the early research of Azizov *et al.,* described in the work by Rusanov *et al.* in the 1980s, who reported 14 % NO concentration with an impressive EC as low as 0.2 MJ/(mol N) at a pressure of 10 - 100 Torr [62]. It is important to note that the reactor walls were cooled by liquid N_2, which was not taken into account in the EC calculation. Their hypothesis was that the energy barrier for N_2 dissociation and NO formation is indeed lowered through overpopulation of the vibrational states, or in other words, an elevated vibrational temperature of N_2 (T_vN_2) with respect to the gas temperature (T_g), which can indeed be observed in plasmas at certain conditions [40, 172]. This allows the chemical reactions to proceed with higher efficiency without the need of heating the gas to high temperatures or elevating the pressure. However, despite significant experimental efforts, the EC of 0.2 MJ/(mol N) has never been reproduced up to now, and especially in atmospheric pressure plasmas, which are more relevant for industrial application, it turns out to be unrealistic. In addition, the theoretical calculations performed by Rusanov et al.62, which were meant to explain this low EC, used very strong approximations, and they cannot be reproduced with recent rate coefficient data.

For this reason, we decided to re-evaluate the theoretical calculations by Rusanov *et al.,* in order to predict a more realistic minimum EC for NF into NO, especially for atmospheric air plasmas. Before we explain our new model in section 5.3, we first briefly summarize the studies performed in literature for NO formation in the last two decades.

5.2 Literature overview of NO formation studies in both low pressure and atmospheric pressure plasmas

The majority of studies investigating the kinetics of NO formation at VT non-equilibrium are conducted in low pressure plasmas [173]. Indeed, low pressure plasmas typically operate at lower T_g, which allow to establish a steady state of VT non-equilibrium, since the VT relaxation rates (which destroy the VT non-equilibrium) strongly increase with rising T_g and pressure [172]. The cross sections for vibrational excitation of N_2 are high, and at low reduced electric field (i.e., ratio of electric field over gas number density, E/N < 100 Td), nearly all of the electron energy is deposited in the vibrational states [32]. One of the first comprehensive evaluations of NO formation in N_2/O_2 plasmas, at a pressure of 2 Torr, was performed by Guerra *et al.* in 2001 [174]. This model revealed however that NO is not formed by VT non-equilibrium, but through collisions of the metastable N_2 (A^3) state with O atoms. In 2009, Pintassilgo *et al.* investigated NO formation in a low pressure pulsed air discharge, with pulse lengths between 0.1 – 10 ms and pressure of 1 Torr [175]. They showed that for short pulse duration (order of 0.1 - 10 ms) the kinetics of the electronically excited states dominate the production of NO, while for long pulse duration (> 10 ms) the vibrationally excited states become more important. One of the first studies on ns-pulsed air discharges, at 60 Torr, was conducted by Uddi *et al.*, in 2009 [176]. The authors measured the density of NO and O in the plasma afterglow and compared them to their modelling results, but could not conclude about the dominant mechanism for NO formation. In 2014, Shkurenkov *et al.* also investigated the kinetics of NO formation in a ns-pulsed air discharge, by combined experiments and modelling, at a pressure of 100 Torr [177]. The model was significantly extended compared to the model by Uddi *et al.* [176], to capture all possible reactions leading to NO formation with electronically excited states. The model presented excellent agreement between the measured density of N, O and NO, both in the discharge and the afterglow, despite the elevated T_vN_2 in the afterglow. These results strongly indicated that the vibrationally excited states play a negligible role in NO formation under these conditions, and further solidified the importance of electronically excited states. All these investigations conducted at low pressure suggest that NO formation is primarily driven by interactions with electronically excited states and not through VT non-equilibrium.

At atmospheric pressure, collisional quenching of the electronically excited states is significantly faster, which leads to fast gas heating and equilibration of T_vN_2 and T_g [32, 178]. One of the first studies suggesting that the vibrational states can be utilized for NO

formation at atmospheric pressure, i.e., through the vibrationally-enhanced Zeldovich mechanism, was conducted by Wang *et al.* for a classical gliding arc discharge [179]. This led to a significant effort by our research group PLASMANT to find the most efficient conditions for NO formation, assuming VT non-equilibrium [53, 57, 97, 180]. In our more recent work, however, we found that elevating the pressure in the reactor to 3 barg leads to even better results than at atmospheric pressure when using a DC (gliding) arc discharge [59]. This indicates that VT non-equilibrium is not responsible for the observed results, since increasing the collision frequency and residence time should lead to relaxation of the vibrational states. By changing the conceptual approach of modelling, we were further able to explain the formation of NO, assuming (VT) thermal equilibrium [181]. Almost simultaneously, Esposito *et al.* highlighted the shortcomings of the old kinetic data used for modelling the vibrationally-enhanced Zeldovich mechanism, which further confirmed the hypothesis that NO formation in atmospheric pressure air plasma is typically driven by thermal processes [182]. Most recently, Qiao *et al.* revealed that T_vN_2 is equal to T_g and no VT non-equilibrium was observed in an atmospheric pressure DC glow discharge [183]. Additionally, Tatar *et al.* performed spontaneous Raman measurements of T_vN_2 and T_g in a microwave air plasma at 0.65 bar [184], and their results showed that the plasma is indeed in thermal equilibrium and that the production of NO can be perfectly described by a thermal equilibrium model. These results further solidify the idea that typical arc and microwave discharges, which are most extensively used for NF, operate at thermal equilibrium, and special considerations must be taken in order to achieve VT non-equilibrium.

Yu *et al.*, achieved VT non-equilibrium by igniting a DC glow discharge in a preheated gas flow at a pressure of 1 bar [68]. The authors could keep T_g at 2000 K and T_v at 3300 K by reducing the residence time of the gas in the plasma. Lo *et al.* conducted one of the first investigations of T_vN_2 and T_g as a function of time in a ns-pulsed atmospheric pressure air discharge [185]. They showed that T_vN_2 can be significantly enhanced in the short timescale over which the pulse is applied, with T_vN_2 reaching 5000 K and T_g remaining at 1000 K, but they did not measure NO concentration and EC. Vice versa, Abdelaziz *et al.* achieved a very low EC of 1.6 MJ/(mol N), utilizing ns-pulsed plasma in oxygen-enriched air at atmospheric pressure, but they did not measure T_vN_2 and T_g, although it is unlikely that VT non-equilibrium was achieved in this experiment, since VT relaxation occurs more rapidly due to the higher O_2 fraction [60]. Recently, Qiao *et al.* directly measured VT non-equilibrium in a µs-pulsed glow discharge plasma sustained for 200 µs at a pressure of 1 bar, with T_vN_2 = 5000 K and T_g = 3500 K [186].

It is clear from above that some experimental studies do report VT non-equilibrium, both at low pressure and atmospheric pressure, but they could not reveal whether the N_2 vibrational states were responsible for NO formation. There has been a clear lack in predictive models, able to guide the experimental research towards more optimal conditions for NF at VT non-equilibrium. As a result, the field has mostly been driven by trial-and-error, and up to now, a conclusive proof of efficient NF driven by VT non-equilibrium in atmospheric pressure air plasmas has not been found. Despite this, a multitude of experiments have reported elevated T_vN_2 with respect to T_g, which indicates that the process is in principle possible. Therefore, we developed a new global model, incorporating the most recent VT relaxation rate coefficients, together with recent rate coefficients for the most important reactions responsible for NF, by using the data provided in the Stellar database [187]. We use this model to calculate a new minimum EC in atmospheric pressure air plasma, re-evaluating the earlier predictions by Rusanov et al. [62]. We hope these results can guide experimental research in order to evaluate whether NF under VT non-equilibrium is possible and energy efficient.

5.3 Description of the model

This global model is similar to the model described in previous chapter for the CO_2 plasma. It solves the vibrational energy balance equations of N_2, O_2 and NO, the gas heat balance equation, and the species balance equations for N, O, NO, O_2 and N_2. The system of equations is solved in COMSOL 6.2 [83].

For each of the five species mentioned above we solve the continuity equation:

$$\rho_p \frac{dw_s}{dt} = R_s \tag{5.1}$$

where ρ_p is the mass density, w_s is the mass fraction of species s, and R_s is the net rate of change of the species mass density, based on the gas phase reactions.

Our model includes 12 reversible chemical reactions, presented in Table 5.1. Note that electronically excited states are not included in our model. This is justified because of the fast collisional quenching of the electronically excited states at atmospheric pressure, which will only result in gas heating, and not contribute to efficient NO formation [32, 178].

Table 5.1. Chemical reactions included in the model, with references where the rate coefficients are adopted from.

№	Chemical reaction	Ref
R5.1	$N_2 + N_2 \rightleftharpoons N+N+N_2$	[187]
R5.2	$N_2 + O_2 \rightleftharpoons N+N+O_2$	[187]
R5.3	$N_2 + NO \rightleftharpoons N+N+NO$	[187]
R5.4	$N_2 + N \rightleftharpoons N+N+N$	[187]
R5.5*	$N_2 + O \rightleftharpoons N+N+O$	[187]
R5.6	$O_2 + N_2 \rightleftharpoons O+O+N_2$	[187]
R5.7	$O_2 + O_2 \rightleftharpoons O+O+O_2$	[187]
R5.8	$O_2 + NO \rightleftharpoons O+O+NO$	[187]
R5.9	$O_2 + N \rightleftharpoons O+O+N$	[187]
R5.10	$O_2 + O \rightleftharpoons O+O+O$	[187]
R5.11*	$O_2 + N \rightleftharpoons NO+O$	[187, 188]
R5.12	$N_2 + O \rightleftharpoons NO+N$	[187, 188]

* The rate coefficients are assumed to be equal to those of R5.4 and R5.10, respectively

The vibrational energy balance equations are expressed as:

$$n_{N_2, O_2, NO} \cdot \frac{dE_v^{N_2, O_2, NO}}{dt} = Q_R^{N_2, O_2, NO} - Q_{VT} \quad (5.2)$$

Where $n_{N_2, O_2, NO}$ is the number density of N_2, O_2 and NO, $E_v^{N_2, O_2, NO}$ is the average vibrational energy, $Q_R^{N_2, O_2, NO}$ is the rate of change of vibrational energy due to chemical reactions, and Q_{VT} is the vibrational energy loss rate due to VT relaxation.

The rate of change in vibrational energy due to chemical reactions $Q_R^{N_2, O_2, NO}$ is given as:

$$Q_R^{N_2, O_2, NO} = \sum_i - \left(R_{f,i} \left(\Delta\varepsilon_{f,i} - E_v^{N_2, O_2, NO} \right) - R_{r,i} \left(\Delta\varepsilon_{r,i} - E_v^{N_2, O_2, NO} \right) \right) \quad (5.3)$$

Where $R_{f,i}$ is the forward reaction rate of reaction i, i.e., direction in which the species of interest (N_2, O_2 or NO) is destroyed, $\Delta\varepsilon_{f,i}$ is the average vibrational energy lost in the forward direction of reaction i, $R_{r,i}$ is the reverse reaction rate, i.e., direction in which the species is formed, and $\Delta\varepsilon_{r,i}$ is the average vibrational energy gained due to the reverse reaction. For each species (N_2/O_2/NO), the summation in equation 5.3 is performed over all the reactions involving the species of interest.

The rate coefficients (k) and average vibrational energy ($\Delta\varepsilon$) are calculated by averaging over the elementary vibrational state-specific reaction rate coefficients (k_j), assuming a Boltzmann vibrational distribution function between the vibrational states:

$$k = \sum_{v=j} k_j(T) \frac{\exp\left(-\frac{\varepsilon_j}{T_v}\right)}{\sum_v \exp\left(-\frac{\varepsilon_j}{T_v}\right)} \tag{5.4}$$

$$k \cdot \Delta\varepsilon = \sum_{v=j} k_j(T) \frac{\exp\left(-\frac{\varepsilon_j}{T_v}\right)}{\sum_v \exp\left(-\frac{\varepsilon_j}{T_v}\right)} \varepsilon_j \tag{5.5}$$

where $k_j(T)$ is the elementary rate coefficient taken from the Stellar database [187] and ε_j is the energy of the j^{th} vibrational level. To validate our calculations, we compared the reaction rate coefficients calculated for $T = T_v$ with the available equilibrium rate coefficients measured experimentally and we found good agreement. The reverse rate coefficients of R5.1-R5.10 are calculated using the detailed balance principle:

$$k_r = \sum_{v=j} \frac{\exp\left(-\frac{\varepsilon_j}{T}\right) k_{f,j}}{K_{eq}(T)} \tag{5.6}$$

where K_{eq} is the equilibrium constant of the reaction. For R5.11 and R5.12, the reverse rate coefficients are calculated based on the elementary rate coefficients provided in the Stellar database, according to equation 5.4.

The Q_{VT} term in equation 5.2, which is responsible for VT relaxation, is calculated from the modified Landau-Teller expression, taken from [189]:

$$Q_{VT} = 4k_B \frac{T_g}{T_v^{N_2, O_2, NO}} \left(T - T_v^{N_2, O_2, NO}\right) n_{N_2, O_2, NO} \sum_d n_d \langle \left(\Delta\varepsilon_c^{vibr}\right) \rangle^{VT} \tag{5.7}$$

Here k_B is the Boltzmann constant, T_g is the gas temperature, $T_v^{N_2, O_2, NO}$ is the vibrational temperature, $n_{N_2, O_2, NO}$ is the number density, n_d is the number density of each species acting as collisional partner for VT relaxation, and $\langle \left(\Delta\varepsilon_c^{vibr}\right) \rangle^{VT}$ is an energy operator, which is precomputed as a function of T_g and T_v and stored in the model as a lookup table for each collisional partner. This approach has been benchmarked with experimental VT relaxation times and good agreement was found [189]. In addition, this dramatically accelerates the computational efficiency of the model, allowing for further extending to higher dimensions without loss of accuracy.

The vibrational temperature $T_v^{N_2, O_2, NO}$ is calculated from the average vibrational energy $E_v^{N_2, O_2, NO}$ assuming a Boltzmann distribution function, where the energy levels are taken from the Stellar database:

$$E_v^{N_2,O_2,NO}\left(T_v^{N_2,O_2,NO}\right) = \sum_i \left(\varepsilon_i^{N_2,O_2,NO}\right) \frac{\exp\left(-\frac{\varepsilon_i^{N_2,O_2,NO}}{T_v^{N_2,O_2,NO}}\right)}{\sum \exp\left(-\frac{\varepsilon_i^{N_2,O_2,NO}}{T_v^{N_2,O_2,NO}}\right)} \quad (5.8)$$

Here, $E_v^{N_2,O_2,NO}$ is stored as a function of $T_v^{N_2,O_2,NO}$ by means of a lookup table. $T_v^{N_2,O_2,NO}$ is estimated by also using eq. 5.8.

The gas heat balance equation is given as:

$$N_n \cdot C_p \frac{dT_g}{dt} = Q_{VT} + Q_{chem} - Q_R \quad (5.9)$$

Where N_n is the neutral number density, C_p is the heat capacity of the mixture for which the vibrational contributions of N_2, O_2 and NO are subtracted, Q_{VT} is the gas heating due to VT relaxation, and Q_{chem} is the gas heating or cooling due to chemical reactions, obtained by multiplying the reaction rate of each reaction with the reaction enthalpy excluding the vibrational heat. The last term Q_R represents the energy exchange between the gas and the vibrational modes of N_2, O_2 and NO, obtained by summing the vibrational energy gained or lost by N_2, O_2 and NO during chemical reactions, as given by equation 5.3. However, in this case the average vibrational energy is not substracted from the average vibrational energy involved in the reaction.

The heat capacity, enthalpy and entropy of each species are taken from the NASA polynomials and the vibrational contributions were substracted [160]. We have used a similar approach in our previous chapter for CO_2 splitting, and very good agreement was found between the model and experiments (see previous chapter).

We calculate NO formation based on the above chemical reactions, and we evaluate the corresponding energy cost by:

$$EC\ [MJ/(mol\ N)] = \frac{H_{mix} - H_{mix,300}}{x_{NO}} \quad (5.10)$$

H_{mix} is the mixture enthalpy, $H_{mix,300}$ is the mixture enthalpy at 300 K and x_{NO} is the mole fraction of NO produced in the mixture. H_{mix} is given by:

$$\begin{aligned} H_{mix} = {} & N_A E_v^{N_2}(T_v N_2) x_{N_2} + N_A E_v^{O_2}(T_v O_2) x_{O_2} + N_A E_v^{NO}(T_v NO) x_{NO} \\ & + H_{N_2}(T_g) x_{N_2} + H_{O_2}(T_g) x_{O_2} + H_{NO}(T_g) x_{NO} + H_N(T_g) x_N \\ & + H_O(T_g) x_O \end{aligned} \quad (5.11)$$

Where N_A is the Avogadro constant

5.4 Results and discussion

We first present the results for steady state calculations and varying T_vN_2, as a function of $T_vO_2 = T_vNO = T_g$. We can assume the latter is true, because the rate coefficients for vibrational excitation of N_2 are much higher than for O_2 and NO, and at low reduced electric field, which is the case here (E/N < 100 Td), nearly all of the electron energy is deposited in excitation of N_2 [32]. Note that VT relaxation and vibrational energy exchanges by chemical reactions are neglected in these simulations, i.e., T_vN_2, T_vO_2, T_vNO and T_g are kept fixed. This means we do not solve the vibrational energy balance equations and the gas heat balance equation, but only the species continuity equations at fixed temperatures.

We will then proceed to transient simulations where VT relaxation is again neglected (hence, again solving only the species continuity equations and not the vibrational energy balance and heat balance equations). This allows to determine the theoretical maximum NO concentration and minimum EC, when VT non-equilibrium could be sustained, and thus, the optimal duration of VT non-equilibrium, similar to the experiments conducted in [68, 186], where VT non-equilibrium was sustained in the µs timescale.

Subsequently, we will couple the species continuity equations to the vibrational energy balance and heat balance equations, and account for VT relaxation and vibrational energy transfer in our transient simulations, to investigate conditions where VT non-equilibrium cannot be sustained, similar to ns-pulsed plasmas, like the ones investigated in [60, 185], where VT non-equilibrium was created over 10 – 100 ns and the system was then left to relax.

Finally, we will clarify why the minimum EC of 0.2 MJ/(mol N) for NF, estimated by Rusanov *et al.* [62], cannot be reached in atmospheric pressure air plasmas, even at VT non-equilibrium.

5.4.1 Evaluating the minimum EC for NF at steady state, assuming continuous VT non-equilibrium

The simulations at steady state assume a constant T_g, as well as T_vO_2, T_vNO and T_vN_2 during the entire simulation, hence they only solve the species continuity equations, based on the chemistry at fixed temperature, as explained above. To evaluate the minimum EC at these steady state conditions, we solved the model for different values of T_g, assuming that $T_vO_2 = T_vNO = T_g$ (see above), for T_vN_2 of 4000 K, 6000 K and 8000 K. Figure 5.1 presents the EC (a, b) and NO concentration (c), as a function of T_g for these

three values of T_vN_2, as well as the corresponding data for thermal equilibrium. The latter was calculated by setting $T_vN_2 = T_vO_2 = T_vNO = T_g$.

We can see that the EC generally decreases with rising gas temperature and reaches a minimum at 3100 K, after which it rises again, for all conditions except for T_vN_2 = 8000 K (Figure 5.1 a). For the thermal equilibrium condition, the minimum EC is 2.6 MJ/(mol N) (see detail in Figure 5.1b), which is slightly different from the value of 2.7 MJ/(mol N) calculated in our previous work [181]. We believe the reason for this small difference is due to integration errors in our previous calculation of the heat capacity. By using the enthalpy difference, as in the present model, these numerical errors are removed and we believe the value in this chapter to be more accurate. For T_vN_2 = 4000 K, the EC is consistently lower than the equilibrium EC in the range of 1500 – 4000 K, after which the values become equal to each other.

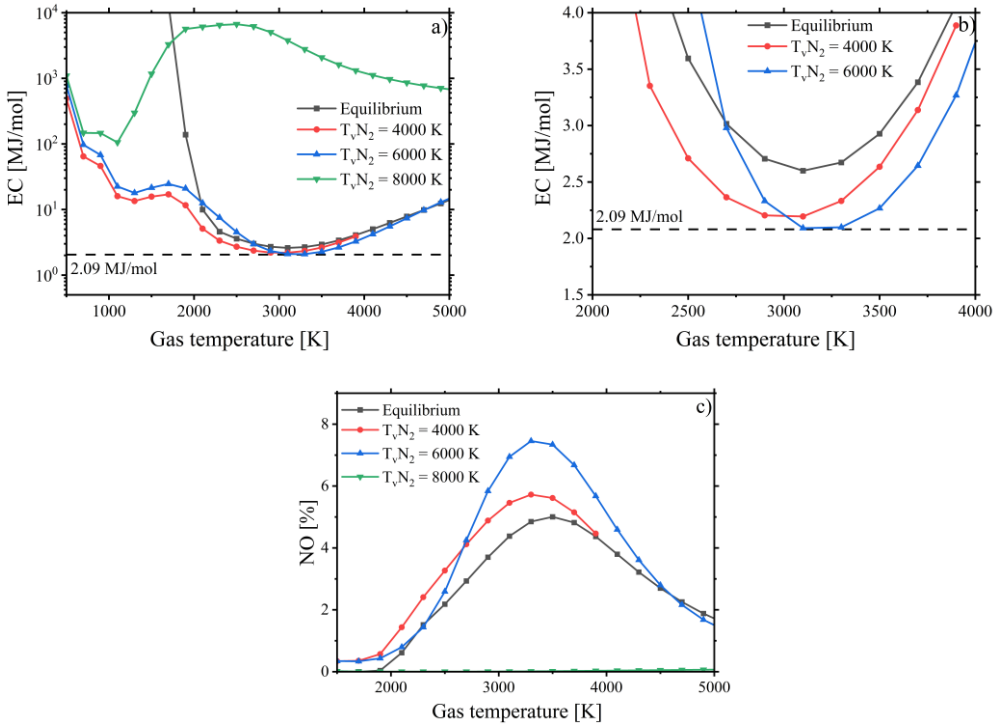

Figure 5.1. EC (a, b) and NO concentration (c) as a function of T_g, for T_vN_2 of 4000 K, 6000 K and 8000 K, as well as for thermal equilibrium.

The minimum EC for T_vN_2 = 4000 K is 2.19 MJ/(mol N) at T_g = 3100 K (see Figure 5.1b), which is clearly below the minimum EC at thermal equilibrium of 2.6 MJ/(mol N). When T_vN_2 is elevated to 6000 K, the EC in the range of 500 – 2900 K is higher than that of T_vN_2 = 4000 K, and it is even higher than the thermal equilibrium EC between T_g = 2100 K and 2500 K. Above 2500 K, the EC quickly decreases, reaching the lowest value for the steady state solution of all conditions investigated, namely 2.09 MJ/(mol N) (see Figure 5.1b). Above 3100 K, the EC continues to be lower than the thermal equilibrium EC, until reaching T_g = 4500 K, where both values equal each other.

These results are also reflected in the NO concentration (Figure 5.1 c). We can see that the NO concentration reaches a maximum value of 7.45 % for T_vN_2 = 6000 K, and 5.73 % for T_vN_2 = 4000 K, both at T_g = 3300 K. This maximum value is shifted towards lower temperature compared to the maximum value at thermal equilibrium, which occurs at T_g = 3500 K and is equal to 5 %. At the temperature of the lowest EC (i.e., 3100 K), the NO concentration is 6.94 % and 5.45 %, for T_vN_2 = 6000 K and 4000 K, respectively, while it is 4.38 % for the thermal equilibrium calculation. Interestingly, for T_vN_2 = 8000 K, there is barely any NO produced (Figure 5.1 c). As a result, the EC is extremely high in the full temperature range (Figure 5.1 a).

To explain these results, we investigated how R5.11 and R5.12 change as a function of T_g for the most efficient condition of Figure 5.1 (T_vN_2 = 6000 K) and for the condition at which no NO was produced (T_vN_2 = 8000 K). In Figure 5.2 we present the absolute reaction rates of R5.11 and R5.12, both in forward and reverse direction, as a function of T_g, for (a) T_vN_2 = 6000 K and (b) T_vN_2 = 8000 K. Note that the total rate of both forward reactions is always equal to the total rate of both reverse reactions in steady state, as there is no net NO formation anymore at steady state.

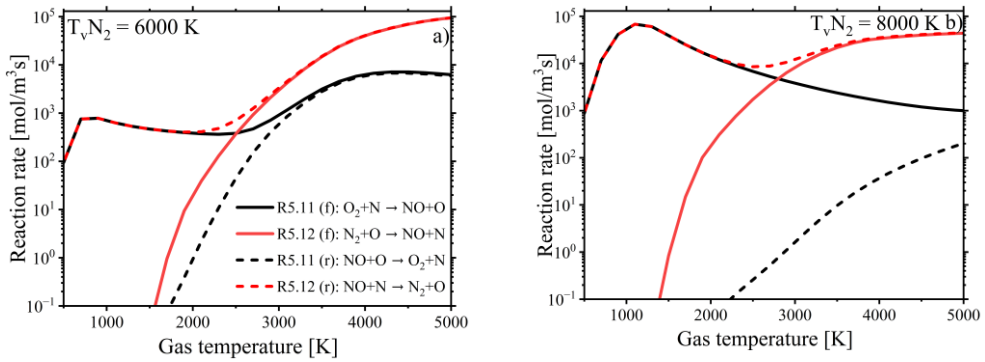

Figure 5.2. Absolute reaction rates of R5.11 ($O_2 + N \rightleftharpoons NO+O$) and R5.12 ($N_2 + O \rightleftharpoons NO+N$), in both forward (solid lines) and reverse (dashed lines) direction, for (a) T_vN_2 = 6000 K and (b) T_vN_2 = 8000 K.

Both when T_vN_2 is 6000 and 8000 K, and in the low gas temperature region from 500 to 2300 K, the production of NO is driven by the forward rate of R5.11, while the destruction is driven by the reverse rate of R5.12 (Figure 5.2 a, b). This is because N_2 is dissociated as a result of R5.1-R5.5, and despite the fact that the energy barrier of R5.12 is reduced as a result of the VT non-equilibrium, this is still not enough to significantly enhance the rate. In addition, at these lower gas temperatures, the reverse rate coefficient of R5.12 is high compared to the forward rate coefficient of R5.11, which has a significantly higher energy barrier, leading to low NO concentrations. As T_g further increases, the forward rate of R5.11 becomes less significant due to depletion of O_2, while the forward rate of R5.12 increases, because at these high gas temperatures there is more energy to overcome the reaction barrier with the help of VT non-equilibrium.

For our most efficient condition of T_g = 3100 K, and T_vN_2 is 6000 K (Figure 5.2a), the forward rate of R5.12 is nearly four times higher than the forward rate of R5.11. When the gas temperature is even higher, the N atom density increases further, and the reverse rate of R5.12 rises faster than the forward rate of R5.11, due to depletion of O_2. Importantly, the increase in forward rate of R5.12 is not stronger anymore than the increase in reverse rate of R5.12, due to the elevated N atom fraction, leading to faster destruction of NO and lower steady state NO concentrations, as observed in Figure 5.1c above.

When T_vN_2 is 8000 K (Figure 5.2 b), the effect is even more pronounced, i.e., the N atom density increases significantly due to more (vibrationally-enhanced) N_2 dissociation, and this high N atom density is detrimental. Indeed, similar to the higher destruction of NO at higher gas temperatures for T_vN_2 of 6000 K, this results in lower steady state NO concentrations, even at lower T_g, which is reflected in the extremely high EC and low NO concentration across the entire T_g range in Figure 5.1 (a, c) , due to the high reverse rate of R5.12 and the limited action of the forward rate of R5.11 (because of the depleted O_2). It is thus clear that significantly elevating the vibrational temperature with respect to the gas temperature, i.e., T_vN_2 above 6000 K, is not beneficial for NF.

5.4.2 Evaluating the minimum EC for NF as a function of time, neglecting VT relaxation: Optimum duration of the VT non-equilibrium

The steady state conditions help us identify which temperature range (both T_g and T_vN_2) is most suitable for energy-efficient NF in atmospheric pressure air plasma, but they do not give information on how the system evolves in time. For this purpose, we performed transient simulations, in which we again kept the temperatures fixed, hence again neglecting VT relaxation and only solving for the species continuity equations as a

function of time. Determining the time at which the NO concentration reaches stable values will allow us to establish suitable pulse duration or residence time, which can be targeted experimentally (assuming that VT non-equilibrium can be maintained during these pulses). As mentioned in the Introduction, the pulse lengths investigated until now were not deliberately chosen to maximize the potential of VT non-equilibrium for NF, but seem to be chosen more or less arbitrarily.

Figure 5.3 presents (a) the calculated EC, NO, N and O mole fractions, and (b) the absolute rates of R5.11 and R5.12, as a function of time for $T_g = T_vO_2 = T_vNO$ = 3100 K (where the minimum EC is reached at steady state) and T_vN_2 = 6000 K. We present the values for T_vN_2 = 6000 K, since it is the most efficient condition for our investigation, based on Figure 5.1(a,b). We see that the EC reaches a minimum of 1.82 MJ/(mol N) at t = 1.65×10^{-4} s. After this time, the EC increases, reaching its steady state value of 2.09 MJ/(mol N). Surprisingly, the EC is below 2 MJ/(mol N) between t = 5.5×10^{-5} s and 8.25×10^{-4} s. The lowest EC value corresponds to an NO concentration of 8.33 %.

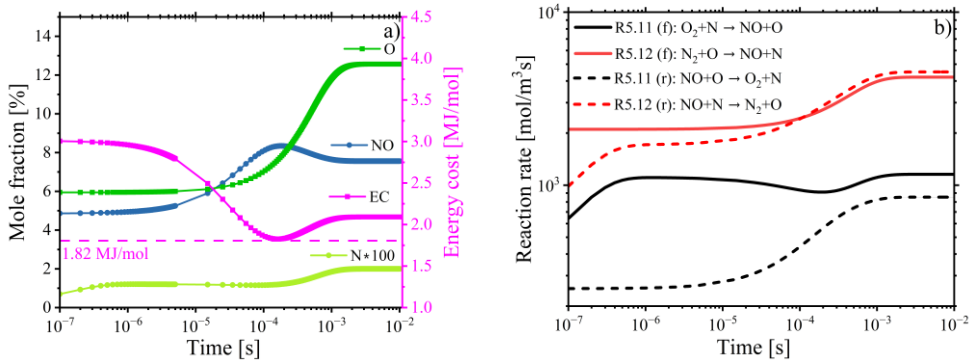

Figure 5.3. Calculated EC, NO, N and O mole fractions (a), and absolute rates of R5.11 and R5.12 (in both forward (solid lines) and reverse (dashed lines) direction (b), as function of time for $T_g = T_vO_2 = T_vNO$ = 3100 K and T_vN_2 = 6000 K.

When looking at the absolute rates of R5.11 and R5.12 as a function of time (Figure 5.3b), we can see that in the region of t = 1×10^{-7} – 7.5×10^{-5} s, both forward rates contribute to NO production (although the rate of R5.12 is clearly higher than of R5.11), while destruction proceeds mainly through the reverse of R5.12. When the O atom density increases (Figure 5.3a), the forward rate of R5.12 is further enhanced, leading to significant NO production until we reach the maximum NO density at t = 1.65×10^{-4} s. However, due to the accumulation of N and O atoms in the system (Figure 5.3a), the reverse rates of R5.11 and R5.12 increase (Figure 5.3b), after which the NO concentration starts decreasing until reaching steady state.

These results suggest that when we use pulsed plasmas in air at atmospheric pressure to create VT non-equilibrium, the pulse duration has to be longer than 5.5×10^{-5} s (i.e., 55 μs) in order to observe significant improvement in NO formation and EC, assuming indeed that this VT non-equilibrium can be sustained during the pulse, as is the case in these simulations. Qiao *et al.* investigated an air plasma at atmospheric pressure with pulses of 2×10^{-4} s, in which T_vN_2 was slightly above 5000 K and T_g was 3500 K [186]. Their results suggest that conditions for the lowest possible EC are indeed possible in air plasmas at atmospheric pressure for long pulses (order of 200 μs). Despite the fact that the authors did not measure the NO concentration in their experiment, we believe that such conditions will be ideal for NF under VT non-equilibrium. Our time-dependent results show that the minimum EC in atmospheric pressure air plasma is 1.82 MJ/(mol N), achieved at $t = 1.65\times10^{-4}$ s.

Although we now evaluated the conditions for the theoretical most efficient EC, it is important to stress that our model does not calculate what energy is needed to sustain the VT non-equilibrium at such high T_g, since we keep T_vN_2 and T_g constant. Indeed, the dominant VT relaxation process is upon collision with O atoms, which directly competes with R5.12 (i.e., NO formation by the second Zeldovich reaction), and this could significantly limit the efficiency of the system. In order to estimate this energy, we integrated Q_{VT} as a function of time until the point of the lowest EC, i.e., $t = 1.65\times10^{-4}$ s. Our results show that the energy needed to sustain this level of VT non-equilibrium is 3.8 times higher (0.57 MJ/(mol N)) than the enthalpy of the system (0.15 MJ/(mol N), used to calculate the EC, eq. 5.10-5.11 above), which means that most of the vibrational energy will be lost by VT relaxation instead of being channeled to NO formation. In other words, the minimum EC of 1.82 MJ/(mol N) cannot be achieved in practice in atmospheric pressure pulsed air plasma, unless VT relaxation would be slowed down significantly, so that more energy can be channeled into R5.12. This would, however, be very challenging, because actions to slow down the VT relaxation would at the same time negatively affect R5.12. In summary, our model predicts that elevated NO concentration (up to 8.33 %) can be obtained for pulses longer than 55 μs, but the EC will always be higher than 1.82 MJ/(mol N).

5.4.3 Evaluating the minimum EC for NF as a function of time, accounting for VT relaxation after short (ns) pulses: The optimum condition corresponds to (VT) thermal equilibrium but chemical non-equilibrium

To evaluate whether ns-pulsed plasmas can reach a very low EC based on VT non-equilibrium, we performed transient simulations considering all possible processes,

including VT relaxation and all possible vibrational energy transfers. For this purpose, we selected the most efficient condition for the steady state and transient simulations, highlighted in Figure 5.1 and Figure 5.3, i.e., T_vN_2 = 6000 K and Tg = 3100 K, as initial temperatures, and we calculate how the species densities, as well as T_vN_2, T_vO_2, T_vNO and T_g evolve with time. Since the air mixture is partially dissociated at 3100 K (i.e. the O mole fraction is 6 %), we can expect VT relaxation to be fast because of the high O atom density, which provides the fastest channel for VT relaxation of N_2. Hence, VT non-equilibrium will not last very long, so we do not expect a low EC due to the vibrationally-enhanced Zeldovich mechanism. Surprisingly however, Abdelaziz *et al.* achieved a very low EC of 1.6 MJ/(mol N) in a 10 ns-pulsed plasma in oxygen-enriched air [60]. The question thus arises: which mechanism, if not the vibrationally-enhanced Zeldovich mechanism, can explain this low EC in ns-pulsed plasmas.

In order to determine the potential of ns-pulsed plasmas for achieving very low EC, we set the initial composition equal to the thermodynamic equilibrium composition at 3100 K, and we define an elevated temperature of T_vN_2 = either 6000 K or 8000 K as initial condition, hence starting from VT non-equilibrium. Then we examine how the composition and temperature evolve with time, when VT relaxation and vibrational energy exchange during chemical reactions are included in the simulation.

Figure 5.4 presents T_vN_2, T_vO_2, T_vNO, T_g and the EC as a function of time, for initial T_vN_2 of 6000 K (a) and 8000 K (b). Interestingly, we can see that T_vN_2 reaches equilibrium within 2.5×10^{-5} s when T_vN_2 starts from both 6000 K and 8000 K, indicating that the initial T_vN_2 has only a weak influence on the relaxation time, which seems to be predominantly driven by T_g. When T_vN_2 = 8000 K, T_vO_2 drops slightly below the gas temperature at 1×10^{-6} s, due to energy exchange resulting from R5.11, indicating fast production of NO. Despite this, the minimum EC is not reached in this non-equilibrium phase, but only at t = 1.3×10^{-4} s for T_vN_2 = 6000 K, reaching a value of 2.3 MJ/(mol N) (Figure 5.4 a) and at t = 7.5×10^{-5} s for T_vN_2 = 8000 K, reaching a value of 2.17 MJ/(mol N) (Figure 5.4 b). The fact that the latter condition reaches the minimum EC earlier in time is due to the higher T_g, resulting from relaxing the additional vibrational energy at the start of the simulation. At both conditions, the minimum EC is reached at a time when $T_vN_2 = T_vO_2 = T_vNO = T_g$, and not during VT non-equilibrium.

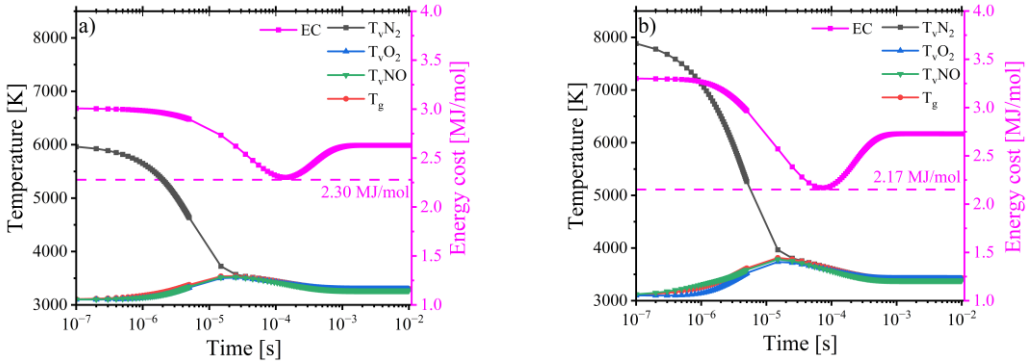

Figure 5.4. T_vN_2, T_vO_2, T_vNO, T_g and the EC as a function of time for initial T_vN_2 of 6000 K (a) and 8000 K (b).

Our initial analysis, at steady state conditions (section 5.4.1 above), indicated that elevating the vibrational temperature above 6000 K would destroy the NO through the reverse reaction R5.12 and the depletion of O_2. Interestingly, this is not the case for the transient simulations with VT relaxation included. Figure 5.5 presents the calculated mole fractions of N, O and NO for T_vN_2 = 6000 K (a) and 8000 K (b).

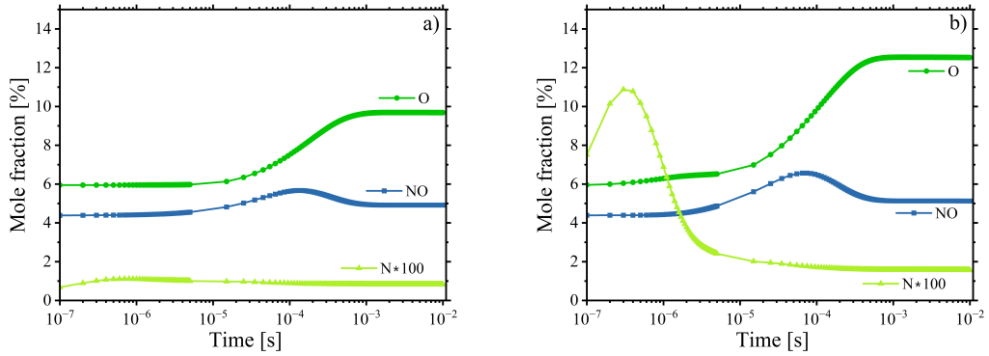

Figure 5.5. Mole fractions of N (multiplied by 100), O and NO, for initial T_vN_2 =6000 K (a) and 8000 K (b).

NO cannot be formed efficiently within the short timescales over which the VT non-equilibrium can exist (1×10^{-7}-2.5×10^{-5}; cf. Figure 5.5). Until t = 2.5×10^{-5} s (i.e., the end of VT non-equilibrium; cf. Figure 5.4 above), the N atom density is much lower for T_vN_2 = 6000 K (Figure 5.5 a) compared to T_vN_2 = 8000 K (Figure 5.5 b), demonstrating the higher N_2 dissociation degree at higher T_vN_2. Despite this, also as T_vN_2 = 8000 K, nearly all of the N atoms recombine to N_2 before the maximum NO density is reached, indicating that they play a negligible role in NO formation. These results strongly suggest that the NO formed under these ns-pulsed plasma conditions is not created through the vibrationally-enhanced Zeldovich mechanism, because at this stage there is no VT non-

equilibrium anymore, and the species created during the VT non-equilibrium phase have already recombined.

Instead, our results highlight a new effect, namely thermal production of NO in a chemical non-equilibrium system. Since the gas temperature increases very fast (cf. the time-scale in Figure 5.4), this leads to an increase in the forward rates of R5.11 and R5.12, while the densities of N and O are still too low to activate the reverse reactions. As a result, we observe an increase in NO density, until the N and O atoms reach their equilibrium values, causing a rise in the reverse rates and destruction of the formed NO. The EC is now lower for T_vN_2 = 8000 K since the gas temperature reaches higher values as a result of the fast VT relaxation.

To verify our hypothesis, we performed the same simulation, but assuming that all of our reactions (R5.1-R5.12) only depend on T_g and not on T_vN_2, T_vO_2 or T_vNO, so they are not affected by VT non-equilibrium. Figure 5.6 presents the EC, and the NO, N and O mole fractions, as a function of time for T_vN_2 = 8000 K, when R5.1-5.12 only depend on T_g. The minimum EC is again reached at t = 7.5×10^{-5} s, but it is slightly elevated to 2.24 MJ/(mol N), compared to 2.17 MJ/(mol N) in Figure 5.4b (where R5.11 and R5.12 were also affected by T_vN_2, T_vO_2 or T_vNO, thus allowing reduction of the energy barrier by vibrational excitation). The O atom density during this simulation is practically the same as in Figure 5.5b, but the peak in N atom density in the beginning of the simulation is gone, since this was a result of R5.1-R5.5 being a function of both T_vN_2 and T_g. This result proves that all of the N atoms recombine back to N_2 because of the fast reverse reactions (R5.1-R5.5).

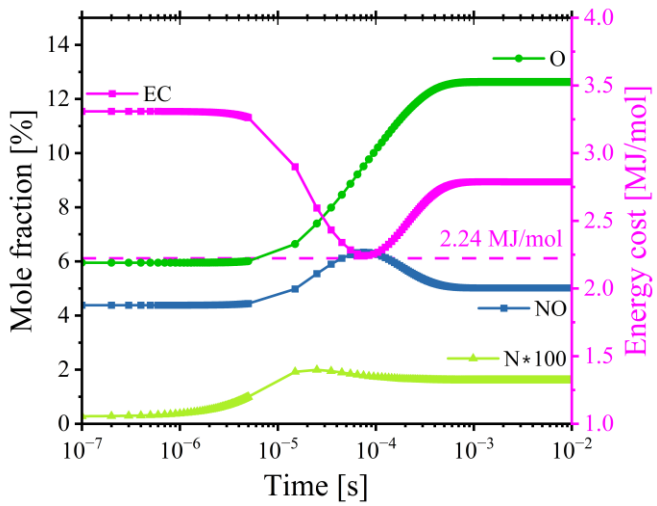

Figure 5.6. EC, NO, N and O mole fractions, as a function of time for T_vN_2=8000 K, when R5.1-R5.12 only depend on T_g and are not affected by VT non-equilibrium.

Hence, in ns-pulsed plasmas, VT non-equilibrium plays a negligible role in enhancing NF. The fast gas heating creates a state of chemical non-equilibrium, where the species densities have not yet reached steady state, because the forward and reverse reactions are not yet equal to each other. This chemical non-equilibrium seems to provide a more efficient thermal pathway for NF. It is well established in literature that thermal NF is more efficient at an N_2/O_2 ratio of 1 [57, 59, 172], and since we show ns-pulsed plasma is driven by thermal effects under chemical non-equilibrium, we believe the typical strategies of increasing pressure and enriching the gas with O_2 should also give better results. Since the N_2/O_2 ratio was equal to 1 in the study by Abdelaziz *et al.*[60], VT relaxation occurs more rapidly due to the higher O atom fraction, and it is unlikely that VT non-equilibrium influences the Zeldovich mechanism at those conditions. Hence, the low value of 1.6 MJ/(mol N) reported in their paper is likely due to chemical non-equilibrium effects combined with the oxygen-enriched gas, rather than VT non-equilibrium.

The ns-pulsed plasmas are thus significantly different from the μs-pulsed plasmas (with pulses of around 200 μs), like the ones investigated by Qiao *et al.* [186], in atmospheric pressure, where VT non-equilibrium was sustained during the pulses. We believe that this effect of chemical non-equilibrium at thermal equilibrium for ns-pulsed plasmas has been overlooked in literature and can potentially enable a new route towards efficient NF, through short pulsing.

5.4.4 Comparison with the work of Rusanov *et al*. [62]: Redefining the theoretical minimum EC

Finally, we want to stress that, for the conditions investigated in this chapter, even considering strong VT non-equilibrium, we could not reach an EC as low as 0.2 MJ/(mol N) at atmospheric pressure, as reported by Rusanov *et al.* [62]. Many papers on plasma-based NF use this value as the theoretical minimum, even at atmospheric pressure (although it was reported for low pressure) and as a benchmark value for the technology [18, 57, 180, 181]. The experiments described by Rusanov *et al.* achieved such remarkable values in an electron-cyclotron resonance (ECR) microwave plasma in a pressure range of 10 – 100 Torr and an N_2/O_2 ratio of 1 [62]. In order to explain these results, the authors constructed a theoretical framework, assuming that the system cannot equilibrate, similar to the assumption we made in section 5.4.1 and 5.4.2, but also with the reverse reaction R5.12 assumed to be negligible. Indeed, if we neglect the

reverse reaction of R5.12 (i.e., N recombination with NO), our model also predicts such a low EC. However, our results show that the reverse reaction R5.12 is extremely important at atmospheric pressure.

Additionally, as a result of neglecting this reverse reaction, the critical T_g beyond which the EC starts to increase (after its minimum value of 0.2 MJ/(mol N)) was estimated by Rusanov *et al.* to be 1500 K [62]. Our new model results show that T_g in fact has to be twice as high (i.e., 3100 K) in order for the process to reach the minimum EC.

Furthermore, the additional N atoms produced due to the VT non-equilibrium dissociation of N_2 further promote the reverse reaction R5.12, which makes the strong VT non-equilibrium conditions not beneficial. Our model predicts that the theoretical minimum EC for NF in atmospheric pressure air plasma is 1.82 MJ/(mol N), assuming that VT non-equilibrium can be sustained, but it is unlikely that this value can be achieved in practice, because of the much faster VT relaxation, which increases the energy consumption of the system. Therefore, a more realistic minimum EC, accounting for VT relaxation (which will happen in practice) is 2.17 MJ/(mol N).

5.5 Conclusions

In this chapter, we developed a VT non-equilibrium global model, describing NO formation under conditions with elevated T_vN_2. We used recent rate coefficients based on the Stellar database, averaged over a Boltzmann distribution function of vibrational states as a function of T_v and T_g.

In steady state, our model suggests that the minimum EC for NF in atmospheric pressure air plasmas is achieved at T_vN_2 = 6000 K and $T_vO_2 = T_vNO = T_g$ = 3100 K, with a value of 2.09 MJ/(mol N) for an NO concentration of 7.0 %. This simulation neglects VT relaxation, and thus assumes that VT non-equilibrium can be maintained ($T_vN_2 >> T_vO_2 = T_vNO = T_g$). When simulating the process as a function of time, again neglecting VT relaxation, and thus assuming that VT non-equilibrium can be maintained, e.g., during long (> 55 μs) pulses, the minimum EC is predicted to be 1.82 MJ/(mol N), and it is reached at 165 μs. Despite the fact that similar T_vN_2 and T_g were already experimentally achieved in μs-pulsed atmospheric pressure air plasmas in literature [186], when we take into account the energy needed to sustain this VT non-equilibrium, it is in fact impossible to reach this EC. When T_vN_2 is even higher (8000 K), the reverse reaction of R5.12 (i.e., recombination of N with NO) leads to almost complete destruction of the formed NO and a rise in the EC, due to the significant number of N atoms formed at these conditions (upon vibrationally-induced dissociation of N_2).

When simulating the process as a function of time, and including VT relaxation and other vibrational energy exchanges due to chemical reactions, hence corresponding to more realistic conditions, e.g., mimicking ns-pulsed plasmas where VT relaxation occurs after the pulses, our model predicts a higher minimum EC of 2.17 MJ/(mol N), with initial T_vN_2 = 8000 K and initial T_vO_2 = T_vNO = T_g = 3100 K. Our model further reveals that the mechanism for NO formation under these conditions is different from the mechanism at μs timescales, where VT non-equilibrium can be maintained over a longer time (due to the longer pulse duration). Indeed, in ns-pulsed plasmas, our model reveals that NO is formed mostly under (VT) thermal equilibrium (i.e., no vibrationally-enhanced Zeldovich mechanism and no vibrationally-enhanced dissociation), resulting in thermal equilibrium production, but under chemical non-equilibrium conditions (i.e., when the species densities have not yet reached steady state). Indeed, due to the fast gas heating, there is net production of NO, resulting from the rise in rate coefficients with T_g. We believe this effect has been overlooked in literature and presents new opportunities to push the boundaries of the EC for plasma based NF, specifically in ns-pulsed plasmas.

Importantly, our model predicts that for atmospheric pressure air plasmas, the theoretical EC limit of 0.2 MJ/(mol N), predicted by Rusanov *et al.* [62], cannot be achieved, due to the importance of the reverse reaction R5.12: N + NO → N_2 + O, which was neglected by Rusanov *et al.* in their previous analysis. Hence, researchers should not use this value as the theoretical minimum, and benchmark value, for plasma-based NF.

Finally, although our predicted minimum EC of 1.82 MJ/(mol N) (assuming VT non-equilibrium can be maintained) or 2.17 MJ/(mol N) (in case of VT (thermal) equilibrium but chemical non-equilibrium) is higher than the evaluation by Rouwenhorst *et al.* for plasma-based NF to be commercially competitive with the Haber-Bosch + Ostwald process (corresponding to a target of 1-1.5 MJ/(mol N)) [61], we believe the EC can be further reduced, e.g., by applying heat recovery for gas preheating, or operating at a higher N_2/O_2 ratio and higher pressure for a ns-pulsed plasma.

Chapter 6.
Overall conclusions and outlook for future work

In this thesis, we investigated the processes of plasma-based NF, with one chapter focusing on plasma-based CO_2 conversion, which typically uses the same plasma types and proceeds through similar mechanisms. We focused on the fundamental principles determining the plasma efficiency and laid the foundations for reaching low EC for NF. Here we summarize our main results and provide an outlook of where the field of plasma-based NF should be focusing on in the future.

In **Chapter 2**, we developed the first self-consistent axisymmetric 2D CFD model for a N_2 DC plasma. Our model reveals that the electron emission mechanisms on the cathode surface do not influence the positive column of the plasma at atmospheric pressure. Importantly, the additional voltage required to sustain the glow regime leads to higher deposited power in the plasma, without changing any of the plasma parameters. As a result, gas conversion processes will not benefit from sustaining the glow regime and arc discharge plasma will present better efficiency. In addition, the model predicts that plasma contraction mainly results from the high velocity flow in the periphery, meaning that high flow rates will inevitably lead to less gas being treated by the plasma. These important conclusions are very valuable for future plasma reactor designs. No special care should be taken in order to sustain the glow regime, and large volume plasma discharges can be sustained by using segmented cathodes.

In **Chapter 3**, we explored elevating the pressure in an RGA plasma reactor from 0 to 3 barg. We observed a clear improvement in the performance metrics, with the EC dropping to 1.8 MJ/(mol N) and achieving a high PR of 69 g/h, with an N_2/O_2 ratio of 1. These results clearly demonstrate the potential of high pressure arc plasma for industrial application, since it eliminates the inverse correlation between PR and EC. Increasing the pressure presents a new pathway towards energy-efficient NF, which was not considered before.

In **Chapter 4**, we introduced a new approach to modeling the vibrational degrees of freedom; the model is developed for CO_2 plasmas, for which clear benchmark experiments were available, but it can also be applied to air plasmas for NF. Our fully self-consistent kinetic model captures both vibrational and gas heating kinetics in a

pulsed CO_2 glow discharge at low pressure. By incorporating separate energy balance equations for vibrational, gas, and electron temperatures, the model provides a novel, self-consistent treatment of electron kinetics through coupling with an electrical circuit. Validation against experimental measurements of the temporal evolution of CO_2 vibrational temperature and gas temperature showed good agreement, laying the groundwork for advanced multidimensional plasma models with integrated vibrational kinetics.

In **Chapter 5**, we developed a VT non-equilibrium global model for NO formation in atmospheric pressure air plasmas with elevated T_vN_2, following the same concept as the model of Chapter 4. Using updated rate coefficients from the Stellar database, the model predicts a minimum EC of 2.09 MJ/(mol N) for 7% NO concentration under steady state conditions. Our time-dependent simulations predict even a lower EC of 1.82 MJ/(mol N), but this value is practically unachievable due to the high energy needed to maintain VT non-equilibrium. In conditions similar to ns-pulsed plasmas, the minimum EC increases to 2.17 MJ/(mol N), but our model reveals a new mechanism – thermal NO production under chemical non-equilibrium. We further show that the theoretical EC limit of 0.2 MJ/(mol N) proposed by Rusanov *et al.*, neglected the impact of the reverse Zeldovich reaction $N + NO \rightarrow N_2 + O$, which is very important, and including this reaction, it is clear that such low EC cannot be achieved at atmospheric pressure.

Overall, this thesis lays the foundations for further pushing the limits of NF, and other gas conversion applications, such as CO_2 conversion, by developing a new modelling approach (i.e. **Chapter 4** and **Chapter 5**), which account for the vibrational kinetics with limited computational cost, and can therefore be integrated in CFD plasma modelling (as presented in **Chapter 2**). CFD modelling is essential for understanding the complexity of the plasma behavior, and designing new and efficient plasma reactors, for later commercial applications.

This thesis also reveals a clear pathway towards optimization of plasma-based NF, by showing four key factors:

1) DC plasmas in arc regime are more efficient than in glow regime, if operated under the same conditions.
2) Increasing the pressure in a plasma reactor can lead to a clear reduction in the EC (achieving values as low as 1.8 MJ/(mol N)), without sacrificing the PR.
3) The minimum EC determined by Rusanov *et al.* of 0.2 MJ/(mol N) cannot be achieved at atmospheric pressure, and a more realistic value is 2.17 MJ/(mol N).
4) Fast gas heating (as a result of ns-pulsed discharge) creates chemical non-equilibrium, which reduces the EC for NF at atmospheric pressure.

There is still a lot of work to be performed in order to reach the 1-1.5 MJ/(mol N) target, evaluated by Rouwenhorst *et al.* as the minimum EC needed for plasma-based NF to be

competitive with the HB-Ostwald process. In this thesis, we highlighted some important aspects, needed for designing improved plasma reactors that can yield better performance. We developed the foundations of modelling improved plasma reactors using CFD, which can be obtained by combining the models developed in **Chapter 2, 4 and 5**. Furthermore, our model reveals that in order to further reduce the EC, we need to employ short pulsing, creating a plasma arc, which establishes chemical non-equilibrium, instead of trying to create VT non-equilibrium at atmospheric pressure. In addition, energy recovery in the form of gas preheating, using the hot gas leaving the plasma reactor, can potentially further reduce the EC. We believe that this strategy, in combination with high pressure and oxygen enrichment, may lead to energy-efficient plasma-based NF, which can hopefully compete with the HB-Ostwald process.

Appendix

Appendix A, belonging to Chapter 2

A1 – Chemical reactions included in the N_2 model of Chapter 2

Table A1 Electron impact reactions

Reaction		Rate coefficient[a,b] [$m^3\ s^{-1}$]	Ref.
R2.1	$e + N_2 \rightarrow e + N_2$	$k_1 = f(E/N)$	31, 190
R2.2	$e + N_2 \rightarrow e + N_2(X, v \leq 8)$	$k_2 = f(E/N)$	31, 190
R2.3	$e + N_2 \rightleftharpoons e + N_2(A^3\Sigma_u^+)$	$k_3 = f(E/N)$	31, 190
R2.4	$e + N_2 \rightleftharpoons e + N_2(B^3\Pi_g)$	$k_4 = f(E/N)$	31, 190
R2.5	$e + N_2 \rightleftharpoons e + N_2\ (a'^1\Sigma_u^-)$	$k_5 = f(E/N)$	31, 190
R2.6	$e + N_2 \rightleftharpoons e + N_2(C^3\Pi_u)$	$k_6 = f(E/N)$	31, 190
R2.7	$e + N_2(X, v) \rightarrow e + e + N_2^+$	$k_7 = f(E/N)$	31, 190
R2.8	$e + N_2(X, v) \rightarrow e + N + N(^2D)$	$k_8 = f(E/N)$	31, 190
R2.9	$e + N \rightarrow e + N$	$k_9 = f(E/N)$	191, 192
R2.10	$e + N \rightleftharpoons e + N(^2D)$	$k_{10} = f(E/N)$	191, 192
R2.11	$e + N \rightleftharpoons e + N(^2P)$	$k_{11} = f(E/N)$	191, 192
R2.12	$e + N \rightarrow e + e + N^+$	$k_{12} = f(E/N)$	191, 192

[a] The rate coefficient of the reverse process is calculated by the principle of detailed balance.

[b] The rate coefficient is calculated after integrating the cross section $\sigma_k(\varepsilon)$ by an electron energy distribution function calculated using BOLSIG+ [31].

Table A2 Ion conversion reactions

Reaction		Rate coefficient[c] [$m^3\ s^{-1}$][d]	Ref.
R2.13	$N + N_2^+ \rightarrow N^+ + N_2$	$k_{13} = 7.2 \times 10^{-19}(T_g/300)$	69
R2.14	$N^+ + N_2 \rightarrow N + N_2^+$	$k_{14} = 1.0 \times 10^{-18}$	69
R2.15[d]	$N_2 + N_2 + N^+ \rightarrow N_2 + N_3^+$	$k_{15} = 1.7 \times 10^{-41}(300/T_g)^{2.1}$	69
R2.16[d]	$N_2 + N_2 + N_2^+ \rightarrow N_2 + N_4^+$	$k_{16} = 5.2 \times 10^{-41}(300/T_g)^{2.2}$	69
R2.17	$N_2(A^3\Sigma_u^+) + N_2^+ \rightarrow N + N_3^+$	$k_{17} = 3.0 \times 10^{-16}$	69

R2.18	$N + N_3^+ \rightarrow N_2 + N_2^+$	$k_{18} = 6 \times 10^{-17}$	69
R2.19	$N_2 + N_3^+ \rightarrow N_2 + N_2 + N^+$	$k_{19} = 6.0 \times 10^{-16} \exp(-17000/(T_g + T_v))$	193
R2.20	$N_2(A^3\Sigma_u^+) + N_3^+ \rightarrow N_2 + N_2 + N^+$	$k_{20} = 6.0 \times 10^{-16}$	64
R2.21	$N + N_4^+ \rightarrow N_2 + N_3^+$	$k_{21} = 1.0 \times 10^{-15}$	69
R2.22	$N + N_4^+ \rightarrow N_2 + N_2 + N^+$	$k_{22} = 1.0 \times 10^{-17}$	69
R2.23	$N_2 + N_4^+ \rightarrow N_2 + N_2 + N_2^+$	$k_{23} = 8.1 \times 10^{-17} \exp(-4842/(T_g + T_v))$	193

[c] In the expressions for the reaction coefficients, T_g is in [K].

[d] The units of the rate coefficients for these three-body reactions are [$m^6 s^{-1}$].

Table A3 Associative ionization and Penning ionization reactions

Associative ionization		Rate coefficient[c] [$m^3 s^{-1}$]	Ref.
R2.24	$N(^2D) + N(^2P) \rightarrow N_2^+ + e$	$k_{24} = 1.92 \times 10^{-21} T_g^{0.98} [1 - \exp(-3129/T_g)]^{-1}$	69
R2.25	$N(^2P) + N(^2P) \rightarrow N_2^+ + e$	$k_{25} = 3.2 \times 10^{-21} T_g^{0.98} [1 - \exp(-3129/T_g]^{-1}$	69
R2.26	$N_2\left(a'^1\Sigma_u^-\right) + N(^2P) \rightarrow N_3^+ + e$	$k_{26} = 1 \times 10^{-17}$	69
R2.27	$N_2(A^3\Sigma_u^+) + N_2\left(a'^1\Sigma_u^-\right) \rightarrow N_4^+ + e$	$k_{27} = 0.5 \times 5 \times 10^{-17}$	69
R2.28	$N_2\left(a'^1\Sigma_u^-\right) + N_2\left(a'^1\Sigma_u^-\right) \rightarrow N_4^+ + e$	$k_{28} = 0.5 \times 2 \times 10^{-16}$	69
Penning ionization			

R2.29	$N_2(A^3\Sigma_u^+) + N_2\left(a'^1\Sigma_u^-\right) \rightarrow N_2^+ + N_2 + e$	$k_{29} = 0.5 \times 5 \times 10^{-17}$	69
R2.30	$N_2\left(a'^1\Sigma_u^-\right) + N_2\left(a'^1\Sigma_u^-\right) \rightarrow N_2^+ + N_2 + e$	$k_{30} = 0.5 \times 2 \times 10^{-16}$	69

[c] In the expressions for the reaction coefficients, T_g is in [K].

Table A4 Electron-ion recombination reactions

Reaction		Rate coefficient[e] [$m^3 s^{-1}$]	Ref.
R2.31	$e + N_2^+ \rightarrow N + N(^2D)$	$k_{31} = 0.11 \times 2 \times 10^{-13}(300/T_e)^{0.5}$	69
R2.32	$e + N_2^+ \rightarrow N + N(^2P)$	$k_{32} = 0.77 \times 2 \times 10^{-13}(300/T_e)^{0.5}$	69
R2.33	$e + N_2^+ \rightarrow N(^2D) + N(^2D)$	$k_{33} = 0.11 \times 2 \times 10^{-13}(300/T_e)^{0.5}$	69
R2.34[d]	$e + N_2 + N_2^+ \rightarrow N_2 + N_2$	$k_{34} = 6 \times 10^{-39}(300/T_e)^{1.5}$	64
R2.35	$e + N^+ \rightarrow N$	$k_{35} = 7 \times 10^{-18}$	64
R2.36[d]	$e + e + N^+ \rightarrow e + N$	$k_{36} = 7.0 \times 10^{-32}(300/T_e)^{4.5}$	64
R2.37[d]	$e + e + N_2^+ \rightarrow N_2 + e$	$k_{37} = 1.0 \times 10^{-31}(300/T_e)^{4.5}$	69
R2.38[d]	$e + N_2 + N^+ \rightarrow N_2 + N$	$k_{38} = 6.07 \times 10^{-34} {T_e}^{-2.5}$	69
R2.39	$e + N_3^+ \rightarrow N_2 + N$	$k_{39} = 2.0 \times 10^{-13}(300/T_e)^{0.5}$	69
R2.40	$e + N_4^+ \rightarrow N_2 + N_2$	$k_{40} = 2.0 \times 10^{-12}(300/T_e)^{0.5}$	69

[d] The units of the rate coefficients of these three-body reactions are [$m^6 s^{-1}$].

[e] In the expressions for the reaction coefficients, T_e is in [K].

Table A5 Thermal dissociation and three-body recombination reactions

Thermal dissociation & three-body recombination		Rate coefficient[c] [$m^3 s^{-1}$][d,f]	Ref.
R2.41	$N_2 + N \rightarrow N + N + N$	$k_{41} = 6.6 \times 5.4 \times 10^{-14} \exp(-113200/T_g)\,[1 - \exp(-3354/T_g)]$	172
R2.42	$N_2 + N_2 \rightarrow N + N + N_2$	$k_{42} = 4.98 \times 10^{-9} T_g^{-1.5} \exp(-113260/T_g)$	69

R2.43[d]	$N + N + N_2 \rightarrow N_2 + N_2$	$k_{43} = 1.91 \times 10^{-45}$	172
R2.44[d]	$N + N + N \rightarrow N + N_2$	$k_{44} = 3 \times 1.8 \times 10^{-45} \exp(435/T_g)$	172
Reactions involving electronically excited molecules and atoms			
R2.45	$N_2(v_1) + N_2(v_2) \rightarrow N_2 + N_2(A^3\Sigma_u^+)$	$k_{45} = 0.5 \times 10^{-22}, v_{1,2} \geq 12$	64
R2.46	$N_2(v_1) + N_2(v_2) \rightarrow N_2 + N_2(B^3\Pi_g)$	$k_{46} = 1 \times 10^{-21}, v_{1,2} \geq 14$	64
R2.47	$N_2(v_1) + N_2(v_2) \rightarrow N_2 + N_2(a'^1\Sigma_u^-)$	$k_{47} = 1 \times 10^{-21}, v_{1,2} \geq 16$	64
R2.48	$N_2(v_1) + N_2(v_2) \rightarrow N_2 + N_2(C^3\Pi_u)$	$k_{48} = 3.25 \times 10^{-23}, v_{1,2} \geq 25$	64
R2.49	$N_2(A^3\Sigma_u^+) + N_2(v+6) \rightarrow N_2(B^3\Pi_g) + N_2(v)$	$k_{49} = 3 \times 10^{-17}$	64
R2.50	$N_2(A^3\Sigma_u^+) + N_2(A^3\Sigma_u^+) \rightarrow N_2 + N_2(B^3\Pi_g)$	$k_{50} = 3.0 \times 10^{-16}$	172
R2.51	$N_2(A^3\Sigma_u^+) + N_2(A^3\Sigma_u^+) \rightarrow N_2 + N_2(C^3\Pi_u)$	$k_{51} = 1.6 \times 10^{-16}$	69
R2.52	$N_2(A^3\Sigma_u^+) + N_2 \rightarrow N_2 + N_2$	$k_{52} = 3.0 \times 10^{-22}$	69
R2.53	$N_2(A^3\Sigma_u^+) + N \rightarrow N_2 + N(^2P)$	$k_{53} = 4.0 \times 10^{-17}(300/T_g)^{2/3}$	69
R2.54	$N_2(B^3\Pi_g) + N_2 \rightarrow N_2 + N_2(A^3\Sigma_u^+)$	$k_{54} = 3.0 \times 10^{-17}$	69
R2.55	$N_2(B^3\Pi_g) + N_2 \rightarrow N_2 + N_2$	$k_{55} = 2.0 \times 10^{-18}$	69
R2.56	$N_2(a'^1\Sigma_u^-) + N_2 \rightarrow N_2 + N_2(B^3\Pi_g)$	$k_{56} = 1.9 \times 10^{-19}$	69
R2.57	$N_2(C^3\Pi_u) + N_2 \rightarrow N_2 + N_2(a'^1\Sigma_u^-)$	$k_{57} = 1.0 \times 10^{-17}$	69
R2.58[f]	$N_2(B^3\Pi_g) \rightarrow N_2(A^3\Sigma_u^+) + hv$	$k_{58} = 1.5 \times 10^5$	69

R2.59[f]	$N_2(C^3\Pi_u) \rightarrow N_2(B^3\Pi_g) + hv$	$k_{59} = 2.4 \times 10^7$	64
R2.60[d]	$N + N + N_2 \rightarrow N_2(A^3\Sigma_u^+) + N_2$	$k_{60} = 8.3 \times 10^{-46} \exp(500/T_g)$	69
R2.61	$N(^2D) + N_2 \rightarrow N + N_2$	$k_{61} = 6.0 \times 10^{-21}$	69
R2.62	$N(^2P) + N \rightarrow N(^2D) + N$	$k_{62} = 1.8 \times 10^{-18}$	172
R2.63	$N(^2P) + N_2 \rightarrow N_2 + N$	$k_{63} = 6.0 \times 10^{-20}$	69
R2.64	$N(^2P) + N_2 \rightarrow N_2 + N(^2D)$	$k_{64} = 2.0 \times 10^{-24}$	69

[c] In the expressions for the reaction coefficients, T_g is in [K].

[d] The units of the rate coefficients of these three-body reactions are [$m^6 s^{-1}$].

[f] The units of the rate coefficients of these radiative decay reactions are [s^{-1}].

Table A6 Diffusion coefficients in N_2

Species	Diffusion coefficient [$m^2\,s^{-1}$]	Reference
$N_2(X^1\Sigma_g^+)$, $N_2(A^3\Sigma_u^+)$, $N_2(a'^1\Sigma_u^-)$, $N_2(B^3\Pi_g)$, $N_2(C^3\Pi_u)$	$0.17 \times 10^{-4} \cdot \left(\frac{T}{300\ K}\right)^{1.7816}$	64
$N(^4S)$	$0.28 \times 10^{-4} \cdot \left(\frac{T}{300\ K}\right)^{1.5}$	172
$N(^2D)$	$0.227 \times 10^{-4} \cdot \left(\frac{T}{300\ K}\right)^{1.5}$	172
$N(^2P)$	$0.185 \times 10^{-4} \cdot \left(\frac{T}{300\ K}\right)^{1.5}$	172
N^+	$7.8 \times 10^{-6} \cdot \left(\frac{T}{300\ K}\right)^{1.7816}$	64
N_2^+	$4.8 \times 10^{-6} \cdot \left(\frac{T}{300\ K}\right)^{1.7816}$	64
N_3^+	$4.8 \times 10^{-6} \cdot \left(\frac{T}{300\ K}\right)^{1.7816}$	64
N_4^+	$5.8 \times 10^{-6} \cdot \left(\frac{T}{300\ K}\right)^{1.7816}$	64

A2 - Comparison of the model results of Chapter 2 with experiments

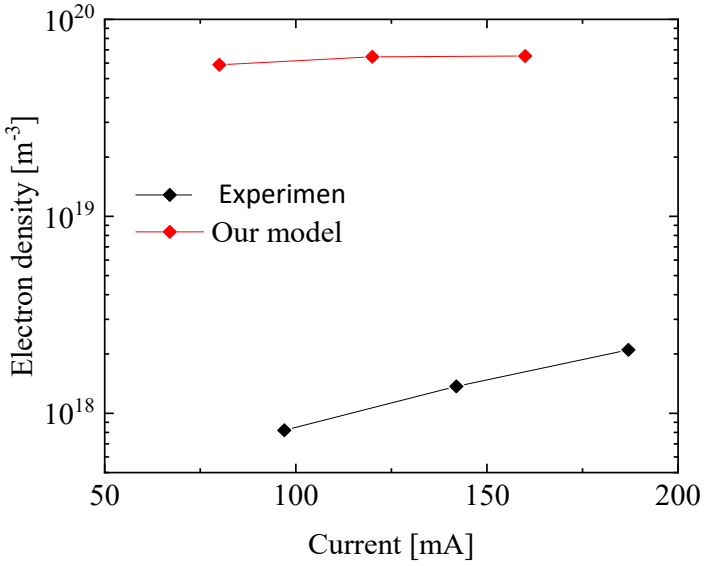

Figure A2.1. Comparison of the electron density (at z = 1 cm) from our model, with the results of [69].

Our model was calculated for the experimental conditions in [69] and the results of the electron density as a function of the current are presented in Figure A2.1. Our calculated electron density is about one order of magnitude larger than the value of [69], and is more or less constant upon increasing current, while the data of [69] rise with current. Even though we have the same kinetic mechanisms as in [69], our model is not able to reproduce the results. We attribute this to the complicated gas flow behavior of the experiment, which is not explained in detail. Our modelling approach requires information of the full geometry in order to calculate the flow field. We performed additional comparison with the experiments in [64] presented in Figure A2.2.

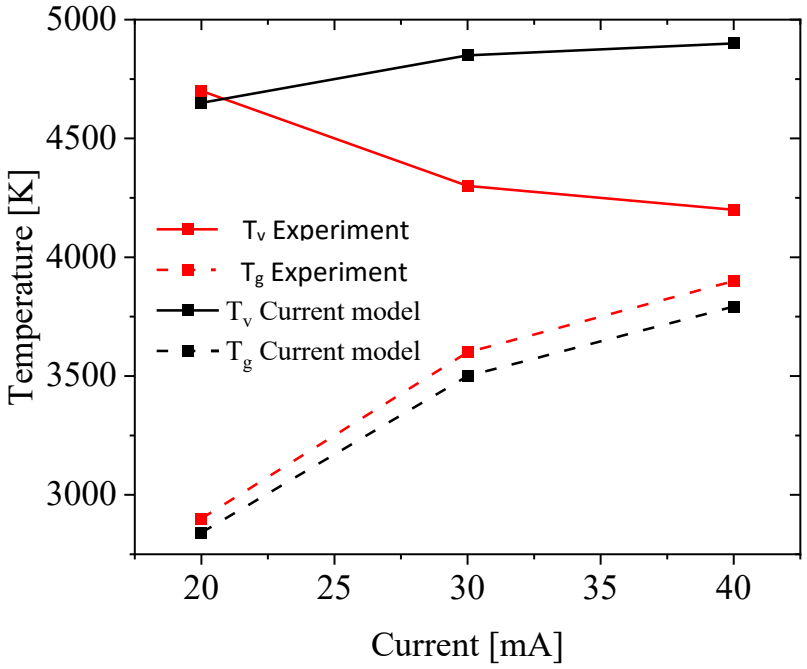

Figure A2.2. Comparison of the vibrational temperature T_v and gas temperature T_g (at z = 1 cm) for our model and the experimental results in [64], as a function of current.

There is good agreement between the experiment and our model for the gas temperature as a function of current. The experimental vibrational temperature, however, shows a decreasing trend as a function of current and approaches (near) equilibrium with the gas temperature, while our model shows an increase in vibrational temperature and strong deviation from equilibrium. The discrepancy between our model and these experiments might be because some kinetic pathway is still missing, or because we do not have all information on the full geometry of these experiments, which would be needed for an accurate description, due to the strong coupling between gas flow and plasma behavior in our model.

However, we believe our present model can already qualitatively describe the differences between arc and glow regime, and the effect on the plasma column, which was the purpose of the work in Chapter 2.

Appendix B, belonging to Chapter 3

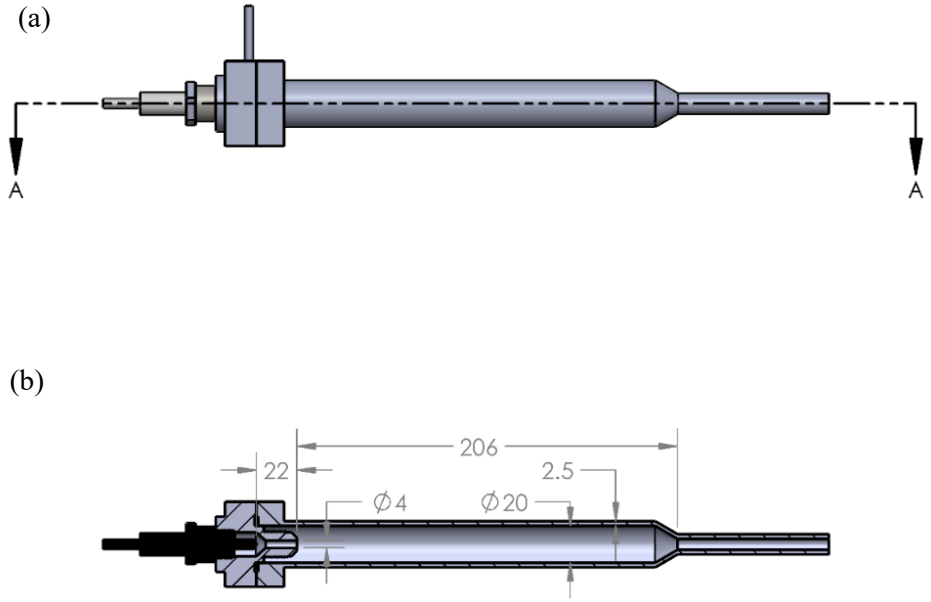

Figure B1. Detailed scheme of the RGA plasma reactor: side view (a) and cross section (b). The dimensions are presented in mm. The spark plug (serving as the ground electrode) is marked in black in the bottom image.

B1 - Pressure and mass flow rates of the experiments in Chapter 3

In order to confirm that the mass flow controllers provide a constant mass flow rate within the used range of pressure values, we performed tests with N_2 at four different pressures (0-3 barg), as shown in Figure B2. The gas (N_2) was supplied using an MFC into the inlet of the same reactor, and regulated and monitored in the same way as described above, and is shown in Figure B2. A mass flow meter (MFM, Sensidyne Gilibrator 3) was connected to the outlet of the RGA reactor, and the volumetric flow rate of N_2 passing through it was recorded. At the mass flow rate setting on the MFC of 4 and 8 Ln/min, the mass flow rate detected by the MFM in the whole range of 0-3 barg did not deviate from 4 and 8 Ln/min by more than 0.6% (i.e., the flow rate did not exceed 4.02 and 8.05 Ln/min, respectively). Therefore, the mass flow rate was assumed constant due to negligible deviations. At the same time, within the reactor an increase in pressure resulted in a lower volumetric flow rate, and hence a lower gas velocity and a longer

residence time. We also stress that the definition of normal liters (Ln) used in this chapter follows that of the MFC manufacturer, and corresponds to 0 °C, 1 atm (0 barg).

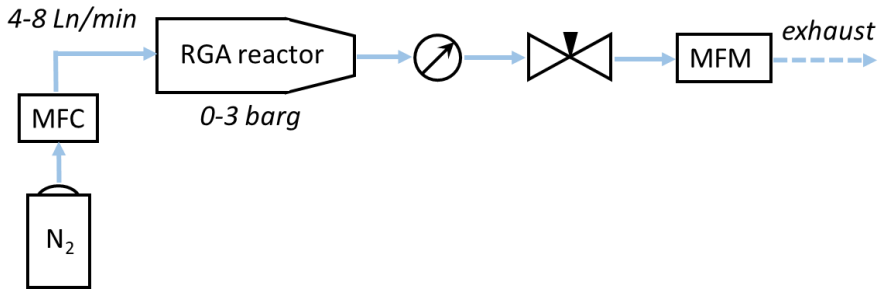

Figure B2. Schematic representation of the experiments on the MFC flow rate assessment.

B2 - Analysis of the plasma reactor outlet for NO_x

The total flow of the RGA reactor gas outlet was split using an MFC (as shown in Figure 3.1 in Chapter 3), which was set to provide a post-reaction gas mixture flow rate of 0.5 Ln/min into the NDIR analyzer. The analyzer comprised three individual NO_x sensors: NO, NO_2 (0-20 and 0-10 vol%, respectively), and N_2O (0-2000 ppm). All sensors had detection limit (4 σ) and accuracy of ≤ 0.5%FS. Prior to each set of measurements, zero and span calibrations were performed.

The quantitative analysis was performed when the concentrations of NO and NO_2 reached a steady-like state, i.e., did not vary by more than 0.02 vol% within a period of at least 5 min. The NDIR was calibrated using calibration gases (16.02 vol% NO in He, 7.80 vol% NO_2 in He, 964 ppm N_2O in He) purchased from Praxair. In all experiments, no N_2O was detected.

B3 - Calculation of plasma power, energy consumption and production rate values

The plasma power was calculated as an average of instantaneous plasma power values, expressed in eq. B1:

$$P\ (W) = \frac{1}{n}\sum_{i=1}^{n} V_i \times I_i = \frac{1}{n}\sum_{i=1}^{n} V_{HV_i}\ (V) \times I_i\ (A) = \frac{1}{n}\sum_{i=1}^{n} V_{HV_i}\ (V) \times \frac{V_{shunt_i}\ (V)}{R_{shunt}\ (\Omega)} \quad \text{(B1)}$$

The plasma power-based and the plug-to-NO_x energy consumption (EC) were calculated as shown in eq. B2 and B3, respectively:

$$EC\ \left(\frac{MJ}{mol}\right) = \frac{Plasma\ power\ (W)}{\frac{Mass\ flow\ rate_{\ total\ NO_x}\left(\frac{Ln}{min}\right)}{22.4\left(\frac{Ln}{mol}\right)\times 60\left(\frac{s}{min}\right)}} \times 10^{-6}\left(\frac{MJ}{J}\right) \quad \text{(B2)}$$

$$Plug-to-NO_x\ EC\ \left(\frac{MJ}{mol}\right) = \frac{Power\ consumed\ by\ the\ PSU\ (W)}{\frac{Mass\ flow\ rate_{\ total\ NO_x}\left(\frac{Ln}{min}\right)}{22.4\ \left(\frac{Ln}{mol}\right)\ \times\ 60\ \left(\frac{s}{min}\right)}} \times 10^{-6}\left(\frac{MJ}{J}\right) \quad \text{(B3)}$$

where the mass flow rates are calculated using eq. B4 and B5:

$$Mass\ flow\ rate_{total\ NO_x}\left(\frac{Ln}{min}\right) = \sum Mass\ flow\ rate_{NO_x}\left(\frac{Ln}{min}\right) \quad \text{(B4)}$$

$$Mass\ flow\ rate_{NO_x}\left(\frac{Ln}{min}\right) = \frac{\left(Mass\ flow\ rate_{\ N_2}^{\ inlet} + Mass\ flow\ rate_{\ O_2}^{\ inlet}\right)\left(\frac{Ln}{min}\right)\times\frac{C_{NO_x}\ (ppm)}{10^6}}{1+\frac{C_{NO_2}\ (ppm)}{2\times 10^6}} \quad \text{(B5)}$$

Similarly, total NO_x production rate (PR) was calculated as in eq. B6:

$$\sum PR_{NO_x}\left(\frac{g}{h}\right) = \frac{Mass\ flow\ rate_{NO}\left(\frac{Ln}{min}\right)\ \times 30\ \left(\frac{g}{mol}\right)\ +\ Mass\ flow\ rate_{NO_2}\left(\frac{Ln}{min}\right)\ \times 46\ \left(\frac{g}{mol}\right)}{22.4\ \left(\frac{Ln}{mol}\right)} \times 60\left(\frac{min}{h}\right) \quad \text{(B6)}$$

We specifically note that the formulae presented in eq. B2-B6 account for gas contraction due to the stoichiometry of NO_2 formation, which is often overlooked in literature reports. Indeed, when reporting an important metric such as EC or PR, the gas contraction must be taken into account, in order to present data accurately.

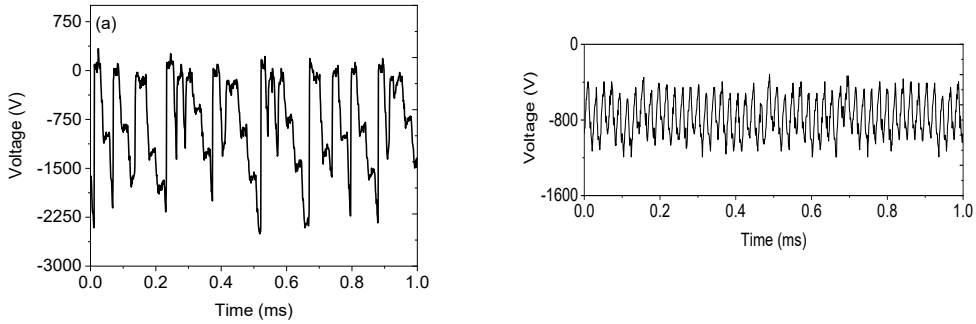

Figure B3. Voltage as a function of time for the restrike (a) and takeover mode (b).

Table B1. Comparison of production rate (PR) and plasma-based energy consumption (EC) at constant flow rate and power for different pressures and N_2:O_2 ratios.

Entry	Flow rate (Ln/min)	Pressure (barg)	Power (W)	PR (g/h)	EC (MJ/(mol N))
N_2:O_2 feed gas ratio of 4:1					
1	4	0	404	15.5	3.5
2	4	1	427	17.5	3.5
3	4	2	410	17.9	3.3
4	4	3	403	17.9	3.6
5	8	0	423	12.4	4.3
6	8	1	419	19.6	3.0
7	8	2	431	24.5	2.6
8	8	3	427	27.3	2.5
9	12	0	437	11.3	4.7
10	12	1	441	17.2	3.4

11	12	2	440	21.9	2.9
12	12	3	430	28.3	2.3
N_2:O_2 feed gas ratio of 1:1					
13	4	0	439	15.7	4.0
14	4	1	439	22.2	3.1
15	4	2	456	23.0	3.2
16	4	3	445	22.2	3.3
17	8	0	641	21.0	4.2
18	8	1	640	37.6	2.6
19	8	2	642	45.6	2.3
20	8	3	617	46.9	2.1
21	12	0	710	29.5	3.3
22	12	1	758	59.0	1.9
23	12	2	766	68.7	1.8
24	12	3	765	68.9	1.8

Table B2. Measured values of power consumed by the PSU, and plug-to-NO_x energy consumption (EC), for different experimental conditions with N_2:O_2 ratio = 4:1.

Pressure (barg)	Supplied current (mA)	Power consumed by PSU (W)			Plug-to-NO_x EC (MJ/(mol N))		
4 Ln/min							
0	500	786.7	±	37.7	9.5	±	0.9
	600	903.3	±	12.5	9.8	±	0.6
	700	1053.3	±	34.0	10.1	±	0.3
	800	1186.7	±	26.2	10.9	±	0.2

	900	1313.3	±	12.5	11.4	±	0.2
	1000	1440.0	±	14.1	12.0	±	0.1
	400	660.0	±	0.0	8.7	±	0.1
	500	786.7	±	9.4	8.0	±	0.4
	600	913.3	±	9.4	8.5	±	0.3
1	700	1080.0	±	63.8	9.4	±	0.6
	800	1273.3	±	4.7	10.5	±	0.1
	900	1366.7	±	17.0	11.0	±	0.2
	1000	1486.7	±	4.7	12.2	±	0.2
	400	686.7	±	9.4	6.3	±	0.4
	500	803.3	±	17.0	6.8	±	0.1
	600	950.0	±	8.2	8.1	±	0.3
2	700	1063.3	±	4.7	9.7	±	0.5
	800	1280.0	±	16.3	12.0	±	0.7
	900	1380.0	±	0.0	13.9	±	0.6
	1000	1513.3	±	4.7	15.5	±	0.4
	300	583.3	±	4.7	6.2	±	0.7
	400	696.7	±	4.7	6.0	±	0.1
	500	820.0	±	8.2	7.3	±	0.2
	600	960.0	±	8.2	8.8	±	0.5
3	700	1070.0	±	8.2	10.7	±	0.1
	800	1290.0	±	14.1	13.2	±	0.3
	900	1393.3	±	9.4	14.5	±	0.1
	1000	1530.0	±	0.0	16.5	±	0.1
8 Ln/min							
	600	966.7	±	59.1	14.0	±	1.3
	700	1123.3	±	30.9	14.6	±	0.8
0	800	1283.3	±	12.5	15.0	±	0.7
	900	1413.3	±	17.0	15.7	±	0.2
	1000	1520.0	±	8.2	15.6	±	0.3

1	500	830.0	±	8.2	9.2	±	0.4
	600	976.7	±	9.4	8.7	±	1.4
	700	1110.0	±	8.2	7.9	±	0.6
	800	1256.7	±	9.4	8.2	±	0.6
	900	1410.0	±	0.0	8.2	±	0.5
	1000	1570.0	±	0.0	9.0	±	0.3
2	400	713.3	±	12.5	6.2	±	0.1
	500	840.0	±	8.2	6.8	±	0.1
	600	980.0	±	16.3	7.3	±	0.4
	700	1143.3	±	9.4	7.9	±	0.3
	800	1300.0	±	0.0	8.0	±	0.4
	900	1436.7	±	9.4	8.0	±	0.3
	1000	1593.3	±	9.4	8.3	±	0.3
3	400	723.3	±	9.4	5.9	±	0.1
	500	866.7	±	17.0	6.4	±	0.1
	600	996.7	±	9.4	6.5	±	0.3
	700	1170.0	±	21.6	6.7	±	0.4
	800	1306.7	±	4.7	6.9	±	0.3
	900	1446.7	±	9.4	7.1	±	0.1
	1000	1616.7	±	12.5	7.4	±	0.1
12 Ln/min							
0	600	1013.3	±	17.0	12.9	±	0.3
	700	1130.0	±	14.1	12.2	±	0.6
	800	1293.3	±	40.3	12.0	±	0.5
	900	1430.0	±	28.3	12.1	±	0.3
	1000	1570.0	±	8.2	13.0	±	0.2
1	600	1000.0	±	8.2	9.1	±	0.1
	700	1146.7	±	12.5	8.9	±	0.5
	800	1300.0	±	8.2	9.4	±	0.4
	900	1446.7	±	12.5	9.7	±	0.4
	1000	1610.0	±	8.2	10.3	±	0.3

2	500	856.7	±	9.4	7.5	±	0.1
	600	1006.7	±	17.0	7.6	±	0.2
	700	1163.3	±	12.5	8.1	±	0.2
	800	1320.0	±	8.2	8.7	±	0.3
	900	1476.7	±	12.5	9.1	±	0.2
	1000	1640.0	±	8.2	9.2	±	0.7
3	400	726.7	±	30.9	5.4	±	0.3
	500	883.3	±	26.2	5.7	±	0.3
	600	1000.0	±	0.0	5.9	±	0.3
	700	1180.0	±	32.7	6.4	±	0.3
	800	1340.0	±	14.1	6.8	±	0.3
	900	1466.7	±	12.5	7.0	±	0.4
	1000	1640.0	±	0.0	7.5	±	0.5

B4 - Calculation of equilibrium NO concentration.

The calculation of the equilibrium NO concentration is performed using the sigmoidal fitting functions provided by D'Angola *et al.* [103]:

$$\sigma(T, c, \Delta) = \frac{e^{q}}{e^{q} + e^{-q}}, \qquad q = \frac{T - c}{\Delta} \tag{B7}$$

where T is the gas temperature. The dependence of the sigmoid on pressure is expressed through the fitting constants c and Δ.

$$\sigma_i(T, c, \Delta) = \sigma(T, c_i, \Delta_i) \tag{B8}$$

The pressure-dependent parameters c, Δ, a are expressed as a function of the pressure logarithm as:

$$logC = \sum_{j=0}^{n} \alpha_j x^j \tag{B9}$$

Where *logC* represents any of the fitting parameters and $x = \log(P)$ is the logarithm of the pressure *P.*

The concentration of NO is given as:

$$NO\ vol\% = 100 \times \max\left[0, \sum_{j=1}^{n} a_j \sigma_j(T)\right] \quad \text{(B10)}$$

The values of the fitting constants are listed in Table B3.

Table B3. Constants for determining the pressure-dependent concentration of NO.

		α_0	α_1	α_2	α_3	α_4
σ_1	$\log a_1$	-2.397641	9.644207e-2	-	-	-
	$\log c_1$	7.942600	2.917164e-2	6.775381e-4	2.209082e-5	-
	$\log \Delta_1$	6.780323	6.029139e-2	4.276063e-4	-	-
σ_2	$a_2 = -a_1 - a_3$	-	-	-	-	-
	$\log c_2$	8.274503	6.655621e-2	2.214534e-3	3.856329e-5	
	$\log \Delta_2$	6.495225	7.930874e-2	−1.952605e-3	−7.384374e-4	−5.231985e-5
σ_3	$\log(-a_3)$	−2.923272	1.671984e-1	-	-	-
	$\log c_3$	8.364477	7.365241e-2	2.771836e-3	−5.013391e-6	−5.293616e-6
	$\log \Delta_3$	7.549495	9.399569e-2			

B5 - Calculation of the pressure-dependent rate coefficient R3.5.

The pressure-dependent rate coefficient is calculated by adding a broadening factor *F* to the Lindemann-Hinshelwood relation, as described in Baulch *et al.* [104]:

$$k = k_\infty \left(\frac{k_0[M]/k_\infty}{1 + k_0[M]/k_\infty}\right) F \quad \text{(B11)}$$

Where k is the reaction rate coefficient, $k_\infty = 4.9 \cdot 10^{-10} T^{-0.4} \frac{cm^3}{s}$ is the reaction rate coefficient in the high-pressure limit, $k_0 = 9.2 \cdot 10^{-28} T^{-1.6} \frac{cm^6}{s}$ is the reaction rate coefficient in the low pressure limit, and $[M]$ is the gas number density calculated from the ideal gas law.

The broadening factor *F* is given by:

$$logF = \frac{logF_c}{1 + \left[\frac{\log\left(\frac{k_0[M]}{k_\infty}\right)}{N}\right]^2} \quad \text{(B12)}$$

Where $N = 0.75 - 1.27 logF_c$ and $F_c = 0.8$.

Table B4. Measured values of power consumed by the PSU, and plug-to-NO_x energy consumption (EC), for different experimental conditions with N_2:O_2 ratio of 1:1.

Pressure (barg)	Supplied current (mA)	Power consumed by PSU (W)			Plug-to-NO_x EC (MJ/(mol N))		
4 Ln/min							
0	500	713.3	±	9.4	9.0	±	0.4
	600	856.7	±	17.0	8.8	±	0.4
	700	1003.3	±	26.2	9.1	±	0.7
	800	1150.0	±	35.6	9.4	±	0.4
	900	1276.7	±	23.6	10.0	±	0.1
	1000	1410.0	±	8.2	10.5	±	0.1
1	400	576.7	±	20.5	5.8	±	0.2
	500	736.7	±	24.9	5.8	±	0.2
	600	853.3	±	30.9	6.0	±	0.2
	700	1016.7	±	18.9	7.0	±	0.1
	800	1183.3	±	33.0	8.3	±	0.4
	900	1333.3	±	9.4	9.8	±	0.2
	1000	1500.0	±	8.2	11.2	±	0.1
2	400	603.3	±	4.7	4.9	±	0.1
	500	746.7	±	12.5	5.4	±	0.1
	600	886.7	±	4.7	6.2	±	0.2

	700	1010.0	±	16.3	7.1	±	0.2
	800	1176.7	±	12.5	8.6	±	0.2
	900	1336.7	±	17.0	10.1	±	0.3
	1000	1500.0	±	16.3	11.7	±	0.4
	400	663.3	±	30.9	4.9	±	0.2
	500	786.7	±	26.2	5.8	±	0.3
	600	930.0	±	37.4	7.3	±	0.7
3	700	1073.3	±	33.0	8.6	±	0.8
	800	1196.7	±	4.7	10.0	±	0.4
	900	1360.0	±	14.1	11.5	±	0.2
	1000	1500.0	±	14.1	12.7	±	0.3
8 Ln/min							
	700	1083.3	±	83.8	11.2	±	0.7
0	800	1253.3	±	75.9	10.0	±	0.1
	900	1446.7	±	12.5	9.6	±	0.3
	1000	1543.3	±	33.0	8.3	±	0.5
	700	1110.0	±	32.7	5.4	±	0.2
1	800	1286.7	±	9.4	5.2	±	0.1
	900	1460.0	±	8.2	5.3	±	0.1
	1000	1580.0	±	0.0	5.6	±	0.1
	600	916.7	±	54.4	3.8	±	0.1
	700	1110.0	±	21.6	4.2	±	0.1
2	800	1280.0	±	16.3	4.5	±	0.1
	900	1436.7	±	30.9	4.9	±	0.1
	1000	1586.7	±	9.4	5.4	±	0.1
	600	946.7	±	20.5	3.8	±	0.1
	700	1056.7	±	20.5	4.1	±	0.1
3	800	1190.0	±	29.4	4.5	±	0.1
	900	1380.0	±	16.3	4.8	±	0.1
	1000	1573.3	±	45.0	5.4	±	0.2

12 Ln/min							
0	900	1543.3	±	12.5	7.3	±	0.3
	1000	1726.7	±	17.0	6.3	±	0.1
1	900	1636.7	±	18.9	4.4	±	0.1
	1000	1816.7	±	12.5	4.7	±	0.1
2	900	1720.0	±	8.2	4.0	±	0.1
	1000	1893.3	±	12.5	4.5	±	0.1
3	800	1580.0	±	8.2	3.7	±	0.1
	900	1773.3	±	4.7	4.3	±	0.1
	1000	1940.0	±	14.1	5.0	±	0.1

Appendix C, belonging to Chapter 4

C1 - Chemistry set of the CO_2 model in Chapter 4

The electron-impact processes, described by energy-dependent cross sections and the EEDF, are taken from specific databases within the LxCat database, as detailed in the reference column of Table C1. The cross sections for direct electron-impact dissociation of CO_2 have been modified compared to the original set, following the adjustments in Biondo *et al*. [132]. The consistency of these updated cross sections with the swarm

parameters was verified in the same study. For all other reactions, the rate coefficients and corresponding references are given in Table C1.

Table C1. Chemistry set used in Chapter 4. Rate coefficients are in s^{-1}, cm^3/s or cm^6/s, for radiative decay, two-body and three-body reactions, respectively, while T_e and T_g are both expressed in K. Nn represents the total neutral density in cm^{-3}, while M is a colliding partner and k_M the corresponding rate coefficient. Most of the electron-impact processes are described by energy-dependent cross sections and the EEDF, as indicated in the table.

Reaction	Rate expression	Ref.
Electron-impact processes		
$e + CO_2 \rightarrow e + CO_2$	EEDF	194
$e + CO_2 \rightarrow e + e + CO_2^+$	EEDF	194
$e + CO_2 \rightleftharpoons e + CO_2(v_1v_2v_3)$[a]	EEDF	194
$e + CO_2 \rightleftharpoons e + CO_2(e1,e2)$	EEDF	132, 194
$e + CO_2 \rightarrow e + CO + O(^1D)$	EEDF	132, 195
$e + CO_2 \rightarrow e + CO(a^3\Pi) + O$	EEDF	132, 195
$e + CO_2 \rightarrow CO + O^-$	EEDF	194
$e + CO \rightarrow e + CO$	EEDF	196
$e + CO \rightarrow e + e + CO^+$	EEDF	196
$e + CO \rightleftharpoons e + CO(v)$	EEDF	196
$e + CO \rightleftharpoons e + CO(a^3\Pi,\ a'^3\Sigma^+,\ A^1\Pi,\ b^3\Sigma^+,\ B^1\Sigma^+,\ C^1\Sigma^+,\ E^1\Sigma^+)$	EEDF	196
$e + CO \rightarrow e + C + O$	EEDF	196
$e + CO \rightarrow C + O^-$	EEDF	196
$e + O_2 \rightarrow e + O_2$	EEDF	197,198
$e + O_2 \rightarrow e + e + O_2^+$	EEDF	197,198
$e + O_2 \rightleftharpoons e + O_2(v)$	EEDF	197,198
$e + O_2 \rightleftharpoons e + O_2(a^1\Delta_g,\ b^1\Sigma_g^+,\ A^3\Sigma_u^+,\ C^3\Delta_u,\ c^1\Sigma_u^-)$	EEDF	197,198
$e + O_2 \rightarrow e + O + O$	EEDF	197,198
$e + O_2 \rightarrow e + O + O(^1D)$	EEDF	197,198
$e + O_2 \rightarrow O + O^-$	EEDF	197,198
$e + O_2 + M \rightarrow O_2^- + M$	$k_{CO_2,CO} = 3.3 \times 10^{-30}$, $k_O = 1 \times 10^{-31}$, $k_{O_2} = 1.4 \times 10^{-29} \times 300/T_e \times e^{-\frac{600}{T_g}} \times e^{\left(\frac{700(T_e-T_g)}{T_eT_g}\right)}$	199-201

$e + O \rightarrow e + O$	EEDF	202
$e + O \rightarrow e + e + O^+$	EEDF	202
$e + O \rightarrow O^-$	$k_M = 1 \times 10^{-31} \times Nn$	200
$e + O \rightleftharpoons e + O(^1D, ^1S)$	EEDF	202
$e + C \rightarrow e + C$	EEDF	191
$e + O_3 \rightarrow e + O_3$	EEDF	202
$e + O_3 \rightarrow e + e + O_3^+$	EEDF	202
$e + O_3 \rightarrow O_2 + O^-$	EEDF	202
$e + O_3 \rightarrow O + O_2^-$	EEDF	202
	Electronic relaxation	
$CO(a^3\Pi) + O_2 \rightarrow CO + 2O$	2.4×10^{-11}	144
$CO(a^3\Pi) + O_2 \rightarrow CO_2 + O$	1.2×10^{-11}	144
$CO(a^3\Pi) + CO \rightarrow CO_2 + C$	9.12×10^{-13}	144
$CO(a^3\Pi) + CO_2 \rightarrow 2CO + O$	5×10^{-12}	144
$CO(a^3\Pi) + M \rightarrow CO + M$	$k_O = 1.9 \times 10^{-10}$, $k_{O_2} = 2.4 \times 10^{-11}$, $k_{CO} = 5.6088 \times 10^{-11}$, $k_{CO_2} = 5 \times 10^{-12}$	144
$CO(a^3\Pi) \rightarrow CO$	1/0.012	203
$O(^1D) + M \rightarrow O + M$	$k_O = 8 \times 10^{-12}$, $k_{O_2} = 6.4 \times 10^{-12} e^{67/T_g}$, $k_{CO} = 4.7 \times 10^{-11} e^{62.542/T_g}$, $k_{CO_2} = 7.9 \times 10^{-11} e^{133/T_g}$	201
$O(^1D) + O_2 \rightleftharpoons O + O_2(a^1\Delta_g)$	$1.6 \times 10^{-12} e^{67/T_g}$	204
$O(^1D) + O_2 \rightarrow O + O_2(b^1\Sigma_g^+)$	$2.56 \times 10^{-11} e^{67/T_g}$	201,205
$O(^1D) + O_2(a^1\Delta_g) \rightarrow O + O_2$	3×10^{-11}	141
$O(^1D) + O_3 \rightarrow 2O_2$	$0.47 \times 2.5 \times 10^{-10}$	206, 207
$O(^1D) + O_3 \rightarrow O_2 + 2O$	$0.53 \times 2.5 \times 10^{-10}$	206, 207
$O(^1D) + CO \rightarrow CO_2$	8×10^{-11}	208
$O(^1D) + CO_2 \rightarrow O_2 + CO$	2.4×10^{-13}	209
$O(^1D) \rightarrow O$	6.8×10^{-3}	205, 210
$O(^1S) + M \rightarrow O + M$	$k_O = 3.33 \times 10^{-11} e^{-300/T_g}$, $k_{O_2} = 4.3 \times 10^{-12} e^{-850/T_g}$, $k_{CO} = 7.4 \times 10^{-14} e^{-957.37/T_g}$, $k_{CO_2} = 3.09 \times 10^{-13}$	205, 210-213
$O(^1S) + M \rightarrow O(^1D) + M$	$k_O = 5 \times 10^{-11} e^{-301/T_g}$, $k_{O_2} = 1.333 \times 10^{-12} e^{-850/T_g}$, $k_{CO} = 9.4 \times 10^{-14}$, $k_{CO_2} = 2.394 \times 10^{-13}$	201, 211, 214, 215
$O(^1S) + O_2 \rightarrow O + O_2(a^1\Delta_g)$	$1.5 \times 10^{-12} e^{-850/T_g}$	201
$O(^1S) + O_2 \rightarrow O + O_2(b^1\Sigma_g^+)$	$7.3 \times 10^{-13} e^{-850/T_g}$	201
$O(^1S) + O_2 \rightarrow O + O_2(A^3\Sigma_u^+, C^3\Delta_u, c^1\Sigma_u^-)$	$2.967 \times 10^{-12} e^{-850/T_g}$	201

$O(^1S) + O_2(a^1\Delta_g) \rightarrow O + O_2$	1×10^{-10}	204
$O(^1S) + O_2(a^1\Delta_g) \rightarrow O + O_2(b^1\Sigma_g^+)$	1.3×10^{-10}	204
$O(^1S) + O_2(a^1\Delta_g) \rightarrow O(^1D) + O_2$	3.6×10^{-11}	204
$O(^1S) + O_2(a^1\Delta_g) \rightarrow 3O$	3.23×10^{-11}	201
$O(^1S) + O_2(a^1\Delta_g) \rightarrow O + O_2(A^3\Sigma_u^+, C^3\Delta_u, c^1\Sigma_u^-)$	7.905×10^{-11}	201
$O(^1S) + O_2(a^1\Delta_g) \rightarrow O(^1D) + O_2(a^1\Delta_g)$	1.7×10^{-12}	201
$O(^1S) + O_2(a^1\Delta_g) \rightarrow O(^1D) + O_2(b^1\Sigma_g^+)$	2.89×10^{-11}	201
$O(^1S) \rightarrow O(^1D)$	1.3	205
$O(^1S) \rightarrow O$	0.078	205
$O_2(a^1\Delta_g) + M \rightarrow O_2 + M$	$k_O = 7 \times 10^{-16}$, $k_{O_2} = 2.2 \times 10^{-18} \left(\frac{T_g}{300}\right)^{0.8}$, $k_{CO,CO_2} = 3.8 \times 10^{-18} e^{-205/T_g}$	201, 216, 217
$O_2(a^1\Delta_g) + O_2(a^1\Delta_g) \rightarrow O_2 + O_2(b^1\Sigma_g^+)$	$7 \times 10^{-28}\ T_g^{3.8} e^{700/T_g}$	218
$O_2(a^1\Delta_g) + O \rightarrow O_2 + O$	1×10^{-32} Nn	219, 220
$O_2(a^1\Delta_g) + O_3 \rightarrow 2O_2 + O$	$4.5 \times 10^{-11} e^{-2380/T_g}$	216
$O_2(a^1\Delta_g) + CO \rightleftharpoons O(^1D) + CO_2$	$(1\text{-}0.07) \times 1.209 \times 10^{-16}\ T_g^{1.6} e^{-13710/T_g}$	221
$O_2(a^1\Delta_g) \rightarrow O_2$	2.6×10^{-4}	205
$O_2(b^1\Sigma_g^+) + M \rightarrow O_2 + M$	$k_O = 8 \times 10^{-14}$, $k_{O_2} = 4 \times 10^{-17}$, $k_{CO} = 3.3 \times 10^{-15}$, $k_{CO_2} = 4 \times 10^{-13}$	207, 214
$O_2(b^1\Sigma_g^+) + M \rightarrow O_2(a^1\Delta_g) + M$	$k_O = 8 \times 10^{-14}$, $k_{CO,O_2} = 4.3 \times 10^{-22} T_g^{2.4} e^{-241/T_g}$, $k_{CO_2} = 4.5 \times 10^{-13}$	200, 217
$O_2(b^1\Sigma_g^+) + O_2(b^1\Sigma_g^+) \rightarrow O_2(a^1\Delta_g) + O_2$	$3.6 \times 10^{-17} \left(\frac{T_g}{300}\right)^{0.5}$	204
$O_2(b^1\Sigma_g^+) \rightarrow O_2$	0.083	205, 210
$O_2(b^1\Sigma_g^+) \rightarrow O_2(a^1\Delta_g)$	0.0025	205, 210
$O_2(A^3\Sigma_u^+, C^3\Delta_u, c^1\Sigma_u^-) + M \rightarrow O_2 + M$	$k_O = 4.95 \times 10^{-12}$, $k_{O_2} = 2.32 \times 10^{-14}$, $k_{CO} = 2.5 \times 10^{-15}$, $k_{CO_2} = 5 \times 10^{-14}$	201, 214
$CO(a^3\Pi) \rightarrow CO(a'^3\Sigma^+)$	1×10^4	222
$CO(A^1\Pi) \rightarrow CO$	1×10^4	222
$CO(b^3\Sigma^+) \rightarrow CO(a^3\Pi)$	$1/8.6 \times 10^{-8}$	223

$CO(B^1\Sigma^+) \rightarrow CO$	$1/2.5 \times 10^{-8}$	222
$CO(B^1\Sigma^+) \rightarrow CO(A^1\Pi)$	1.11×10^{7}	224
$CO(C^1\Sigma^+) \rightarrow CO$	$1/1.4 \times 10^{-9}$	222
$CO(E^1\Sigma^+) \rightarrow CO$	$k_O = 1.9 \times 10^{-10}$, $k_{O_2} = 2.4 \times 10^{-11}$, $k_{CO} = 5.6088 \times 10^{-11}$, $k_{CO_2} = 5 \times 10^{-12}$	This study

Neutral reactions		
$CO + O \rightleftharpoons CO_2$	$3 \times 10^{-14} \times e^{-\frac{1219}{T_g}} / (1 + \frac{3 \times 10^{-14} \times e^{-\frac{1219}{T_g}}}{10^{-32} \times e^{-\frac{1580}{T_g}} \times c\_eff[M]})$, with c_eff = 3.5, 6, 1.5, 1, for M = CO_2, O_2, CO, and C and O, respectively	225
$CO + O_2 \rightleftharpoons CO_2 + O$	$4.15 \times 10^{-12} \times e^{-24054/T_g}$	225
$CO + O_3 \rightleftharpoons CO_2 + O_2$	4×10^{-25}	205
$O + O \rightleftharpoons O_2$	$2.4 \times 10^{-21} + 0.5 \times 3.8 \times 10^{-30} T_g^{-1} \times e^{-170/T} \times (Nn - n_O - n_{O_2(a^1\Delta_g)})$	205, 216
$O + O \rightleftharpoons O_2(a^1\Delta_g)$	$0.33 \times 3.8 \times 10^{-30} T_g^{-1} \times e^{-170/T_g} \times (Nn - n_O - n_{O_2(a^1\Delta_g)})$	216
$O + O \rightarrow O_2(b^1\Sigma_g^+)$	$0.17 \times 3.8 \times 10^{-30} T_g^{-1} \times e^{-170/T_g} \times Nn$	216
$O + O \rightarrow O_2(A^3\Sigma_u^+, C^3\Delta_u, c^1\Sigma_u^-)$	$1.2 \times 10^{-34} \times Nn$	201
$O + O + O \rightleftharpoons O_2 + O$	$2.5 \times 10^{-31} T_g^{-0.63}$	218
$O + O + O_2(a^1\Delta_g) \rightleftharpoons O_2 + O_2(a^1\Delta_g)$	7.4×10^{-33}	204
$O + O + O \rightarrow O_2 + O(^1S)$	$1.4 \times 10^{-30} \times e^{-650/T_g}$	205
$O + O + O \rightleftharpoons O_2(a^1\Delta_g) + O$	$6.93 \times 10^{-35} T_g^{-0.63}$	204
$O + O + M \rightleftharpoons O_3 + M$	$k_{CO_2,CO} = 1.81 \times 10^{-33} \left(\frac{T_g}{300}\right)^{-1.2}$, $k_{O_2} = 6.9 \times 10^{-34} \left(\frac{T_g}{300}\right)^{-1.25}$, $k_O = 2.1 \times 10^{-34} \times e^{245/T_g}$	201, 216, 218
$O + O_3 \rightleftharpoons O_2 + O_2$	$0.5 \times 1.8 \times 10^{-11} \times e^{-2300/T_g}$	201
$O + O_3 \rightleftharpoons O_2 + O_2(a^1\Delta_g)$	$0.33 \times 1.8 \times 10^{-11} \times e^{-2300/T_g}$	201
$O + O_3 \rightarrow O_2 + O_2(b^1\Sigma_g^+)$	$0.17 \times 1.8 \times 10^{-11} \times e^{-2300/T_g}$	201
$C + O \rightleftharpoons CO$	$2.14 \times 10^{-29} \left(\frac{T_g}{300}\right)^{-3.08} e^{-2114/T_g} \times Nn$	225

$C + O_2 \rightleftharpoons O + CO$	$^{9.63}$ x $10^{-11} \times e^{-290/T_g}$	225
$C + CO_2 \rightleftharpoons CO + CO$	1×10^{-15}	225
Electron-ion recombination		
$e + CO_2^+ \rightarrow CO + O$	$4.2 \times 10^{-7} \left(\frac{T_e}{300}\right)^{-0.75}$	226
$e + O_2^+ \rightarrow O + O$	$0.32 \times 1.95 \times 10^{-7} \left(\frac{T_e}{300}\right)^{-0.7}$	178, 227
$e + O_2^+ \rightarrow O + O(^1D)$	$0.43 \times 1.95 \times 10^{-7} \left(\frac{T_e}{300}\right)^{-0.7}$	178, 227
$e + O_2^+ \rightarrow O(^1D) + O(^1D)$	$0.2 \times 1.95 \times 10^{-7} \left(\frac{T_e}{300}\right)^{-0.7}$	178, 227
$e + O_2^+ \rightarrow O(^1D) + O(^1S)$	$0.04 \times 1.95 \times 10^{-7} \left(\frac{T_e}{300}\right)^{-0.7}$	178, 227
$e + O_2^+ \rightarrow O_2$	$6 \times 10^{-27} \left(\frac{T_e}{300}\right)^{-1.5} \times Nn$	200
$e + O^+ \rightarrow O(^1D)$	$5 \times 10^{-13} T_e^{-0.5}$	204
$e + O^+ \rightarrow O$	$6 \times 10^{-27} \left(\frac{T_e}{300}\right)^{-1.5} \times Nn$	200
$e + CO^+ \rightarrow C + O$	$2.75 \times 10^{-7} \left(\frac{T_e}{300}\right)^{-0.55}$	228
$e + CO_4^+ \rightarrow CO_2 + O_2$	$1 \times 10^{-6} \left(\frac{T_e}{300}\right)^{-0.5}$	229
$e + C_2O_2^+ \rightarrow CO + CO$	$1.3 \times 10^{-6} \left(\frac{T_e}{300}\right)^{-0.34}$	230
$e + C_2O_3^+ \rightarrow CO_2 + CO$	$5.4 \times 10^{-8} \left(\frac{T_e}{300}\right)^{-0.7}$	141
$e + C_2O_4^+ \rightarrow CO_2 + CO_2$	$2 \times 10^{-5} T_e^{-0.5} T_g^{-1}$	141
$e + O_3^+ \rightarrow O_2 + O$	$1.95 \times 10^{-7} \left(\frac{T_e}{300}\right)^{-0.7}$	This study
$e + O_4^+ \rightarrow O_2 + O_2$	$1.4 \times 10^{-6} \left(\frac{T_e}{300}\right)^{-0.5}$	201
$e + A^+ \rightarrow A$ A = C, CO, CO_2, O_3	$5.5 \times 10^{-25} \left(\frac{T_g}{T_e}\right)^{3/2} \times Nn$	231, 232
$e + AB^+ \rightarrow A + B$ AB = C_2O_2, C_2O_3, C_2O_4, CO_4, O_4	$5.5 \times 10^{-25} \left(\frac{T_g}{T_e}\right)^{3/2} \times Nn$	231, 232
$e + e + A^+ \rightarrow e + A$ A = O, C, CO, O_2, CO_2, O_3	$1 \times 10^{-19} \left(\frac{300}{T_e}\right)^{4.5}$	200, 233

$e + e + AB^+ \rightarrow e + A + B$ $AB = C_2O_2, C_2O_3, C_2O_4, CO_4, O_4$	$1 \times 10^{-19} \left(\frac{300}{T_e}\right)^{4.5}$	200, 233
Ion-neutral reactions		
$O + CO_2^+ \rightleftharpoons CO + O_2^+$	1.64×10^{-10}	234
$O + CO_2^+ \rightleftharpoons CO_2 + O^+$	9.63×10^{-11}	234
$O_2 + CO_2^+ \rightleftharpoons CO_2 + O_2^+$	5.5×10^{-11}	235, 236
$CO_2 + CO_2^+ \rightarrow C_2O_4^+$	$7 \times 10^{-28} \times Nn$	237
$C + O_2^+ \rightleftharpoons O + CO^+$	5.2×10^{-11}	238
$C + O_2^+ \rightleftharpoons O_2 + C^+$	5.2×10^{-11}	238
$O_2 + O_2^+ \rightarrow O_4^+$	$2.4 \times 10^{-30} \left(\frac{T_g}{300}\right)^{-3.2} \times Nn$	239
$CO_2 + O_2^+ + M \rightarrow CO_4^+ + M$	$k_{CO,O,O_2} = 2.3 \times 10^{-29}$, $k_{CO_2} = 1.2 \times 10^{-2}$	239-241
$CO_2 + CO^+ \rightleftharpoons CO + CO_2^+$	1×10^{-15}	242
$O_2 + CO^+ \rightleftharpoons CO + O_2^+$	$1.5 \times 10^{-10} \left(\frac{T_g}{300}\right)^{-1.1}$	236, 243
$O + CO^+ \rightleftharpoons CO + O^+$	1.4×10^{-10}	244
$C + CO^+ \rightleftharpoons CO + C^+$	1.4×10^{-10}	238
$CO + CO^+ \rightarrow C_2O_2^+$	$1.48 \times 10^{-28} \times Nn$	245, 246
$O + O^+ \rightleftharpoons O_2^+$	$1 \times 10^{-29} \left(\frac{T_g}{300}\right)^{0.5} \times Nn$	200
$O_2 + O^+ \rightleftharpoons O + O_2^+$	$2 \times 10^{-11} \left(\frac{T_g}{300}\right)^{-0.4}$	205, 210
$O_2(a^1\Delta_g) + O^+ \rightleftharpoons O + O_2^+$	$2e \times 10^{-11} \left(\frac{T_g}{300}\right)^{-0.5}$	247
$O_3 + O^+ \rightleftharpoons O_2 + O_2^+$	1×10^{-10}	205
$O_2 + C^+ \rightleftharpoons CO + O^+$	$0.62 \times 9.9 \times 10^{-10}$	248
$O_2 + C^+ \rightleftharpoons O + CO^+$	$0.38 \times 9.9 \times 10^{-10}$	248
$CO_2 + C^+ \rightleftharpoons CO + CO^+$	1.1×10^{-9}	248
$C_2O_2^+ \rightarrow CO + CO^+$	$1 \times 10^{-12} \times Nn$	147
$O_2 + C_2O_2^+ \rightarrow 2CO + O_2^+$	5.4×10^{-12}	249
$CO + C_2O_3^+ \rightarrow CO_2 + C_2O_2^+$	1.1×10^{-9}	237
$C_2O_4^+ \rightarrow CO_2 + CO_2^+$	$f(E/N)$	237
$CO + C_2O_4^+ \rightarrow CO_2 + C_2O_3^+$	9×10^{-10}	237
$O_2 + C_2O_4^+ \rightarrow CO_2 + CO_2 + O_2^+$	$0.94 \times 2 \times 10^{-10}$	241
$O_2 + C_2O_4^+ \rightarrow CO_2 + CO_4^+$	$0.06 \times 2 \times 10^{-10}$	241
$O_2(a^1\Delta_g) + O^- \rightleftharpoons O + O_2^-$	$1 \times 10^{-10} \left(\frac{T_g}{300}\right)^{-0.5}$	204
$O_2 + O^- \rightarrow O + O_2^-$	$f(E/N)$	250

$O_2 + O^- \rightarrow O_3^-$	$1.11 \times 10^{-30} \left(\frac{T_g}{300}\right)^{-1} \times Nn$	200
$O_3 + O^- \rightarrow O + O_3^-$	1.4×10^{-9}	251
$O_3 + O^- \rightleftharpoons O_2 + O_2^-$	3×10^{-10}	251
$CO_2 + O^- + M \rightleftharpoons CO_3^- + M$	$k_{CO_2,CO,O} = 1.46 \times 10^{-28} \left(\frac{T_g}{300}\right)^{-1.5}$, $k_{O_2} = 2.29 \times 10^{-28} \left(\frac{T_g}{300}\right)^{-2.06}$	252
$O + O_2^- \rightarrow O_2 + O^-$	$1.5 \times 10^{-10} \left(\frac{T_g}{300}\right)^{0.5}$	204, 253
$O(^1D,^1S) + O_2^- \rightarrow O + O + O^-$	1.5×10^{-10}	204
$O_2 + O_2^- \rightarrow O + O_3^-$	3.5×10^{-15}	254
$O_2 + O_2^- \rightarrow O_4^-$	$3.5 \times 10^{-31} \left(\frac{T_g}{300}\right)^{-1} \times Nn$	200, 210
$O_3 + O_2^- \rightleftharpoons O_2 + O_3^-$	1.3×10^{-9}	251
$CO + O_2^- \rightleftharpoons CO_3^-$	$1 \times 10^{-30} \times Nn$	255
$CO_2 + O_2^- + M \rightarrow CO_4^- + M$	$k_{CO_2,CO,O} = 1 \times 10^{-29}$, $k_{O_2} = 4.7 \times 10^{-29}$	142, 256
$O_3^- \rightarrow O_2 + O^-$	$f(E/N)$	250
$O + O_3^- \rightarrow O_2 + O_2^-$	$2.5 \times 10^{-10} \left(\frac{T_g}{300}\right)^{0.5}$	204
$O + O_3^- \rightarrow O_3 + O^-$	1×10^{-13}	201
$O_2(a^1\Delta_g) + O_3^- \rightleftharpoons O_2 + O_2 + O^-$	1×10^{-10}	204
$O_2(b^1\Sigma_g^+) + O_3^- \rightarrow O_2 + O_2 + O^-$	1×10^{-10}	204
$CO_2 + O_3^- \rightleftharpoons O_2 + CO_3^-$	$5.5 \times 10^{-10} \left(\frac{T_g}{300}\right)^{-0.49}$	204,255
$O(^1D,^1S) + O_3^- \rightarrow O + O + O_2^-$	1×10^{-10}	201
$O(^1D,^1S) + O_3^- \rightarrow O + O_2 + O^-$	1×10^{-10}	201
$O_4^- \rightarrow O_2 + O_2^-$	$1 \times 10^{-10} \times e^{-1044/T_g} \times Nn$	200
$O + O_4^- \rightleftharpoons O_2 + O_3^-$	4×10^{-10}	257
$O + O_4^- \rightleftharpoons O_2 + O_2 + O^-$	3×10^{-10}	200
$O(^1D,^1S) + O_4^- \rightarrow O + O_2 + O_2^-$	1×10^{-10}	201
$O(^1D,^1S) + O_4^- \rightarrow O_2 + O_2 + O^-$	1×10^{-10}	201
$O_2(a^1\Delta_g) + O_4^- \rightleftharpoons O_2 + O_2 + O_2^-$	1×10^{-10}	204
$O_2(b^1\Sigma_g^+) + O_4^- \rightarrow O_2 + O_2 + O_2^-$	1×10^{-10}	204
$O_3 + O_4^- \rightleftharpoons 2O_2 + O_3^-$	3×10^{-10}	204
$CO + O_4^- \rightleftharpoons O_2 + CO_3^-$	2×10^{-11}	242
$CO_2 + O_4^- \rightarrow O_2 + CO_4^-$	3×10^{-10}	257

$O + CO_3^- \rightleftharpoons CO_2 + O_2^-$	8×10^{-11}	258, 259
$O(^1D,^1S) + CO_3^- \rightarrow CO_2 + O + O^-$	1×10^{-10}	204
$O + CO_4^- \rightarrow O_2 + CO_3^-$	$0.8 \times 1.4 \times 10^{-10}$	229, 253
$O + CO_4^- \rightarrow CO_2 + O_2 + O^-$	$0.1 \times 1.4 \times 10^{-10}$	229, 253
$O + CO_4^- \rightarrow CO_2 + O_3^-$	$0.1 \times 1.4 \times 10^{-10}$	229, 253
$O(^1D,^1S) + CO_4^- \rightarrow CO_2 + O + O_2^-$	1×10^{-10}	204
$O_2 + CO_4^- \rightarrow CO_2 + O_4^-$	2×10^{-14}	204
$O_2(a^1\Delta_g) + CO_4^- \rightarrow CO_2 + O_2 + O_2^-$	1×10^{-10}	204
$O_2(b^1\Sigma_g^+) + CO_4^- \rightarrow CO_2 + O_2 + O_2^-$	1×10^{-10}	204
$O_3 + CO_4^- \rightarrow CO_2 + O_2 + O_3^-$	4.3×10^{-10}	251
$O_3 + CO_4^- \rightarrow O_2 + O_2 + CO_3^-$	3×10^{-11}	251
$CO + CO_4^- \rightarrow CO_2 + CO_3^-$	1×10^{-16}	255
Ion-ion recombination		
$A^- + B^+ \rightarrow A + B$	$2 \times 10^{-7}\left(\frac{T_g}{300}\right)^{-0.5} + 2 \times 10^{-25}\left(\frac{T_g}{300}\right)^{-2.5} \times Nn$	204, 218
$A^- + B^+ \rightarrow AB$	$1 \times 10^{-25}\left(\frac{T_g}{300}\right)^{-2.5} \times Nn$	218
$A^- + BC^+ \rightarrow A + B + C$	1×10^{-7}	218
$O^- + O^+ \rightarrow O + O(^1D)$	$4.9 \times 10^{-10}\left(\frac{T_g}{300}\right)^{-0.5}$	204
$O^- + O_2^+ \rightarrow O + O_2(a^1\Delta_g)$	$6.3 \times 10^{-10}\left(\frac{T_g}{300}\right)^{-2}$	201
$O^- + O_2^+ \rightarrow O + O_2(b^1\Sigma_g^+)$	$1.3 \times 10^{-10}\left(\frac{T_g}{300}\right)^{-2}$	201
$O_2^- + O_2^+ \rightarrow O_2 + O_2(a^1\Delta_g)$	$2.9 \times 10^{-10}\left(\frac{T_g}{300}\right)^{-2}$	201
$O_2^- + O_2^+ \rightarrow O_2 + O_2(b^1\Sigma_g^+)$	$4 \times 10^{-10}\left(\frac{T_g}{300}\right)^{-2}$	201
Electron detachment		
$O^- \rightarrow O + e$	$4 \times 10^{-12} \times Nn$	260

$O^- + O \rightarrow O_2 + e$	$2 \times 10^{-10} \left(\frac{T_g}{300}\right)^{0.5}$	204
$O^- + O(^1D, ^1S) \rightarrow O + O + e$	1×10^{-10}	204
$O^- + O_2 \rightarrow O_2 + O + e$	$2.3 \times 10^{-9} \times e^{-26000/T_g}$	261, 262
$O^- + O_2 \rightarrow O_3 + e$	$5 \times 10^{-15} \left(\frac{T_g}{300}\right)^{0.5}$	204
$O^- + O_2(a^1\Delta_g) \rightarrow O_3 + e$	$3 \times 10^{-10} \left(\frac{T_g}{300}\right)^{0.5}$	204
$O^- + O_2(b^1\Sigma_g^+) \rightarrow O_2 + O + e$	$6.9 \times 10^{-10} \left(\frac{T_g}{300}\right)^{0.5}$	204
$O^- + O_3 \rightarrow O_2 + O_2 + e$	5×10^{-12}	251
$O^- + C \rightarrow CO + e$	5×10^{-10}	238
$O^- + CO \rightarrow CO_2 + e$	$6 \times 10^{-10} \left(\frac{T_e}{300}\right)^{-0.39}$	263
$O_2^- + O(^1D, ^1S) \rightarrow O_2 + O + e$	1.5×10^{-10}	204
$O_2^- \rightarrow O_2 + e$	$2.7 \times 10^{-10} \left(\frac{T_g}{300}\right)^{0.5} e^{-5590/T_g} \times Nn$	199,262
$O_2^- + O \rightarrow O_3 + e$	$1.5 \times 10^{-10} \left(\frac{T_g}{300}\right)^{-2}$	201,253
$O_2^- + O_2(a^1\Delta_g) \rightarrow O_2 + O_2 + e$	$2 \times 10^{-10} \left(\frac{T_g}{300}\right)^{0.5}$	204, 264
$O_2^- + O_2(b^1\Sigma_g^+) \rightarrow O_2 + O_2 + e$	$3.6 \times 10^{-10} \left(\frac{T_g}{300}\right)^{0.5}$	201, 204
$O_3^- \rightarrow O_3 + e$	$2.3 \times 10^{-11} \times Nn$	220
$O_3^- + O \rightarrow O_2 + O_2 + e$	3×10^{-10}	201
$O(^1D, ^1S) + O_3^- \rightarrow O + O_3 + e$	1×10^{-10}	201
$O_3 + O_3^- \rightarrow O_2 + O_2 + O_2 + e$	3×10^{-10}	265
$CO + O_3^- \rightarrow O_2 + CO_2 + e$	1×10^{-13}	255, 266
$O(^1D, ^1S) + O_4^- \rightarrow O + 2O_2 + e$	1×10^{-10}	201
$O_4^- + O_2(a^1\Delta_g) \rightarrow 3O_2 + e$	1×10^{-10}	204
$O_4^- + O_2(b^1\Sigma_g^+) \rightarrow 3O_2 + e$	1×10^{-10}	204
$CO_3^- + O \rightarrow CO_2 + O_2 + e$	5×10^{-13}	This study
$CO_3^- + O(^1D, ^1S) \rightarrow CO_2 + 2O + e$	1×10^{-10}	204
$CO_3^- + CO \rightarrow 2CO_2 + e$	5×10^{-13}	142

CO_4^- + O(^{1}D,^{1}S) → CO_2 + O_2 + O + e	1 x 10^{-10}	204
CO_4^- + O_2($a^1\Delta_g$) → CO_2 + 2O_2 + e	1 x 10^{-10}	204
CO_4^- + O_2($b^1\Sigma_g^+$) → CO_2 + 2O_2 + e	1 x 10^{-10}	204

[a]excitation to v_3 = 2-5 is included by applying the Fridman scaling 40and threshold energy shift to the cross sections for e + CO_2 ⇌ e + CO_2(v_3=1), as described in 121.

C2 - Details on some rate coefficients for V-T, V-V-T and V-T relaxation

The rate coefficients of intra-molecular V-V-T relaxation are taken from Biondo *et al*. [132], whereas for inter-molecular V-V-T relation, it is taken from Bass [267], as O_2(i_{O2}=1) + CO_2 ⇌ O_2 + CO_2(i_2=2) with a forward rate coefficient of 2 x 10^{-12} $\left[\frac{cm^3}{s}\right]$ $(T_g/300[K])^{0.5}$. The reverse rate is computed from the detailed balance principle. The transitions within higher vibrational levels, *i.e.* i_{O2} > 1 and i_2 > 2, are included with the same rate, without applying any scaling law. Finally, $Q_{VT_{12}}$ represents the energy transferred from T_{12} to T_g through V-T relaxation. This term includes the transitions listed in Table C2, taken from the survey of Blauer and Nickerson [152]. The notation used for the vibrational levels involved in the transitions is CO_2($i_1i_2i_3$).

Table C2. List of V-T transitions included in $Q_{VT_{12}}$.

V-T transition
CO_2(100) + M ⇋ CO_2(000) + M, M = CO_2, CO, O_2
CO_2(010) + M ⇋ CO_2(000) + M, M = CO_2, CO, O_2
CO_2(100) + M ⇋ CO_2(010) + M, M = CO_2, CO, O_2
CO_2(200) + M ⇋ CO_2(020) + M, M = CO_2, CO, O_2
CO_2(200) + M ⇋ CO_2(001) + M*, M = CO_2, CO, O_2
CO_2(030) + M ⇋ CO_2(100) + M, M = CO_2, CO, O_2

*The energy lost from T_{12} corresponds to ε_{200}, whereas $\varepsilon_{200} - \varepsilon_{001}$ is transferred to T_g and ε_{001} is transferred to T_3.

$Q_{VT_{12}}$ contains also V-T relaxation from the bending mode of CO_2 upon collisions with O atoms, with a rate coefficient of $2 \times 10^{-12}[\frac{cm^3}{s}] \cdot \sqrt{T_g/300[K]}$ taken from Terraz *et al*. [151].

$CO_2(00i_3)$ + CO ⇋ CO_2 + $CO(i_{CO})$ is taken from 152 with a rate coefficient of $1.66 \times 10^{-24} \left[\frac{cm^3}{s}\right] \cdot e^{28.7 - 153 \cdot T_g^{-2/3}}$, while, $CO_2(001) + O_2 \leftrightharpoons CO_2(010) + O_2(i_{O2}=1)$, is included from López-Puertas *et al*. [268], with a rate coefficient of $3 \times 10^{-15} \left[\frac{cm^3}{s}\right] \cdot (1 + 0.02 \cdot (T_g - 210))$. Q_{VT_3} includes the transitions listed in Table A3, taken from [152].

Table C3. List of V-T transitions included in Q_{VT_3}.

V-T transition
$CO_2(001) + M \leftrightharpoons CO_2(100) + M$, M = CO_2, CO, O_2
$CO_2(001) + M \leftrightharpoons CO_2(010) + M$, M = CO_2, CO, O_2
$CO_2(001) + M \leftrightharpoons CO_2(110) + M$, M = CO_2, CO, O_2

In addition to those listed in Table C3, Q_{VT_3} incorporates also V-T deactivation by collisions with O atoms, $CO_2(001) + O \leftrightharpoons CO_2(0i_20) + O$, with i_2 = 1, 2, 3 and 4. The rate coefficient for this transition is $2 \times 10^{-13}[\frac{cm^3}{s}] \cdot \sqrt{T_g/300[K]}$ and assumed independent of i_2 [151].

We would like to point out that all rate coefficients for CO_2 V-T and intra-molecular V-V-T relaxation involving higher vibrational levels are scaled based on the Schwartz–Slawsky–Herzfeld (SSH) theory [121, 132].

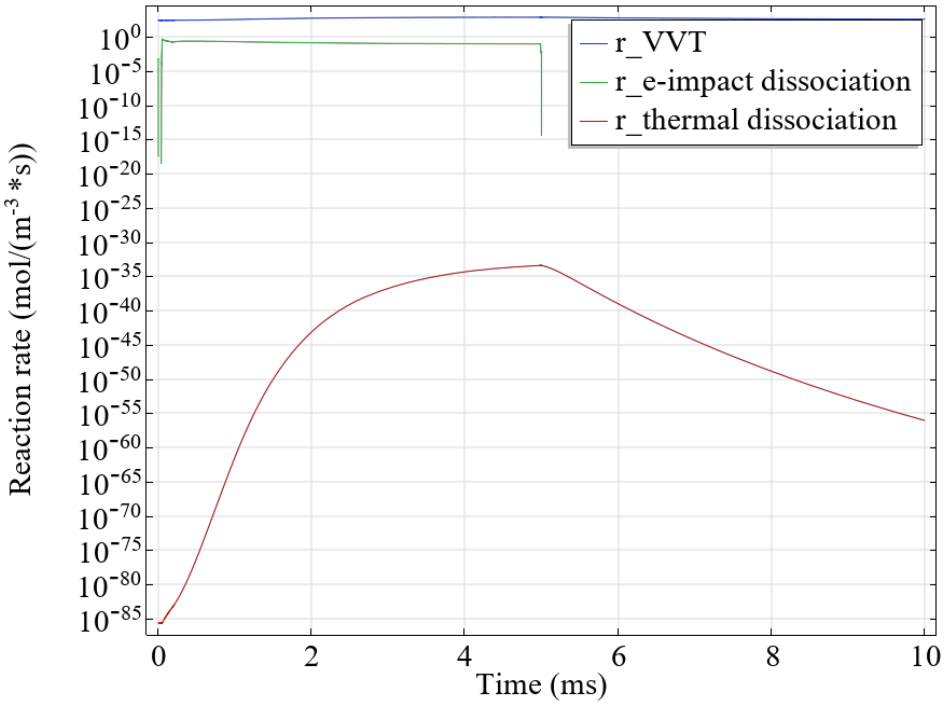

Figure C1. Rate of vibrational-vibrational-translational (VVT) relaxation, electron-impact (e-impact) dissociation and thermal dissociation reactions, as a function of the simulation time, for the single-pulse measurement of Klarenaar *et al.* [*108*].

Figure C1 shows that the rates of e-impact dissociation and thermal dissociation are 3 and more than 35 orders of magnitude lower than for vibrational relaxation, and thus, chemical reactions do not affect the loss/gain in vibrational energy.

References

(1) Arrhenius, S. On the Influence of Carbonic Acid in the Air upon the Temperature of the Ground. *Phil. Mag* **1986**, *41*.

(2) Zhou, X.; Li, Y.; Xiao, C.; Chen, W.; Mei, M.; Wang, G. High-impact Extreme Weather and Climate Events in China: Summer 2024 Overview. Springer: 2025.

(3) Nes, K.; Schaefer, K. A.; Gammans, M.; Scheitrum, D. P. Extreme weather events, climate expectations, and agricultural export dynamics. *American Journal of Agricultural Economics* **2025**.

(4) Paris Agreement. United Nations Framework Convention on Climate Change (UNFCCC): Paris, 2015.

(5) *Global Update – November 2024: As the climate crisis worsens, the warming outlook stagnates*; Climate Action Tracker, 2024. https://climateactiontracker.org/documents/1277/CAT_2024-11-14_GlobalUpdate_COP29.pdf.

(6) *Systems Change Lab*; World Resources Institute, Bezos Earth Fund, Washington, DC, 2025. https://www.systemschangelab.org.

(7) *State of Climate Action (SoCA) 2023*; World Resources Institute, Bezos Earth Fund, Washington, DC, 2023. https://systemschangelab.org/sites/default/files/2023-11/SoCA_2023_rev7.pdf.

(8) Shuka, P. R.; Iii, I. P. o. C. C. W. G. *Climate Change 2022: Mitigation of Climate Change : Working Group III Contribution to the Sixth Assessment Report of the Intergovernmental Panel on Climate Change*; Cambridge University Press, 2022.

(9) Wei, M.; McMillan, C. A.; De La Rue Du Can, S. Electrification of Industry: Potential, Challenges and Outlook. *Curr Sustainable Renewable Energy Rep* **2019**, *6*, 140-148.

(10) Snoeckx, R.; Bogaerts, A. Plasma technology–a novel solution for CO 2 conversion? *Chemical Society Reviews* **2017**, *46*, 5805-5863.

(11) Bogaerts, A.; Neyts, E. C. Plasma Technology: An Emerging Technology for Energy Storage. *ACS Energy Lett.* **2018**, *3*, 1013-1027.

(12) D-CRBN. https://d-crbn.com/ (accessed 2025 03 02).

(13) N2Applied. https://n2applied.com/ (accessed 2025 03 02).

(14) NitroCapt. https://nitrocapt.com/ (accessed 2025 03 02).

(15) HiiROC. https://hiiroc.com/ (accessed 2025 03 02).

(16) Smith, C.; Hill, A. K.; Torrente-Murciano, L. Current and future role of Haber–Bosch ammonia in a carbon-free energy landscape. *Energy & Environmental Science* **2020**, *13*, 331-344.

(17) Association, I. F. I. *Fertilizers, climate change and enhancing agricultural poroductivity sustainably*; International Fertilizer Industry Association 2009. https://www.fertilizer.org//images/Library_Downloads/2009_climate_change_brief.pdf.

(18) Rouwenhorst, K. H.; Jardali, F.; Bogaerts, A.; Lefferts, L. From the Birkeland–Eyde process towards energy-efficient plasma-based NO X synthesis: a techno-economic analysis. *Energy & environmental science* **2021**, *14*, 2520-2534.
(19) Kyriakou, V.; Garagounis, I.; Vasileiou, E.; Vourros, A.; Stoukides, M. Progress in the Electrochemical Synthesis of Ammonia. *Catalysis Today* **2017**, *286*, 2-13.
(20) Chen, F. F. *Introduction to plasma physics and controlled fusion*; Springer, 1984.
(21) Crookes, W. On radiant matter; a lecture delivered to the British Association for the Advancement of Science, at Sheffield, Friday, August 22, 1879. *American Journal of Science* **1879**, *3*, 241-262.
(22) Tonks, L. The birth of "plasma". *American Journal of Physics* **1967**, *35*, 857-858.
(23) Langmuir, I. Oscillations in ionized gases. *Proceedings of the National Academy of Sciences* **1928**, *14*, 627-637.
(24) Jones, E. W. Electric arc lamps. **1911**.
(25) Eyde, H. S. The manufacture of nitrates from the atmosphere by the electric arc—Birkeland-Eyde process. *Journal of the Royal Society of Arts* **1909**, *57*, 568-576.
(26) Sahoo, A.; Tripathy, S. Development in plasma arc welding process: a review. *Materials today: proceedings* **2021**, *41*, 363-368.
(27) Vardelle, A.; Moreau, C.; Themelis, N. J.; Chazelas, C. A perspective on plasma spray technology. *Plasma Chemistry and Plasma Processing* **2015**, *35*, 491-509.
(28) Ramakrishnan, S.; Gershenzon, M.; Polivka, F.; Kearney, T. N.; Rogozinski, M. W. Plasma generation for the plasma cutting process. *IEEE Transactions on plasma science* **1997**, *25*, 937-946.
(29) Abe, H.; Yoneda, M.; Fujiwara, N. Developments of plasma etching technology for fabricating semiconductor devices. *Jpn. J. Appl. Phys.* **2008**, *47*, 1435.
(30) Boulos, M. I.; Fauchais, P.; Pfender, E. *Thermal plasmas: fundamentals and applications*; Springer Science & Business Media, 2013.
(31) Hagelaar, G.; Pitchford, L. C. Solving the Boltzmann equation to obtain electron transport coefficients and rate coefficients for fluid models. *Plasma sources science and technology* **2005**, *14*, 722.
(32) Flitti, A.; Pancheshnyi, S. Gas heating in fast pulsed discharges in N2–O2 mixtures. *The European Physical Journal Applied Physics* **2009**, *45*, 21001.
(33) Maerivoet, S.; Tsonev, I.; Slaets, J.; Reniers, F.; Bogaerts, A. Coupled multi-dimensional modelling of warm plasmas: Application and validation for an atmospheric pressure glow discharge in CO2/CH4/O2. *Chemical Engineering Journal* **2024**, *492*, 152006.
(34) Raizer, Y. P.; Allen, J. E. *Gas discharge physics*; Springer, 1997.
(35) Fridman, A.; Nester, S.; Kennedy, L. A.; Saveliev, A.; Mutaf-Yardimci, O. Gliding arc gas discharge. *Progress in Energy and Combustion Science* **1999**, *25*, 211-231.
(36) Marshak, I. S. Strong-current pulse (spark) discharges in gas, used in pulsed light sources. *Sov. Phys. Usp.* **1962**, *5*, 478.

(37) Minesi, N.; Stepanyan, S.; Mariotto, P.; Stancu, G. D.; Laux, C. O. Fully ionized nanosecond discharges in air: the thermal spark. *Plasma Sources Science and Technology* **2020**, *29*, 085003.
(38) Gao, Y.; Zhang, S.; Sun, H.; Wang, R.; Tu, X.; Shao, T. Highly efficient conversion of methane using microsecond and nanosecond pulsed spark discharges. *Applied energy* **2018**, *226*, 534-545.
(39) Kogelschatz, U. Dielectric-barrier discharges: their history, discharge physics, and industrial applications. *Plasma chemistry and plasma processing* **2003**, *23*, 1-46.
(40) Fridman, A. *Plasma Chemistry*; Cambridge University Press, 2008.
(41) Hubert, J.; Moisan, M.; Ricard, A. A new microwave plasma at atmospheric pressure. *Spectrochimica Acta Part B: Atomic Spectroscopy* **1979**, *34*, 1-10.
(42) Kabouzi, Y.; Calzada, M. D.; Moisan, M.; Tran, K. C.; Trassy, C. Radial contraction of microwave-sustained plasma columns at atmospheric pressure. *Journal of Applied Physics* **2002**, *91*, 1008-1019.
(43) Van Poyer, H. M.; Tsonev, I.; Maerivoet, S. J.; Albrechts, M. C.; Bogaerts, A. Influence of radial transport and turbulent effects on CO2 conversion in a microwave plasma reactor: Insights from a multi-dimensional thermo-chemical flow model. *Chemical Engineering Journal* **2025**, 160688.
(44) Hong, J.; Prawer, S.; Murphy, A. B. Plasma Catalysis as an Alternative Route for Ammonia Production: Status, Mechanisms, and Prospects for Progress. *ACS Sustainable Chemistry & Engineering* **2017**, *6*, 15-31.
(45) Gorbanev, Y.; Engelmann, Y.; van't Veer, K.; Vlasov, E.; Ndayirinde, C.; Yi, Y.; Bals, S.; Bogaerts, A. Al2O3-Supported Transition Metals for Plasma-Catalytic NH3 Synthesis in a DBD Plasma: Metal Activity and Insights into Mechanisms. *Catalysts* **2021**, *11*.
(46) Chen, H.; Yuan, D.; Wu, A.; Lin, X.; Li, X. Review of low-temperature plasma nitrogen fixation technology. *Waste Dispos Sustain Energy* **2021**, *3*, 201-217.
(47) Winter, L. R.; Chen, J. G. N2 Fixation by Plasma-Activated Processes. *Joule* **2021**, *5*, 300-315.
(48) Rouwenhorst, K. H. R.; Engelmann, Y.; van 't Veer, K.; Postma, R. S.; Bogaerts, A.; Lefferts, L. Plasma-driven catalysis: green ammonia synthesis with intermittent electricity. *Green Chemistry* **2020**, *22*, 6258-6287.
(49) Hollevoet, L.; Vervloessem, E.; Gorbanev, Y.; Nikiforov, A.; De Geyter, N.; Bogaerts, A.; Martens, J. A. Energy-Efficient Small-Scale Ammonia Synthesis Process with Plasma-Enabled Nitrogen Oxidation and Catalytic Reduction of Adsorbed NOx. *ChemSusChem* **2022**, *15*, e202102526.
(50) Li, L.; Tang, C.; Cui, X.; Zheng, Y.; Wang, X.; Xu, H.; Zhang, S.; Shao, T.; Davey, K.; Qiao, S. Z. Efficient Nitrogen Fixation to Ammonia through Integration of Plasma Oxidation with Electrocatalytic Reduction. *Angew Chem Int Ed Engl* **2021**, *60*, 14131-14137.

(51) Rouwenhorst, K. H. R.; Jardali, F.; Bogaerts, A.; Lefferts, L. From the Birkeland-Eyde process towards energy-efficient plasma-based NO X synthesis: a techno-economic analysis. *Energy Environ Sci* **2021**, *14*, 2520-2534.
(52) Pei, X.; Gidon, D.; Graves, D. B. Specific energy cost for nitrogen fixation as NOx using DC glow discharge in air. *Journal of Physics D: Applied Physics* **2019**, *53*.
(53) Kelly, S.; Bogaerts, A. Nitrogen fixation in an electrode-free microwave plasma. *Joule* **2021**, *5*, 3006-3030.
(54) Lei, X.; Cheng, H.; Nie, L.; Lu, X. Nitrogen Fixation as NOx Enabled by a Three-Level Coupled Rotating Electrodes Air Plasma at Atmospheric Pressure. *Plasma Chemistry and Plasma Processing* **2022**, *42*, 211-227.
(55) Korolev, Y. D.; Frants, O. B.; Landl, N. V.; Suslov, A. I. Low-Current Plasmatron as a Source of Nitrogen Oxide Molecules. *IEEE Transactions on Plasma Science* **2012**, *40*, 2837-2842.
(56) Patil, B. S.; Peeters, F. J. J.; van Rooij, G. J.; Medrano, J. A.; Gallucci, F.; Lang, J.; Wang, Q.; Hessel, V. Plasma assisted nitrogen oxide production from air: Using pulsed powered gliding arc reactor for a containerized plant. *Aiche J* **2018**, *64*, 526-537.
(57) Jardali, F.; Van Alphen, S.; Creel, J.; Ahmadi Eshtehardi, H.; Axelsson, M.; Ingels, R.; Snyders, R.; Bogaerts, A. NOx production in a rotating gliding arc plasma: potential avenue for sustainable nitrogen fixation. *Green Chemistry* **2021**, *23*, 1748-1757.
(58) Van Alphen, S.; Ahmadi Eshtehardi, H.; O'Modhrain, C.; Bogaerts, J.; Van Poyer, H.; Creel, J.; Delplancke, M.-P.; Snyders, R.; Bogaerts, A. Effusion nozzle for energy-efficient NOx production in a rotating gliding arc plasma reactor. *Chemical Engineering Journal* **2022**, *443*.
(59) Tsonev, I.; O'Modhrain, C.; Bogaerts, A.; Gorbanev, Y. Nitrogen fixation by an arc plasma at elevated pressure to increase the energy efficiency and production rate of no x. *ACS Sustainable Chemistry & Engineering* **2023**, *11*, 1888-1897.
(60) Abdelaziz, A. A.; Teramoto, Y.; Kim, D.-Y.; Nozaki, T.; Kim, H.-H. Critical Considerations in Power Measurements for the Precise Estimation of Energy Costs in Plasma NO x Synthesis. *Plasma Chemistry and Plasma Processing* **2024**, 1-20.
(61) Rouwenhorst, K. H.; Jardali, F.; Bogaerts, A.; Lefferts, L. Correction: From the Birkeland–Eyde process towards energy-efficient plasma-based NO X synthesis: a techno-economic analysis. *Energy & environmental science* **2023**, *16*, 6170-6173.
(62) Rusanov, V. D.; Fridman, A. A.; Sholin, G. V. The physics of a chemically active plasma with nonequilibrium vibrational excitation of molecules. *Sov. Phys. Usp.* **1981**, *24*, 447-474.
(63) Raizer, Y. P. *Gas Discharge Physics*; Springer Berlin Heidelberg, 1991.
(64) Akishev, Y.; Grushin, M.; Karalnik, V.; Petryakov, A.; Trushkin, N. On basic processes sustaining constricted glow discharge in longitudinal N2 flow at atmospheric pressure. *Journal of Physics D: Applied Physics* **2010**, *43*, 215202.

(65) Rogoff, G. L. Gas heating effects in the constriction of a high-pressure glow discharge column. *The Physics of Fluids* **1972**, *15*, 1931-1940.
(66) Kelly, S.; van de Steeg, A.; Hughes, A.; van Rooij, G.; Bogaerts, A. Thermal instability and volume contraction in a pulsed microwave N2 plasma at sub-atmospheric pressure. *Plasma Sources Science and Technology* **2021**, *30*, 055005.
(67) Yu, L.; Pierrot, L.; Laux, C. O.; Kruger, C. H. Effects of vibrational nonequilibrium on the chemistry of two-temperature nitrogen plasmas. *Plasma Chemistry and Plasma Processing* **2001**, *21*, 483-503.
(68) Yu, L.; Laux, C. O.; Packan, D. M.; Kruger, C. H. Direct-current glow discharges in atmospheric pressure air plasmas. *Journal of applied physics* **2002**, *91*, 2678-2686.
(69) Prevosto, L.; Kelly, H.; Mancinelli, B. Modelling of an atmospheric pressure nitrogen glow discharge operating in high-gas temperature regimes. *Plasma Chemistry and Plasma Processing* **2016**, *36*, 973-992.
(70) Naidis, G. V. Simulation of convection-stabilized low-current glow and arc discharges in atmospheric-pressure air. *Plasma Sources Science and Technology* **2007**, *16*, 297-303.
(71) Kabouzi, Y.; Calzada, M.; Moisan, M.; Tran, K.; Trassy, C. Radial contraction of microwave-sustained plasma columns at atmospheric pressure. *Journal of applied physics* **2002**, *91*, 1008-1019.
(72) Lowke, J. Simple theory of free-burning arcs. *Journal of physics D: Applied physics* **1979**, *12*, 1873.
(73) Shneider, M.; Mokrov, M.; Milikh, G. Dynamic contraction of the positive column of a self-sustained glow discharge in air flow. *Physics of Plasmas* **2014**, *21*.
(74) Shneider, M.; Mokrov, M.; Milikh, G. Dynamic contraction of the positive column of a self-sustained glow discharge in molecular gas. *Physics of Plasmas* **2012**, *19*.
(75) Boxman, R. L.; Sanders, D. M.; Martin, P. J. *Handbook of vacuum arc science & technology: fundamentals and applications*; William Andrew, 1996.
(76) Benilov, M. S. Understanding and modelling plasma–electrode interaction in high-pressure arc discharges: a review. *Journal of Physics D: Applied Physics* **2008**, *41*.
(77) Baeva, M. Non-equilibrium modeling of tungsten-inert gas arcs. *Plasma Chemistry and Plasma Processing* **2017**, *37*, 341-370.
(78) Baeva, M.; Benilov, M.; Almeida, N.; Uhrlandt, D. Novel non-equilibrium modelling of a DC electric arc in argon. *Journal of Physics D: Applied Physics* **2016**, *49*, 245205.
(79) Liang, P.; Trelles, J. 3D numerical investigation of a free-burning argon arc with metal electrodes using a novel sheath coupling procedure. *Plasma Sources Science and Technology* **2019**, *28*, 115012.
(80) Almeida, N.; Benilov, M.; Naidis, G. Unified modelling of near-cathode plasma layers in high-pressure arc discharges. *Journal of Physics D: Applied Physics* **2008**, *41*, 245201.

(81) Wang, H.-X.; Zhu, T.; Sun, S.-R.; Liu, G.; Murphy, A. B. Chemical nonequilibrium modelling of a free-burning nitrogen arc. *Journal of Physics D: Applied Physics* **2020**, *53*, 505205.
(82) Kolev, S.; Bogaerts, A. Similarities and differences between gliding glow and gliding arc discharges. *Plasma Sources Science and Technology* **2015**, *24*, 065023.
(83) *COMSOL Multiphysics® v. 6.2*; COMSOL AB: Stockholm, Sweden, https://www.comsol.com/ (accessed.
(84) Konuma, M. *Film deposition by plasma techniques*; Springer Science & Business Media, 2012.
(85) Haase, J. R.; Go, D. B. Analysis of thermionic and thermo-field emission in microscale gas discharges. *Journal of Physics D: Applied Physics* **2016**, *49*, 055206.
(86) Lide, D. R. *CRC handbook of chemistry and physics*; CRC press, 2004.
(87) Plasma Module User's Guide, pp. 120, COMSOL Multiphysics® v. 6.2. COMSOL AB, Stockholm, Sweden: 2023.
(88) Li, Y.; Luo, Y.; Man, C.; Pei, X.; Lu, X.; Graves, D. B. Enhancing nitrogen fixation efficiency in glow-like discharge by reducing cathode-fall voltage. *Plasma Sources Science and Technology* **2024**, *33*, 105014.
(89) Fulcheri, L.; Rohani, V.; Fabry, F.; Traisnel, N. Experimental electrical characterization of a low-current tip–tip arc discharge in helium atmosphere at very high pressure. *Plasma Sources Science and Technology* **2010**, *19*.
(90) Gueye, P.; Cressault, Y.; Rohani, V.; Fulcheri, L. MHD modeling of rotating arc under restrike mode in 'Kvaerner-type' torch: II. Dynamics and stability at 20 bar pressure. *Journal of Physics D: Applied Physics* **2019**, *52*.
(91) Eliasson, B.; Kogelschatz, U.; Xue, B.; Zhou, L.-M. Hydrogenation of Carbon Dioxide to Methanol with a Discharge-Activated Catalyst. *Industrial & Engineering Chemistry Research* **1998**, *37*, 3350-3357.
(92) Uytdenhouwen, Y.; Bal, K. M.; Michielsen, I.; Neyts, E. C.; Meynen, V.; Cool, P.; Bogaerts, A. How process parameters and packing materials tune chemical equilibrium and kinetics in plasma-based CO2 conversion. *Chemical Engineering Journal* **2019**, *372*, 1253-1264.
(93) Iwarere, S.; Rohani, V.; Ramjugernath, D.; Fabry, F.; Fulcheri, L. Hydrocarbons synthesis from syngas by very high pressure plasma. *Chemical Engineering Journal* **2014**, *241*, 1-8.
(94) Adamovich, I.; Agarwal, S.; Ahedo, E.; Alves, L. L.; Baalrud, S.; Babaeva, N.; Bogaerts, A.; Bourdon, A.; Bruggeman, P. J.; Canal, C.; et al. The 2022 Plasma Roadmap: low temperature plasma science and technology. *Journal of Physics D: Applied Physics* **2022**, *55*.
(95) Wutzke, S. A.; Pfender, E.; Eckert, E. R. G. Study of electric arc behavior with superimposed flow. *AIAA Journal* **1967**, *5*, 707-713.

(96) Trelles, J. P.; Pfender, E.; Heberlein, J. Multiscale Finite Element Modeling of Arc Dynamics in a DC Plasma Torch. *Plasma Chemistry and Plasma Processing* **2006**, *26*, 557-575.
(97) Vervloessem, E.; Gorbanev, Y.; Nikiforov, A.; De Geyter, N.; Bogaerts, A. Sustainable NOx production from air in pulsed plasma: elucidating the chemistry behind the low energy consumption. *Green Chemistry* **2022**, *24*, 916-929.
(98) Bian, W.; Song, X.; Shi, J.; Yin, X. Nitrogen fixed into HNO3 by pulsed high voltage discharge. *Journal of Electrostatics* **2012**, *70*, 317-326.
(99) Pei, X.; Gidon, D.; Yang, Y.-J.; Xiong, Z.; Graves, D. B. Reducing energy cost of NO production in air plasmas. *Chemical Engineering Journal* **2019**, *362*, 217-228.
(100) Noguès, E.; Fauchais, P.; Vardelle, M.; Granger, P. Relation Between the Arc-Root Fluctuations, the Cold Boundary Layer Thickness and the Particle Thermal Treatment. *Journal of Thermal Spray Technology* **2007**, *16*, 919-926.
(101) Attri, P.; Koga, K.; Okumura, T.; Takeuchi, N.; Shiratani, M. Green route for ammonium nitrate synthesis: fertilizer for plant growth enhancement. *RSC Adv* **2021**, *11*, 28521-28529.
(102) Burm, K. T. A. L. Plasma: The Fourth State of Matter. *Plasma Chemistry and Plasma Processing* **2012**, *32*, 401-407.
(103) D'Angola, A.; Colonna, G.; Gorse, C.; Capitelli, M. Thermodynamic and transport properties in equilibrium air plasmas in a wide pressure and temperature range. *The European Physical Journal D* **2007**, *46*, 129-150.
(104) Baulch, D. L.; Bowman, C. T.; Cobos, C. J.; Cox, R. A.; Just, T.; Kerr, J. A.; Pilling, M. J.; Stocker, D.; Troe, J.; Tsang, W.; et al. Evaluated Kinetic Data for Combustion Modeling: Supplement II. *Journal of Physical and Chemical Reference Data* **2005**, *34*, 757-1397.
(105) Ingels. Low pressure generating plasma reactor closed loop process and system. 20210402362, 2021.
(106) Ghorui, S.; Heberlein, J. V. R.; Pfender, E. Thermodynamic and Transport Properties of Two-Temperature Nitrogen-Oxygen Plasma. *Plasma Chemistry and Plasma Processing* **2008**, *28*, 553-582.
(107) Rivallan, M.; Aiello, S.; Thibault-Starzyk, F. Microsecond time-resolved Fourier transform infrared analytics in a low pressure glow discharge reactor. *Review of Scientific Instruments* **2010**, *81*, 103111.
(108) Klarenaar, B. L. M.; Engeln, R.; Van Den Bekerom, D. C. M.; Van De Sanden, M. C. M.; Morillo-Candas, A. S.; Guaitella, O. Time evolution of vibrational temperatures in a CO ₂ glow discharge measured with infrared absorption spectroscopy. *Plasma Sources Science and Technology* **2017**, *26*, 115008.
(109) Amat, G.; Pimbert, M. On Fermi resonance in carbon dioxide. *Journal of Molecular Spectroscopy* **1965**, *16*, 278-290.
(110) Jacobs, R. R.; Pettipiece, K. J.; Thomas, S. J. Rotational relaxation rate constants for CO2. *Applied Physics Letters* **1974**, *24*, 375-377.

(111) Dang, C.; Reid, J.; Garside, B. K. Detailed vibrational population distributions in a CO2 laser discharge as measured with a tunable diode laser. *Appl. Phys. B* **1982**, *27*, 145-151.
(112) Klarenaar, B. L. M.; Grofulović, M.; Morillo-Candas, A. S.; Bekerom, D. C. M. V. D.; Damen, M. A.; Sanden, M. C. M. V. D.; Guaitella, O.; Engeln, R. A rotational Raman study under non-thermal conditions in a pulsed CO ₂ glow discharge. *Plasma Sources Science and Technology* **2018**, *27*, 045009.
(113) Van Den Bekerom, D. C. M.; Palomares Linares, J. M.; Van Veldhuizen, E. M.; Nijdam, S.; Van De Sanden, M. C. M.; Van Rooij, G. J. How the alternating degeneracy in rotational Raman spectra of CO ₂ and C ₂ H ₂ reveals the vibrational temperature. *Appl. Opt.* **2018**, *57*, 5694.
(114) Klarenaar, B. L. M.; Morillo-Candas, A. S.; Grofulović, M.; Sanden, M. C. M. V. D.; Engeln, R.; Guaitella, O. Excitation and relaxation of the asymmetric stretch mode of CO ₂ in a pulsed glow discharge. *Plasma Sources Science and Technology* **2019**, *28*, 035011.
(115) Damen, M. A.; Martini, L. M.; Engeln, R. Temperature evolution in a pulsed CO ₂ –N ₂ glow discharge measured using quantum cascade laser absorption spectroscopy. *Plasma Sources Science and Technology* **2020**, *29*, 065016.
(116) Damen, M. A.; Martini, L. M.; Engeln, R. Vibrational quenching by water in a CO ₂ glow discharge measured using quantum cascade laser absorption spectroscopy. *Plasma Sources Science and Technology* **2020**, *29*, 095017.
(117) Vervloedt, S. C. L.; Budde, M.; Engeln, R. Influence of oxygen on the ro-vibrational kinetics of a non-equilibrium discharge in CO ₂ –O ₂ mixtures. *Plasma Sources Science and Technology* **2023**, *32*, 015004.
(118) Hurlbatt, A.; Gibson, A. R.; Schröter, S.; Bredin, J.; Foote, A. P. S.; Grondein, P.; O'Connell, D.; Gans, T. Concepts, Capabilities, and Limitations of Global Models: A Review. *Plasma Processes and Polymers* **2017**, *14*, 1600138.
(119) Alves, L. L.; Bogaerts, A.; Guerra, V.; Turner, M. M. Foundations of modelling of nonequilibrium low-temperature plasmas. *Plasma Sources Science and Technology* **2018**, *27*, 023002.
(120) Aerts, R.; Martens, T.; Bogaerts, A. Influence of Vibrational States on CO ₂ Splitting by Dielectric Barrier Discharges. *J. Phys. Chem. C* **2012**, *116*, 23257-23273.
(121) Kozák, T.; Bogaerts, A. Splitting of CO ₂ by vibrational excitation in non-equilibrium plasmas: a reaction kinetics model. *Plasma Sources Science and Technology* **2014**, *23*, 045004.
(122) Treanor, C. E. Vibrational Energy Transfer in High-Energy Collisions. *The Journal of Chemical Physics* **1965**, *43*, 532-538.

(123) Kozák, T.; Bogaerts, A. Evaluation of the energy efficiency of CO ₂ conversion in microwave discharges using a reaction kinetics model. *Plasma Sources Science and Technology* **2014**, *24*, 015024.
(124) Berthelot, A.; Bogaerts, A. Modeling of plasma-based CO ₂ conversion: lumping of the vibrational levels. *Plasma Sources Science and Technology* **2016**, *25*, 045022.
(125) Berthelot, A.; Bogaerts, A. Modeling of CO ₂ Splitting in a Microwave Plasma: How to Improve the Conversion and Energy Efficiency. *J. Phys. Chem. C* **2017**, *121*, 8236-8251.
(126) Silva, T.; Grofulović, M.; Klarenaar, B. L. M.; Morillo-Candas, A. S.; Guaitella, O.; Engeln, R.; Pintassilgo, C. D.; Guerra, V. Kinetic study of low-temperature CO ₂ plasmas under non-equilibrium conditions. I. Relaxation of vibrational energy. *Plasma Sources Science and Technology* **2018**, *27*, 015019.
(127) Grofulović, M.; Silva, T.; Klarenaar, B. L. M.; Morillo-Candas, A. S.; Guaitella, O.; Engeln, R.; Pintassilgo, C. D.; Guerra, V. Kinetic study of CO ₂ plasmas under non-equilibrium conditions. II. Input of vibrational energy. *Plasma Sources Science and Technology* **2018**, *27*, 115009.
(128) Silva, T.; Grofulović, M.; Terraz, L.; Pintassilgo, C. D.; Guerra, V. Dynamics of Gas Heating in the Afterglow of Pulsed CO2 and CO2–N2 Glow Discharges at Low Pressure. *Plasma Chemistry and Plasma Processing* **2020**, *40*, 713-725.
(129) Kotov, V. Vibrational relaxation and triggering of the non-equilibrium vibrational decomposition of CO ₂ in gas discharges. *Plasma Sources Science and Technology* **2022**, *31*, 094002.
(130) Kotov, V. Two-modes model of the non-equilibrium plasma chemical dissociation of CO ₂. *Plasma Sources Science and Technology* **2021**, *30*, 055003.
(131) Pietanza, L. D.; Colonna, G.; Capitelli, M. Non-equilibrium plasma kinetics of CO ₂ in glow discharges: a comparison with existing modeling and experimental results. *Plasma Sources Science and Technology* **2022**, *31*, 104001.
(132) Biondo, O.; Fromentin, C.; Silva, T.; Guerra, V.; Van Rooij, G.; Bogaerts, A. Insights into the limitations to vibrational excitation of CO ₂ : validation of a kinetic model with pulsed glow discharge experiments. *Plasma Sources Science and Technology* **2022**, *31*, 074003.
(133) Smith, K.; Thomson, R. M. *Computer Modeling of Gas Lasers*; Springer US, 1978.
(134) Kustova, E. V.; Nagnibeda, E. A. On a correct description of a multi-temperature dissociating CO2 flow. *Chemical Physics* **2006**, *321*, 293-310.
(135) Kustova, E.; Mekhonoshina, M.; Kosareva, A. Relaxation processes in carbon dioxide. *Physics of Fluids* **2019**, *31*, 046104.
(136) Kunova, O.; Kosareva, A.; Kustova, E.; Nagnibeda, E. Vibrational relaxation of carbon dioxide in state-to-state and multi-temperature approaches. *Phys. Rev. Fluids* **2020**, *5*, 123401.

(137) Kustova, E.; Mekhonoshina, M. Novel approach for evaluation of CO2 vibrational relaxation times. *Chemical Physics Letters* **2021**, *764*, 138288.
(138) Adamovich, I. V.; Macheret, S. O.; Rich, J. W.; Treanor, C. E. Vibrational Energy Transfer Rates Using a Forced Harmonic Oscillator Model. *Journal of Thermophysics and Heat Transfer* **1998**, *12*, 57-65.
(139) Pietanza, L. D.; Colonna, G.; Capitelli, M. Self-Consistent State-to-State Kinetic Modeling of CO2 Cold Plasmas: Insights on the Role of Electronically Excited States. *Plasma Chemistry and Plasma Processing* **2024**, *44*, 1431-1468.
(140) Koelman, P.; Heijkers, S.; Tadayon Mousavi, S.; Graef, W.; Mihailova, D.; Kozak, T.; Bogaerts, A.; Van Dijk, J. A Comprehensive Chemical Model for the Splitting of CO₂ in Non-Equilibrium Plasmas. *Plasma Processes and Polymers* **2017**, *14*, 1600155.
(141) Cenian, A.; Chernukho, A.; Borodin, V. Modeling of Plasma-Chemical Reactions in Gas Mixture of CO ₂ lasers. II. Theoretical Model and its Verification. *Contrib. Plasma Phys.* **1995**, *35*, 273-296.
(142) Shields, H.; Smith, A. L. S.; Norris, B. Negative ion effects in TEA CO ₂ lasers. *Journal of Physics D: Applied Physics* **1976**, *9*, 1587-1603.
(143) Phelps, A. V. The diffusion of charged particles in collisional plasmas: Free and ambipolar diffusion at low and moderate pressures. *J. RES. NATL. INST. STAN.* **1990**, *95*, 407.
(144) Silva, A. F.; Morillo-Candás, A. S.; Tejero-del-Caz, A.; Alves, L. L.; Guaitella, O.; Guerra, V. A reaction mechanism for vibrationally-cold low-pressure CO ₂ plasmas. *Plasma Sources Science and Technology* **2020**, *29*, 125020.
(145) Guerra, V.; Loureiro, J. Self-consistent electron and heavy-particle kinetics in a low-pressure-glow discharge. *Plasma Sources Science and Technology* **1997**, *6*, 373.
(146) Ellis, H. W.; Pai, R. Y.; McDaniel, E. W.; Mason, E. A.; Viehland, L. A. Transport properties of gaseous ions over a wide energy range. *Atomic Data and Nuclear Data Tables* **1976**, *17*, 177-210.
(147) Cenian, A. Study of nonequilibrium vibrational relaxation of CO2 molecules during adiabatic expansion in a supersonic nozzle. The treanor type distribution - existence and generation. *Chemical Physics* **1989**, *132*, 41-48.
(148) Marrone, P. V.; Treanor, C. E. Chemical relaxation with preferential dissociation from excited vibrational levels. *The Physics of Fluids* **1963**, *6*, 1215-1221.
(149) Kosareva, A.; Kunova, O.; Kustova, E.; Nagnibeda, E. Hybrid approach to accurate modeling of coupled vibrational-chemical kinetics in carbon dioxide. *Physics of Fluids* **2022**, *34*.
(150) Pintassilgo, C. D.; Guerra, V.; Guaitella, O.; Rousseau, A. Study of gas heating mechanisms in millisecond pulsed discharges and afterglows in air at low pressures. *Plasma Sources Science and Technology* **2014**, *23*, 025006.

(151) Terraz, L.; Silva, T.; Morillo-Candas, A.; Guaitella, O.; Tejero-del-Caz, A.; Alves, L. L.; Guerra, V. Influence of N ₂ on the CO ₂ vibrational distribution function and dissociation yield in non-equilibrium plasmas. *Journal of Physics D: Applied Physics* **2020**, *53*, 094002.
(152) Blauer, J.; Nickerson, G. A survey of vibrational relaxation rate data for processes importantto CO2-N2-H2O infrared plume radiation. In *7th Fluid and PlasmaDynamics Conference*, 1974/06/17/, 1974; American Institute of Aeronautics and Astronautics: Palo Alto,CA,U.S.A. DOI: 10.2514/6.1974-536.
(153) Fromentin, C.; Silva, T.; Dias, T. C.; Morillo-Candas, A. S.; Biondo, O.; Guaitella, O.; Guerra, V. Study of vibrational kinetics of CO ₂ and CO in CO ₂ –O ₂ plasmas under non-equilibrium conditions. *Plasma Sources Science and Technology* **2023**, *32*, 024001.
(154) Fromentin, C.; Silva, T.; Dias, T. C.; Baratte, E.; Guaitella, O.; Guerra, V. Validation of non-equilibrium kinetics in CO ₂ –N ₂ plasmas. *Plasma Sources Science and Technology* **2023**, *32*, 054004.
(155) Thomson, R. M. The thermal conductivity of gases with vibrational internal energy. *Journal of Physics D: Applied Physics* **1978**, *11*, 2509-2516.
(156) Eucken, A. On the thermal conductivity, the specific heat and the viscosity of gases. *Physikalische Zeitschrift* **1913**, *14*, 324-333.
(157) Neufeld, P. D.; Janzen, A. R.; Aziz, R. A. Empirical Equations to Calculate 16 of the Transport Collision Integrals Ω(l, s)* for the Lennard-Jones (12–6) Potential. *The Journal of Chemical Physics* **1972**, *57*, 1100-1102.
(158) Brokaw, R. S. Predicting Transport Properties of Dilute Gases. *Ind. Eng. Chem. Proc. Des. Dev.* **1969**, *8*, 240-253.
(159) Kee, R. J.; Coltrin, M. E.; Glarborg, P. *Chemically Reacting Flow: Theory and Practice*; Wiley, 2003.
(160) McBride, B. J.; Zehe, M. J.; Sanford, G. NASA Glenn Coefficients for Calculating Thermodynamic Properties of Individual Species. 2002.
(161) Goos, E.; Burcat, A.; Ruscic, B. EXTENDED THIRD MILLENIUM IDEAL GAS AND CONDENSED PHASE THERMOCHEMICAL DATABASE FOR COMBUSTION WITH UPDATES FROM ACTIVE THERMOCHEMICAL TABLES.
(162) Illies, A. J. Thermochemistry for the gas-phase ion-molecule clustering of CO2+CO2, SO2+CO2, N2O+N2O, O2+CO2, NO+CO2, O2+N2O and NO+N2O: description of a new hybrid drift tube/ion source with coaxial electron beam and ion exit apertures. *J. Phys. Chem.* **1988**, *92*, 2889-2896.
(163) Linstrom, P. NIST Chemistry WebBook, NIST Standard Reference Database 69. National Institute of Standards and Technology: 1997.
(164) Vermeiren, V.; Bogaerts, A. Improving the Energy Efficiency of CO₂ Conversion in Nonequilibrium Plasmas through Pulsing. *J. Phys. Chem. C* **2019**, *123*, 17650-17665.

(165) Nagnibeda, E.; Kustova, E. *Non-Equilibrium Reacting Gas Flows*; Springer Berlin Heidelberg, 2009.
(166) Moruzzi, J. L.; Phelps, A. V. Survey of Negative-Ion—Molecule Reactions in O2, CO2, H2O, CO, and Mixtures of These Gases at High Pressures. *The Journal of Chemical Physics* **1966**, *45*, 4617-4627.
(167) Ranjan, R.; Goodyear, C. C. Collisional detachment from atmospheric negative ions. *J. Phys. B: At. Mol. Phys.* **1973**, *6*, 1070-1078.
(168) Naidis, G. V.; Babaeva, N. Y. Modeling of repetitively pulsed low-pressure CO2 discharges. *Physics of Plasmas* **2022**, *29*, 044501.
(169) Paulson, J. F.; Dale, F.; Mosher, R. L. Production of C2O4+ in an Ion-molecule Reaction. *Nature* **1964**, *204*, 377-378.
(170) Rakshit, A. B.; Warneck, P. Formation and reactions of O2+·CO2, O2+·H2O and O2+(CO2)2 ions. *International Journal of Mass Spectrometry and Ion Physics* **1981**, *40*, 135-155.
(171) Patil, B.; Wang, Q.; Hessel, V.; Lang, J. Plasma N2-fixation: 1900–2014. *Catalysis today* **2015**, *256*, 49-66.
(172) Capitelli, M.; Ferreira, C. M.; Gordiets, B. F.; Osipov, A. I. *Plasma kinetics in atmospheric gases*; Springer Science & Business Media, 2013.
(173) Liu, J.; Nie, L.; Liu, D.; Lu, X. Plasma for nitrogen fixation by using N2/O2 mixture: Reaction pathway, energy flow, and plasma reactor. *Plasma Processes and Polymers* **2024**, *21*, 2300153.
(174) Guerra, V.; Sa, P.; Loureiro, J. Role played by the N2 (A3Σu+) metastable in stationary N2 and N2-O2 discharges. *Journal of Physics D: Applied Physics* **2001**, *34*, 1745.
(175) Pintassilgo, C.; Guaitella, O.; Rousseau, A. Heavy species kinetics in low-pressure dc pulsed discharges in air. *Plasma Sources Science and Technology* **2009**, *18*, 025005.
(176) Uddi, M.; Jiang, N.; Adamovich, I.; Lempert, W. Nitric oxide density measurements in air and air/fuel nanosecond pulse discharges by laser induced fluorescence. *Journal of Physics D: Applied Physics* **2009**, *42*, 075205.
(177) Shkurenkov, I.; Burnette, D.; Lempert, W. R.; Adamovich, I. V. Kinetics of excited states and radicals in a nanosecond pulse discharge and afterglow in nitrogen and air. *Plasma Sources Science and Technology* **2014**, *23*, 065003.
(178) Popov, N. A.; Starikovskaia, S. M. Relaxation of electronic excitation in nitrogen/oxygen and fuel/air mixtures: fast gas heating in plasma-assisted ignition and flame stabilization. *Progress in Energy and Combustion Science* **2022**, *91*, 100928.
(179) Wang, W.; Patil, B.; Heijkers, S.; Hessel, V.; Bogaerts, A. Nitrogen fixation by gliding arc plasma: better insight by chemical kinetics modelling. *ChemSusChem* **2017**, *10*, 2145-2157.

(180) Vervloessem, E.; Aghaei, M.; Jardali, F.; Hafezkhiabani, N.; Bogaerts, A. Plasma-based n2 fixation into no x: insights from modeling toward optimum yields and energy costs in a gliding arc plasmatron. *ACS Sustainable Chemistry & Engineering* **2020**, *8*, 9711-9720.
(181) Tsonev, I.; Eshtehardi, H. A.; Delplancke, M.-P.; Bogaerts, A. Importance of geometric effects in scaling up energy-efficient plasma-based nitrogen fixation. *Sustainable Energy & Fuels* **2024**, *8*, 2191-2209.
(182) Esposito, F. On the relevance of accurate input data for vibrational kinetics in air cold plasmas: the case of nitrogen fixation. *Plasma Sources Science and Technology* **2022**, *31*, 094010.
(183) Qiao, J.-J.; Yang, Q.; Wang, D.-Z.; Pei, X.-K.; Xiong, Q. Assessing the efficacy of an atmospheric air DC glow discharge system for sustainable nitrogen fixation: a vibrational coherent anti-Stokes Raman scattering study. *Plasma Sources Science and Technology* **2024**, *33*, 055004.
(184) Tatar, M.; Vashisth, V.; Iqbal, M.; Butterworth, T.; van Rooij, G.; Andersson, R. Analysis of a plasma reactor performance for direct nitrogen fixation by use of three-dimensional simulations and experiments. *Chemical Engineering Journal* **2024**, *497*, 154756.
(185) Lo, A.; Cessou, A.; Boubert, P.; Vervisch, P. Space and time analysis of the nanosecond scale discharges in atmospheric pressure air: I. Gas temperature and vibrational distribution function of N2 and O2. *Journal of Physics D: Applied Physics* **2014**, *47*, 115201.
(186) Qiao, J.-J.; Yang, Q.; Wang, D.-Z.; Xiong, Q. Energy efficiency of N2 vibrational excitation in the spark-and-glow phases of a long-pulse air discharge at atmospheric pressure. *Plasma Sources Science and Technology* **2023**, *32*, 11LT01.
(187) Lino da Silva, M.; Lopez, B.; Guerra, V.; Loureiro, J. A multiquantum state-to-state model for the fundamental states of air: The stellar database. *ESA Special Publication* **2012**, *714*, 16.
(188) Bose, D.; Candler, G.; Bose, D.; Candler, G. Thermal nonequilibrium rates of the Zeldovich reactions. In *35th Aerospace Sciences Meeting and Exhibit*, 1997; p 133.
(189) Oblapenko, G. Calculation of vibrational relaxation times using a kinetic theory approach. *J. Phys. Chem. A* **2018**, *122*, 9615-9625.
(190) SIGLO database. available at: www.lxcat.net. (accessed 7 December 2022).
(191) Wang, Y.; Zatsarinny, O.; Bartschat, K. B-spline R-matrix-with-pseudostates calculations for electron-impact excitation and ionization of nitrogen. *Physical Review A* **2014**, *89*, 062714.
(192) BSR database. (accessed 29 April 2022).
(193) Slovetskii, D. Mechanisms of chemical reactions in nonequilibrium plasma. Nauka, Moscow: 1980.
(194) Alves, L. L. The IST-LISBON database on LXCat. *J. Phys.: Conf. Ser.* **2014**, *565*, 012007.

(195) Polak, L.; Slovetsky, D. Electron impact induced electronic excitation and molecular dissociation. *International Journal for Radiation Physics and Chemistry* **1976**, *8*, 257-282.
(196) Ogloblina, P.; Tejero-del-Caz, A.; Guerra, V.; Alves, L. L. Electron impact cross sections for carbon monoxide and their importance in the electron kinetics of CO ₂ –CO mixtures. *Plasma Sources Science and Technology* **2020**, *29*, 015002.
(197) Gousset, G.; Ferreira, C. M.; Pinheiro, M.; Sa, P. A.; Touzeau, M.; Vialle, M.; Loureiro, J. Electron and heavy-particle kinetics in the low pressure oxygen positive column. *Journal of Physics D: Applied Physics* **1991**, *24*, 290-300.
(198) Alves, L. L.; Coche, P.; Ridenti, M. A.; Guerra, V. Electron scattering cross sections for the modelling of oxygen-containing plasmas*. *The European Physical Journal D* **2016**, *70*, 124.
(199) Pack, J. L.; Phelps, A. V. Electron Attachment and Detachment. II. Mixtures of O2 and CO2 and of O2 and H2O. *The Journal of Chemical Physics* **1966**, *45*, 4316-4329.
(200) Kossyi, I. A.; Kostinsky, A. Y.; Matveyev, A. A.; Silakov, V. P. Kinetic scheme of the non-equilibrium discharge in nitrogen-oxygen mixtures. *Plasma Sources Science and Technology* **1992**, *1*, 207-220.
(201) Feoktistov, V. A.; Mukhovatova, A. V.; Popov, A. M.; Rakhimova, T. V. Self-consistent modelling of low-pressure RF discharges in oxygen plasma. *Journal of Physics D: Applied Physics* **1995**, *28*, 1346-1383.
(202) Morgan, L. W. Morgan (Kinema Research & Software).
(203) Donovan, R. J.; Husain, D. Vibrational excitation of carbon monoxide following quenching of the a 3? state. *Trans. Faraday Soc.* **1967**, *63*, 2879.
(204) Murakami, T.; Niemi, K.; Gans, T.; O'Connell, D.; Graham, W. G. Chemical kinetics and reactive species in atmospheric pressure helium–oxygen plasmas with humid-air impurities. *Plasma Sources Science and Technology* **2012**, *22*, 015003.
(205) Zinn, J.; Sutherland, C. D.; Stone, S. N.; Duncan, L. M.; Behnke, R. Ionospheric effects of rocket exhaust products—heao-c, skylab. *Journal of Atmospheric and Terrestrial Physics* **1982**, *44*, 1143-1171.
(206) Cobos, C.; Castellano, E.; Schumacher, H. J. The kinetics and the mechanism of ozone photolysis at 253.7 nm. *Journal of Photochemistry* **1983**, *21*, 291-312.
(207) Baulch, D. L.; Cox, R. A.; Hampson, R. F.; Kerr, J. A.; Troe, J.; Watson, R. T. Evaluated Kinetic and Photochemical Data for Atmospheric Chemistry: Supplement II. CODATA Task Group on Gas Phase Chemical Kinetics. *Journal of Physical and Chemical Reference Data* **1984**, *13*, 1259-1380.
(208) Tully, J. C. Reactions of O(1 D) with atmospheric molecules. *The Journal of Chemical Physics* **1975**, *62*, 1893-1898.
(209) Sedlacek, A. J.; Harding, D. R.; Weston, R. E.; Kreutz, T. G.; Flynn, G. W. Probing the O(1 D)+CO2 reaction with second-derivative modulated diode laser spectroscopy. *The Journal of Chemical Physics* **1989**, *91*, 7550-7556.

(210) Bortner, M.; Baurer, T. Defense Nuclear Agency reaction rate hand-book, Revision number 7. *Unknown* **1978**.
(211) Black, G.; Sharpless, R. L.; Slanger, T. G.; Lorents, D. C. Quantum yields for the production of O(1 S), N(2 D), and N2(A 3Σ+ u) from the vacuum uv photolysis of N2O. *The Journal of Chemical Physics* **1975**, *62*, 4266-4273.
(212) Slanger, T. G.; Black, G. O(1 S) interactions—the product channels. *The Journal of Chemical Physics* **1978**, *68*, 989-997.
(213) Capetanakis, F. P.; Sondermann, F.; Höser, S.; Stuhl, F. Temperature dependence of the quenching of O(1 S) by simple inorganic molecules. *The Journal of Chemical Physics* **1993**, *98*, 7883-7887.
(214) Stuhl, F.; Welge, K. H. Deactivation of O(¹ S) and O ₂ (b ¹ Σ _g ⁺). *Can. J. Chem.* **1969**, *47*, 1870-1877.
(215) Slanger, T. G.; Black, G. O(1 S) quenching by O(3 P). *The Journal of Chemical Physics* **1976**, *64*, 3763-3766.
(216) Hampson, R. F.; Garvin, D.; Transportation, U. S. D. o.; Standards, U. S. N. B. o. *Reaction Rate and Photochemical Data for Atmospheric Chemistry, 1977*; U.S. Department of Commerce, National Bureau of Standards, 1978.
(217) Didyukov, A. I.; Kulagin, Y. A.; Shelepin, L. A.; Yarygina, V. N. Analysis of the rates of the processes involving singlet oxygen molecules. *Sov. J. Quantum Electron.* **1989**, *19*, 578-587.
(218) Gordiets, B. F.; Ferreira, C. M.; Guerra, V. L.; Loureiro, J. M. A. H.; Nahorny, J.; Pagnon, D.; Touzeau, M.; Vialle, M. Kinetic model of a low-pressure N/sub 2/-O/sub 2/ flowing glow discharge. *IEEE Transactions on Plasma Science* **1995**, *23*, 750-768.
(219) Vasiljeva, A. N.; Klopovskiy, K. S.; Kovalev, A. S.; Lopaev, D. V.; Mankelevich, Y. A.; Popov, N. A.; Rakhimov, A. T.; Rakhimova, T. V. On the possibility of O ₂ (a ¹ _g) production by a non-self-sustained discharge for oxygen–iodine laser pumping. *Journal of Physics D: Applied Physics* **2004**, *37*, 2455-2468.
(220) Gudmundsson, J. T.; Thorsteinsson, E. G. Oxygen discharges diluted with argon: dissociation processes. *Plasma Sources Science and Technology* **2007**, *16*, 399-412.
(221) Sharipov, A.; Starik, A. Theoretical Study of the Reaction of Carbon Monoxide with Oxygen Molecules in the Ground Triplet and Singlet Delta States. *J. Phys. Chem. A* **2011**, *115*, 1795-1803.
(222) Hesser, J. E.; Dressler, K. Radiative Lifetimes of Ultraviolet Molecular Transitions. *The Journal of Chemical Physics* **1966**, *45*, 3149-3150.
(223) Schwenker, R. P. Experimental Oscillator Strengths of CO and CO+. *The Journal of Chemical Physics* **1965**, *42*, 1895-1897.

(224) Moore, J. H.; Robinson, D. W. Study of Some Electronic Transition Probabilities in CO and CN. *The Journal of Chemical Physics* **1968**, *48*, 4870-4874.
(225) Smith, G. P.; Golden, D. M.; Frenklach, M.; Moriarty, N. W.; Eiteneer, B.; Goldenberg, M.; Bowman, T. C.; Hanson, R. K.; Song, S.; Gardiner, W. C., Jr.; et al. GRI-Mech 3.0.
(226) Viggiano, A. A.; Ehlerding, A.; Hellberg, F.; Thomas, R. D.; Zhaunerchyk, V.; Geppert, W. D.; Montaigne, H.; Larsson, M.; Kaminska, M.; Österdahl, F. Rate constants and branching ratios for the dissociative recombination of CO2+. *The Journal of Chemical Physics* **2005**, *122*, 226101.
(227) Guðmundsson, J. T.; Lieberman, M. *Recombination rate coefficients in oxygen discharges*; Science Institute, University of Iceland.
(228) Rosén, S.; Peverall, R.; Larsson, M.; Le Padellec, A.; Semaniak, J.; Larson, Å.; Strömholm, C.; Van der Zande, W.; Danared, H.; Dunn, G. Absolute cross sections and final-state distributions for dissociative recombination and excitation of CO+(v= 0) using an ion storage ring. *Physical Review A* **1998**, *57*, 4462.
(229) Thomas G. Beuthe, T. G. B.; Jen-Shih Chang, J.-S. C. Chemical Kinetic Modelling of Non-Equilibrium Ar-CO ₂ Thermal Plasmas. *Jpn. J. Appl. Phys.* **1997**, *36*, 4997.
(230) Whitaker, M.; Biondi, M. A.; Johnsen, R. Electron-temperature dependence of dissociative recombination of electrons with C O + · (CO) n -series ions. *Physical Review A* **1981**, *23*, 1481-1485.
(231) Sennhauser, E. S.; Armstrong, D. A.; Warman, J. M. The temperature dependence of three-body electron ion recombination in gaseous H2O, NH3 and CO2. *Radiation Physics and Chemistry (1977)* **1980**, *15*, 479-483.
(232) Babaeva, N. Y.; Naidis, G. V. On streamer dynamics in dense media. *Journal of Electrostatics* **2001**, *53*, 123-133.
(233) Aleksandrov, N. L.; Kindysheva, S. V.; Kirpichnikov, A. A.; Kosarev, I. N.; Starikovskaia, S. M.; Starikovskii, A. Y. Plasma decay in N ₂ , CO ₂ and H ₂ O excited by high-voltage nanosecond discharge. *Journal of Physics D: Applied Physics* **2007**, *40*, 4493-4502.
(234) Fehsenfeld, F. C.; Dunkin, D. B.; Ferguson, E. E. Rate constants for the reaction of CO2+ with O, O2 and NO; N2+ with O and NO; and O2+ with NO. *Planetary and Space Science* **1970**, *18*, 1267-1269.
(235) Ferguson, E. E.; Van Dorenai, J. M.; Viggiano, A. A.; Morris, R. A.; Paulson, J. F.; Stewart, J. D.; Sunderlin, L. S.; Armentrout, P. B. Internal and translational energy effects on the charge- transfer reaction of CO+2 with O2. *International Journal of Mass Spectrometry and Ion Processes* **1992**, *117*, 261-282.
(236) Fox, J. L.; Benna, M.; McFadden, J. P.; Jakosky, B. M. Rate coefficients for the reactions of CO 2 + with O: Lessons from MAVEN at Mars. *Icarus* **2021**, *358*, 114186.

(237) Coxon, P.; Moruzzi, J. L. Ion-molecule reactions in CO ₂ and CO ₂ -CO mixtures. *Journal of Physics D: Applied Physics* **1977**, *10*, 969-977.
(238) Prasad, S. S.; Huntress, W. T., Jr. A model for gas phase chemistry in interstellar clouds. I - The basic model, library of chemical reactions, and chemistry among C, N, and O compounds. *ApJS* **1980**, *43*, 1.
(239) Adams, N. G.; Bohme, D. K.; Dunkin, D. B.; Fehsenfeld, F. C.; Ferguson, E. E. Flowing Afterglow Studies of Formation and Reactions of Cluster Ions of O2+, O2−, and O−. *The Journal of Chemical Physics* **1970**, *52*, 3133-3140.
(240) Smith, D.; Adams, N. G.; Miller, T. M. A laboratory study of the reactions of N+, N2+, N3+, N4+, O+, O2+, and NO+ ions with several molecules at 300 K. *The Journal of Chemical Physics* **1978**, *69*, 308-318.
(241) Rakshit, A. B.; Warneck, P. Routes to the formation of association products in CO2 from reactions of CO2· CO2+ ions with several neutral molecules. *Zeitschrift für Naturforschung A* **1980**, *35*, 358-360.
(242) Adams, N. G.; Smith, D.; Grief, D. Reactions of HnCO+ ions with molecules at 300 K. *International Journal of Mass Spectrometry and Ion Physics* **1978**, *26*, 405-415.
(243) Miller, T. M.; Wetterskog, R. E.; Paulson, J. F. Temperature dependence of the ion–molecule reactions N++CO, C++NO, and C+, CO+, CO+2+ O2 from 90–450 K. *The Journal of Chemical Physics* **1984**, *80*, 4922-4925.
(244) Fehsenfeld, F. C.; Ferguson, E. E. Thermal Energy Reaction Rate Constants for H+ and CO+ with O and NO. *The Journal of Chemical Physics* **1972**, *56*, 3066-3070.
(245) Chong, S.-L.; Franklin, J. L. High-Pressure Ion–Molecule Reactions in Carbon Monoxide and Carbon Monoxide–Methane Mixtures. *The Journal of Chemical Physics* **1971**, *54*, 1487-1495.
(246) Sieck, L. W.; Gorden, R. Photoionization of CO2-CO-O2 mixtures. Formation and reactions of ion clusters. *J. RES. NATL. BUR. STAN. SECT. A.* **1974**, *78A*, 315.
(247) Dias, T. C.; Fromentin, C.; Alves, L. L.; Tejero-del-Caz, A.; Silva, T.; Guerra, V. A reaction mechanism for oxygen plasmas. *Plasma Sources Science and Technology* **2023**, *32*, 084003.
(248) Smith, D.; Adams, N. G. Reaction of simple hydrocarbon ions with molecules at thermal energies. *International Journal of Mass Spectrometry and Ion Physics* **1977**, *23*, 123-135.
(249) Sieck, L. W. Reactions of (CO ₂) ₂ ⁺ and (CO) ₂ ⁺ association ions. *Int J of Chemical Kinetics* **1978**, *10*, 335-366.
(250) Kinsman, P. R.; Rees, J. A. Ionization, attachment and ion—Molecule reactions in oxygen. *International Journal of Mass Spectrometry and Ion Physics* **1970**, *5*, 71-81.

(251) Williams, S.; Campos, M. F.; Midey, A. J.; Arnold, S. T.; Morris, R. A.; Viggiano, A. A. Negative Ion Chemistry of Ozone in the Gas Phase. *J. Phys. Chem. A* **2002**, *106*, 997-1003.
(252) Zymak, I.; Žabka, J.; Polášek, M.; Tran, T. D.; Španěl, P.; Smith, D. Experimental study of the reaction of O− ions with CO2 molecules with different ternary gases at temperatures relevant to the martian ionosphere. *Icarus* **2021**, *354*, 114057.
(253) Albritton, D. L. Ion-neutral reaction-rate constants measured in flow reactors through 1977. *Atomic Data and Nuclear Data Tables* **1978**, *22*, 1-89.
(254) Lifshitz, C.; Wu, R. L. C.; Tiernan, T. O.; Terwilliger, D. T. Negative ion–molecule reactions of ozone and their implications on the thermochemistry of O3−. *The Journal of Chemical Physics* **1978**, *68*, 247-260.
(255) Parkes, D. A. Oxygen negative ion reactions with carbon dioxide and carbon monoxide. Part 2. *J. Chem. Soc., Faraday Trans. 1* **1973**, *69*, 198.
(256) Fehsenfeld, F. C.; Ferguson, E. E. Laboratory studies of negative ion reactions with atmospheric trace constituents. *The Journal of Chemical Physics* **1974**, *61*, 3181-3193.
(257) Fehsenfeld, F. C.; Ferguson, E. E.; Bohme, D. K. Additional flowing afterglow measurements of negative ion reactions of D-region interest. *Planetary and Space Science* **1969**, *17*, 1759-1762.
(258) Fehsenfeld, F. C.; Schmeltekopf, A. L.; Schiff, H. I.; Ferguson, E. E. Laboratory measurements of negative ion reactions of atmospheric interest. *Planetary and Space Science* **1967**, *15*, 373-379.
(259) Niles, F. E. Airlike Discharges with CO2, NO, NO2, and N2O as Impurities. *The Journal of Chemical Physics* **1970**, *52*, 408-424.
(260) Cenian, A.; Chernukho, A.; Borodin, V.; Śliwiński, G. Modeling of Plasma-Chemical Reactions in Gas Mixture of CO ₂ Lasers I. Gas Decomposition in Pure CO ₂ Glow Discharge. *Contrib. Plasma Phys.* **1994**, *34*, 25-37.
(261) Frommhold, L. Über verzögerte Elektronen in Elektronenlawinen, insbesondere in Sauerstoff und Luft, durch Bildung und Zerfall negativer Ionen (O [−]). *Fortschr. Phys.* **1964**, *12*, 597-642.
(262) Phelps, A. V. Laboratory studies of electron attachment and detachment processes of aeronomic interest. *Can. J. Chem.* **1969**, *47*, 1783-1793.
(263) McFarland, M.; Albritton, D. L.; Fehsenfeld, F. C.; Ferguson, E. E.; Schmeltekopf, A. L. Flow-drift technique for ion mobility and ion-molecule reaction rate constant measurements. III. Negative ion reactions of O− with CO, NO, H2, and D2. *The Journal of Chemical Physics* **1973**, *59*, 6629-6635.
(264) Fehsenfeld, F. C.; Albritton, D. L.; Burt, J. A.; Schiff, H. I. Associative-detachment reactions of O [−] and O ₂ [−] by O ₂ (¹ Δ _g). *Can. J. Chem.* **1969**, *47*, 1793-1795.

(265) Khvorostovskaya, L. E.; Yankovsky, V. A. Negative Ions, Ozone, and Metastable Components in dc Oxygen Glow Discharge. *Contrib. Plasma Phys.* **1991**, *31*, 71-88.
(266) Willis, C.; Boyd, A. W. Excitation in the radiation chemistry of inorganic gases. *International Journal for Radiation Physics and Chemistry* **1976**, *8*, 71-111.
(267) Bass, H. E. Vibrational relaxation in CO2/O2 mixtures. *The Journal of Chemical Physics* **1973**, *58*, 4783-4786.
(268) López-Puertas, M.; Rodrigo, R.; López-Moreno, J. J.; Taylor, F. W. A non-LTE radiative transfer model for infrared bands in the middle atmosphere. II. CO2 (2.7 and 4.3 μm) and water vapour (6.3 μm) bands and N2(1) and O2(1) vibrational levels. *Journal of Atmospheric and Terrestrial Physics* **1986**, *48*, 749-764.

List of publications

First author (or shared first author) papers:

1. Tsonev, I., Biondo, O., & Bogaerts, A. (2025). Simulation of a pulsed CO2 plasma based on a six-temperature energy approach. *Plasma Sources Science and Technology, 34, 015014*. https://doi.org/10.1088/1361-6595/adad14 (= Chapter 4)
2. Tsonev, I., Maerivoet, S., Slaets, J., Reniers, F., & Bogaerts, A. (2024). Coupled multi-dimensional modelling of warm plasmas: Application and validation for an atmospheric pressure glow discharge in CO2/CH4/O2. Chemical Engineering Journal, 492, 152006. https://doi.org/10.1016/j.cej.2024.152006 (not used in the thesis)
3. Tsonev, I., Eshtehardi, H. A., Delplancke, M. P., & Bogaerts, A. (2024). Importance of geometric effects in scaling up energy-efficient plasma-based nitrogen fixation. *Sustainable Energy & Fuels*, *8*, 2191-2209. https://doi.org/10.1039/D3SE01615C (not used in the thesis)
4. Tsonev, I., Boothroyd, J., Kolev, S., & Bogaerts, A. (2023). Simulation of glow and arc discharges in nitrogen: effects of the cathode emission mechanisms. Plasma Sources Science and Technology, 32(5), 054002. https://doi.org/10.1088/1361-6595/acc96c (= Chapter 2)
5. Tsonev, I., O'Modhrain, C., Bogaerts, A., & Gorbanev, Y. (2023). Nitrogen fixation by an arc plasma at elevated pressure to increase the energy efficiency and production rate of NOx. *ACS Sustainable Chemistry & Engineering*, *11*, 1888-1897. https://doi.org/10.1021/acssuschemeng.2c06357 (= Chapter 3)
6. Tsonev, I., Atanasov, N., Atanasova, G., Krcma, F., & Bogdanov, T. (2018). Atmospheric pressure microwave plasma torch for biomedical applications. *Plasma Medicine*, *8, 403-409*. https://doi.org/10.1615/PlasmaMed.2019028816 (not used in the thesis)

Co-author papers:

1. Van Poyer, H. M., Tsonev, I., Maerivoet, S. J., Albrechts, M. C., & Bogaerts, A. (2025). Influence of radial transport and turbulent effects on CO2 conversion in a microwave plasma reactor: Insights from a multi-dimensional thermo-chemical flow model. *Chemical Engineering Journal*, 507, 160688. https://doi.org/10.1016/j.cej.2025.160688
2. Vertongen, R., Tsonev, I., & Bogaerts, A. (2025). Enhancing CO2 conversion with gas quenching in arc plasma. *Chemical Engineering Journal*, 505, 159487. https://doi.org/10.1016/j.cej.2025.159487
3. Fedirchyk, I., Tsonev, I., Marnef, R. Q., & Bogaerts, A. (2024). Plasma-assisted NH3 cracking in warm plasma reactors for green H2 production. *Chemical Engineering Journal*, 499, 155946. https://doi.org/10.1016/j.cej.2024.155946
4. Albrechts, M., Tsonev, I., & Bogaerts, A. (2024). Investigation of O atom kinetics in O2 plasma and its afterglow. *Plasma Sources Science and Technology*, 33, 045017. https://doi.org/10.1088/1361-6595/ad3f4a
5. Wang, K., Ceulemans, S., Zhang, H., Tsonev, I., Zhang, Y., Long, Y., Fang, M., Li, X., Yan, J. and Bogaerts, A. (2024). Inhibiting recombination to improve the performance of plasma-based CO2 conversion. *Chemical Engineering Journal*, 481, 148684. https://doi.org/10.1016/j.cej.2024.148684
6. Albrechts, M., Tsonev, I., & Bogaerts, A. (2024). Can post-plasma CH 4 injection improve plasma-based dry reforming of methane? A modeling study. *Green Chemistry*, 26, 9712-9728. https://doi.org/10.1039/D4GC02889A
7. Benova, E., Marinova, P., Tafradjiiska-Hadjiolova, R., Sabit, Z., Bakalov, D., Valchev, N., Traikov, L., Hikov, T., Tsonev, I. and Bogdanov, T. (2022). Characteristics of 2.45 GHz Surface-Wave-Sustained Argon Discharge for Bio-Medical Applications. *Applied Sciences*, 12, 969. https://doi.org/10.3390/app12030969
8. Bogdanov, T., Tsonev, I., & Traikov, L. (2020, July). Microwave plasma torch for wound treatment. In *Journal of Physics: Conference Series,* 1598, 012001. https://doi.org/10.1088/1742-6596/1598/1/012001
9. Tsvetkov, V., Hinkov, A., Todorov, D., Benova, E., Tsonev, I., Bogdanov, T., Shishkov, S. and Shishkova, K. (2020). Effect of plasma-activated medium and

water on replication and extracellular virions of herpes simplex Virus-1. *Plasma Medicine*, 10(1), 15-26.
https://doi.org/10.1615/PlasmaMed.2020033626

10. Todorova, Y., Yotinov, I., Topalova, Y., Benova, E., Marinova, P., Tsonev, I., & Bogdanov, T. (2019). Evaluation of the effect of cold atmospheric plasma on oxygenases' activities for application in water treatment technologies. *Environmental Technology*, 40(28), 3783–3792. https://doi.org/10.1080/09593330.2018.1491631
11. Nedyalkova, S., Bozhanova, V., Benova, E., Marinova, P., Tsonev, I., Bogdanov, T., & Koleva, M. (2019). Study on the effect of cold plasma on the germination and growth of durum wheat seeds contaminated with Fusarium graminearum. *Int. J. Innov. Approaches Agric. Res*, 3, 623-635. https://doi.org/10.29329/ijiaar.2019.217.8
12. Bogdanov, T., Tsonev, I., Marinova, P., Benova, E., Rusanov, K., Rusanova, M., Atanassov, I., Kozáková, Z. and Krčma, F. (2018). Microwave plasma torch generated in argon for small berries surface treatment. *Applied Sciences*, 8(10), 1870.
https://doi.org/10.3390/app8101870
13. Krčma, F., Tsonev, I., Smejkalová, K., Truchlá, D., Kozáková, Z., Zhekova, M., Marinova, P., Bogdanov, T. and Benova, E. (2018). Microwave micro torch generated in argon based mixtures for biomedical applications. *Journal of Physics D: Applied Physics*, 51(41), 414001.
https://doi.org/10.1088/1361-6463/aad82b

Patent applications

1. European patent application on "Industrial plasma reactor" May 2023: (No. EP23173835.2)
Inventors: I. Tsonev and A. Bogaerts

Conference contributions

Oral presentations:

1. Plasma 101: From TVs to lightning – understand how plasma can make the world a better place – Invited webinar talk in the framework of an EU-FTI project. 17 June, 2021.
2. Non-equilibrium high flow rate plasma reactor for nitrogen fixation – 25th International Symposium on Plasma Chemistry, 21-26 May, 2023, Kyoto, Japan.

Poster presentations:

1. Simulation of a pulsed CO_2 plasma based on a six-temperature energy approach – Europhysics Conference on Atomic and Molecular Physics of Ionized Gases, 9-13 July, 2024, Brno, Czech Republic.
2. Glow and arc discharges in atmospheric pressure nitrogen – International Conference on Phenomena in Ionized Gasses, 9-14 July, 2023, Egmond aan Zee, The Netherlands.